CHEMICAL VAPOR DEPOSITION OF NITRIDES FOR ELECTRONIC DEVICE APPLICATIONS

BY

STEVEN WAYNE JOHNSTON

A DISSERTATION PRESENTED TO THE GRADUATE SCHOOL OF THE UNIVERSITY OF FLORIDA IN PARTIAL FULFILLMENT OF THE REQUIREMENTS FOR THE DEGREE OF DOCTOR OF PHILOSOPHY

UNIVERSITY OF FLORIDA

2000

LD
1780
20 00
.J73

UNIVERSITY OF FLORIDA
3 1262 08554 4624

I dedicate this dissertation to my parents, to my grandmothers Gladys Player and Della Johnston, and to the memory of my late grandfather Thomas Johnston.

ACKNOWLEDGEMENTS

I would like to express my gratitude to the many people who have helped, both professionally and personally, to make this work possible. First I would like to thank my supervisor and mentor, Dr. Tim Anderson, who has given me encouragement and support for five years and knowledge that I will use throughout my life. I am also in debt to Dr. Lisa McElwee-White of the Department of Chemistry for providing the precursor complexes for a substantial portion of this work and for securing funding for the tungsten nitride project. Thanks must also be given to Dr. Paul Holloway, Dr. Fan Ren, and Dr. Spyros Svronos for offering their insight and expertise in assisting me in interpreting the results of my work and for agreeing to be part of my defense committee.

I would like to thank my many coworkers in my research group as well as other departments, in particular Daniel Crunkleton, Muhsin Ider, Omar Bchir, and Dr. Albert Davydov for their support through the years. Special thanks must be given to Dr. Roger Aparicio for the incalculable hours he spent teaching me the experimental system I used, the intricacies of thermodynamic equilibrium modeling, and for continued friendship after his graduation. I must also acknowledge Dr. Jianyun Shen and Dr. Weidong Zhuang for assistance and expertise in the collaborative work on equilibrium in the Ga-N and W-N systems. I am very grateful to Pete Axson and Dennis Vince for their assistance in repairing and modifying my experimental system, the SEM, and general lab modifications. Thanks also go to members of Dr. McElwee-White's research group–

Carlos, Ying, Yue, Cara, Ayed, Jennifer, and Denise - for synthesizing the chemicals for the tungsten nitride portion of my work.

I must acknowledge Yunaima Hernandez for her close friendship that has continued even in the years after her graduation. She has always been someone I've turned to for "non-sugarcoated" advice on all matters. Amalia Cuadra has been a wonderful friend ever since we met under circumstances that are not conducive to closeness. I will always treasure our probing late-night discussions, her affable personality and infectious laughter, and her assistance in conducting thin film depositions and characterization.

My deepest thanks go to Dr. Nesrin Olten for the love and strength she gave me during some of the darkest moments of my life so far. Çok teşekkür ederim, Umarim herşey iyi olacak ve birbirimize kavuşacağız, and Patates.

I owe a tremendous amount to Angela Hays for her love and support during my years as an undergraduate and graduate student. Knowing that she was backing me made obtaining both degrees much easier than they otherwise would have been.

Finally I would like to thank my family-my sisters Stephanie and Andrea, my mother Kay and my father Wayne--for the love and strength they've given me throughout my life. Their sacrifice and encouragement throughout the years has contributed heavily to the person I am today and, though not always acknowledged, has never gone unrecognized.

TABLE OF CONTENTS

PAGE

ACKNOWLEDGEMENTS iii

ABSTRACT viii

1. INTRODUCTION
    - 1.1 Statement of Problem 1
    - 1.2 Overview of the Literature
        - 1.2.1 Boron Phosphide (BP) 5
        - 1.2.2 Boron Nitride (BN) 11
        - 1.2.3 Tungsten Nitride (WN_X) 19
        - 1.2.4 Gallium Nitride (GaN) 26
    - 1.3 Thermodynamic Equilibrium Modeling
        - 1.3.1 Introduction 31
        - 1.3.2 Computational Methods 33
        - 1.3.3 The Chemical System and Thermochemical Data ... 37
    - 1.4 Chemical Vapor Deposition Process
        - 1.4.1 Overview 39
        - 1.4.2 Experimental System and Procedure 46
    - 1.5 Overview and Scope of the Present Work 54

2. THERMODYNAMIC MODELING OF BP, BN, AND GaN CVD
    - 2.1 Boron Phosphide
        - 2.1.1 Introduction 57
        - 2.1.2 Results and Discussion 61
        - 2.1.3 Conclusions 90
    - 2.2 Boron Nitride
        - 2.2.1 Introduction 91
        - 2.2.2 Results and Discussion 95
        - 2.2.3 Conclusions 112
    - 2.3 Gallium Nitride
        - 2.3.1 Introduction 113
        - 2.3.2 Strain Energy Formula Derivation 114
        - 2.3.3 Lattice Mismatch and Strain Energy Calculation 119
        - 2.3.4 Results and Discussion 123
        - 2.3.5 Conclusions 134

3. GROWTH OF BP BY CVD
    - 3.1 Introduction 135

3.2 Experimental......135
3.3 Results and Discussion
    3.3.1 Growth Rate......137
    3.3.2 Microhardness......141
    3.3.3 Conductivity......142
    3.3.4 Surface Morphology......142
    3.3.5 X-ray Diffraction......150
    3.3.6 FTIR and Raman Spectroscopy......151
    3.3.7 AES and TEM......157
3.4 Conclusions......161

4. GROWTH OF BN BY CVD
4.1 Introduction......163
4.2 Experimental......164
4.3 Results and Discussion
    4.3.1 Surface Morphology......166
    4.3.2 FTIR and Raman Spectroscopy......171
    4.3.3 AES and XPS......181
    4.3.4 TEM......187
4.4 Conclusions......187

5. GROWTH OF WN_X BY MOCVD
5.1 Introduction......189
5.2 Experimental......190
5.3 Results and Discussion–Precursor Characterization......193
5.4 Results and Discussion–Thin Film Growths
    5.4.1 Surface Morphology......197
    5.4.2 X-ray Diffraction......200
    5.4.3 AES and SIMS......203
    5.4.4 Four Point Probe......206
5.5 Conclusions......207

6. CONCLUSIONS AND RECOMMENDATIONS FOR FUTURE WORK
6.1 Conclusions......209
6.2 Recommendations for Future Work......213

REFERENCES......217

APPENDICES

A. FORTRAN SOURCE CODE OF MODIFIED EQUILIBRIUM ALGORITHM......246
B. USER'S GUIDE FOR THE FORTRAN SOURCE CODE OF APPENDIX A......305

C. FORTRAN SOURCE CODE FOR ENSURING ACCURATE THERMOCHEMICAL DATA TRANSFER TO THE CHOSPEC.DAT INPUT FILE.. 323
D. USER'S GUIDE FOR THE FORTRAN SOURCE CODE OF APPENDIX C.. 331

BIOGRAPHICAL SKETCH.. 334

Abstract of Dissertation Presented to the Graduate School
of the University of Florida in Partial Fulfillment of the
Requirements for the Degree of Doctor of Philosophy

CHEMICAL VAPOR DEPOSITION OF NITRIDES FOR ELECTRONIC DEVICE APPLICATIONS

By

Steven Wayne Johnston

August 2000

Chairman: Dr. Timothy J. Anderson
Major Department: Chemical Engineering

The chemical vapor deposition (CVD) of boron phosphide (BP), boron nitride (BN), and tungsten nitride (WN_x) thin films onto a variety of substrates was investigated. The purpose of the BP and BN studies was to study the viability of depositing and stabilizing the cubic phase of boron nitride (cBN). Tungsten nitride growths were conducted to determine the suitability of novel imido precursors for copper/silicon diffusion barrier applications.

Thermodynamic models of various BP, BN, and GaN based systems were developed using BCl_3-PCl_3-H_2, BCl_3-NH_3-H_2, and Ga-N as reactants, respectively. Results revealed conditions leading to many solid phase domains including BP, cBN, and GaN. Reactant ratios were systematically varied and the influence of HCl and an inert gas (He) was studied. Phase diagrams generated for the strained Ga-N system showed the profound influence of lattice mismatch induced strain energy on a system's thermodynamic equilibrium.

CVD of cubic BP thin films from BCl_3, PCl_3, and H_2 reactants onto silicon, sapphire, diamond, silicon carbide, and nickel substrates revealed a kinetically controlled growth process. Characterization revealed roughly spherical island coalescence growth and little contamination. BP films were subsequently in-situ nitrided using NH_3 diluted in a H_2 carrier gas stream in an attempt to obtain cubic BN using the underlying cBP template. Attempts by 5 other researchers have produced contradictory results with film characterization limited mostly to X-ray diffraction (XRD). A much wider array of deposition conditions and analysis techniques were used to characterize films in this study. Results indicate cBN stabilization may be possible using in-situ cBP nitridation. These are the first results ever confirmed using multiple characterization techniques.

Metal-organic CVD (MOCVD) of tungsten nitride thin films was also investigated. Results using a solid-source delivery system were unsuccessful due to the low vapor pressure and poor thermal sublimation profiles of each precursor. Film growths using an ultrasonic delivery system, where the precursors are dissolved into a solvent and injected into the reactor in a nebulized mist, proved to be more successful. Low resistivity WN_X films deposited at low temperature were obtained. A U.S. patent application has been submitted as a result of this work.

CHAPTER 1
INTRODUCTION

1.1 Statement of Problem

Both economic and technological requirements have motivated advancements in the growth of wide band gap semiconductor thin films ($E_g > 2.0$ eV) [1,2]. Many solid state devices and other materials combinations such as ceramic matrices utilize thin films that have been sequentially deposited on an underlying film or substrate. This stacking of film layers enables the production of devices of variable composition, thickness, etching patterns, and function from one film layer to the next. Applications of thin films can be found in the microelectronics industry (diffusion barriers, transistors, ultra-large scale integrated circuits, and high power rectifiers), optoelectronics and telecommunications industry (solid state lasers and optical fibers), photoelectrochemical industry (protective window coatings), as well as passivating and wear resistant coatings. As a group, wide band gap semiconductors possess many sought after properties including resistance to oxidation and chemical attack, resistance to wear, short wavelength photon production upon electron-hole recombination, and stability under extreme electronic and optoelectronic operating conditions. Device fabrication from these materials with operating characteristics exceeding the current industry standards should thus be possible. For instance, the band gap of GaN is 3.4 eV while the largest band gap possible using the $Ga_xIn_{1-x}As_yP_y$ or Al_xGa_{1-}

$_x$As$_y$Sb$_{1-y}$ systems is 2.3 eV [3]. Thus GaN light emission is in the ultraviolet (UV) wavelength while the other systems emit in the visible spectrum.

Despite these advantageous properties, reliable, low cost methods to produce thin film devices using these materials have not been known until recently. Moreover, for cubic boron nitride (cBN), this information is still largely unknown. Not only must desired film properties such as purity, doping levels, crystallinity, and surface morphology be considered, the ease and cost of producing each film must also be evaluated. Furthermore, auxiliary concerns such as precursor, product, and by-product toxicity, environmental impact, and reactor throughput must be evaluated before a particular process is industrially practical.

Chemical vapor deposition (CVD) has been used in the microelectronics industry for over thirty years to deposit a wide range of materials including ceramics, dielectrics, conductors, and insulators. Metal-organic chemical vapor deposition (MOCVD) has emerged in the last 20 years as a viable alternative to strictly thermal halide CVD. Moreover, as processing requirements become more stringent (e.g., smaller feature sizes, larger cost investment of manufacturing larger diameter wafers) the suitability of using the CVD/MOCVD technique for microelectronic applications likewise increases. It has a higher throughput, smaller equipment and maintenance costs, and less pump-down time than do ultra-high vacuum (UHV) techniques such as molecular beam epitaxy (MBE). Its crystal purity is generally greater than those of various melt and ion sputtering techniques while its film conformality to underlying features and elimination of shadowing effects makes it a more attractive deposition method than physical sputtering.

Products generated using CVD include high performance ceramic tool bits, protective coatings against oxidation and wear, lasers, light emitting diodes, and field effect transistors. This method has been used to deposit numerous material systems including such commercially important materials as SiO_2, $Al_xGa_{1-x}As$, $Ga_xIn_{1-x}N_yP_{1-y}$ ($x,y \leq 1$), BN, CdS, $CuInSe_2$, and GaN. There are three general types of CVD: thermal, metal-organic, and energetic particle bombardment techniques such as plasma, ion, and laser assisted CVD.

Thermal CVD is the most common and longest used technique in industry. It is in many ways the simplest of the three types of CVD. Advantages of this technique include the wide array of available precursors, mostly in liquid and gas states, as well as lower energy costs compared to energized particle CVD. Furthermore, the technology associated with it is simple and fairly well understood on both theoretical and experimental levels. Disadvantages focus primarily on the usually high deposition temperature required for halide precursor chemistries (e.g., $GaCl_3$, $SiCl_4$) and the historic use of highly toxic gases (e.g., AsH_3 and PH_3). While high processing temperature can improve the film's eventual crystalline perfection, it also tends to enhance unintentional impurity incorporation and can alter the results of previous processing steps. Thermal CVD, like all other CVD processes, is also limited to film thickness control of 2-3 monolayers unlike UHV techniques such as MBE that allow single monolayer growth control.

More recently MOCVD has attracted widespread interest. MOCVD is used primarily to lower the required deposition temperature and to avoid the formation of HX (X=Br, Cl, I) compounds resulting from precursor decomposition and reaction of the halide precursor with a H_2 carrier gas. The formation of these HX compounds can lead to both substrate and film etching as well as corrosion of the deposition system itself.

Disadvantages of MOCVD include the limited number of available precursors as well as, in some cases, the toxicity of these precursors. Furthermore, only recently has precursor purity approached that of the traditionally available CVD gas sources. If suitable precursors are available, however, then MOCVD incorporates in it many if not all of the favorable deposition features of CVD along with its own unique advantages.

Energetic particle CVD is used to promote precursor dissociation and chemical reaction inside the reactor by supplying the necessary energy for chemical bond breaking via energetic radiation. It can also be used to seed/implant films and promote stabilization of metastable phases (e.g., cubic boron nitride). This can also result in a decrease in the required deposition temperature that is beneficial if temperature-sensitive substrates or films (e.g., low k dielectric polymers or low-melting point metals) are used. Another potential advantage is the reaction selectivity that is possible when radiation of precisely controlled energy is used. Disadvantages arise from the fact that the substrate and later the film are being constantly bombarded by energized particles. Impurities can be incorporated in the growing films from the incident ion beam, surface bonds can be broken by high-energy radiation which is undesirable for large grain or epitaxial film growth, and non-equilibrium defect (interstitial and vacancies) generation can occur. All can substantially alter the electrical, mechanical, and chemical properties of the thin film. The experiments for this dissertation research were conducted using either thermal CVD or MOCVD. Under certain experimental conditions (i.e., inert carrier gas, low pressure, and high temperature) a plasma was formed. The effect of this plasma on the resulting precursor dissociation and film growth, however, is believed to have been negligible. A more in-depth review of CVD fundamentals and effects of operating parameters on film growth will be presented in section 1.4.

Table 1.1 Mechanical and electrical properties of BP, BN, and GaN compared to Si

Property	Si	BP	BN	BN	GaN
Crystal Structure	Diamond	ZB	ZB	Hexagonal	Wurtzitic
Lattice Constant (Å)	5.431	4.537	3.615	a=2.534 c=4.191	a=3.210 c=5.237
Band Gap (eV)	1.1	2.3	6.4	5.8	3.4
Band Transition	Indirect	Indirect	Indirect	Indirect	Direct
Conductivity Types	p,n	p,n	p,n	p,n	p (low), n
Electrical Resistivity (Ω-cm)	10^5	10^{12}	10^{14}-10^{17}	N/A	10^{-3}-10^{-2}
Density (g/cm^3)	2.33	2.40	3.48	2.18	6.10
Hardness (GPa)	11	30-35	40-60	N/A	N/A
Melting Point (°C)	1410	* 1130	3000	** 2600	*** 782
Linear Thermal Expansion Coefficient (W/cm-°C) x 10^6	2.9	4.0	4.8	2.7	5.6
Thermal Conductivity (W/cm-°C)	1.5	3.5	13	N/A	1.3

Note: ZB = Zincblende

* BP decomposition to $B_{13}P_2$

** hBN decomposition to B(s) + N_2

*** GaN sublimes (1 atm) at this temperature

1.2 Overview of the Literature

A listing of many of the relevant properties of the semiconducting compounds considered as well as their comparison to silicon is shown in Table 1.1.

1.2.1 Boron Phosphide

Boron monophosphide (BP) is a III-V semiconducting compound. It has a $\overline{T}^2_d$-F43m space group and a lattice parameter of 4.5383Å [4]. Welker and Weiss were the first to predict that boron phosphide crystallizes in a zincblende structure (Figure 1.1) [5].

Popper and Ingles and Perri et al. indeed observed this zincblende crystal structure a few years later [6,7]. Although BP only crystallizes in the zincblende structure, it was observed first by Williams and Ruehrwein [8] and later by Matkovich, Spinar and Wang, and Peret [9-11] that BP decomposes into a rhombohedral subphosphide. On the basis of weight loss and chemical analyses of the decomposition product Williams and Ruehrwein determined that BP undergoes decomposition to $B_{5-7}P$ subphosphide, tentatively assumed to be B_6P analogous to the boron silicon compound B_6Si. A year later, however, Matkovich determined this decomposition product to be $B_{13}P_2$ based on calculations of the rhombohedral unit cell size and density. He also used weight loss during BP decomposition at 1600 °C to determine a boron to phosphorus ratio of 6.3. Chemical analysis of the same samples yielded ratios ranging from 6.4 to 6.5. Spinar and Wang, and Peret et al. corroborated the $B_{13}P_2$ stoichiometry in a series of calculations and X-ray analysis experiments, respectively.

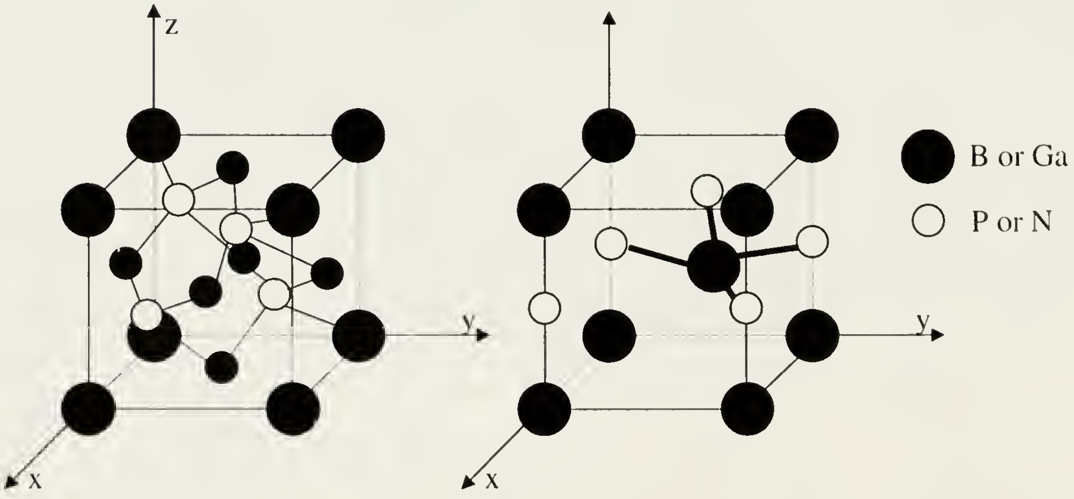

Figure 1.1 Schematic of a) zincblende and b) wurtzitic crystal structures

An amorphous modification, B_xP (x>1), of variable stoichiometry has also been reported [8,12-14]. This variable stoichiometry is not unexpected, particularly at elevated temperatures, since as BP begins to decompose into $B_{13}P_2$ it must gradually lose phosphorus atoms. Groot et al. have shown that this amorphous boron-rich compound can be deposited at lower temperatures (<900 to 1120 °C) and a wide range of initial molar ratios [15].

While research on the growth of BP is very limited compared to many of the III/V compounds, it does possess physical properties that make it attractive for several applications. It was first thought that BP was a wide band gap semiconductor with a transition energy near 6.0 eV [16,17]. Subsequent studies, however, have indicated that boron phosphide actually has a much smaller indirect energy gap of 2.0 eV [18,19]. BP also exhibits many of the characteristics of hard ceramics. These include being a Vickers hardness similar to that of TiN [12,20,21], a high thermal conductivity, low thermal expansion, and good resistance to chemical corrosion and wear [22]. BP also has a high carrier mobility for both holes and electrons [4,23].

The combination of these properties makes it an attractive material for many applications including thermoelectrics [24], power rectifiers [25], transistors [26], and solid state neutron devices [27]. Investigations of BP for use in diode applications (including tunneling diodes) have been conducted by several authors [28-33]. Takenaka produced Sb/n-BP Schottky diodes by mask evaporating Sb onto n-BP wafers. He measured a refractive index of 3.1 and a dielectric constant of 11 which satisfies the relation in III-V compounds that the dielectric constant is slightly larger than the square of the refractive index. Two years later Takenaka et al. produced a BP wide band gap emitter transistor with a common emitter current gain (β) of 16 and an injection efficiency of 94% for the emitter heterojunction. Kumashiro made Au/n-BP Schottky diodes with a barrier height of 1.4 eV. These results were similar to those of Takenaka and consistent with the unified model for Schottky barrier formation in III/V compounds, which predicts that barrier height is independent of the metal and is 2/3 of the energy bandgap (2/3*(2.0 eV) ≈1.4 eV).

Perhaps the most promising industrial application of BP is its use as a ceramic hard coating [12,34,35], specifically as a protective optical window for photoelectrochemical cells (PEC) [36-39]. In fact, Harris has commented that BP is an excellent protective coating in low temperature applications where emittance is not an issue and some loss of transmittance can be tolerated [40]. Goossens et al. showed that the conduction bands of Si and BP are well aligned but a 0.9 eV barrier exists for holes transported from the Si to the BP valence band. They then utilized this barrier to fabricate an p-Si/n-BP heterojunction photo-electrochemical cell where electrons were easily transported through the BP film layer to the outside electrolytic solution while holes were confined in the Si by the barrier. Takenaka et al. produced a BP window solar cell with a conversion efficiency of 8.3% while the same solar cell without the BP window was only 6.5% efficient [33].

Moisson first reported the formation of BP in 1891 from the reaction of boron iodide with phosphorus to form BPI_2 and its subsequent reaction with iodine to form BP and I_2 (41-43). Besson also prepared boron phosphide in 1891 from the reaction of BBr_3 and PH_3 and decomposition of the resulting BBr_3PH_3 adduct (13). After these reports though, interest in BP research apparently waned and papers on the topic were not again published until the late 1950's. Since then several techniques have been used with varying success to synthesize BP crystals. Probably the simplest technique is direct BP crystal synthesis from the its pure elements. Popper and Ingles and Perri et al. used an evacuated, sealed silica tube reactor at 1100 and 1000 °C, respectively [6,7]. Kobayashi used pressures from 5 to 25 kbar and temperatures from 500 to 2500 °C to synthesize BP crystals [44]. Ananthanarayanan et al., in a slight variation from direct crystal growth from the pure elements, used mixtures of the B-O-P system at pressures and temperatures above 20 kbar and 1200 °C to grow BP crystals [45]. They researched 3 different mixtures: a) B and BPO_4, b) B and P_2O_5, and c) B, P_2, and B_2O_3.

A flux melt method from the elements using a solution of a metal melt containing dissolved boron and phosphorus has also been used. Stone utilized a nickel melt at 1400 °C to synthesize BP crystals [46]. Wang et al. investigated used the flux method and several different melts (Ni, Fe, Pt, and Ge) to convert a microcrystalline powder to single crystals [19]. Sterns and Greene, Burmeister and Greene, and Iwami et al. used a Ni melt and the same method as Wang et al. [47-51]. Chu et al. extended this study to a Cu melt, reexamined the previous Ni melt work, and used an accelerated container rotation technique to obtain larger single crystals compared to the traditional stationary container metal flux technique [52,53]. Kato et al. further examined BP synthesis using a Cu melt [54]. Finally a high pressure metal flux method was employed by Kumashiro et al. in the N-B-P and Cu-B-P systems to prevent decomposition of the BP crystals into $B_{13}P_2$ at temperatures above 1130 °C [55].

Vickery examined BP formation from the thermal dissociation of adducts formed by mixing BCl_3/PCl_5 and BBr_3/PH_3 precursors [56]. These were used to form $BCl_3 \bullet PCl_5$ and $BBr_3 \bullet PH_3$ adducts, respectively. The phosphine containing adduct was found to result in a higher BP yield. Samsonov investigated the reaction of solid amorphous boron with phosphine (PH_3) and reported the formation of BP using this intermediate process between the strictly condensed phase chemistries described above and the vapor phase deposition techniques described below [57].

Schroten investigated using a vapor-liquid-solid (VLS) mechanism by dipping various substrates in a nickel or silver acetate solution prior to BP CVD growth using the BBr_3-PBr_3-H_2 chemical system [58]. He found that BP whisker growth occurred if the substrates were dipped in either solution before growth. In contrast, if the substrates were not dipped then BP layers were deposited.

Most applicable to the microelectronics industry, BP films have been successfully deposited using chemical vapor deposition. MOCVD of BP has been performed by reacting methyl and ethyl alkyls of boron with PH_3 (59). Thermal CVD growths by hydride and halide chemistries have also been reported by numerous investigators in the 700 to 1300 °C temperature range at different precursor partial pressures and system total pressures. B_2H_6 and PH_3 precursors using a H_2 carrier gas have been used extensively and high quality films have been deposited using them (60-68). Although halide based chemistries produce large amounts of HCl or HBr byproducts which can subsequently etch the growing film, pit the substrate, or damage the reactor system itself, they have attracted widespread interest since the precursors themselves are far less toxic than their hydride based counterparts. The BBr_3-PCl_3-H_2 [61,69-71], BBr_3-PBr_3-H_2 [12,15,72-75], BCl_3-PH_3-H_2 [8], and BCl_3-PCl_3-H_2 [20,49] systems have all been used successfully to deposit BP. Motojima used the BCl_3-PCl_3-H_2 system but considered reactions involving Ar gas [35] and a nickel impurity [76]. These experiments were generally conducted at or near atmospheric pressure with a temperature range of approximately 750 to 1200 °C. The lower temperature marks the limit where the boron/halide bonds dissociate efficiently while the upper temperature is a result of the aforementioned decomposition of BP into its subphosphide $B_{13}P_2$.

Chemical vapor transport of BP previously formed by either the pure element, metal flux or CVD methods has been achieved using reactive vapors. Typically the transporting medium are the group VI elements of the periodic table [77] and iodine [78]. Chu et al. investigated phosphorus trichloride, bromine, and iodine as transport agents and found that iodine and bromine resulted in better BP crystal synthesis [69].

1.2.2 Boron Nitride

Boron nitride is a III/V indirect band gap semiconductor which crystallizes in two dense forms with sp^3 bonding - cubic (cBN) [79,80] and wurtzitic (wBN) [81] and two graphite-like forms with sp^2 bonding - hexagonal (hBN) [82,83] and rhombohedral (rBN) [83,84]. These forms parallel similar modifications of carbon, namely diamond and graphite, respectively. A highly disordered sp^2 bonded turbostratic form of boron nitride (tBN) has also been reported [80,85]. The lattice parameter of cBN is 3.6157 Å while that of the hexagonal structure is a=2.5039 and c=6.6612 Å [4].

Having properties similar to those of diamond, cBN has attracted widespread interest as a promising semiconductor device material [80,81,86]. It possesses the largest band gap energy (≈6.4 eV) [87,88] in the III/V family and good thermal conductivity [89] which make it a candidate for the same high-temperature (>600 °C) and high-power electronic device applications envisioned for diamond [90-92]. At nearly 5000 kg/mm^2 its Vickers hardness is second only to that of diamond [87,88,93,94] and hence an ideal candidate for ultrahard protective coatings. Powers et al. have report a negative electron affinity for cBN which may open up numerous novel electronic device capabilities in the future including high brightness electron emitters [95].

In addition cBN has several advantageous properties over diamond. First it can be doped to give both n- and p-type conductivity (unlike diamond which can only be easily doped p-type) [79,96]. Therefore, cBN could be used to produce short wavelength optoelectronic devices [97-99]. In fact, a UV light emitting photodiode with a peak wavelength near 260 nm has been produced from a cBN bulk crystal p-n junction formed by a high-temperature / high-pressure method (discussed below) [96-98,100]. Furthermore, unlike diamond, cBN: i) will not react with carbide forming metals [88,101,102], ii) has a high resistance to oxidation at temperatures up to 1300 ^{o}C [87,88], and iii) can be passivated with an oxide layer [92] thus making it an attractive material for use in machining ferrous alloys. Finally, thin films of cBN can be deposited at lower temperatures compared to diamond, which can prevent thermal damage to prior device patterning steps [102]. The interest in hBN, though not as great as that of cBN, lies mainly in its use as a refractory material and a lubricant [103,104].

Despite cBN's many advantageous properties, two major obstacles in obtaining device quality cBN is the lack of an effective, low cost technique for thin film growth and the lack of large area thin films. Wentorf first studied the direct transformation of hexagonal boron nitride crystals to cubic boron nitride crystals using catalytic agents at elevated temperatures and pressures [80,105]. Several authors later studied this phase transformation using a variety of catalysts with Mishima et al. reporting cBN single crystals ≈ 3mm in size [106-116]. Although each produced cBN crystals, there was significant variation in the pressure-temperature (P-T) phase transformation line depending on the catalyst used. Balchan et al. and Bundy et al. subsequently studied this transformation without using catalytic agents and determined that they were in fact not needed for cBN formation [81,117]. Unfortunately there are problems with this method relating to the size of cBN crystal, background impurity levels, the lack of a thin film (which is required for microelectronic device applications), and the extreme processing conditions required (minimum of 45 kbar and 1600 ^{o}C using catalysts and 115 kbar and 2300 ^{o}C without catalysts).

Efforts to produce cBN by thermal CVD have resulted in verifiable and reproducible growth of only hBN or amorphous BN [118]. In 1921 Mayer et al., using BCl_3 and NH_3 as precursors, were the first to successfully deposit hBN films [119]. Previous to this BN had only been synthesized in the powder form. Hydride CVD chemistries investigated focus on B_2H_6-NH_3-H_2-N_2(Ar) [120-122] and BH_3-NH_3 [84,123-125]. Rand and Roberts found for the B_2H_6-NH_3-X system deposition rates between 12.5 to 60 nm/min for X=H_2 or He and roughly 100 nm/min for X=N_2. Boronian deposited BN films thinner than 1000Å on quartz substrates at slightly higher temperatures.

CVD of BN films has also been accomplished using BCl_3 and NH_3 as precursors in either a reactive (H_2) or inert (Ar) carrier gas atmosphere. Each has been extensively studied [84,126-138]. It was found that substrate selection influenced the resulting BN film's preferred crystallographic orientation [84,126,127]. Takahashi et al. determined that iron and nickel substrates were best for forming BN crystalline deposition with the first layer of BN growth apparently initiated by a catalytic interaction with the substrate [131,132]. Pierson investigated the reaction between BF_3-NH_3 [139] while Constant and Feurer studied the decomposition of hexachloroborazine ($B_3N_3Cl_6$) [140]. As with the other more widely researched CVD chemistries, both analyses indicated the presence of only hexagonal BN films. Nakamura studied BN deposition employing metal-organic CVD using triethylboron or trimethoxyborane and ammonia in hydrogen and molecular flow CVD (MFCVD) using decaborane with ammonia [141,142]. X-ray diffraction (XRD) and Fourier transform infrared spectroscopy (FTIR) determined the BN films consisted of hexagonal and amorphous BN crystals for MOCVD and MFCVD, respectively. Low pressure CVD (LPCVD) has been studied using the pyrolysis of trichloroborazole [143,144], pyrolysis of borazine [145], BCl_3-NH_3 [146], and B_2H_6-NH_3 [147], and borazine [145,148]. Guentert was able to obtain continuous hBN thin films at pressures as low as 2.6 Pa.

There have been reports of cBN film synthesis using either thermal or low energetic deposition processes. Examples include hot filament assisted evaporation of boron [149,150], MOCVD [151,152], and ‘non-assisted’ PLD [153-159]. In one of these cases the primary supporting evidence of cBN formation [155] was later discovered [160] to be a transmission electron microscopy (TEM) analysis artifact. As noted by Mirkarimi et al., analysis of these results generally was performed by an insufficient number of supporting characterization techniques or the characterization data contain irregularities or inconsistencies. Furthermore, unlike cBN synthesis from energetic particle processes, these techniques have not been readily reproduced in other laboratories around the world [161].

Thin cBN films have been produced, and verifiably reproduced, using direct growth energized particle techniques. In fact, recent advances in energized particle deposition have yielded films of phase purity approaching 90% cBN/10% hBN [162]. These films have been characterized by a wide variety of techniques, each of which indicates the presence of cBN. Given the inability to form cBN thin films using the above non-energized techniques, virtually all cBN research over the last 10 years has focused on these energized growth methods. Given this fact and the plethora of papers published during this short time period, this literature review will concentrate primarily on the more recent reports since the mid-1980's. The energized growth techniques recently investigated include plasma-assisted CVD (PACVD), sputtering, electron beam evaporation/activated reactive evaporation, and ion-assisted laser deposition.

Plasma-assisted CVD (PACVD) was one of the first techniques used to deposit nearly pure cBN films [101,163-167]. Source gases investigated that have resulted in cBN film depositions include B_2H_6 in N_2 [163,164,168-171], B_2H_6 in NH_3 [172], BH_3 and NH_3 in H_2 [173], $NaBH_4$ in NH_3 [174], $hBN(CH_3)_3$ in N_2 [175], and $B_3N_3H_3(CH_3)_3$ in N_2 [176]. The use of hydride precursors, especially B_2H_6, is attractive because of their ability to lower to the required deposition temperature ($\leq 400\ ^{o}C$). The toxicity concerns associated with diborane (and phosphine in BP deposition) must be, however, weighed against its lower deposition temperature requirement.

Sputtering is a common deposition technique due to its simplicity. For microelectronic device applications, however, it has limited use because of its inability to adequately pattern underlying high aspect ratio contact holes due to shadowing effects. It should be emphasized, though, that for certain less aggressive topographies (such as coating abrasive cutting wheels for ultra-hard machining applications), sputtered cBN deposition is very applicable. Regardless, after an initial period of low content cBN depositions [177-179], high cBN content sputtered films are now routine [178,180-198].

Inagawa et al. were the first to deposit nearly pure cBN phase films using electron beam evaporation [199]. They characterized their films using FTIR and transmission electron diffraction (TED) and found that mixing argon to the reactant N_2 gas assists formation of the cubic phase of BN. Numerous other authors have subsequently investigated this deposition technique with similar success [200-214]. Films have been successfully deposited both when the substrate was and was not biased. In a slight deviation from the typical process Lu et al. grew high content cBN films using a Kaufman-like source that generated energetic neutrals instead of ions [215]. Chopra and coworkers, in a process similar to Inagawa et al. [199], have modified the traditional technique by using activated reactive evaporation of H_3BO_3 in an NH_3 plasma [216]. Carbon and oxygen contaminates, however, were reported in the films.

Ion assisted laser deposition has been used extensively to deposit polycrystalline BN films [162,217-222]. Using this technique researchers have managed to obtain films with a high cBN content ($\geq$ 85%). As Mirkirimi et al. note, although laboratory success has been achieved, the prospects for industrial application using this technique are questionable due to scale-up limitations and particle incorporation (originating from the target) in the film [161]. Typically the laser is pulsed at the target. Mineta et al., however, have synthesized cBN films by using a continuous CO_2 laser focused on a hBN target with a traditional ion flux [233]. There have also been a number of reports of ion beam deposition, where an electron beam rather than a laser is used to evaporate a boron or hBN target [218,220,224-242].

Other energized deposition techniques that have been successfully used to deposit high content cBN films include i) mass-separated ion-beam deposition (MSIBD) [243,244],

ii) use of a low-density supersonic plasma jet fed by BCl_3 and N_2 [245], iii) cathodic arc evaporation [246-248].

Formation of BN films has been reported using nitridation of cubic boron phosphide samples at both atmospheric and high pressure. Vickery first reported results using this process in 1959 [56]. BP films, described in the previous BP section, were nitrided at 800 °C in a 5% NH_3/95% N_2 environment. X-ray diffraction, the only characterization reported, indicated the stabilization of the cubic phase. Future work on cBP→cBN transformation promised at the end of the article was never published. Nearly two decades later Samsonov et al. and Bartnitskaya et al. nitrided BP samples in NH_3 and N_2 gas flows at temperatures between 700 and 1300 °C [249,250]. Unlike Vickery, they concluded from XRD results that nitrogen replacement of phosphorus atoms in BP is accompanied by a change in the lattice structure of the cubic BP to hexagonal BN. Hauser received a Swiss patent in 1980 for the deposition of BP using the BCl_3-PCl_3-H_2 system and its subsequent nitridation using NH_3 [251]. He interpreted XRD data of a 3 μm thick sample as containing cBN. V.L. Solozhenko et al. studied the reaction of ammonia with BP at temperature and pressure combinations of 1000K/2.7GPa, 1000K/4.2GPa, and 940K/8.0Gpa [252]. At the lowest pressure a hexagonal/rhombohedral mixture was observed while at the highest pressure a nearly pure cBN phase was present. This high pressure result is expected as it agrees well with the aforementioned work of Williams and Ruehrwein and other high pressure cBN researchers. R.F. Davis et al. investigated a slight variation in this procedure by coupling the nitridation with an ECR nitrogen plasma source. Their BN phase identification using XRD and FTIR was inconclusive [253]. It must be emphasized that the close proximity of the cubic and hexagonal reflection peaks makes XRD an unreliable technique in distinguishing crystal structure if it is the sole characterization tool employed.

One major problem with boron nitride thin film growth is the lack of a substrate with a close lattice match. Boron nitride's lattice mismatch with silicon, silicon carbide, gallium nitride, and boron phosphide are all greater than –17%. Diamond is one of the closest lattice matched commercially available substrates with a mismatch value of +1.5%. Yet, the cost of diamond substrates has made their widespread use for cBN film growth prohibitive. Although lattice mismatch is generally minimized to enhance epitaxial growth, a large lattice-mismatch can possibly be used to alter a film's final phase. The nitridation of cBP intends to possibly utilize the lattice mismatch induced strain energy to stabilize the resulting BN film in the cubic phase. McKenzie et al. have proposed that compressive stress created by the bombardment of the substrate by an incoming flux of reactive ions preferentially promotes cBN growth over hBN by the occurrence of a thermal spike [254]. This thermal spike coupled with the high compressive stress generated by the impinging ions simulates for a short time ($\approx 10^{-11}$ seconds) the high temperature/high pressure conditions successfully used by Bundy and Wentorf and others to convert hBN to cBN and to stabilize the resulting cBN product. Davis has also proposed a similar model for the formation of compressive stress in thin films by ion bombardment [255]. Mirkarimi and coworkers have proposed that the ion irradiation creates vacancies and interstitials when it impinges on the as-deposited hBN layer [220]. These point defects in turn produce local volumetric strain and thus stress in the film which, when sufficient in energy, allow the stabilization of the transformation of the cBN phase. It is proposed that the inherent strain energy (tensile not compressive) resulting from the cBP/Si lattice mismatch may simulate the pressure effect of the high pressure-temperature method and the stress energy generated during ion bombardment in energized particle methods, thus allowing BN growth by a pseudo-thermal CVD technique. Since BP is harder than the Si substrate, a thin BP film must be deposited.

It has recently been shown that from a strictly thermodynamic viewpoint, cubic boron nitride should be stable at lower temperature and pressure [256-258]. For instance, Solozhenko has calculated for the B-N system that the cubic phase is the most stable BN phase up to approximately 1576 K at pressures approaching 0 GPa. Thus depositing cBN without the use of energized particles is thermodynamically favored, and warrants further investigation. Further explanation and review, including thermodynamic equilibrium results of the B-N-H-Cl system used in this dissertation, are presented in chapter 2 of this work.

1.2.3 Tungsten Nitride

Tungsten nitride (WN_x) is a material that previous research has shown to be a viable diffusion barrier between an underlying semiconducting layer and an overlying metallization layer [259]. Tungsten nitride is a group VI refractory metal nitride with variable stoichiometry whose properties include high hardness, high chemical stability, and high electrical conductivity [260]. Although a wide range of stoichiometry has been reported for WN_x (e.g., atomic N %= 33.3, 40-50, 50, 67, 43-62.5), it is typically represented by the WN (δ), W_2N (δ_H^{II}), or WN_2 (δ_R^{V}) chemical formulas. W_2N is a zincblende material with a lattice parameter of 4.126 Å while WN and WN_2 have simple hexagonal and rhombohedral crystal structures, respectively. The lattice mismatch between

W_2N and Si is –24% with Si having the larger lattice parameter. GaAs, another material on which W_2N has been deposited, results in a –27% lattice mismatch with GaAs having the larger lattice parameter. WN and amorphous WN_x have been reported to transform into polycrystalline W_2N under vacuum and after annealing, respectively. The first is due to the preferential volatilization of N to the vacuum environment, while the second is commonly reported for various refractory metal nitrides such as TiN and TaN due to increased film crystallinity. W_2N in turn continues to lose N and decomposes into W(s) + N_2(gas) at elevated temperatures. No known band gap has been reported for any stoichiometry.

WN_x research has mainly focused on its use as a diffusion barrier to prevent intermixing of metals (primarily Al or Cu) with Si or GaAs in contact structures [261-271]. WN_x films to date have proven to possess many of the properties of an ideal diffusion barrier including: chemical and mechanical stability, high electrical conductivity, and resistance to interdiffusion between its bordering materials [272]. Pecz et al. report that despite the formation of W_5Si_3 and W_2C phases after sputtered WN_x layers were deposited on 4H-SiC, contacts retained Schottky characteristics after annealing at 1200 °C [273]. In addition, its low resistivity, high stability under annealing conditions, and high Schottky barrier height [274-279] make it a suitable material in the fabrication of self-aligned gate field effect transistors (SAGFETs) where WN_x is used for the gate metallization [280-288]. In fact Seshita has produced a 20 GHz, 8 bit multiplexer IC implemented with a 0.5 μm WN_x/W gate GaAs MESFET while Oh has used an ion-implanted WN_x 0.25 μm gate MESFET for application to MMIC and digital IC [289-291]. Nagaoka used a WN_x/W SAGFET on GaAs for use in a 1.9-GHz digital mobile communications system [292]. WN_x can also be used as an encroachment suppressor into Si and SiO_2 during LPCVD with WF_6, a top electrode for a Ta_2O_5 DRAM, a glue layer between W and Si, and a wetting layer for Al-reflow.

Traditionally diffusion barrier research has centered on titanium nitride (TiN_x) and to a lesser extent tantalum nitride (TaN_x) [293-296]. Titanium nitride thin films have been deposited by several CVD methods including $TiCl_4$ and NH_3 [297-300], and TiI_4 and NH_3 [301,302], plasma-assisted CVD [303], MOCVD using tetrakisdimethylaminotitanium (TDMAT) with NH_3 [300,304-307], tetrakisdiethylaminotitanium (TDEAT) with NH_3 [308-312], tetrakisdimethylamidotitanium (TMT) with both NH_3 and a plasma activated H_2/N_2 mixture [313,314], and thermal decomposition of a single source precursor [297,315].

Other techniques investigated include, but are not limited to, sputtering [293,316-321], ion-assisted deposition [322-326], laser-assisted deposition [321-327], energetic cluster impact deposition [328], vacuum arc deposition [329]. In a variation to TiN deposition, Sun et al. have investigated $Al_xTi_{1-x}N$ thin films using MOCVD of terakisdimethylamidotitanium (TDMAT) and dimethyl aluminum hydride (DMAH) with good step coverage reported at growth temperatures below 300 °C [330].

Research on WN_x and TaN_x thin film deposition, though still more limited than that of TiN, has increased greatly over the past decade. This is due in part to the ongoing transition from aluminum to copper-based metallization and the resulting need to find diffusion barriers that are more chemically and thermodynamically stable than the traditional Ti/TiN. Both WN_x and TaN_x appear to promise better copper interdiffusion barrier integrity than TiN at elevated temperature due to the tendency of TiN to deposit in a columnar grain structure and thus TiN being more vulnerable to Cu interdiffusion than Al interdiffusion. WN_x, appears, however, to have two distinct technological advantages over TaN_x for copper diffusion barrier purposes. Chemical mechanical polishing (CMP), a technique used to planarize a surface after barrier deposition and copper trench filling using the dual-damascene technique, is a crucial step in the production of microelectronic circuitry. During CMP, TaN_x is removed at a rate 18 times slower than copper while WN_x is removed only 1.5 times faster. The slower TaN_x removal rate necessitates a two step CMP process including changing the slurry and pad used. Thus the wafer per hour (WPH) throughput is decreased and the cost per wafer is increased. WN_x, by virtue of its 1.5 times faster removal rate compared to copper, requires only a single CMP processing step. Furthermore, post-CMP analysis of WN_x indicates that when it is used as a barrier layer the Cu experiences approximately 100Å of dishing while Cu experiences nearly 1000Å of dishing in a TaN diffusion barrier based system. Thus, WN_x can be planarized to a much higher degree. Finally, fewer interlevel dielectric (ILD) scratches are reported for WN_x CMP compared to TaN. The combination of these steps results in costs savings per wafer, a higher wafer throughput, and a higher quality device for a WN_x based system compared to its TaN counterpart.

The first report of WN_x film formation was from Kilbane and Habig in 1974 using reactive sputtering in an Ar/N_2 gas blend [331]. A few months later Reichelt and Bergman investigated the same system [332]. After those reports, there were apparently no publications on WN_x thin film depositions for nearly a decade. When research subsequently resumed a variety of gases including N_2 [262], a Ar/N_2 gas mixtures [259,261,263,264,266,276,277,280,281,283,333-337], a Ne/N_2 gas combination [333], Ar [264], and other gas mixtures [274,275,278,282,338-344] were widely investigated.

Uchibori et al. reported a significant reduction in the contact resistance of $In_{0.7}Ga_{0.3}As/Ni/W$ system by reactively sputtering a W_2N barrier layer between the Ni and W layers. The ohmic contacts were thermally stable, had a smooth surface, and had resistance values less than 20,000 μΩ-cm [345,346]. Ahn et al. have determined that the efficiency of a sputtered diffusion barrier is optimized when the N_2 to total pressure ratio is greater than 20%. Some properties, however, such as the Schottky contact quality, film stress, and electrical conductivity are acceptable for MESFET applications even if this N_2/total pressure ratio is under 10% [347]. So et al. concluded that both amorphous and polycrystalline sputtered WN_x thin films (x=0.4 or 0.2) were far superior to W in suppressing Si-Al interaction up to 575 °C annealing for 30 minutes (W barriers failed at 450 °C) [259]. They also stated that the $Al/WN_X/Si$ contacts failed at 600 °C and were dominated by localized defects and pinholes in the WN_X barrier. Pokela et al. determined that sputtered amorphous $W_{76}N_{24}$ diffusion barriers were thermally stable up to 750 °C for 30 minutes of annealing while polycrystalline $W_{46}N_{54}$ films were less effective [261].

Ion-assisted deposition [348-351], thermal annealing of W films in NH_3 [352], tungsten evaporation in N_2 or NH_3 [353], and recently the thermal reaction of WS_2 in flowing ammonia [354,355] have also been reported. Yeh et al. concluded that rapid thermal nitridation (RTN) in ammonia of reactively sputtered WN_x films resulted in higher barrier integrity at high temperature between Al/Si and Cu/Si [356]. Lee et al. revealed that with ion-assisted deposition the as-grown amorphous WN_x film's resistivity monotonically increased with the nitrogen composition x [275]. Such a result is not surprising since 1) WN_x always has a higher resistivity than W and 2) while enhancing the barrier properties by "stuffing" any grain boundaries in the film, the N can act as electron scattering sites, increasing the film's resistivity. In another paper, Lee et al. determined that contacts on GaAs made using $WN_{0.27}$ films had a higher thermal stability and Schottky barrier height (0.84 eV) than using pure W films (0.71 eV). These barrier heights are comparable to the best results published for conventional sputtered WN_x [357].

Energized particle techniques, particularly sputtering techniques, have exhibited poor step coverage of small features with high aspect ratios due to shadowing effects, and are prone to the development of tensile stress and vacancy defects [267,338,358,359]. It has been demonstrated by Koblhase et al. and Sherman that stress-induced microcracks cause barrier failure in sputtered TiN films [360,361]. Sputtered WN_x films have also shown a propensity to resistivities as high as 4600 μΩ-cm [264] and low thermal stabilities at temperatures in the range of 400 to 600 °C [272,362]. Thus, the deposition of adequate diffusion barriers using these techniques for the increasingly aggressive device topography of succeeding chip generations is limited.

As a result, research has turned to CVD, PECVD, more recently MOCVD to deposit low stress, low resistivity, and high thermal stability WN_x films. CVD investigations include the reduction of WF_6, WCl_6, or WO_3 by NH_3 [260,265,338,358,359,363-371]. Plasma-assisted CVD has also been widely studied [267,338,359,372-381]. Lai and coworkers concluded that Si substrate encroachment by WF_6 can be suppressed by a N_2/H_2 plasma pretreatment before PECVD using $WF_6/N_2/H_2$ as reactants [382]. Park et al. determined that PECVD WN_X films had resistivities of 50 μΩ-cm after annealing and a bottom step coverage three times that of collimated-TiN films in 3.5 aspect ratio contact holes [383].

The better step coverage was expected for CVD grown WN_x thin films compared to their sputtered counterparts. Unfortunately, there have been several problems reported using the traditional WF_6, WCl_6, and WO_3 CVD precursors. Nakajima et al. have reported that the reduction of WF_6 by NH_3 can result in the formation of $WF_6 \cdot 4NH_3$ gas phase adducts and that the composition of the deposited solid is very sensitive to the ratio of the precursor molar flowrates to that of the carrier gas [363]. Furthermore, the hydrogen halides (HX) produced upon reaction of the WX_6 with H_2 are corrosive byproducts which can rapidly etch the substrate or growing WN_x film [372,384]. Finally, the move toward ultra-low k dielectric materials in an effort to further reduce a device's RC time constant is limiting the barrier deposition to 500 to 600 °C, in order to avoid damaging the temperature sensitive low k materials. Thus the 800 °C and greater deposition temperature necessary to coreact the halide and ammonia precursors is unacceptable.

Recently in an attempt to lower the deposition temperature, avoid adduct formation, and prevent corrosive halide acid vapor by-product production, tungsten nitride has been deposited by MOCVD using a tungsten amido complex as a sole precursor [385-387]. In these investigations, it was determined that the WN_x stoichiometry varied from $x=0.7$ to 1.8 and the films had cubic structures with a lattice parameter ranging from 4.14 to 4.18 Å. It was also determined that the film growth rate increased with temperature and was kinetically controlled at temperatures up to 550 °C, while it was mass-transfer limited above this temperature. Unfortunately, film resistivities monotonically increased as the deposition temperature decreased from 620 to nearly 8000 μΩ-cm over the 450 to 650 °C temperature range studied. Diffusion barrier resistivities should be as low as possible with an ideal upper thin film resistivity limit of 200 μΩ-cm. From AES depth profiles, the oxygen and carbon contaminants were present in the bulk film at approximately 3 and 6 atomic %, respectively. Because of preferential nitrogen sputtering and incorporation of carbon atoms by Ar^+ sputtering, however, actual elemental distributions are difficult to estimate [388]. The same precursor used by Tsai et al. and Chiu and Chuang has also been used in substrate dip-coating [384]. Imido/amido complexes similar to the one used by Tsai et al. and Chiu and Chuang have been used in CVD of TiN_x films [296,390-392].

Kelsey and coworkers recently reported MOCVD growth of tungsten nitride films using tungsten hexacarbonyl ($W(CO)_6$) and ammonia, with oxygen and carbon contamination ≤ 5% at even the lowest deposition temperature. Films deposited below 275 °C were amorphous while those deposited between 275 and 350 °C were polycrystalline. They also reported resistivities as low as 123 μΩ-cm for 50 nm thick films, and a step coverage greater than 90% in 0.25 μm trench structures with 4:1 aspect ratios [389]. While these results are promising the polycrystalline films have been reported to have poor copper diffusion barrier integrity after annealing due to the large grain boundaries present. Copper diffusion barrier integrity studies were not reported in this paper, nor have any been reported to date.

1.2.4 Gallium Nitride

Of all the III/V nitrides, gallium nitride (GaN) is currently the most widely researched for its use in optoelectronic applications. The interest in GaN results from its direct energy gap transition and its emission wavelength in the blue visible region at approximately 359 nm. With Al alloying, GaN can also emit in the ultraviolet region. GaN crystallizes in two different structures: a stable wurtzitic form with a and c lattice parameters of 3.189 and 5.185 Å, respectively, and a metastable zincblende type with a lattice parameter of 4.531 Å [4] (see Figure 1.1). The wurtzitic crystal type has a 3.39 eV band gap while its zincblende counterpart's is slightly lower at 3.20 eV [393,394].

With the incorporation of Al or In, pseudobinary ($Al_xGa_{1-x}N$ and $In_xGa_{1-x}N$) or pseudoternary ($Al_xIn_yGa_{1-x-y}N$; $x+y \leq 1$) compounds with a high degree of optical and electrical confinement can be achieved for quantum well light emitting structures. Since AlN, InN, and GaN have direct band gaps of 6.28, 1.95, and 3.39 eV, respectively, the potential to produce heterojunction optoelectronic devices operating in the ultraviolet and visibile light emitting regions exists [395,396]. Hagen et al. have established the existence of a complete range of solid solutions from x=0 to 1 for the $Al_xGa_{1-x}N$ ternary compound [397]. Yoshida et al. have shown that the lattice parameter of $Al_xGa_{1-x}N$ exhibits a slight negative nonlinear dependence on composition (i.e., slight deviation from Vegard's law which predicts the lattice parameter of the alloy based on the linearity between the endpoint values of AlN and GaN) [398]. In addition, they determined a decrease in the carrier concentration, an increase in the resistivity, an increase in the direct energy gap, and a nearly constant Hall mobility at room temperature with respect to an increase in the Al composition. Quantum well (QW) $Al_{0.14}Ga_{0.86}N$ structures surrounding a GaN well deposited on a AlN buffer layer/sapphire substrate material combination have been reported. The difference between the peak emission from GaN bulk material and the QW consisted of a large offset (35.5 meV) and a smaller shift due to quantum size effects [399].

GaN also has many potential uses in the electronic industries. Field effect transistors (FETs) have been made using GaN and $Al_xGa_{1-x}N$/GaN heterostructures [400,401] with high electron velocities even at elevated temperatures [402]. GaN based heterojunction bipolar transistors (HBTs) have been investigated for use in radar and satellite communications [403,404]. Negative-electron affinity has also been reported for $Al_xGa_{1-x}N$ [405,406] and GaN coated with Cs [407], opening up possible emissive photodetector applications. Electro-optic, piezoelectric modulators [408-411] and photodetectors [412-415] have also been reported using GaN and/or $Al_xGa_{1-x}N$. Khan et al. and Lam et al. have demonstrated a visible light photodetector consisting of a 0.5 μm thick $Al_xGa_{1-x}N$ layer on a basal plane sapphire layer [416,417]. Recently Pearton et al. and Ren and Abernathy have demonstrated the viability of a n-p-n GaN/AlGaN HBT for wide bandwidth amplifiers used in radar and satellite communications [401,403].

GaN's potential use in visible light emitting devices (LEDs) and ultraviolet (UV) lasers has arguably sparked the largest share of interest. This ability would allow a quadratical increase in the current storage capacity of high-density optoelectronic storage devices as well as full color flat panel displays [418]. In 1995 Nichia Chemical demonstrated the first operational blue light emitting laser operating at 416 nm using an $In_{0.2}Ga_{0.8}N/In_{0.05}Ga_{0.95}N$ multi quantum well (MQW) structure consisting of four 30 Å thick undoped $In_{0.2}Ga_{0.8}N$ well layers separated by 60 Å $In_{0.05}Ga_{0.95}N$ barrier layers [419,420]. Furthermore, Cree Research has developed an LED that operates at 430nm producing 500μW power output at 20mA [421]. Both represent significant advancement in laser and LED technology. The GaN based laser is expected to replace the currently used blue-green ZnSe heterostructure based laser because of its longer lifetime and better mechanical properties [418,422].

Since only thermodynamic GaN work was conducted as part of this dissertation research, only a brief literature review of the experimental results will be given. For a more thorough review the reader is referred to the numerous excellent review papers and books widely available in the literature. A number of deposition techniques, mostly variations of CVD/MOCVD, have been used to deposit GaN. Maruska and Tietjan first grew GaN using gallium metal, HCl, and NH_3 sources in H_2 in 1969 [423]. The first CVD based method explored was by Mansevit and coworkers in 1971 [424]. Using MOCVD they deposited GaN on (0001) Al_2O_3 substrates with trimethylgallium (TMG) and NH_3 precursors in a H_2 carrier gas. A small sampling of the other growth methods subsequently investigated include low and atmospheric pressure CVD and MOCVD [425-428], plasma-assisted CVD and MOCVD [429-431], molecular beam epitaxy [408,409], metalorganic molecular beam epitaxy (MOMBE) [432], hydride-metalorganic vapor phase epitaxy (HMOVPE) [432-435], and epitaxial lateral overgrowth (ELOG) [420,436,437]. Kim et al. demonstrated that high quality epitaxial GaN films could be grown using MBE at 800 ^{o}C with a 650 ^{o}C AlN buffer layer [438]. The lower growth temperature of MBE increases the potential for increased indium incorporation for $In_xGa_{1-x}N$ exists compared to MOVPE. HMOVPE utilizing the reaction between HCl gas and the gallium source has been used to produce thick GaN films on 6H-SiC, sapphire, and $LiGaO_2$ substrates. Krylíouk et al. have shown it is then possible to separate the GaN film from the sapphire after growth at 850 ^{o}C. This opens up the possibility of GaN homoepitaxial growth using substrates grown by this technique [433].

Recently the emphasis has focused on MOVPE and ELOG using trimethylgallium (TMG) and ammonia (NH_3) or hydrazine (N_2H_4) as precursors to reduce the required deposition temperature and enhance film quality [425-428,439]. In the past, sapphire (0001) and α(6H)-SiC have been the preferred substrates for GaN deposition. Each results, however, in a large lattice mismatch that, in turn, produces a high dislocation density. For instance, GaN deposited on sapphire and SiC results in a 16.1 and 3.53 % lattice mismatch, respectively. To minimize the impact of this lattice mismatch, a thin (≈ 200 Å) AlN buffer layer is usually grown at low temperature (450 to 600 °C) on the sapphire substrate before growth of the higher temperature GaN epitaxial layer (850 to 1100 °C). This buffer layer appears to assist the deposition process in achieving crystalline uniformity, improving the subsequent GaN film's surface morphology, and relaxing the film/substrate lattice mismatched induced strain [440-443]. In 1989 Akasaki and Amano first reported success using this two step process. Two years later Nakamura reported high quality films using a 200 Å GaN buffer layer with carrier concentrations and Hall mobility values of 5×10^{16} cm^3 and 500 cm^2/Vs at 77K, respectively [444]. Recently Iwaya et al. reported improved film structural quality by use of a second buffer layer [445]. The second buffer layer is grown on the GaN epitaxial layer before a final GaN epilayer is grown on the second buffer layer. Thus, a GaN/AlN/GaN/AlN/Sapphire (0001) sandwich structure is formed. Preliminary results indicate the termination of threading dislocations at the first GaN epilayer/second buffer layer interface and thus a nearly dislocation free top GaN epitaxial layer.

The minimization of dislocations is paramount due to their tendency to significantly degrade a device's optoelectronic capability. The use of buffer layers and novel growth techniques (e.g., epitaxial lateral overgrowth (ELOG)) are two ways to minimize dislocation formation. The other way is to delve directly to the underlying cause of the dislocations and to minimize the film/substrate lattice mismatch. Therefore, substrates other than sapphire or silicon carbide, notably lithium gallium oxide ($LiGaO_2$ or LGO) and lithium aluminum oxide ($LiAlO_2$ or LAO), are attracting attention due to their small lattice mismatches with respect to GaN of 0.036 and 0.003%, respectively, in the c direction. Lattice mismatch induced strain energy has been shown to alter the wavelength emission of an optoelectronic device and potentially result in significant changes in a device's operating characteristics. This is particularly true for MQW structures that are beginning to dominate the optoelectronics industry. Either the minimization of this strain energy or at least a better understanding of its development and influence on a given material system is needed.

1.3 Chemical Equilibrium Modeling

1.3.1 Introduction

Complete modeling of a CVD process involves the determination of a suitable mathematical representation of complex coupled equations involving transport and kinetic phenomena. The transport equations include the continuity of mass, momentum, and energy while the kinetic ones relate the dependence of the various chemical reactions on temperature, pressure, and gas fractions. Furthermore, variables such as reactor geometry and chemical interaction between the substrate, substrate pedestal, and reactor walls must be considered for each system.

In principal, a complete mathematical representation of a particular CVD process is achievable. Unfortunately, the difficulty in obtaining the required kinetic data and also solving the many coupled equations in three dimensional space is not usually practical except for the most well understood systems in the most basic reactor geometries. Therefore simplifications are often made to facilitate the modeling of CVD processes. Perhaps the most common of these simplifications is the assumption that the process is rate limited by diffusion, which implies that the rate of transport of gas reactants through the boundary layer to the substrate surface is much slower (i.e., the rate limiting step – see section 1.4.1) than the reaction kinetics at the gas-solid interface. This assumption is generally valid at high temperature and low gas velocity due to increases in both the boundary layer thickness and the heterogeneous reaction rate. The boundary layer is a relatively stagnant gas layer through which CVD reactants in the bulk gas need to diffuse to reach the growing film/substrate surface. Since the diffusion of gas phase reactants is nearly identical a chemical equilibrium model can reasonably represent the deposition process, although the deposition rates are modulated by the limitation of mass transport. Even at lower temperature and/or higher gas velocity, equilibrium modeling of a CVD system can be used to assess the thermodynamic limits of a particular process.

As outlined by Aparicio, often thermodynamic calculations are performed a priori to yield a wealth of useful information on the process [446]. These calculations can indicate first and foremost to a researcher if deposition of a desired solid from a given reactant system is thermodynamically feasible without the introduction of reacting catalytic agents. If feasible then product yields of all solid phases can be estimated to justify economic expenditures. Furthermore, the suitability of given precursors and their resulting products and by-products for use in a given CVD experimental system can be determined. For instance, an unprotected silicon substrate will be chemically etched by high concentrations of acid vapors such as HCl, HBr, and HF. Therefore in a system such as BCl_3-PCl_3-H_2 where a large amount of HCl production would be expected, care must be taken to prevent the HCl from attacking the underlying substrate, growing film, and previous processing steps, and also to safely remove it from the deposition system. The stability ranges of solid deposits with respect to temperature, pressure, and reactant compositions can be used to produce phase diagrams. This data can then in turn be used to estimate a priori experimental deposition conditions in which the desired solid phase is deposited. Finally, equilibrium results can be used to predict and control dopant and impurity concentrations, to identify rate-limiting steps in the deposition process (thermochemical kinetics), and to dynamically model CVD reactors. It must be emphasized, however, that the basic principles of thermodynamic equilibrium imply an unlimited time span, while dynamic CVD operations are generally modeled in milli- to microsecond time steps.

1.3.2 Computational Methods

An equilibrium model of a CVD system involves a gas phase in equilibrium with one or more condensed pure phases (deposited solids, substrate, reactor chamber) and/or condensed solutions (usually solid solutions). The gas phase is generally treated as an ideal gas mixture while the condensed phases can be either solids or liquids (solid deposition is desired). The problem of finding the equilibrium state of a given system involves the minimization of the Gibbs energy, subject to the constraints of conservation of elemental mass and nonnegativity of all the species' mole numbers. A constant temperature and pressure are normally assigned to the system though these can be replaced by other variables such as constant system volume or constant entropy. To begin any calculation the degrees of freedom of the system must equal 0.

To avoid singularity problems associated with equilibrium computation utilizing less robust algorithms, the two gases that simultaneously contain the required elements and that are thought will be present in the largest mole fraction at equilibrium are generally selected. Fortunately, with more robust algorithms, equilibrium results can often be obtained using the experimental reactants' initial mole fractions without redistributing each reactant's atoms into more thermodynamically stable molecules. The equilibrium solution is found when the calculated set of mole numbers satisfies the convergence criterion of Gibbs energy minimization. The difficulty in finding this solution arises from the fact that while the mass balance constraints are linear in the species mole numbers, the species chemical potential functions, which describe the system's total Gibbs energy, are nonlinear in the same variables. Thus the solution procedure becomes iterative and for the large systems characteristic of CVD, numerical methods and microprocessors must be employed. This is especially true if the convergence criteria is extremely small ($<10^{-5}$) to ensure a greater degree of accuracy.

Computational methods to compute the equilibrium of a complex chemical system can generally be classified as having their origin in either the methods of Brinkley [447] or White et al. [448]. A thorough review of both methods including the stoichiometric Villars-Cruise-Smith (VCS) method [449] used in a portion of this dissertation can be found in Roger Aparicio's dissertation [446].

A flowchart generated by Aparicio is shown in Figure 1.2 [446]. At every iteration (m), the algorithm checks for an optimum set of basis or "component" species and generates a matrix (N) from these species. This iteration is then used with the previous iteration mole numbers to compute the diagonal elements of the Hessian matrix. This is in turn used in conjunction with the species standard state chemical potentials to find the change in the molar extent vector ($\delta\xi$). The algorithm also calculates a step size parameter (ω) which limits the amount of change in the mole numbers vector ($n^{m+1}-n^{m}$) in order to achieve the greatest minimization at each iteration. After a new mole numbers vector (n^{m+1}) is computed, the Gibbs energy changes of reaction j (ΔG_j) are calculated and compared to a user defined convergence criteria ($\varepsilon = 10^{-7}$ usually) to ascertain whether n^{m+1} constitutes a zero of all the ΔG_j and a potential equilibrium solution.

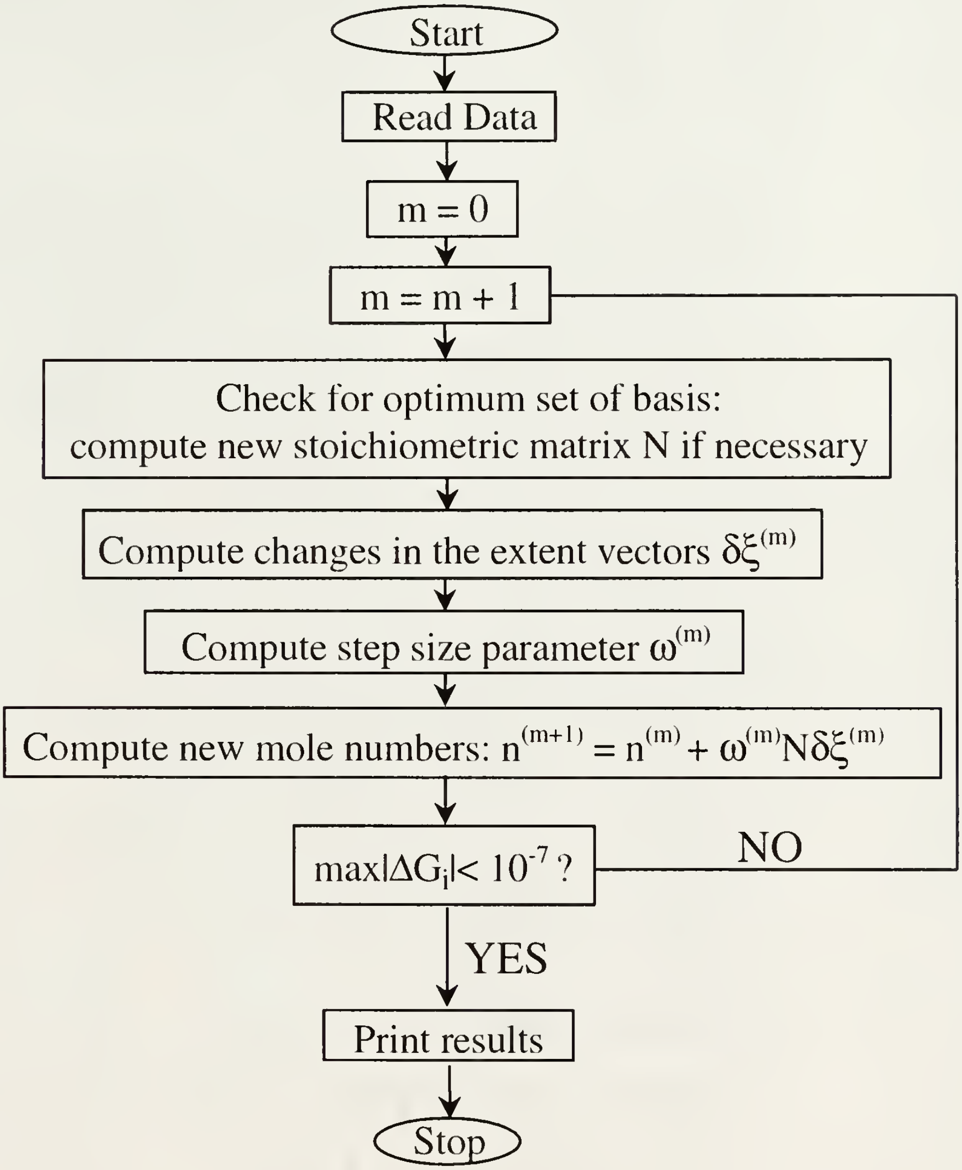
Start
Read Data
m = 0
m = m + 1
Check for optimum set of basis:
compute new stoichiometric matrix N if necessary
Compute changes in the extent vectors $\delta\xi^{(m)}$
Compute step size parameter $\omega^{(m)}$
Compute new mole numbers: $n^{(m+1)} = n^{(m)} + \omega^{(m)} N \delta\xi^{(m)}$
$\max|\Delta G_i| < 10^{-7}$?
NO
YES
Print results
Stop

Figure 1.2 Flowchart of the VCS optimized stoichiometry algorithm [449]

Meyer first developed the FORTRAN algorithm used to calculate many of the results in chapter two of this dissertation [450]. It is a multi-species, multi-phase, multi-reaction stoichiometric equilibrium algorithm based on the stoichiometric algorithm suggested by Cruise, Smith, and Missen that has been extended to include not only a gas phase with an inert species, but also non-ideal multi-component solution and pure condensed phases. Tests of the algorithm to confirm its capability of calculating homogeneous equilibrium in the material systems investigated in this dissertation were made by comparing the results with those published by Kelder in his doctoral dissertation for the PBr_3-H_2 system using a PC-adapted version of SOLGASMIX [73]. Furthermore, calculations performed on a simple, limited species H-N-O system were compared to those obtained using Smith and Missen, ThermoCalc, and IVTAN [448,451,452]. Based on the results of these comparisons, the algorithm was modified by Roger Aparicio and the author. Among these modifications were the inclusion of code to account for the change in the reference state of phosphorus from a crystal at 298 K, to a liquid at 317 K and finally to a gas in the form of P_2 at 1180 K, as well as the direct inclusion of Gibbs energy expressions for 24 B-N-H-Cl molecules. The FORTRAN source code of the modified Meyer program, including all modifications necessary to accomplish the homogenous equilibrium results discussed in sections 2.1 and 2.2 of this dissertation are given in Appendix A.

All calculations for the heterogeneous BCl_3-PCl_3-H_2, BCl_3-NH_3-H_2, and Ga-N systems were performed using ThermoCalc for three reasons. First, singularity problems that prevented convergence at a single equilibrium state were encountered using the Meyer's FORTRAN code in both the BCl_3-PCl_3-H_2 and BCl_3-NH_3-H_2 heterogeneous systems. This is possibly due to the presence of numerous solid phase combinations (6 in each system plus the possibility of no solid deposition). Second, the solid phase diagram mapping features of ThermoCalc are much more advanced than those developed by Meyer, Aparicio, and Johnston. This significantly reduced the time and effort involved in the heterogeneous system equilibrium calculations and subsequent data transfer to a spreadsheet program. Finally, calculations of the Ga-N system were conducted in collaboration with Dr. Jianyun Shen and Shunli Shang of the Institute for Non-ferrous Metals Research in the People's Republic of China. Their familiarity with the commercially available ThermoCalc software dictated its use.

1.3.3 The Chemical System and Thermochemical Data

As discussed by Bessman, there are two possibilities in thermodynamic equilibrium modeling that can lead to erroneous results [453]. The first is the use of inaccurate/outdated thermochemical data, while the second is the omission of species or phases whose presence can significantly alter the equilibrium state. Both possibilities were encountered while reviewing the literature to organize a comprehensive thermochemical database and in comparing the present results with those published by previous assessors.

The chemical system used in the model was defined as a single ideal vapor phase possibly in equilibrium with one or more noniteracting pure solids or solid mixtures. Values of the standard enthalpy of formation and standard entropy, and an expression for the heat capacity were entered for each species (except for many B-N-H-Cl species that were directly included in the Meyer FORTRAN code for reasons discussed below) and are listed in tables 2.1, 2.2, and 2.6 for the B-P-H-Cl, B-N-H-Cl, and Ga-N systems, respectively. Several different databases arising from both experimental data and predictive techniques were considered as thermochemical data sources. Thermochemical compilations included those by Gurvich, the JANAF tables, and Barin and O'Knacke [454-456]. Of these, Gurvich is considered the most critical source since along with property data it contains uncertainties for each species values. In addition, Gurvich contains the latest revisions of the data. The JANAF tables and Barin and O'Knacke are semi-critical, semi-collective databases with outdated data for several important species. In addition, mistakes in two phosphorus containing species (PH and PH_2) are present the JANAF tables, due to the failure to adjust the $\Delta H^o_{f,298}$ values when the reference state was changed from red to white phosphorus. Based on this the data used in the equilibrium calculations, when available, were taken from Gurvich, unless predictive data subsequently described was available.

Despite the critical nature of the Gurvich compilation, large uncertainties exist for several important boron containing species. Therefore, the literature was searched for methods to estimate the thermochemical data of these molecules. Harris and Schlegel's prediction of thermochemical properties for several BH_mCl_n species using the G-2 level of theory have yielded values very different from those published in widely used thermochemical reference sources [457]. For instance, a theoretical $\Delta H^o_{f,298}$ value for BH_2 was calculated to be 332.33 kJ/mol, while other reference books listed 200.832 {1985, data from 1964}, 295.307 {1981}, and 318.255 kJ/mol {1989}. Obviously the accepted published thermodynamic value has progressively moved towards that predicted by the G-2 level of theory. Furthermore, the G-2 level of theory used to calculate the heat of formation was shown to have a mean absolute error of ±5.4 kJ/mol for ca. 125 accurately known experimental molecules. Thus, these predictive thermochemical values for $\Delta H^o_{f,298}$ and S^o_{298} have been used in all calculations presented herein. Allendorf and Melius used the BAC-MP4 method to predict thermodynamic properties of 36 species in the B-N-Cl-H system and compared their values to those of Harris and Schlegel and to other theoretical and experimental works [458]. Good agreement was observed between the values each method predicted. Separate equilibrium calculations were performed using thermodynamic data from each of these works. For the purposes of CVD equilibrium analysis, there was no significant difference in the calculated equilibriums using each set of predicted $\Delta H^o_{f,298}$ and S^o_{298} values. In the B-N-H-Cl system, thermochemical data for 21 species, unavailable in Gurvich, JANAF, or Harris and Schlegel, were taken from the work of Allendorf and Melius and are noted in Table 2.1. The ThermoCalc thermochemical database was used for all calculations for the Ga-N system. Certain modifications that were made to the ThermoCalc database included adjustment of the thermochemical data of GaN as described by Davydov et al. [459] and the inclusion of a variable GaN strain energy term depending on the film/substrate lattice mismatch.

1.4 Chemical Vapor Deposition Process

1.4.1 Overview

Semiconductor films are typically deposited in industry using a variety of deposition techniques depending on their particular device function and specification requirements. As discussed above, halide and hydride chemical vapor deposition and metalorganic chemical vapor deposition have been used to deposit an extensive variety of thin film materials for the electronic, optoelectronic, and hard coatings industry due to its relatively low cost, wide choice of precursors, and high throughput. As the name implies, gaseous precursors are used to chemically deposit a solid thin film on an underlying substrate. Thus, on an elementary level, CVD can be seen as the result of a combination of surface reaction and mass transfer processes. The substrate is placed on a heated pedestal (known as a susceptor if it is inductively heated. Plasma enhanced CVD utilizes ions to aid the deposition process by dissociating the gaseous precursors and thus deposition at lower temperature is possible. In CVD/MOCVD, precursor molecules are thermally dissociated and reacted. In many deposition chemistries, including all MOCVD ones, a cold wall reactor is used. A large temperature gradient can exist. For example, it has been shown to decrease by 700 K at 1.5 to 3.5 cm above the susceptor, though its exact profile is dependent on the gas thermal conductivity, flowrate, and reactor geometry [460].

An illustration of the wide variety of potential reaction pathways is the very simple two component PH_3-H_2 system, which has two precursors that can react to form at least 13 different known molecules (see section 2.1.2). In CVD, both homogeneous and heterogeneous nucleation can occur. Process parameters and reactant combinations should be selected to avoid homogeneous nucleation and resultant particle formation, which can significantly degrade the quality of the film.

The process of depositing solids using CVD can be seen as a series of sequential steps. The slowest of these steps is known as the rate-limiting step and it controls the rate of growth of the solid film. Generally, at elevated temperature, the rate-limiting step is the diffusion of a reactant species through the boundary layer to the substrate surface. At lower temperatures the rate of reaction is usually kinetically limited and the growth rate is therefore controlled by the heterogeneous reaction rate on the film/substrate interface. Similarly, diffusion controlled growth is affected by the overall flow rate through the influence of the gas velocity (ν) on the boundary layer thickness (typically $\alpha\, \nu^{1/2}$), and it is insensitive to the substrate crystallographic orientation. Thus, if the total flow rate is increased, a transition from a diffusion to a kinetically controlled process is often observed.

This is due to the thinning of the boundary layer, through which the gaseous reactants must diffuse to heterogeneously react. The process can be described by the following eight steps:

1) Transport of the precursor gases to the CVD reactor
2) Homogeneous dissociation and reaction of the precursor gases into various intermediate species
3) Diffusion of these species from the gas bulk to the substrate surface through a boundary layer (δ, the boundary layer thickness is typically $\propto v_o^{1/2}$)
4) Adsorption of the species, both reactive and non-reactive, on the substrate surface.
5) Heterogeneous chemical reactions of the reactive species, either between adsorbed species or between adsorbed and gas species, followed by surface diffusion and inclusion into the growing film of the adsorbed species.
6) Desorption of the non-reactive species and reaction by-products
7) Diffusion of these species from the film surface to the gas bulk through the boundary layer
8) Transport of the non-reactive species, reaction by-products, carrier gas, and unreacted reactive species from the deposition zone of the CVD reactor to the exhaust system.

Steps 1 and 8 are usually determined by the nature of the carrier gas (i.e., flowrate and type of gas). Steps 3 and 7 are determined by various process parameters including pressure and total gas flowrate. If either of these two steps are the rate-limiting step then the process can be described as mass transport limited. Steps 4 to 6 all occur on the substrate surface. Thus if any of these three steps are the rate-limiting step then the process is kinetically limited. Substrate crystallographic orientation also typically influences the deposition rate of kinetically controlled processes but not diffusion limited ones. Step 2 can occur throughout the process and is typically slow. Thus it can be the rate-limiting step in the overall process.

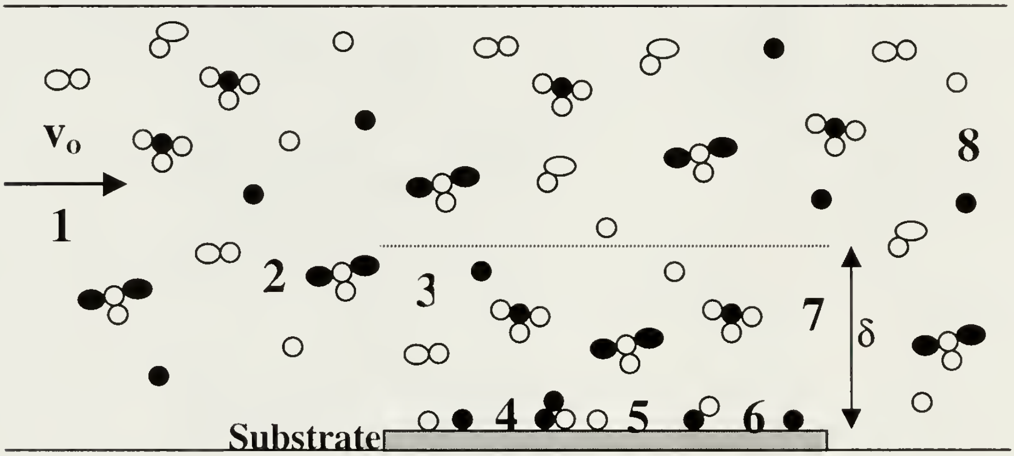

Figure 1.3 Schematic representation of chemical vapor deposition (CVD) process (numbers correspond to the above eight steps of the CVD process)

A schematic representation of the CVD process is shown in Figure 1.3 with v_o being the input gas flowrate or molar average velocity and δ the thickness of the diffusion boundary layer. The diffusion of the various reactant species is assumed to occur through this diffusion boundary layer due to the consumption of reactants at the film/substrate interface. This consumption creates a reactant partial pressure difference between the bulk gas and the surface. The diffusion boundary layer is assumed to be the layer from the film's surface to a point in the bulk gas where the reactant partial pressure is nearly identical (usually ≈ 0.99 of its bulk value) to its input partial pressure. A simplified linear temperature and reactant partial pressure gradient is shown in Figure 1.4 where the subscripts b and s refer to bulk and surface properties. Each property increases as the gas moves to the right of the figure.

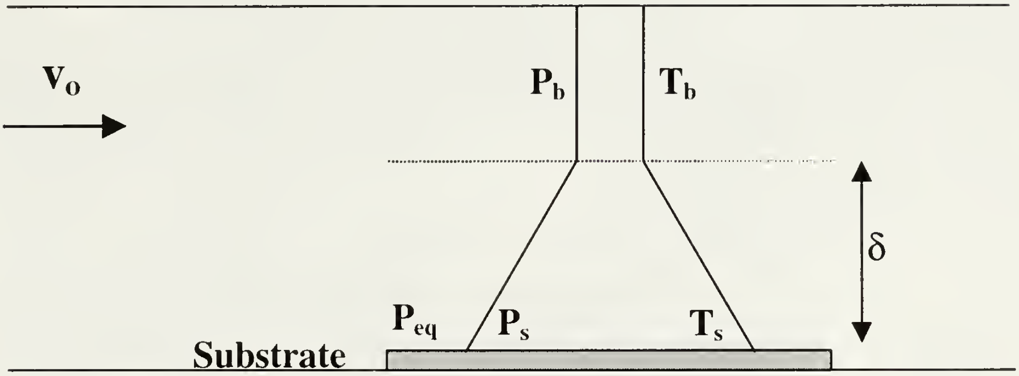

Figure 1.4 Schematic of pressure and temperature gradients in CVD reactor

For reactors operated in mass transfer limited regimes, the ultra-stringent film thickness uniformity requirements in the modern microelectronics industry demand laminar fluid flow inside the reactor as well as a uniform boundary layer thickness. Thickness uniformity can be enhanced in vertical reactor geometries by susceptor rotation during growth. In horizontal reactors a tilted susceptor configuration is commonly used (Figure 1.5). Laminar flow is generally achieved when the Reynold's number is less than 1000. The Reynold's number is the dimensionless ratio of momentum to viscous forces and is defined as:

$$\mathrm{Re} = \frac{\rho v D}{\eta} \qquad \text{Equation 1.1}$$

where ρ is the mass density of the fluid, D is the reactor diameter, v is the fluid velocity, and η is the fluid's viscosity. The thickness of the boundary layer is expressed as:

$$\delta = \sqrt{\frac{x}{\mathrm{Re}}} \qquad \text{Equation 1.2}$$

where x is the distance along the reactor. Therefore as x increases the Reynold's number can be adjusted accordingly by increasing the fluid velocity. This increase in the fluid velocity can be accomplished by decreasing the cross-sectional area available for fluid transport. In other words, the diameter of a tubular reactor can be reduced from D_1 to D_2. Thus a constant boundary layer thickness can be maintained resulting in deposited films with a more uniform thickness.

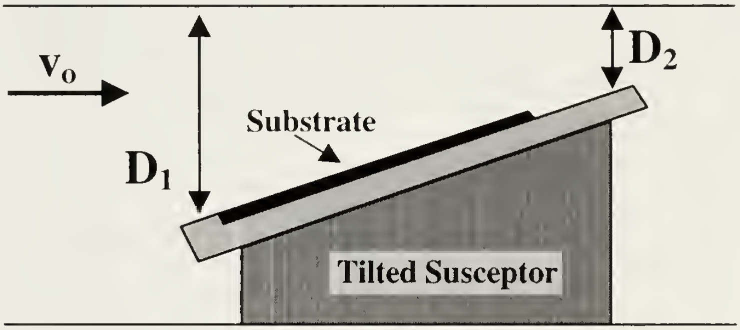

Figure 1.5 Schematic of tilted susceptor design

Many authors, including Fick and van den Brekel, have modeled the mass transfer across this diffusion (boundary) layer [461,462]. As shown by van den Brekel and outlined by Kelder [73], the molar diffusion flux, J_D, in the diffusion layer is given by:

$$J_D = \frac{D_o (T_S - T_b)(p_b - p_S)}{\delta T_o^2 R \ln(T_s / T_b)} \qquad \text{Equation 1.3}$$

where T_o is the room temperature, D_o is the diffusion coefficient at T_o, δ is the diffusion layer thickness, T_S and T_b are the substrate and bulk gas temperatures, respectively, p_b and p_S are the bulk and surface reactant partial pressures, respectively, and R is the universal gas constant. The mass transfer flux, J_{tr}, is given by:

$$J_{tr} = \frac{k_D (p_S - p_{eq})}{RT_S} \qquad \text{Equation 1.4}$$

where k_D is the mass transfer coefficient and p_{eq} is the equilibrium partial pressure, which can be calculated relative to p_S. It is important to note that this approximation is only valid for one reactant. In the stationary state these fluxes are equal and a dimensionless CVD number, N_{CVD}, is defined by:

$$N_{CVD} = \frac{p_b - p_S}{p_S - p_{eq}} = \frac{k_D \delta T_o^2 \ln(T_S / T_b)}{D_o T_S (T_S - T_b)} \qquad \text{Equation 1.5}$$

In the limit where p_S equals p_{eq}, i.e. when the supersaturation (p_S-p_{eq}) approaches zero and consequently $N_{CVD} \gg 1$, all the species approaching the substrate surface will react immediately. The process is then said to be diffusion controlled. When diffusion controlled deposition occurs, small irregularities at the substrate surface result in locally different diffusion layer thicknesses. These locally thin layers result in a higher local surface reactant partial pressure and hence a local increase in the growth rate.

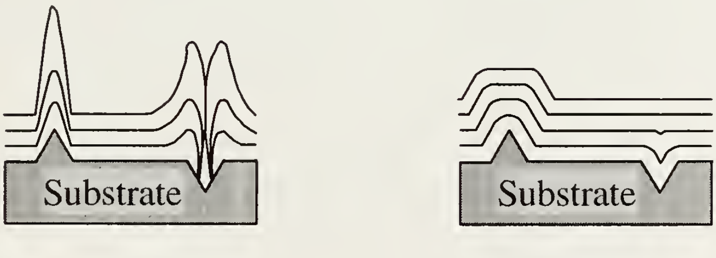

$N_{CVD} \gg 1$ $N_{CVD} \ll 1$

Figure 1.6 Schematic of film growth dependence on N_{CVD} (from reference 73)

As a result CVD growth under these process parameters will result in irregular film surface morphology (Figure 1.6). On the other hand, if p_b approaches p_S, then the process is kinetically controlled ($N_{CVD} \ll 1$) and the diffusion of the gaseous reactants through the boundary layer to the substrate surface is much faster than the surface reaction. Thus the partial pressure of a species near the surface nearly equals its partial pressure in the gas bulk. Since the partial pressures are locally the same at the substrate surface, the film growth rate is also. This leads to a much smoother surface morphology with small surface irregularities disappearing at longer deposition times. Hence, by evaluating the constants in equation 1.5, the nature of the process that dominates growth as well as the resulting surface morphology can be predicted.

1.4.2 Experimental System and Procedure

A schematic and two photographs of the multichemistry CVD system and ultrasonic nebulizing delivery system used to deposit the coatings are shown in Figures 1.7, 1.8, 1.9, and 1.10. The system, a portion of which was designed and constructed as part of this project, consists of four compressed precursor gas sources, three liquid precursor bubbler sources, a solid source metal-organic delivery source, and a liquid ultrasonic delivery source. Reactant mixtures, diluted in flows of Ar, H_2, He, or N_2, were delivered to the reactor through either of two independent flow channels. Two other flow channels were available to supply additional carrier gas, either for further dilution of the precursors in the reactor or to act as a sweeping carrier gas (e.g., for the pyrometer's quartz viewport or to transport the nebulized WN_X precursor/solvent to the reactor). Metering of the compressed gas flowrates was accomplished by means of mass flow controllers (MKS model 1159B). The liquid bubbler sources were delivered to the reactor by bubbling the carrier gas through the column of liquid and thus saturating it with the precursor source. To control the liquid source vapor pressure, each bubbler was immersed in its own constant temperature bath (VWR model 1155), while bubbler pressure control was achieved by measuring the pressure at the inlet and regulating the outlet flow with metering valves. With the assumptions of saturation and ideal gas behavior, the liquid precursor flow can be calculated from the following equation:

$$FR_i = FR_{CG}\left(\frac{P_i^{sat}}{P_t - P_i^{sat}}\right)$$ Equation 1.6

where FR_i is the flow rate of the liquid precursor i (e.g., PCl_3), FR_{CG} the flowrate of the carrier gas (e.g., H_2), P_i^{sat} the vapor pressure of the liquid precursor at the bubbler temperature, and P_t the total bubbler pressure.

Depositions were conducted inside a vertical, 63mm ID quartz reactor with an o-ring seal at both ends. The o-rings were cooled by self-contained cooling water jackets. The substrates were supported by a cylindrical graphite pedestal susceptor, and heated by induction of the susceptor with a 7.5 kW Westinghouse rf generator. Substrate temperature was measured from the bottom with a sheathed type-S thermocouple placed inside the susceptor approximately 2 mm from the surface. At elevated temperatures (>1000 °C), a two-color optical pyrometer (Capintec model ROS-8) focused through a gas-swept quartz viewport was used. The thermocouple output could also used for closed loop temperature control. The actual substrate temperature was calibrated by recording the pyrometer and thermocouple temperature readings at 25 °C increments from 900 to 1250°C.

The pressure in the reactor was regulated by a control loop consisting of a pressure gauge (MKS Baratron 221A) upstream and a throttle valve (MKS model 253A) downstream from the reactor. A Pirani pressure gauge (Sensavac series 315) was used to monitor pressures below 1 Torr. The gases exiting the reactor were first passed through an ice trap to condense particulates before introduction to the vacuum pumps. The remaining gases were then treated in a scrubber unit (containing a 35% NaOH solution) prior to venting the gas stream to the atmosphere via a fume hood. The system was generally operated at atmospheric pressure for BP and BN growths while WN_X growths were conducted near 200 Torr. Vacuum was accomplished by means of a rotary vacuum pump (Leybold model D32C) and a diffusion pump (Varian model HS2) connected in series. The pressure, temperature and flow controls of the system were all automated and operated via computer. For all WN_X experiments, new water cooled reactor o-ring seals were designed and installed to minimize possible oxygen contamination from the atmosphere or water vapor leakage from the o-ring cooling water jackets. In addition, a gate valve was installed at the top of the reactor to reduce the substrate transfer time to the reactor vacuum environment after etching.

All (100) and (111) oriented boron doped silicon substrates (Wacker-Chemitronic GMBH) were degreased by submersion in warm trichloroethylene (TCE), acetone, and methanol for 3 minutes each. They were then dipped in boiling water for 30 seconds to remove any remaining solvent and finally etched in 6:1 buffered oxide etch (BOE) for 2 minutes to remove the native oxide layer. To minimize reoxidation, the time to transfer the silicon substrates to the reactor was less then 5 minutes for BP and BN growths and less than 3 minutes for WN_X growths. The difference is due to the addition of the above-mentioned gate valve. In addition, to ensure the elimination of any remaining oxide, the silicon substrates were reduced in H_2 at 1000 ^oC for 5 minutes prior to deposition. All diamond (Harris Diamond Company), Al_2O_3 (Commercial Crystal Laboratories), β-SiC (Cree Research Inc.), and nickel (Alfa Aesar/Johnson Matthey) substrates were only degreased using the above procedure.

Deposited samples were characterized by a wide array of techniques. Growth rate versus temperature, pressure, total flowrate, and precursor flowrates was determined by FTIR and Raman spectroscopy (see chapter 3 for further explanation). By plotting growth rate versus 1/T for various temperatures, an Arrhenius expression for the activation energy for film deposition on different substrates can be obtained and the effect of kinetics on film deposition is evident. Furthermore, by plotting growth rate versus the square root of the total flowrate the effect of diffusion on film deposition can be seen. A horizontal plot for either of these indicates that deposition is independent on that particular parameter. Each of these spectroscopic techniques is non-destructive and versatile in determining both film thickness and crystallographic phase identification. Strain and impurity incorporation will alter the phonon spectra and can thus also be detected.

X-ray diffraction (XRD) was employed to determine crystallographic growth orientation as well as any film decomposition ($BP \rightarrow B_{13}P_2$) or impurity phase. Epitaxial, polycrystalline, or amorphous structures could also be ascertained. It is expected that epitaxial growth would not occur due to the large lattice mismatched material systems investigated, which resulted in large film/substrate strain energies. This strain, however, may aid in the in-situ nitridation of the BP samples by simulating the high pressure or ion bombardment condition that is generally accepted as necessary for stabilization of the cubic phase of boron nitride.

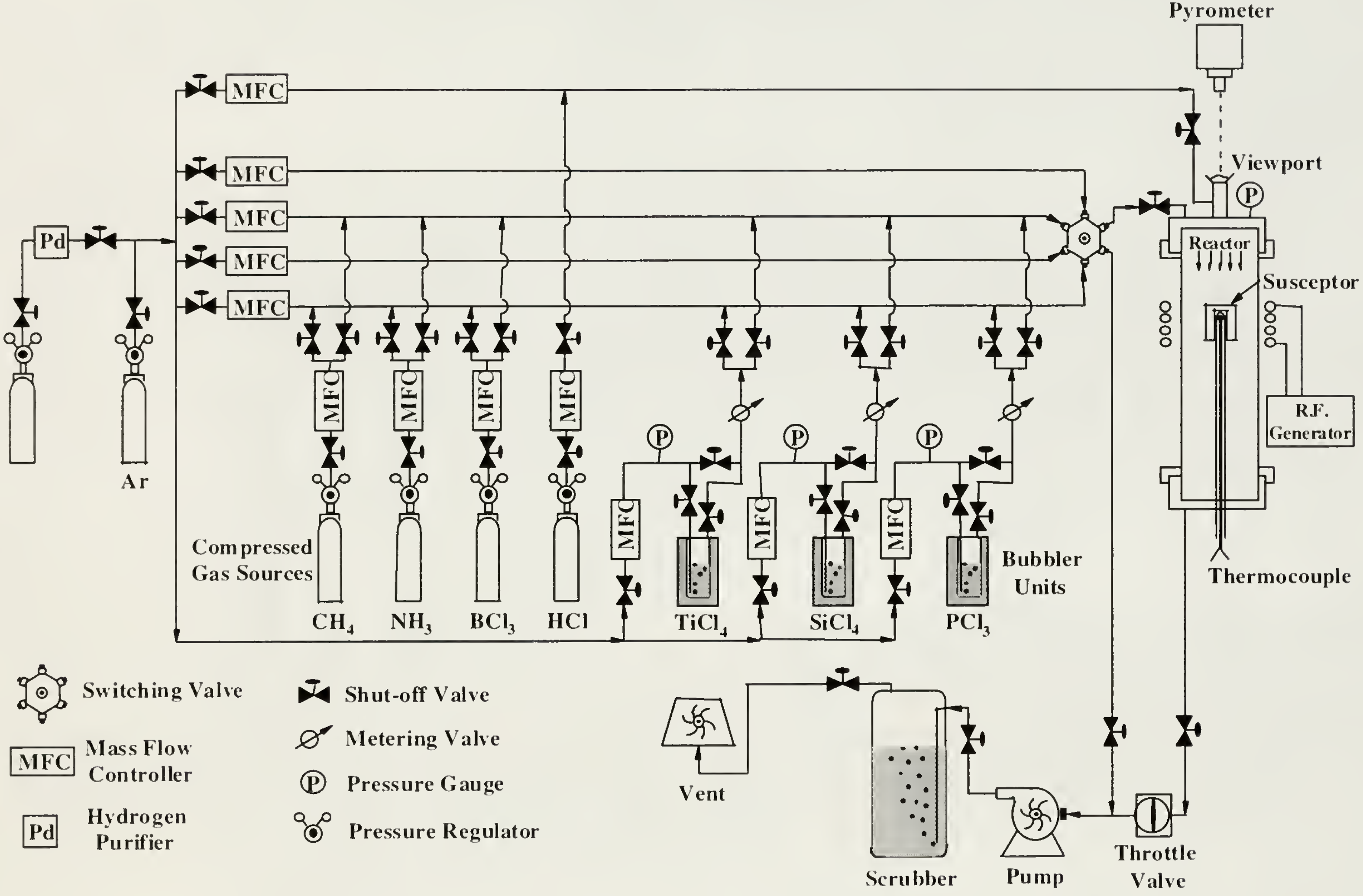
Pyrometer
Viewport
P
Reactor
Susceptor
R.F. Generator
Thermocouple
Pd
Ar
MFC
MFC
MFC
MFC
MFC
Compressed Gas Sources
MFC
MFC
MFC
MFC
CH$_4$
NH$_3$
BCl$_3$
HCl
P
P
P
MFC
MFC
MFC
TiCl$_4$
SiCl$_4$
PCl$_3$
Bubbler Units
Switching Valve
MFC
Mass Flow Controller
Pd
Hydrogen Purifier
Shut-off Valve
Metering Valve
P
Pressure Gauge
Pressure Regulator
Vent
Scrubber
Pump
Throttle Valve

Figure 1.7 Schematic diagram of multichemistry CVD system

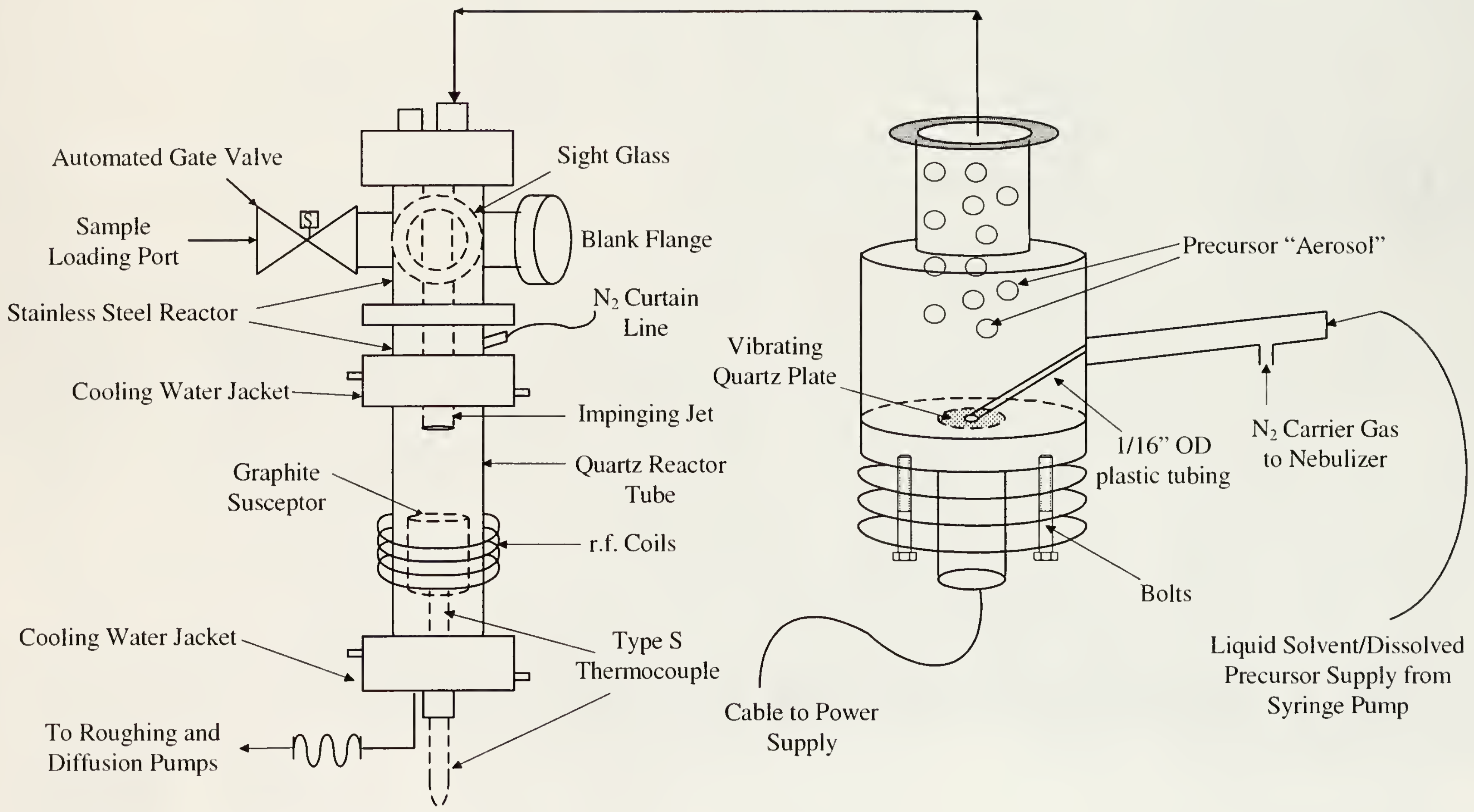
Automated Gate Valve
Sample Loading Port
Stainless Steel Reactor
Cooling Water Jacket
Graphite Susceptor
Cooling Water Jacket
To Roughing and Diffusion Pumps
Sight Glass
Blank Flange
N_2 Curtain Line
Impinging Jet
Quartz Reactor Tube
r.f. Coils
Type S Thermocouple
S
Vibrating Quartz Plate
Cable to Power Supply
Precursor "Aerosol"
1/16" OD plastic tubing
N_2 Carrier Gas to Nebulizer
Bolts
Liquid Solvent/Dissolved Precursor Supply from Syringe Pump

Figure 1.8 Schematic diagram of ultrasonic nebulizing delivery system

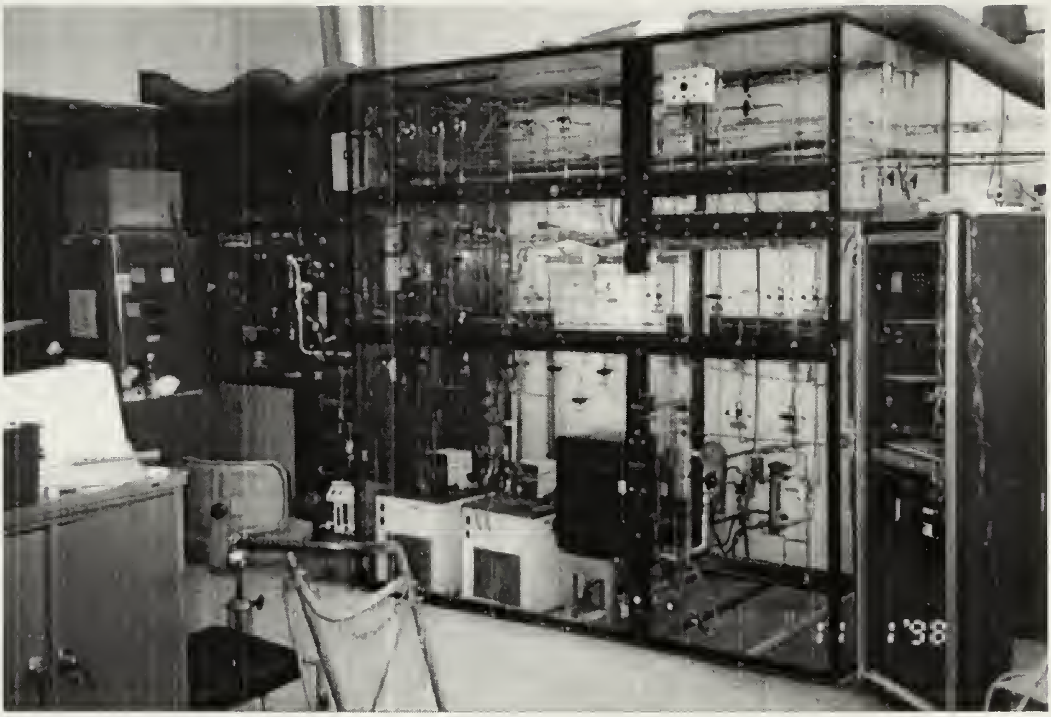

Figure 1.9 Photograph of multichemistry CVD system

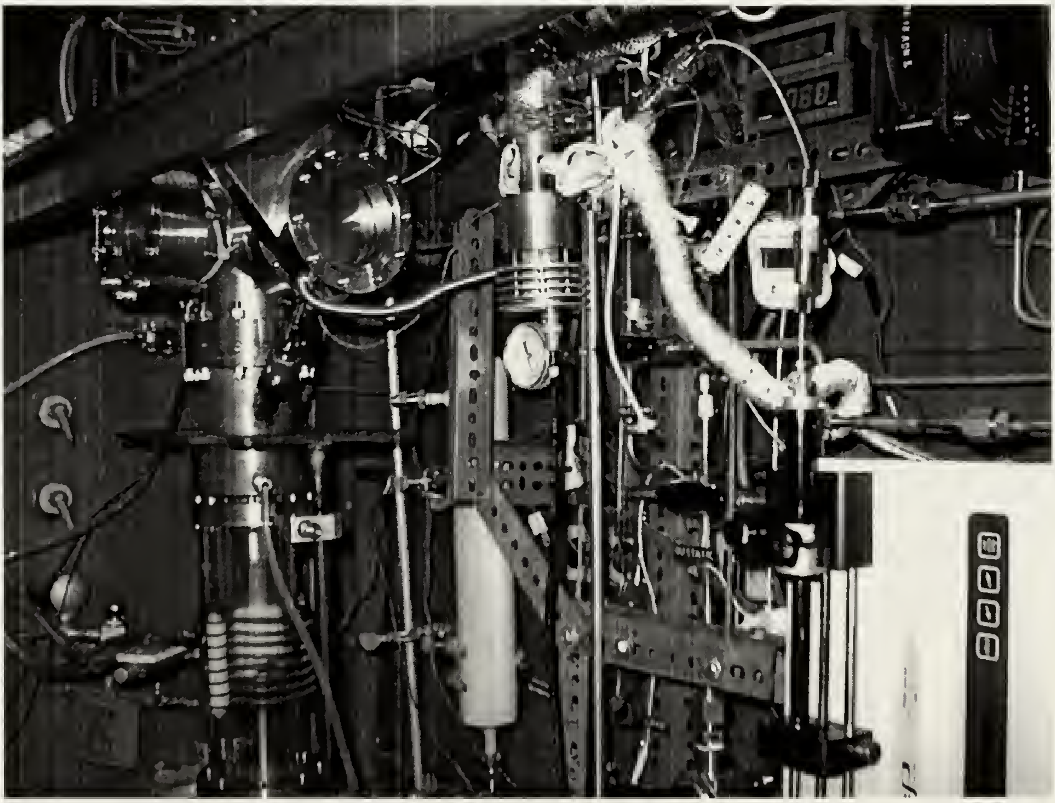

Figure 1.10 Photograph of CVD reactor (left) and metalorganic delivery system (right)

Auger electron spectroscopy (AES) and X-ray photovoltaic spectroscopy (XPS) were used to determine film composition and crystallinity of both the surface and bulk films. While AES is usually a non-destructive technique, it that has been reported to result in graphitization of diamond samples, XPS is a non-destructive technique. Selected samples were also characterized by transmission electron microscopy (TEM). Cross-sectional TEM (XTEM) gives a direct physical image of interface sharpness, film thickness, and crystallinity. Chemical degradation of the substrate surface by HCl that resulted from the use of a halide chemistry was also examined using XTEM.

Surface morphology was examined using scanning electron microscopy (SEM) and atomic force microscopy (AFM) in tapping mode. Variations in the surface morphology as a function of deposition temperature and substrate were examined in detail. BP and BN films were coated with a Au/Pd film (approximately 30 Å thick) to prevent sample charging. Vicker's hardness testing was used to determine the microhardness of the BP films and a current probe was employed to determine the film's doping type.

Studies were also performed on the novel imido tungsten nitride precursor complexes themselves to determine their physical and decomposition properties. Differential thermal analysis (DTA) was used to determine the sample weight loss versus sublimation temperature profile of each precursor. Mass spectrometry (MS) was used to determine the precursor dissociation pathways as well as the fraction of WN compound remaining as a single molecule in the gas phase. The vapor pressure of select precursors was measured and thus their propensity to be transported via a carrier gas from a solid source delivery system to a reactor chamber was determined. All of this information was considered in the final determination of the suitability of these novel precursors for use in MOCVD of WN_x.

1.5 Overview and Scope of the Present Work

Industrially, $Al_xGa_{1-x}As$, $Al_xGa_{1-x}P$, and Si with Al contacts are the standards throughout the world. If the rapid advancement of electronic devices is to continue, then less explored material combinations whose physical properties exceed these current standards must be researched. Increases in device speed and longevity are two of the goals driving the research into new material combinations. Nevertheless, research to date has only begun to explore the potential of “novel” material combinations and their suitability to enhance the overall performance of electronic devices.

In the present work, the application of CVD and MOCVD to deposit BP, BN, and WN_X thin films has been examined. The second chapter describes a thermodynamic approach used to predict equilibrium deposition efficiencies and gas and solid phase compositions of the B-P-H-Cl, B-N-H-Cl, and Ga-N systems and subsystems. Strain energy considerations were included in the Ga-N analysis. Realistic CVD conditions (temperature, pressure, precursor components, and precursor ratios) were examined. In this approach, two separate multiphase, multispecies equilibrium algorithms were used to determine the vapor species and solid phases in equilibrium and their yields as a function of temperature and inlet reactant gas composition.

The third chapter describes in detail an experimental study of BP CVD on various substrates using BCl_3, PCl_3, and H_2 as precursors. Film growths are examined in terms of several properties including morphological, compositional, and electrical. Figures will be presented depicting these properties. The effect of reactor temperature, pressure, precursor flowrates, carrier gas composition, and substrate selection on the resulting BP thin film was examined in 134 separate depositions. The influence of each of these on the deposition rate was also observed. Results proved to be consistent with those observed by Kelder and Schroten who examined a bromine based BP CVD system [73,74].

In the fourth chapter, results from the in-situ nitridation of boron phosphide films are presented. Results are centered on determining the crystal structure of the resulting boron nitride film. The effect of nitridation temperature, pressure, ammonia flowrate, as well as various nitridation procedures attempted are discussed. Eighty-three separate in-situ nitridation experiments were conducted. Final results conflicted, with FTIR and Raman spectroscopy indicating the successful stabilization of cubic BN, while Auger electron spectroscopy detected only hexagonal BN. X-ray photoelectron spectroscopy yielded signature spectra for both cubic and hexagonal BN. Thus it is proposed that a mixture of cubic and hexagonal BN was formed and cBN detection was dependent on the spatial sensitivity of the characterization technique used.

The fifth chapter details attempts to deposit tungsten nitride thin films using novel imido precursors. Two separate delivery systems were constructed and utilized – a vertical solid-source system and an ultrasonic liquid phase system. Results using the solid-source delivery system were disappointing with very low film growth rates, large nonuniformity in film surface coverage, and significant oxygen and carbon contamination. The precursor's very low vapor pressures and poor sublimation profiles readily explain these results. Growths using the ultrasonic delivery system and a heated double tubed impinging jet proved to be far more successful with highly reproducible WN_X thin films. These films had resistivities as low as 447 $\mu\Omega$-cm, which is far lower than those typically reported by other MOCVD, CVD, or sputtered WN_X thin film researchers.

Finally, the sixth chapter provides a summary of conclusions and outlines recommendations for future research.

CHAPTER 2
THERMODYNAMIC MODELING OF BP, BN, AND GaN CVD

2.1 Boron Phosphide

2.1.1 Introduction

Equilibrium analyses of the BCl_3-PCl_3-H_2 homogeneous and heterogeneous systems and subsystems were performed. Each system presented herein is of interest either for practical production applications or for its contribution to understanding the equilibrium of other calculated systems. It has been known for many years that the reduction of boron trichloride by hydrogen can yield boron of high purity [463]. The homogeneous system PCl_3-H_2 is of interest due to its doping possibilities [464-467]. Furthermore, it has been shown that in-situ dry etching and regrowth using PCl_3 in chemical beam epitaxy is a viable technique with advantages over using Cl_2 or HCl as the etchant gas [468]. Production of BP thin films is of commercial interest for the reasons discussed in chapter one. Due to its high vapor pressure at low temperatures (760 Torr at 600 K), the heterogeneous PCl_3-H_2 system is not of interest.

Despite these many applications little work has been done analyzing the thermodynamic restrictions in the BCl_3-PCl_3-H_2 system and its subsystems. Thermodynamic assessments previously done have used an incomplete species list, inaccurate thermodynamic data, and have been limited in scope [469-472]. Advances over the years in researchers' abilities to either more accurately measure or predict a molecule's thermodynamic properties and the discovery and characterization of new species means that these and other works [73, 469-473] should be reexamined.

This work presents the results of complex chemical equilibrium calculations in both the homogeneous and heterogeneous equilibrium compositions of the BCl_3-PCl_3-H_2 system and subsystems as a function of both initial BCl_3 and PCl_3 partial pressures as well as temperature at a total pressure of one atmosphere. When the H_2 equilibrium partial pressure is not shown, it can assumed to be ≈ 1 atmosphere. All species' partial pressures are given in atmospheres. In preliminary calculations, several ion species and the electron gas were considered. Their influence on the overall equilibrium, however, was negligible and thus they were not included in future calculations. The thermodynamics of six separate systems have been examined:

PCl_3 - H_2 - homogeneous equilibrium
BCl_3 - H_2 - homogeneous equilibrium
BCl_3 - H_2 - excess HCl - homogeneous equilibrium
BCl_3 - H_2 - heterogeneous equilibrium
BCl_3 - PCl_3 - H_2 - homogeneous equilibrium
BCl_3 - PCl_3 - H_2 - heterogeneous equilibrium

In separate calculations, amorphous and crystalline boron formation was considered for the BCl_3-H_2 heterogeneous system. Both simulations converged to similar compositions so that only equilibrium values using amorphous boron are shown. It should be noted that amorphous boron would be expected for most of the temperature range considered [474,475]. Crystalline boron was also considered, however, in order to

Table 2.1 Selected Thermochemical Data of the B-P-H-Cl System

Species	$\Delta H^o_{f,298}$ (kcal/mol)	$\Delta S^o_{f,298}$ (kcal/K•mol)	A	B	C	D	C_P^o † Model	Ref.
H_2 (v)	0	0	1.27061E-02	1.68758E-06	-4.06750E+01	-1.03000E-03	1	454
H (v)	52.103	1.18013E-02	4.96797E-03	0	0	0	2	454
Cl_2 (v)	0	0	8.66307E-03	4.57242E-07	-1.10758E-10	-6.03934E+01	3	454
Cl (v)	28.992	1.28225E-02	4.53229E-03	3.32576E-06	-3.75935E-09	1.22618E-12	2	454
HCl (v)	-22.063	2.39532E-03	7.23556E-03	-1.74369E-06	3.08530E-09	-1.01697E-12	2	454
BCl (v)	42.52	2.28813E-02	3.33090E-04	-8.54180E-07	-2.12120E+01	1.35505E-03	1	457, 454
BCl_2 (v)	-6.79	9.70270E-03	2.40318E-03	-1.29203E-06	-9.42679E+01	1.81742E-03	1	457, 454
BCl_3 (v)	-98.63	-1.27159E-02	-6.01326E-03	-2.67012E-06	-1.16453E+02	4.03865E-03	1	457, 454
BH (v)	10.58	2.40033E-02	5.64037E-03	2.89935E-06	-6.71797E-10	4.81334E+01	3	457, 454
BH_2 (v)	79.43	1.37468E-02	6.57204E-03	7.34826E-06	-1.95425E-09	-4.06785E+01	3	457, 454
BH_3 (v)	24.89	-3.31967E-03	3.75562E-03	1.34189E-05	-3.34771E-09	1.08523E+02	3	457, 454
B (v)	133.8	3.52617E-02	4.96783E-03	4.45201E-10	-2.55600E-13	2.17108E-01	3	454
B_2 (v)	198.3	4.54761E-02	3.86269E-03	1.64311E-05	-1.49497E-08	4.33948E-12	2	454
BHCl (v)	34.53	1.35848E-02	-5.91154E-03	-6.53786E-07	-9.90270E+00	2.70359E-03	1	457, 454
BH_2Cl (v)	-18.98	-3.40174E-03	4.90832E-03	1.86997E-05	-9.92565E-09	2.03570E-12	2	457, 454
$BHCl_2$ (v)	-60.68	-6.55380E-03	-2.20923E-02	-2.97364E-06	-3.16838E+01	6.17562E-03	1	457, 454
B_2Cl_4 (v)	-116.9	-2.36874E-02	-2.53415E-02	-6.346570E-06	-4.87600E+01	8.87746E-03	1	454
B_2H_6 (v)	8.748	-4.09787E-02	-1.20007E-01	-7.63418E-06	3.83184E+02	2.31220E-02	1	454
B_5H_9 (v)	17.50	-8.17830E-02	-2.68602E-01	-2.20755E-05	7.45679E+02	5.07514E-02	1	454
B (s, amorph)	1.052	1.57744E-04	3.83604E-03	2.39006E-02	-1.50000E-08	0	1	454
B (s, crystal)	0	0	-5.71212E-03	-2.65664E-07	-1.31516E+02	1.74736E-03	1	454
P (v)	75.645	2.91845E-02	4.95048E-03	9.51850E-08	-1.39185E-10	5.92686E-14	2	454
P_2 (v)	34.417	3.24931E-02	9.07471E-04	-7.06630E-07	-8.51824E+00	1.24740E-03	1	454
P_3 (v)	50.191	3.35215E-02	3.19933E-03	-1.14083E-06	-6.81341E+01	1.82305E-03	1	454
P_4 (v)	14.077	2.76092E-02	6.12806E-03	-1.39655E-06	-1.63210E+02	2.15589E-03	1	454
PH (v)	55.151	2.14984E-02	6.06489E-03	2.16326E-06	-3.53638E-10	2.09641E+01	3	454
PH_2 (v)	28.574	9.76028E-03	6.04630E-03	6.80507E-06	-1.68617E-09	2.61183E+01	3	454
PH_3 (v)	1.298	-6.42101E-03	-4.84111E-02	-3.46993E-06	2.68585E+02	9.69254E-03	1	73, 455

Table 2.1 Continued

Species	$\Delta H^{o}_{f,298}$ (kcal/mol)	$\Delta S^{o}_{f,298}$ (kcal/K•mol)	A (kJ/mol)	B (kJ/mol)	C (kJ/mol)	D (kJ/mol)	C_P^{o} † Model	Ref.
PCl (v)	32.176	2.01364E-02	7.44766E-03	2.46764E-07	-3.71181E+01	1.87886E-04	1	454
PCl_2 (v)	-12.976	5.00789E-03	8.16544E-03	-6.04316E-07	-8.03903E+01	9.05729E-04	1	454
PCl_3 (v)	-69.192	-1.52979E-02	1.05141E-02	-9.52029E-07	-1.24263E+02	1.46819E-03	1	454
PCl_5 (v)	-89.866	-5.53503E-02	1.70049E-02	-1.50168E-06	-2.27131E+02	2.31970E-03	1	454
P (s,l,v)	0	0	•	•	•	•	N/A	455, 454
BP (s)	-27.600	-4.82553E-03	5.25096E-03	6.69933E-06	0	0	1	456
$B_{13}P_2$ (s)	41.826	7.24474E-02	2.09369E-02	8.58031E-05	0	0	1	73

- Heat capacity values entered directly into FORTRAN program. See Appendix A.

† (1) $C_P^{o}(T) = A + BT + CT^{-2} + D\ln(T)$; (2) $C_P^{o}(T) = A + BT + CT^{2} + DT^{3}$; (3) $C_P^{o}(T) = A + BT + CT^{2} + DT^{-2}$;

A, B, C, and D coefficients all have units of kcal/mol accurately compare the results with those previously published. Each of the molecules considered can be grouped into one of five classes - molecules containing hydrogen (BH_x and PH_x), molecules containing boron, hydrogen, and chlorine (BH_xCl_y), molecules containing chlorine (BCl_x and PCl_x), molecules containing only boron and phosphorus (BP and $B_{13}P_2$), and pure molecules (H_x, Cl_x, and B_x). Crystalline boron, diatomic hydrogen, and diatomic chlorine were used as the other reference states throughout the entire temperature range considered. The Meyers FORTRAN algorithm discussed in section 1.3.2 was used for all calculations except the heterogeneous BCl_3-PCl_3-H_2 system. Equilibrium in this system was calculated using ThermoCalc due to conflicting solid phase stabilities calculated by the Meyers program. Values of the standard enthalpy of formation, standard entropy of formation, and heat capacity for each species are summarized in Table 2.1.

2.1.2 Results and Discussion

In this section the thermodynamics of the 6 different systems will be discussed in order.

PCl_3 - H_2 - homogeneous system

Figure 2.1 shows the equilibrium partial pressures of species as a function of T for four different values of $p^o(PCl_3)$. These figures show that essentially all of the Cl results in the stable HCl species at all T and $p^o(PCl_3)$ examined. It is noted in these calculations, as well as those for other systems presented later, that entropy considerations favor the production of smaller molecules (i.e., more moles) as the temperature increases (e.g., P_2 versus P_4, H versus H_2). As temperature increases and the initial partial pressure of PCl_3 remains constant, the P_2 and PH_2 partial pressures increase while that of P_4 and PH_3

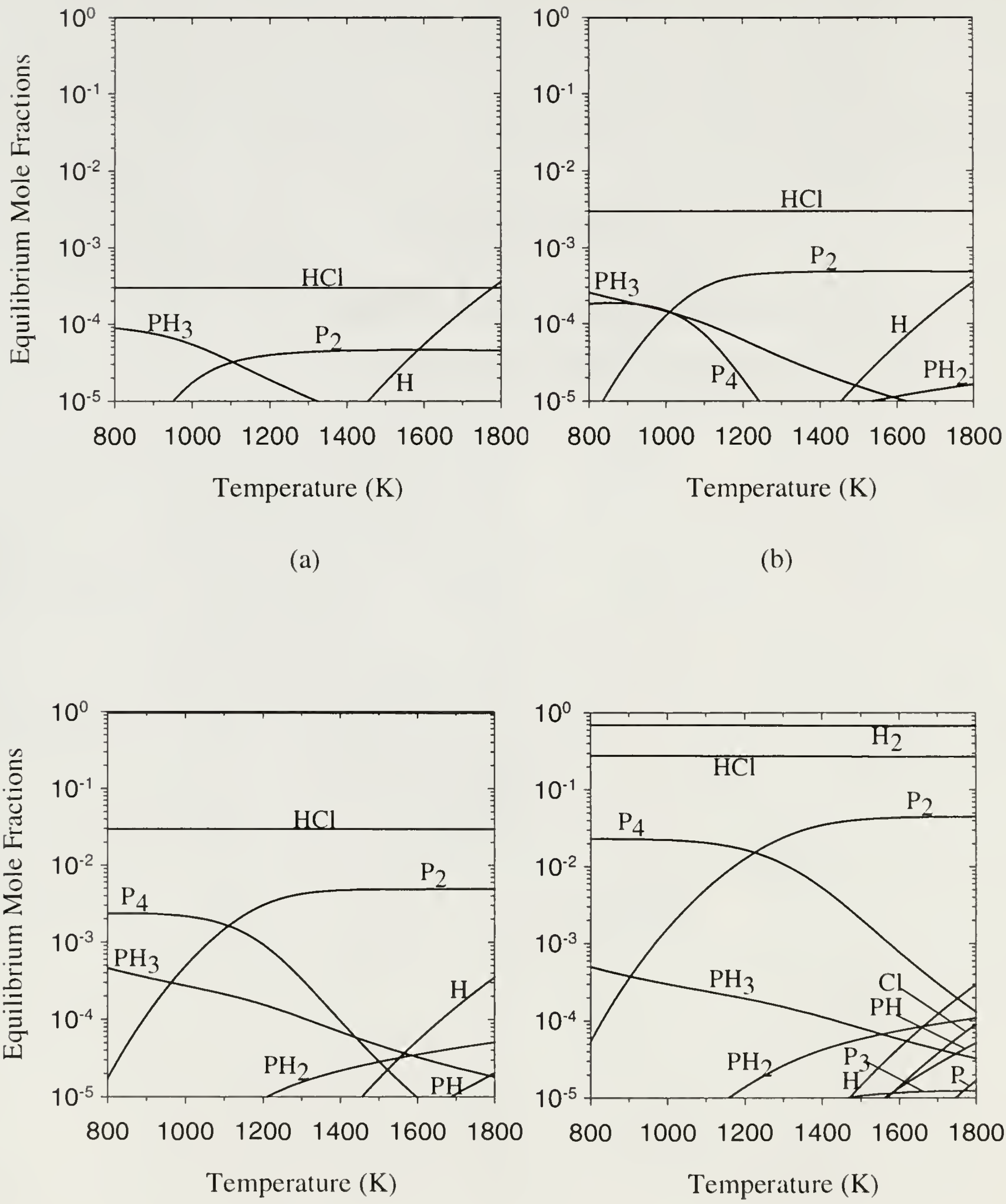

(a)

(b)

(c)

(d)

Figure 2.1: Equilibrium partial pressure (atm) in the homogeneous system PCl_3-H_2 as a function of temperature at constant PCl_3 initial partial pressures a) $p^o(PCl_3)=10^{-4}$; b) $p^o(PCl_3)=10^{-3}$; c) $p^o(PCl_3)=10^{-2}$; d) $p^o(PCl_3)=10^{-1}$.

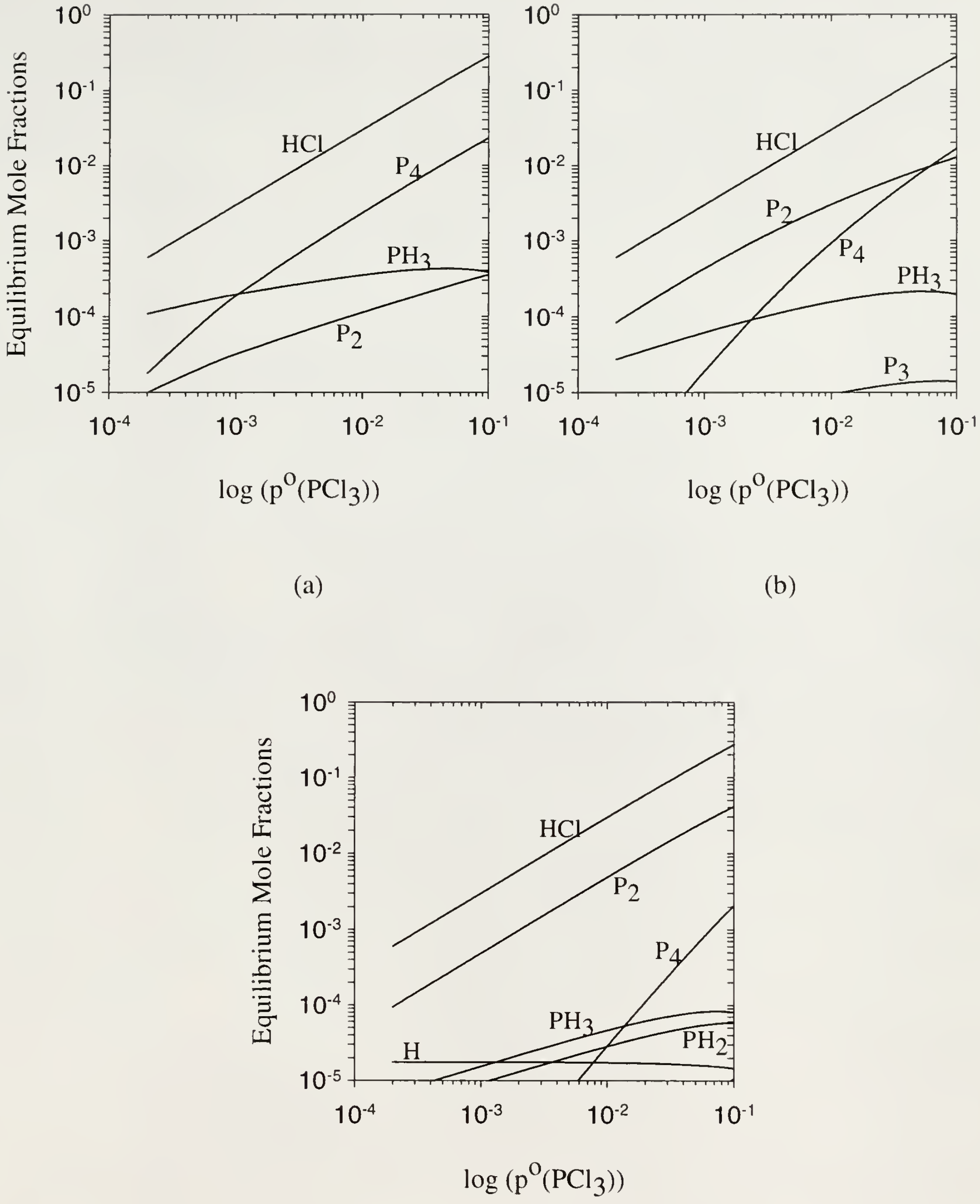

(a)

(b)

(c)

Figure 2.2: Equilibrium partial pressure (atm) in the homogeneous system PCl_3-H_2 as a function of PCl_3 initial partial pressure at constant temperature
a) T=900 K; b) T=1200 K; c) T=1500 K.

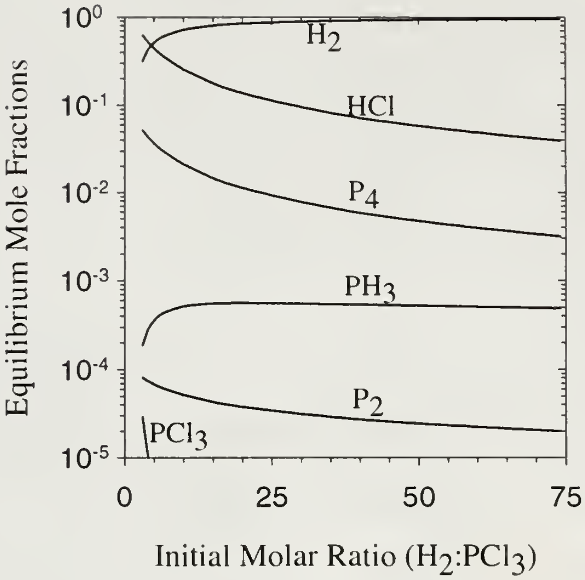

Figure 2.3: Equilibrium partial pressure (atm) in the homogeneous system PCl_3-H_2 as a function of the initial H_2:PCl_3 molar ratio at constant temperature (T=800 K)

decrease. As the $p^o(PCl_3)$ increases, several more species appear with partial pressures in excess of $1x10^{-5}$ including H, PH, and Cl. In addition, the species present in each of the graphs, with the exception of elemental hydrogen, increase with an increase in the initial partial pressure of PCl_3. This is due to the increase in the number of phosphorus and chlorine atoms that can be redistributed to form a greater number of other species. The elemental hydrogen does not change with the PCl_3 initial partial pressure, but increases with temperature as it does in an only hydrogen system.

As shown in Figure 2.2, the partial pressure of each of the phosphorus or chlorine containing species in the homogeneous PCl_3-H_2 system increases as the initial partial pressure of PCl_3 increases. The main gas phase species are P_4, PH_3, and HCl at low temperatures and P_2 and HCl at high temperatures. The HCl partial pressure does not depend on the temperature regardless of the initial PCl_3 partial pressure and increases linearly with PCl_3 initial partial pressures (Figures 2.1 and 2.2). This indicates an essentially complete reaction of the initial PCl_3 to HCl and no other chlorine containing species. There is little effect on the elemental hydrogen partial pressure since the extra hydrogen required to form the additional molecules of PH_3, PH_2, and PH comes from the slight decrease in the H_2 partial pressure.

Figure 2.3 shows the partial pressure variation of the major gas phase species as a function of initial molar ratio (H_2:PCl_3) at 800 K. Relatively flat profiles are observed for all species except PCl_3. At very low molar ratios (i.e. high initial PCl_3 partial pressures) PCl_3 is present at equilibrium with partial pressures above 1×10^{-5} atm. As the molar ratio increases, however, the PCl_3 partial pressure decreases rapidly. PH_3 is present with substantial partial pressures in the current calculations while Milovanova and Krenev do not mention it [471]. It is possible that differences in the thermodynamic data account for this omission. Finally the yield of elemental phosphorus in the gas phase is greater than 90% for all temperatures considered at a PCl_3:H_2 molar ratio of 1:20.

In summary the main gas phase equilibria are:

$$2PCl_3 + 3H_2 \Leftrightarrow P_2 + 6HCl \qquad \text{Equation 2.1}$$

$$4PCl_3 + 6H_2 \Leftrightarrow P_4 + 12HCl \qquad \text{Equation 2.2}$$

$$PCl_3 + 3H_2 \Leftrightarrow PH_3 + 3HCl \qquad \text{Equation 2.3}$$

BCl_3 - H_2 - homogeneous system

In this system the equilibrium was constrained to prevent the formation of solid boron. Figures 2.4 and 2.5 show the equilibrium dependence of the homogeneous BCl_3-H_2 system as a function of temperature and initial BCl_3 partial pressure. The profound effect of temperature and initial BCl_3 partial pressure can immediately be seen. The main

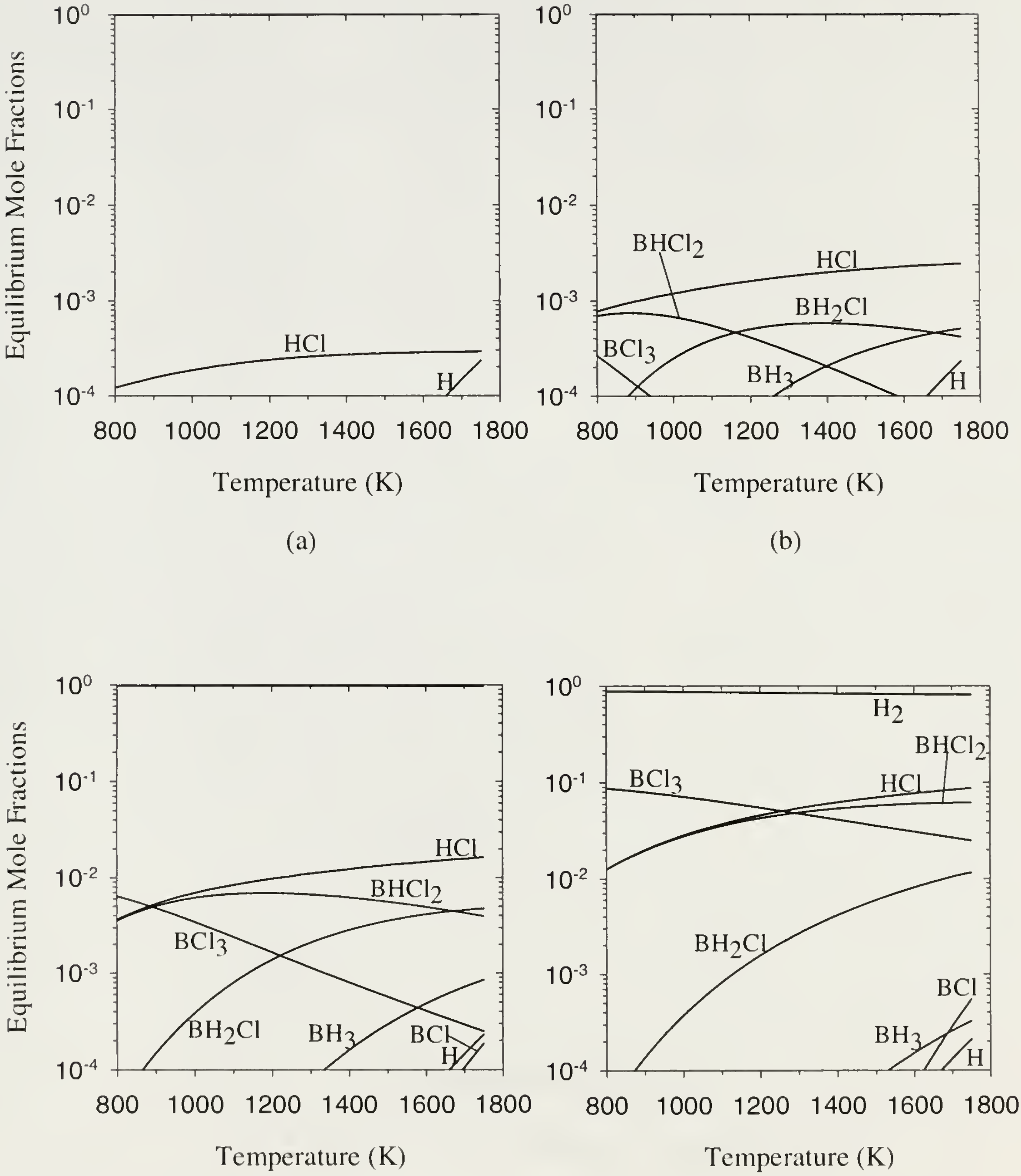

(a) (b)

(c) (d)

Figure 2.4: Equilibrium partial pressure (atm) in the homogeneous system BCl_3-H_2 as a function of temperature at constant BCl_3 initial partial pressures
a) $p^o(BCl_3)=10^{-4}$; b) $p^o(BCl_3)=10^{-3}$; c) $p^o(BCl_3)=10^{-2}$; d) $p^o(BCl_3)=10^{-1}$.

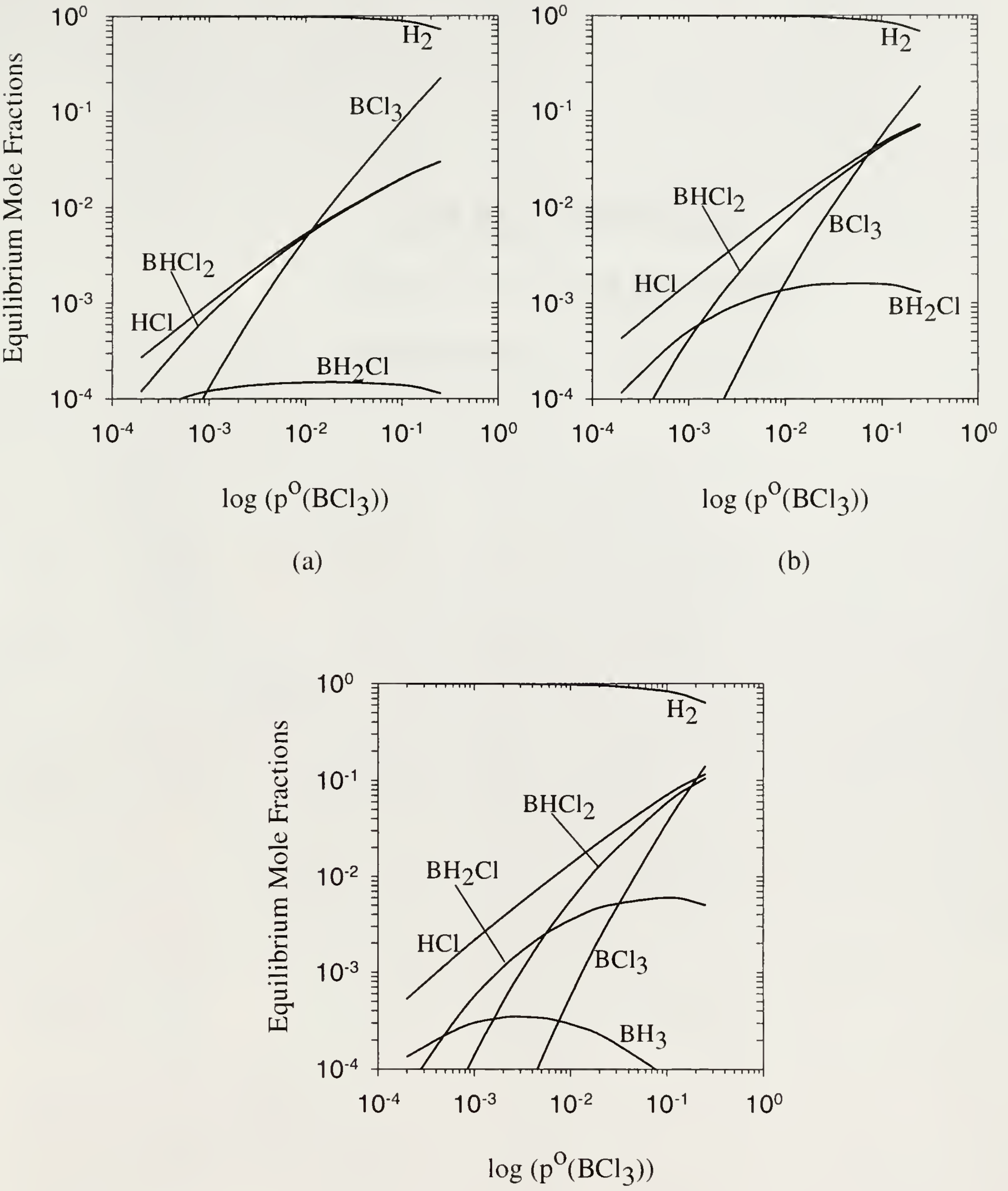

(a)

(b)

(c)

Figure 2.5: Equilibrium partial pressure (atm) in the homogeneous system BCl_3-H_2 as a function of BCl_3 initial partial pressure at constant temperature
a) T=900 K; b) T=1200 K; c) T=1500 K.

boron containing gas phase species are $BHCl_2$, BH_2Cl, and BCl_3 at low temperatures while at high temperatures BH_3 also becomes important. The HCl partial pressure is nearly linear but not constant with respect to both temperature and the initial BCl_3 partial pressure. The BCl_3 reactant does not completely react as the PCl_3 reactant did. The impact of this will be seen in the BCl_3-PCl_3-H_2 homogeneous system (section e).

As the initial BCl_3 concentration is increased, the number of boron and chlorine atoms available to form species increases. Also, as the temperature increases a greater number of species are present, in particular elemental hydrogen. As in the PCl_3-H_2 homogeneous system elemental hydrogen is found to be independent of the initial BCl_3 partial pressure (except at very high $p^o(PCl_3)$ values) since $p^o(BCl_3)$ is still small relative to $p^o(H_2)$. BCl_3 partial pressure is increased at constant temperature, there is a monotonic increase in the equilibrium partial pressure of all species with the exception BH_3 and elemental hydrogen. It is curious to note in Figure 2.5 that the BH_2Cl concentration increases sharply with temperature and shows a maximum with respect to the initial BCl_3 partial pressure at each temperature. For instance a nearly constant equilibrium partial pressure is present at 900 K over the entire range of initial BCl_3 partial pressures (Figure 2.5). As the temperature is subsequently increased, however, the BH_2Cl equilibrium partial pressure profile clearly becomes dependent on the initial BCl_3 partial pressure in a monotonically increasing fashion. Also Figure 2.4a shows that at low temperature and initial $p(BCl_3)$ there is a large difference in the $BHCl_2$ and HCl partial pressures. As the initial $p(BCl_3)$ is increased, however, the difference is reduced to 1×10^{-5} atmospheres (Figure 2.4c). Figure 2.5 indicates that if the temperature is increased a noticeable difference between the partial pressures of each of these species is present over the entire range of initial BCl_3 partial pressures studied. Finally, as temperature is increased elemental chlorine and hydrogen are present in increasing amounts.

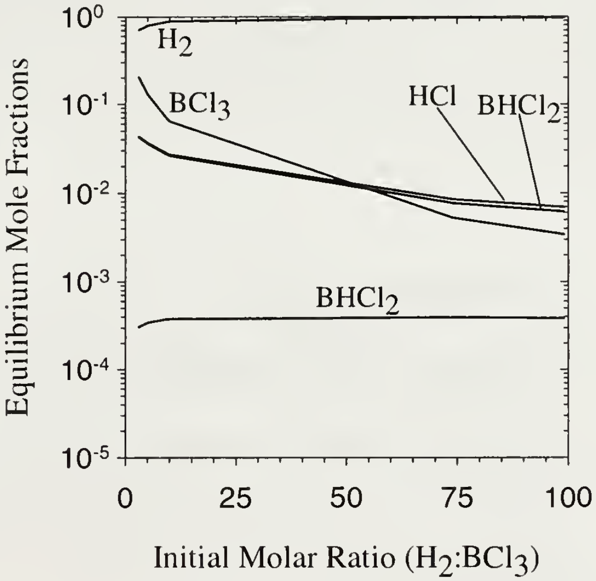

Figure 2.6: Equilibrium partial pressure (atm) in the homogeneous system BCl_3-H_2 as a function of the initial H_2:BCl_3 molar ratio at constant temperature (T=800 K).

In Figure 2.6 the importance of the initial H_2:BCl_3 molar ratio can be seen. The interesting observation made from this graph is the small range of equilibrium partial pressures of the major species at high initial molar ratios. This difference does become more pronounced if the initial molar range is extended to higher values. At an initial H_2:BCl_3 molar ratio of approximately 55:1 the partial pressures of each major species are essentially equal at 1.3×10^{-2} atmospheres. Essentially, when the $p^o(H_2)$ begins to become small relative to the $p^o(BCl_3)$ ($H:Cl = 2/3(p^o(H_2)/p^o(BCl_3))$), there are an insufficient number of H atoms available to form hydrogen containing species (e.g., HCl and $BHCl_2$) and the BCl_3 becomes the dominant species.

In summary the main homogeneous equilibrium reactions are:

$$BCl_3 + H_2 \Leftrightarrow BHCl_2 + HCl \qquad \text{Equation 2.4}$$

$$BCl_3 + 2H_2 \Leftrightarrow BH_2Cl + 2HCl \qquad \text{Equation 2.5}$$

BCl_3 - H_2 - excess HCl - homogeneous system

As before, equilibrium in this system was constrained to prevent the formation of solid boron. The influence of HCl on the overall equilibrium of the BCl_3-H_2 system is important since it was shown in above that PCl_3 reacts to near completion. Thus, if PCl_3 and BCl_3 are present at the same time, the HCl produced by reactions 2.1-2.3 will reduce the equilibrium partial pressures of $BHCl_2$ and BH_2Cl by shifting reactions 2.4 and 2.5 to the left. Comparison of Figures 2.4 and 2.7 shows clearly the reduction of these species partial pressures at equilibrium. The main boron containing gas phase species in the BCl_3-H_2 system when excess HCl is added are $BHCl_2$ and BH_2Cl. The BH_3 and BH_2Cl partial pressures are greatly reduced as the initial excess HCl partial pressure is increased as are the partial pressures of all boron + hydrogen containing species. Furthermore, the BCl_3 partial pressure is much higher when excess HCl is present than it was in section b. This is again due to the equilibria given in reactions 2.4-2.6.

BCl_3 - H_2 - heterogeneous system

In this system the equilibrium is no longer constrained and solid boron formation is considered in the calculations. In contrast to the homogeneous equilibrium of the BCl_3-H_2 system, there is a notable decrease in the $BHCl_2$ partial pressure as the system temperature increases as more solid boron forms. The major gas phase boron containing

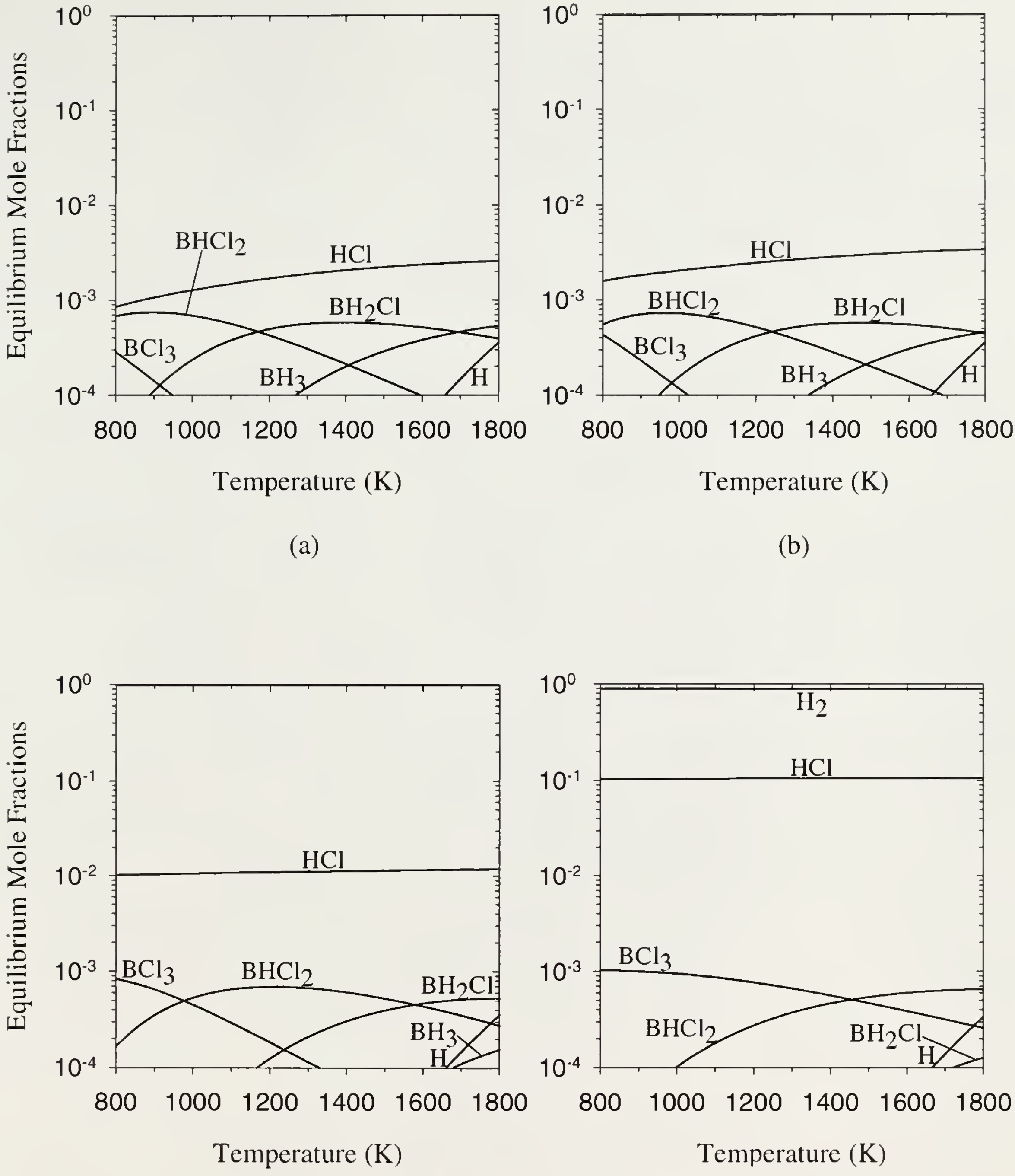

(a)

(b)

(c)

(d)

Figure 2.7: Equilibrium partial pressure (atm) in the homogeneous system BCl_3-H_2-HCl as a function of temperature at constant HCl initial partial pressures ($p^o(BCl_3)=10^{-3}$)
a) $p^o(HCl)=10^{-4}$; b) $p^o(HCl)=10^{-3}$; c) $p^o(HCl)=10^{-2}$; d) $p^o(HCl)=10^{-1}$.

species in the heterogeneous system are the same as in the homogeneous system with nearly identical partial pressures at lower temperatures (i.e., little solid boron is formed). Figure 2.8 shows the strong temperature dependence of the gas phase of the heterogeneous system. At lower temperatures there is a lack of significant solid boron formation and thus the boron containing gas phase species partial pressures are nearly identical for both the homogeneous and heterogeneous BCl_3-H_2 systems. As the temperature is increased, however, the major boron containing gas phase species partial pressures in the heterogeneous system are more than an order of magnitude lower than in the homogeneous case. For instance, at low temperatures and an initial molar BCl_3:H_2 ratio of 1:75, little solid boron is deposited (1.8% at 800 K). Therefore, the difference in the gas phase equilibrium of the two systems would be small. As the temperature is increased at the same initial molar ratio, however, the yield of solid boron deposited increases to 85.7% at 1500 K. The yield is defined as the ratio of the amount of solid boron at equilibrium relative to the initial total amount of boron in the system. Thus more boron is withdrawn from the gas phase and the partial pressures of the major boron containing gas phase species must correspondingly decrease.

Also the HCl partial pressure is non-linear with respect to temperature, especially at higher initial BCl_3 partial pressure (Figure 2.8). At higher temperatures, however, its partial pressure becomes nearly linear with respect to the log of the initial BCl_3 partial pressure (Figure 2.9). This trend is different than that calculated by Kelder for the B-H-Br system. In the bromine system the HBr partial pressure is linear with respect to both temperature and the log of the initial BBr_3 partial pressure. There is essentially no difference in the partial pressures of any non-boron containing compounds between the

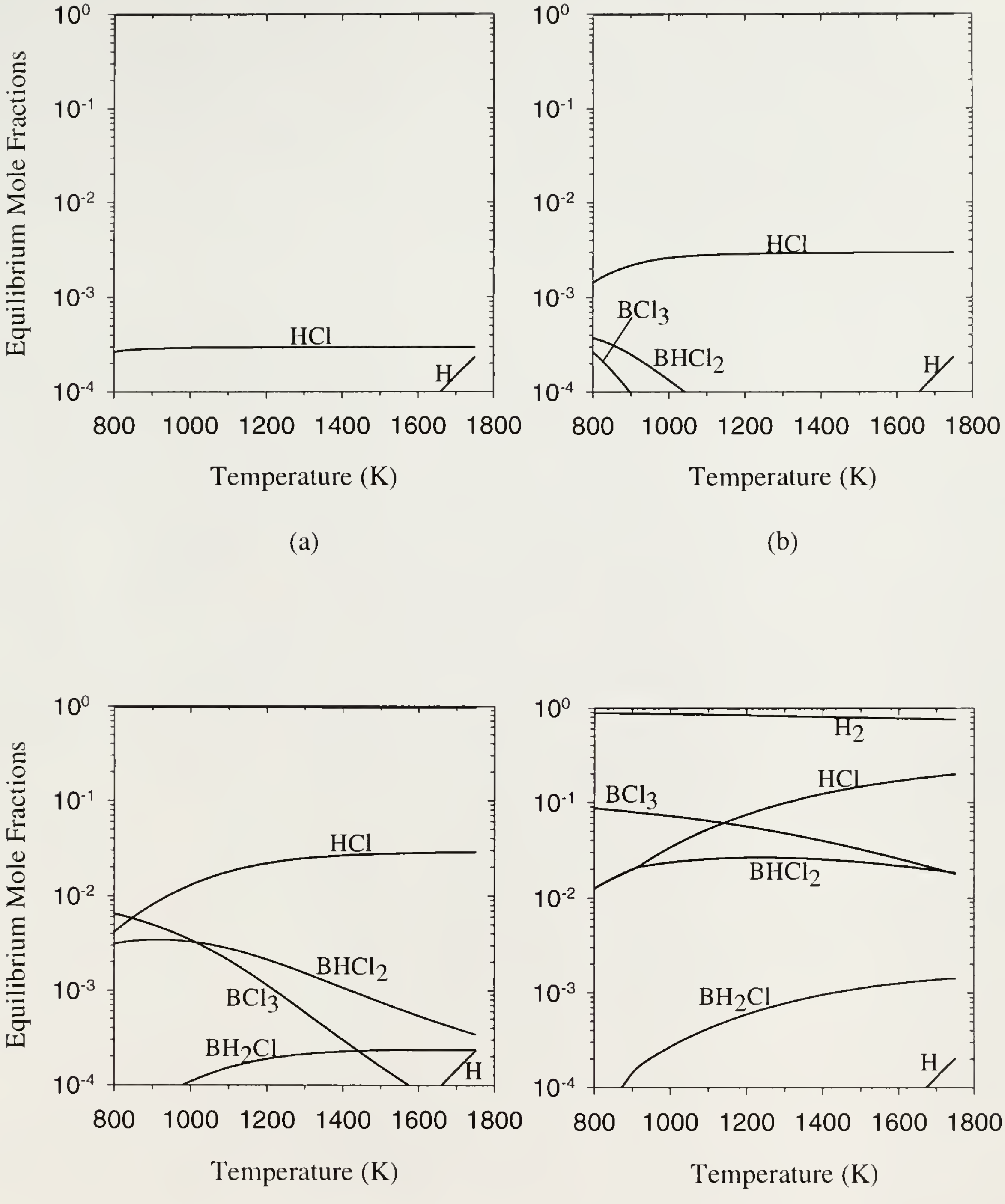

(a)

(b)

(c)

(d)

Figure 2.8: Equilibrium partial pressure (atm) in the heterogeneous system BCl_3-H_2 as a function of temperature at constant BCl_3 initial partial pressures a) $p^o(BCl_3)=10^{-4}$; b) $p^o(BCl_3)=10^{-3}$; c) $p^o(BCl_3)=10^{-2}$; d) $p^o(BCl_3)=10^{-1}$.

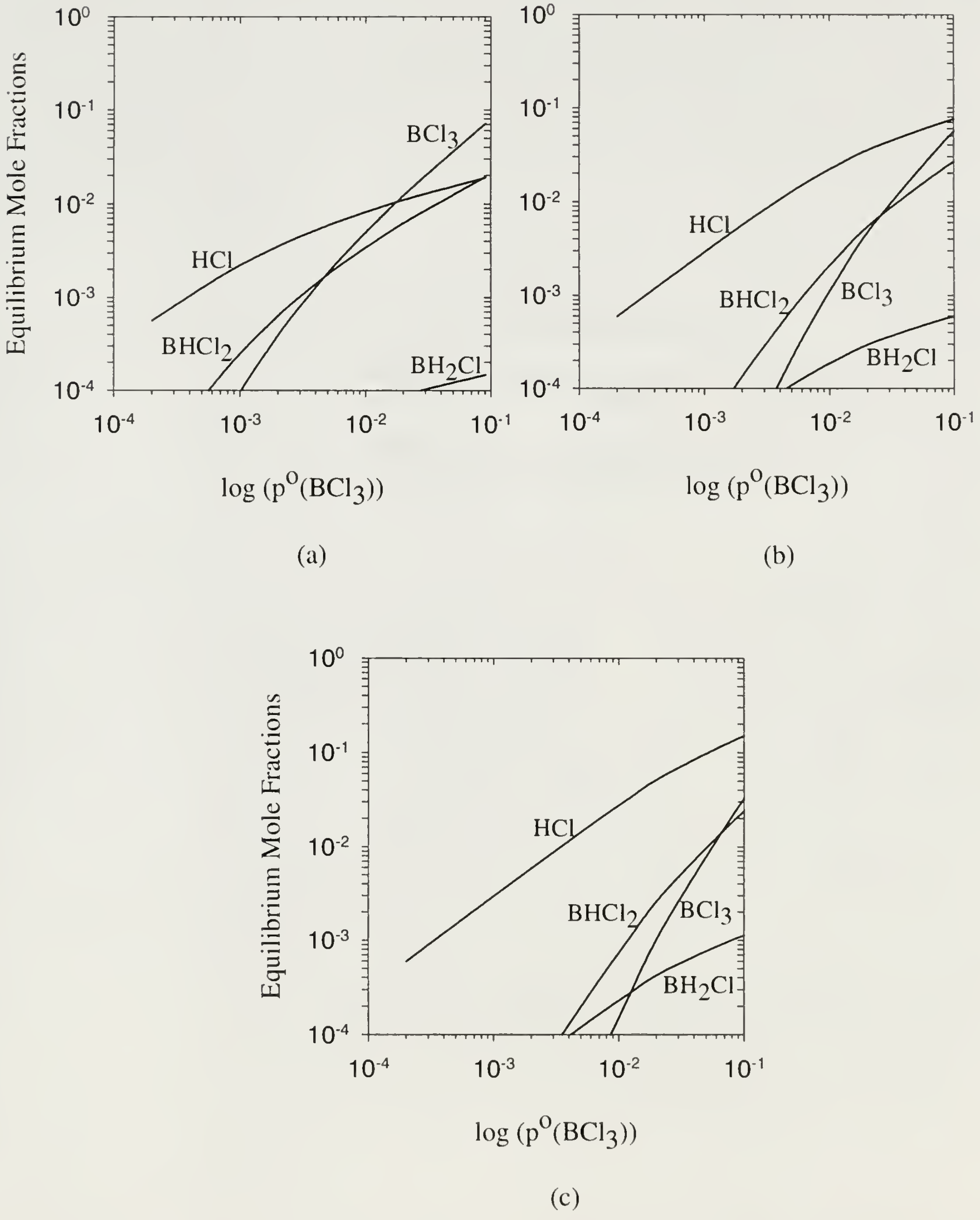

Figure 2.9: Equilibrium partial pressure (atm) in the heterogeneous system BCl_3-H_2 as a function of BCl_3 initial partial pressure at constant temperature
a) T=900 K; b) T=1200 K; c) T=1500 K.

heterogeneous and homogeneous equilibria since only elemental boron is being deposited.

Figure 2.9 illustrates the dependence of the gas phase molecules present at heterogeneous equilibrium on the initial BCl_3 partial pressure at three different temperatures. At low initial BCl_3 partial pressures the HCl partial pressure is relatively insensitive to temperature variations. The equilibrium partial pressure of BCl_3 decreases as temperature increases to compensate for the increased formation of solid boron and other gaseous boron containing species. As noted in the BCl_3-H_2 homogeneous system, as the initial BCl_3 partial pressure is increased there is an increasing number of species whose partial pressures are in excess of 1×10^{-4} atmospheres.

Figure 2.10 shows the dependence of the vapor phase partial pressures on the initial H_2:BCl_3 molar ratio. When compared to the calculations of Milovanova and Krenev [470], the present calculations show higher equilibrium partial pressures for all major species except HCl. The crossover in the $BHCl_2$ - BCl_3 curves occurs much earlier in the present calculations at a molar H_2:BCl_3 ratio of 15 instead of 120 and thus at a much higher BCl_3 partial pressure. BH_2Cl is present at high partial pressures at equilibrium at all H_2:BCl_3 molar ratios with its partial pressure never decreasing below 1.7×10^{-4} atmospheres. As expected all major boron containing species partial pressures decrease with an increase in the initial molar ratio while both H_2 and H equilibrium partial pressures increase.

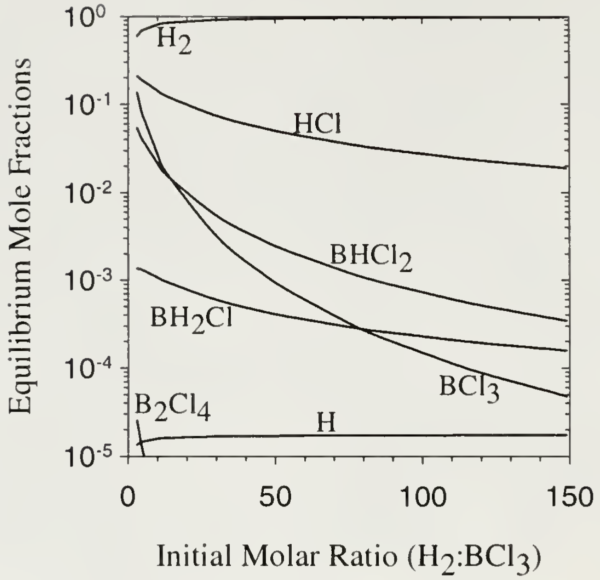

Figure 2.10: Equilibrium partial pressure (atm) in the heterogeneous system BCl_3-H_2 as a function of the initial H_2:BCl_3 molar ratio at constant temperature (T=1000 K).

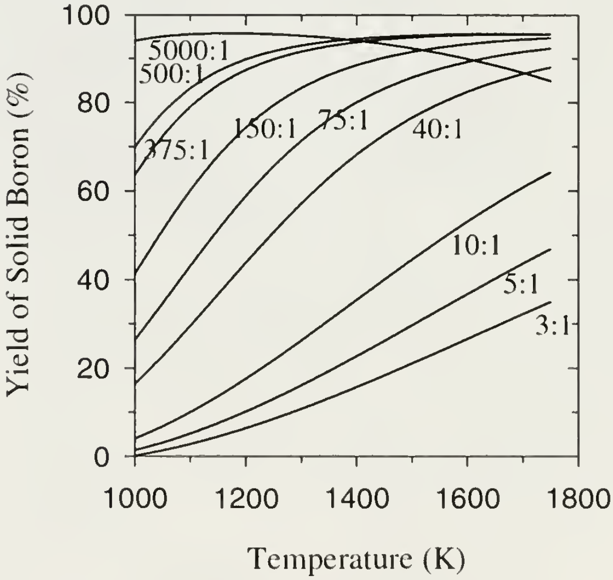

Figure 2.11: Yield of solid boron (%) in the heterogeneous system BCl_3-H_2 as a function of temperature and initial molar ratio (H_2:BCl_3).

The impact of an inclusive species list and an updated thermodynamic database can be seen when Figure 2.11 is compared to a similar graph calculated by Milovanova and Krenev. In their calculations, BH_2Cl was omitted from the species list and a currently outdated thermodynamic database was used. The inclusion of this major species and use of an updated thermodynamic database results in lower percent yields of solid boron than those predicted by Milovanova and Krenev. For instance, Milovanova and Krenev calculated an approximate 70% yield of solid boron at 1000 K and a 150:1 molar ratio while Figure 2.11 shows only a 40% yield at this temperature and molar ratio. The higher $BHCl_2$ equilibrium partial pressure and inclusion of BH_2Cl in the species list result in this difference because each would prevent more of the boron initially available in the system from being able to form solid boron. At higher temperatures similar yields of boron are observed as essentially most of the initial boron deposits. Differences in the final equilibrium deposition of either crystalline or amorphous boron are small (< 1%) when each was considered in separate calculations. The present calculations also considered much larger boron trichloride : hydrogen ratios than those by Milovanova and Krenev. A comparison of the graphs show that a molar ratio of 1:500 roughly corresponds to the previously reported 1:150 molar ratio. In both calculations the yield of boron increases with an increase in the H_2:BCl_3 mole fraction and temperature. At the highest initial H_2: BCl_3 molar ratio considered, 5000:1, the percent yield actually decreases as the temperature increases. This can be explained by the increased partial pressures of several boron containing species in the 10^{-4} to 10^{-6} atmosphere range, especially BH_3 and BH_2Cl, at higher temperatures and lower initial BCl_3 partial pressures. A maximum 95.8% yield of solid boron was calculated at a H_2:BCl_3 molar ratio of 5000:1 and 1150 K. The importance of the above calculations can be seen in their application to the production of highly pure boron [476,477] and single crystal films [478].

From Figures 7-9 the main equilibria are:

$BCl_3 + H_2 \Leftrightarrow BHCl_2 + HCl$

$BCl_3 + 2H_2 \Leftrightarrow BH_2Cl + 2HCl$

$2BCl_3 + 3H_2 \Leftrightarrow 2\langle B\rangle + 6HCl$ Equation 2.6

BCl_3 - PCl_3 - H_2 - homogeneous system

Since the main phosphorus containing species in the homogeneous BCl_3-PCl_3-H_2 system are independent of the initial BCl_3 partial pressure, their partial pressures at equilibrium have already been calculated in the PCl_3-H_2 homogeneous system section. Furthermore, it was noted in above that PCl_3 essentially reacts to completion to form HCl as the only chlorine containing species. Conversely, the main boron containing species partial pressures were found to be dependent on the initial PCl_3 partial pressure. In the homogenous BCl_3-H_2-excess HCl section, the influence of an excess amount of HCl on the homogeneous BCl_3-H_2 equilibrium was examined. Therefore, the HCl produced by independent PCl_3 reactions is simply the excess HCl introduced into the homogeneous BCl_3-H_2 equilibrium. The excess HCl influence on the homogeneous BCl_3-H_2 system is also known from reactions 2.4 and 2.5. Therefore, equilibrium in the homogeneous BCl_3-PCl_3-H_2 system is simply a summation of sections a and c. Kelder identified an identical situation in the BBr_3-PBr_3-H_2 system [73].

BCl_3 - PCl_3 - H_2 - heterogeneous system

The focus of the thermodynamic calculations is the determination of different solid deposition regions in the BCl_3-PCl_3-H_2 heterogeneous system. Particular interest lies in determining limitations that thermodynamics may place on the deposition of pure cubic boron monophosphide (cBP). Five different deposition conditions were considered: a fixed initial BCl_3 partial pressure, a fixed initial H/Cl molar ratio (i.e. fixed initial H_2 partial pressures) , replacement of H_2 with an inert (He), gradual replacement of He with H_2, and addition of HCl to study its etching effect. In addition, limited information on the gas phase was presented. Six different solid phase regimes were found to exist that were highly dependent on the initial precursor ratio and the deposition temperature. The pure regimes are BP, $B_{13}P_2$, and an area where no solid phase deposition occurs. The solid mixture regimes are BP+$B_{13}P_2$, B+BP, and B+$B_{13}P_2$. For clarity, the inlet precursor partial pressure ratio was normalized as

$$\gamma = \frac{p^o(BCl_3)}{p^o(BCl_3)+p^o(PCl_3)} \qquad \text{Equation 2.7}$$

It must be noted that the Cl/H ratio does not change as γ changes if $p^o(BCl_3)+p^o(PCl_3)$ equals a constant. Pure solid boron is formed only if $p^o(PCl_3)$ is 0 (i.e. $\gamma=1$). Solid phosphorus is never deposited even if the initial BCl_3 reactant is 0 (i.e. $\gamma=0$) due to its' high vapor pressure at the lowest temperature examined. It was found that for all solid phase diagrams the transition from the B+BP regime to either BP+$B_{13}P_2$ or B+$B_{13}P_2$ regimes occurred at 1172 K (900 °C). This is the lowest temperature at which $B_{13}P_2$ is deposited for any initial condition considered.

The influence of increasing the initial BCl_3 partial pressure on the different deposition regions is shown in Figure 2.12. In the graphs of Figure 2.12 the initial BCl_3 partial pressure is fixed and the initial PCl_3 partial pressure is varied to correspond to the γ value. Thus at low γ values the initial PCl_3 is high while at high β values the PCl_3 partial pressure is low. Although neither Cl or H appears in a solid phase (all remains in the gas), the Cl/H ratio does vary with γ if $p^o(BCl_3)$ is fixed. At high initial BCl_3 partial pressures and low γ values, both reactants are initially present in high concentrations. This will produce a high HCl partial pressure at equilibrium via reactions 2.1 to 2.5. The HCl will act as an etchant and thus produce a larger region where no deposition will occur (comparison of the size of the single phase vapor region in (a) and (d)). It is also interesting to note the diminishing size of both the $BP+B_{13}P_2$ and $B+B_{13}P_2$ regions as the initial BCl_3 partial pressure is reduced. Conversely, the $B_{13}P_2$ region is greatly expanded and encompasses nearly all γ values and temperatures above 1400 K in Figure 2.12a. One can also conclude that thermodynamically the largest region for cBP deposition is present at high initial BCl_3 partial pressures and high initial PCl_3 partial pressures (i.e. lower γ values), with moderate to low temperatures. As mentioned above, however, this will produce a large amount of HCl. Mizutani et al. have investigated the vapor etching of BP using a 7% HCl mixture in hydrogen [479]. In their study they noted a sharp increase in the etching rate as the HCl concentration was increased. They also noted a rapid increase in the etching rate above 1160 °C (1430 K) that they attributed to the decomposition of BP. This is generally consistent with the calculated results where the BP decomposition temperature ranges from 1486 to 1690 K depending on the initial BCl_3 partial pressure.

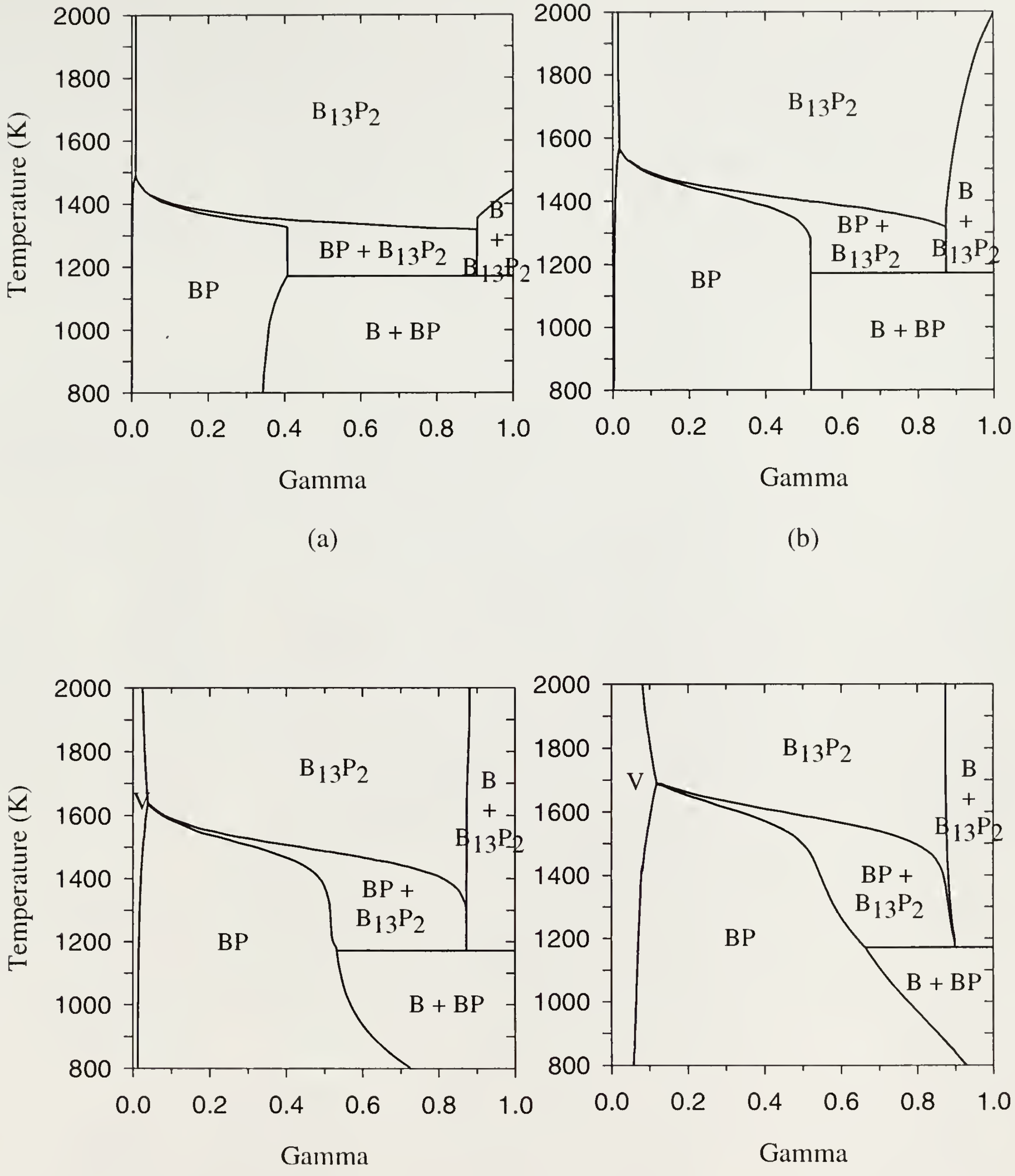

(a)

(b)

(c)

(d)

Figure 2.12: Solid phase diagram for the heterogeneous system BCl_3-PCl_3-H_2 as a function of temperature and BCl_3 fraction gamma as defined by equation 2.7 a) $p^o(BCl_3)=10^{-5}$; b) $p^o(BCl_3)=10^{-4}$; c) $p^o(BCl_3)=10^{-3}$; d) $p^o(BCl_3)=10^{-2}$.

In contrast to the BBr_3-PBr_3-H_2 system studied by Kelder [73], the region where no solid deposition occurs is much smaller for the chlorine-based chemistry. Furthermore, at BCl_3 initial partial pressures of 1×10^{-4} atm the region of BP deposition was determined to exist at higher temperatures for the chlorine chemistry, but the transition from BP to B+BP occurs at a γ value of 0.52 instead of approximately 0.64. At a BCl_3 initial partial pressure of 1×10^{-3} atm larger differences are evident. The BP region follows the same trends as before. At a temperature of 1100 K the BP to B+BP transition occurs at $\gamma=0.54$ in the chlorine system while in the bromine system it occurs at 0.78. Furthermore, the BP+$B_{13}P_2$ region extends to γ values of 0.10 in the chlorine system but stops at approximately 0.65 in the bromine system. Finally $B_{13}P_2$ is present in the γ value range of 0.05 to 0.88 in the chlorine system at high temperature while in the bromine system this range is reduced to 0.55 to 0.95. There are several possible reasons for these differences. Obviously a different chemistry is present in each system. An updated thermodynamic database is also used in the present calculations with values for species such as BH_2 and BH_3. Finally, there is an ongoing disagreement in the literature as to whether BP decomposes into $B_{13}P_2$ or B_6P. The more recent literature favors the decomposition of BP into $B_{13}P_2$, so this species is considered in the current calculations. In his dissertation, Kelder considered the decomposition of BP into B_6P.

Calculations were also performed at fixed H/Cl molar ratios. The initial H_2 partial pressure was set at a certain value and the initial BCl_3 and PCl_3 partial pressures were calculated such that their total sum was constant and equal to 1 atmosphere. The influence of the initial H/Cl molar ratio is seen in Figure 2.13. The precursor ratio was again normalized and designated γ. As before, six different solid regions are present at fixed H/Cl molar ratios. As the H/Cl molar ratio is increased (i.e. initial H_2 partial pressure increased), the BP single phase deposition domain decreases greatly. This is because this domain occurs for $\gamma<0.5$ and P is the limiting element in forming BP. As the $p^o(H_2)$ increases, less P is available to form BP. It is interesting to note that each of the region boundaries become much more linear as the H/Cl ratio is increased. This linearization coincides with a decrease in the transition temperature between the BP, BP+$B_{13}P_2$, and $B_{13}P_2$ regions. At H/Cl ratios equal to 6 ($p^o(H_2) = 0.90$) these transition temperatures at $\gamma=0.20$ are 1690 and 1694. As the ratio is increased to 666 ($p^o(H_2) = 0.999$), however, the temperatures are lowered to 1470 and 1482, respectively. Also, the BP/B+BP boundary shifts from a γ value of 0.88 to 0.52. As in the previous calculations there still exists a region of no solid deposition that decreases rapidly with an increase in the H/Cl molar ratio.

The influence of an inert gas (i.e., He) on the final system equilibrium was examined by replacing the H_2 carrier gas with an inert gas. As expected, there was no solid deposition present when only inert gas was used as a carrier gas, since all of the aforementioned equilibria require HCl to be formed as a reaction product. Since no hydrogen is present in the system to form HCl, neither of the trichloride precursors can dissociate appreciably to form B, BP, or $B_{13}P_2$. As a result of these findings, a series of equilibria were calculated to examine the effect of gradually replacing inert gas with H_2 in the system. A constant (inert gas+H)/Cl ratio of 6 and an initial (BCl_3+PCl_3) partial pressure of 0.10 atm were maintained in order to compare the results with those of Figure 2.13c where the H/Cl ratio equaled 6. Thus when the initial H_2 partial pressure is 0.90 the system will contain no He and be identical to Figure 2.13c.

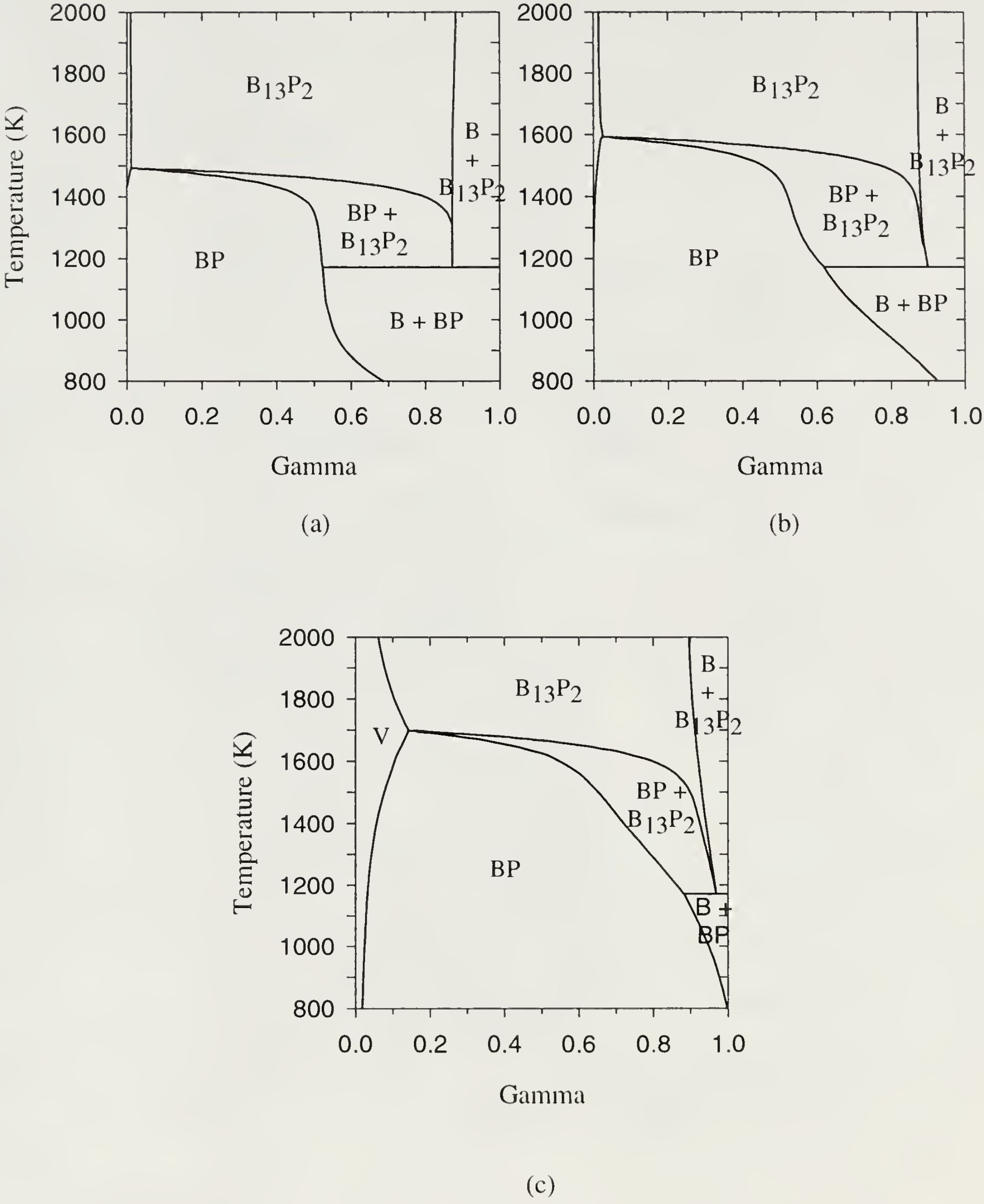

(a)

(b)

(c)

Figure 2.13: Solid phase diagram for the heterogeneous system BCl_3-PCl_3-H_2 as a function of temperature and BCl_3 fraction gamma as defined by equation 2.7 a) H/Cl=666 (i.e. $p^o(H_2)=0.999$); b) H/Cl=66 (i.e. $p^o(H_2)=0.99$); c) H/Cl=6 (i.e. $p^o(H_2)=0.90$).

The results of the calculated equilibria for the He-H-B-P-Cl system are shown in Figure 2.14. At low H_2 partial pressures, very little solid deposition occurs at equilibrium due to the lack of H_2 available to dissociate the trichloride precursors, forming the HCl byproducts. On the other hand, as the H_2 partial pressure is increased to 0.0857 (H:Cl=1), then to 0.25, and then to 0.50 atm, the various domains of solid formation increase in size and move to lower gamma values. It is interesting to note a large shift in the solid phase boundaries as the H_2 partial pressure varies from 0 to 0.25, but a much slower rate of change at the higher partial pressure range of 0.25 to 0.90. Since the sum of the trichloride precursors partial pressures is initially fixed at 0.10 atm, this indicates that roughly a 5:1 initial molar ratio of H_2:BCl_3+PCl_3 is required to dissociate the chlorine precursors to nearly the extent that a 9:1 initial molar ratio would.

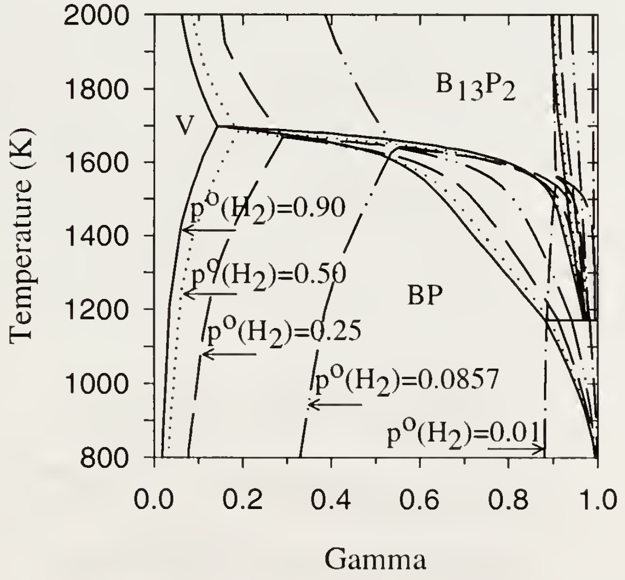

Figure 2.14: Solid phase diagram for the heterogeneous system BCl_3-PCl_3-H_2-He as a function of temperature and BCl_3 fraction gamma as defined by equation 2.7 Initial condition (H+He)/Cl=6).

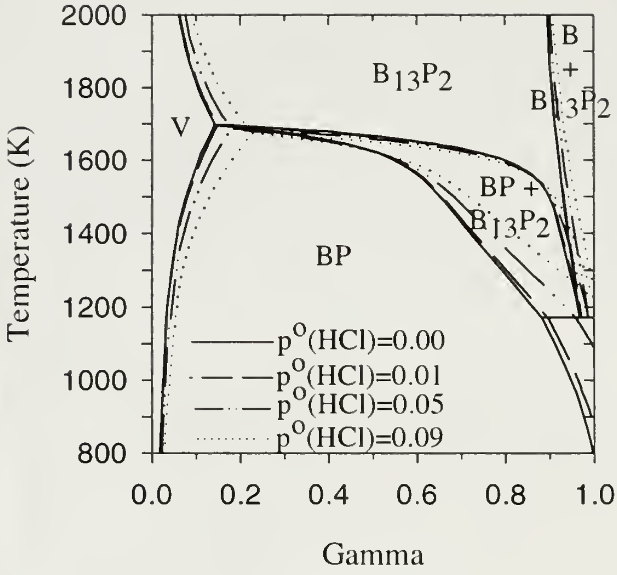

Figure 2.15: Solid phase diagram for the heterogeneous system BCl_3-PCl_3-H_2-HCl as a function of temperature and BCl_3 fraction gamma as defined by equation 2.7 at a constant H/Cl ratio of 6.

The etching effect of HCl was examined at a constant H/Cl molar ratio of 6 and these results were compared to previous calculations. Figure 2.15 shows that as the initial HCl partial pressure was increased the solid phase boundaries are shifted with the region of no solid deposition expanding to higher gamma values. This is again due to the shift in the equilibrium of reactions 2.1 to 2.6 and the etching of the solid phases. Preferential etching of the solid phase mixture of BP+$B_{13}P_2$ is shown by the shift of the BP/BP+$B_{13}P_2$ boundary to higher temperature as the initial HCl partial pressure is increased. There is very little affect on the BP/$B_{13}P_2$ and the $B_{13}P_2$/BP+$B_{13}P_2$ interfaces. In general the introduction of HCl preferentially etches all three regions of the solid phase mixture deposition, BP+$B_{13}P_2$, B+BP, and B+$B_{13}P_2$. The largest phase boundary shift is seen at low temperature and high gamma values where boron in the B+BP regime is preferentially etched. The significance of this result is that the range of pure BP deposition is greatly extended to all gamma values above 0.10 and temperature lower than 1200 K. In contrast, the domain of pure $B_{13}P_2$ deposition has virtually no net change as the initial HCl partial pressure is increased. Thus the $B_{13}P_2$ region must be etched at a rate nearly equal to those of the solid phase mixture regions and at a rate much greater than that of pure BP. Such a trend coincides with experimental research that indicates a large increase in the HCl etching rate of $B_{13}P_2$ (B_6P) compared to that of BP [479] though such a trend may also be the result of kinetics. Such information can be very useful in the commercial chemical vapor deposition of BP for device applications described earlier.

Kelder produced three interesting and informative graphs in his thesis showing the amount of the initial boron and phosphorus in the gas phase that formed the deposited solids (%B and %P). In addition, the gas phase phosphorus partial pressure per phosphorus atom (P_P) was evaluated at a fixed initial BCl_3 partial pressure. The graphs of Figure 2.16 are calculated at an initial BCl_3 partial pressure of $1\text{x}10^{-4}$ atm. The abrupt changes in the curves on each graph are due to the transition between different regions. The boron fractions of the solid deposited, denoted f, are: BP-50%, $B_{13}P_2$-86.7%, B-100%, BP+$B_{13}P_2$-linear from 50 to 86.7%, B+BP-linear from 50 to 100%, and B+$B_{13}P_2$-linear from 86.7 to 100%. In the solid mixture regions, the phosphorus partial pressure is independent of the initial PCl_3 partial pressure (i.e. independent of γ). As noted by Kelder, "from the total pressure of the gaseous phosphorus (P_P) the real equilibrium partial pressures for the phosphorus containing species from section 'a' are obtained. Since the fractions of BBr_3 (BCl_3) and PBr_3 (PCl_3) conversion are known, it is also possible to evaluate the gaseous boron and the HBr (HCl) partial pressures. With the results of section ‘c’ the equilibrium partial pressures of the boron containing species are obtained.” Figure 2.16 shows that as the temperature is increased, the percent of both boron and phosphorus that is initially present that incorporates into the deposited solid(s) decreases. Furthermore, the fraction of boron in the solid increases for lower γ values and the equilibrium partial pressures of the phosphorus containing species shift to higher equilibrium partial pressures over the range of gamma values.

Finally a limited computational examination of the heterogeneous BCl_3-PCl_3-H_2 system has been reported by Milovanova and Krenev [472]. They reported variations in the yields of BP and B_6P over a 800 to 1800 temperature range in 100 K increments and at 5 BCl_3:PCl_3 molar ratios. They calculated the decomposition of BP into B_6P occurring between 1300 and 1400 K for a region of high initial PCl_3 partial pressure (i.e. small γ value) where the current calculations show no solid deposition occurring. Although they considered solid boron in their calculations, the highest γ value used was 0.50. Thus the B+BP and B+$B_{13}P_2$ regions were never examined and the BP+$B_{13}P_2$ region was only calculated at one point (T=1300 K and β=0.50). As in their analysis of the PCl_3-H_2 homogeneous and BCl_3-H_2 heterogeneous systems, important species were not considered in the species list (BH_2Cl) and currently outdated thermodynamic data were used.

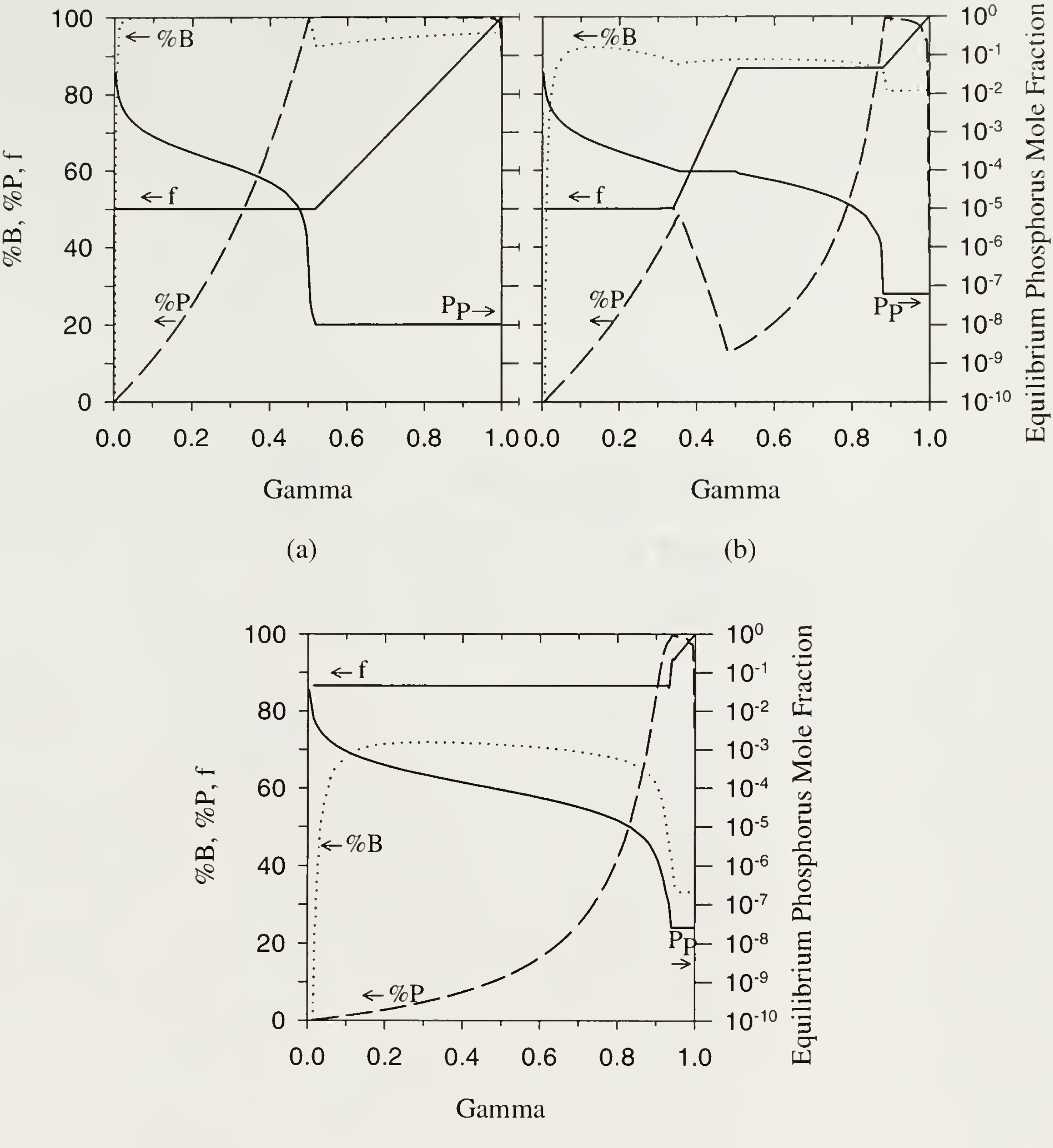

(a)

(b)

(c)

Figure 2.16: Percentages of the total initial moles of boron (%B) and phosphorus (%P) which react to form boron phosphide solid phases for three different temperatures as a function of the BCl_3 fraction gamma as defined by equation 2.7. The percentage of boron in the solid phase is labeled f. The total equilibrium partial pressure of the phosphorus reactant (P_P) in the vapor phase. This is the summation of all the phosphorus containing species calculated per phosphorus atom in each species.
a) T=1000 K; b) T=1400 K; c) T=1800 K.

2.1.3 Conclusions

The importance of an updated, self-consistent thermochemical database is exemplified in the calculations of the BCl_3-PCl_3-H_2 system and subsystems. Homogeneous equilibrium partial pressures in the PCl_3-H_2 system agreed well with those previously calculated by Milovanova and Krenev with the exception of PH_2 and PH_3.

The current calculations show large partial pressures for both species while neither is shown in the previous work. The main species in this system are P_2, P_4, PH_3, and HCl. Finally the PCl_3 reactant is nearly completely reacted at all temperatures and initial PCl_3 partial pressures. Examination of the equilibrium in the BCl_3-H_2 system reveals that the main gas phase species are $BHCl_2$, BH_2Cl, BCl_3, BH_3, and HCl. A strong dependence on temperature and the initial BCl_3 partial pressure is exhibited by both the homogeneous and heterogeneous systems. When excess HCl is added, the formation of $BHCl_2$ and BH_2Cl in the homogeneous system and $BHCl_2$, BH_2Cl, and solid boron in the heterogeneous system are strongly suppressed. A maximum yield of solid boron (95.8%) is found at high temperatures and low initial BCl_3:H_2 molar ratios.

Equilibrium in the BCl_3-PCl_3-H_2 homogeneous system was determined to be independent of the initial PCl_3 partial pressure but dependent on the initial BCl_3 partial pressure. Thus it becomes a summation of the PCl_3-H_2 and the BCl_3-H_2-excess HCl homogeneous systems. Finally the heterogeneous BCl_3-PCl_3-H_2 system was examined. Solid phase diagrams were generated for fixed initial BCl_3 partial pressures, fixed initial H/Cl molar ratios, for gradual replacement of H_2 with an inert, and for the addition of HCl to study its etching effect. Six different solid regimes were identified depending on the temperature and initial precursor ratios. These are pure BP, pure $B_{13}P_2$, a region where no solids are deposited, and solid mixtures of $BP+B_{13}P_2$, B+BP, and $B+B_{13}P_2$. As the initial BCl_3 partial pressure is increased or the initial H/Cl ratio is decreased the regime boundaries are shifted to higher temperature and larger boron mole fraction (smaller γ values). Introduction of an inert gas greatly decreased the regions of solid formation while HCl was found to preferentially etch the solid phase mixture regions. It is believed that the solid phase diagrams presented are the first published for the BCl_3-PCl_3-H_2 heterogeneous system, and that they utilize the most updated thermodynamic database and most inclusive species list presently available.

2.2 Boron Nitride

2.2.1 Introduction

Boron nitride possesses several polymorphic modifications including the dense phases of cubic and wurtzitic boron nitride (cBN and wBN) and the softer phases of hexagonal and rhombohedral boron nitride (hBN and rBN). These dense and softer boron nitride phases are akin to the diamond and graphite forms of carbon, respectively. Due to its diamond-like properties cubic boron nitride (c-BN) is one of the most sought after materials. Diamond has been successfully deposited at both high pressures and high temperatures (HPHT) and by CVD at low pressures and low temperatures (LPLT). Cubic boron nitride has also been successfully deposited at HPHT conditions. LPLT CVD deposition of boron nitride has been attempted by numerous researchers with limited success. Currently only a mixture of hexagonal and cubic boron nitride has been deposited using energized particle CVD techniques, while deposition of c-BN by strictly thermal CVD has never been verified by transmission electron microscopy (TEM), electron energy loss spectroscopy (EELS), or X-ray photovoltaic spectroscopy (XPS). It is hoped that with a greater understanding of the thermodynamic limitations and driving forces present in the deposition of c-BN using a specific chemistry at thermal CVD conditions, that low pressure-low temperature CVD of cBN is achievable.

Bohr et al. have discussed in detail why the experimental deposition of diamond is possible, while that of cubic boron nitride is not, due to the Ostwald and Ostwald-Volmer nucleation rules [480,481]. They also calculated c-BN/h-BN transformation temperatures ranging from 850 to 1600 °C, depending on the thermodynamic properties used. They suggest that an excess of BCl_3 should preferentially promote the formation of the cubic phase over its hexagonal counterpart. This was accomplished in this work by using BCl_3 as an input reactant.

Solozhenko has done extensive work in examining the thermodynamic stability of cubic and hexagonal boron nitride at various temperatures and pressures for the B-N system using a Gibbs energy transformation method [107]. In several papers he has generated P-T phase diagrams for boron nitride and compared these to the generally accepted Bundy-Wentorf phase diagram [81]. Solozhenko attributed the large differences between his results and those of Bundy and Wentorf to the fact that the Bundy-Wentorf "phase diagram" is actually based on experimental "equilibrium" transformations in the presence of different "catalysts". Unfortunately these catalysts did not simply speed the system's approach to equilibrium, but also chemically interacted with boron nitride to possibly form a solution. This resulted in a chemically modified "equilibrium" state and thus the system never reached the true thermodynamic equilibrium condition for pure BN. His calculations of the ΔG^{o}_{tr} polymorphic transformation energy values for the cBN to hBN transformation range from 15 kJ/mol at 100 K to 0 kJ/mol at 1570 K at normal pressure and does not intersect the pressure axis, but meets the temperature one at 1570 K. Thus, cBN appears to be thermodynamically stabile up to 1570 K in the B-N system.

Van Vechten also calculated a P-T diagram using electronegativity differences, with results significantly different than those proposed by Solozhenko [482,483]. For instance, at 0 GPa pressure Van Vechten calculated a phase transition temperature of 4758 K while Solozhenko calculated 1578 K. Differences in the phase diagrams most likely result from Van Vechten's use of then current thermochemical data for c-BN and h-BN, which has been subsequently updated numerous times, as well as the equilibrium modeling method employed. Van Vechten even cautions in his paper "that there are substantial uncertainties in the experimental (thermochemical) data" used in his work. The inaccuracy of Van Vechten's analysis is evidenced by his analyses of the B-P system. His results vary significantly from those of Kelder, Milovanova and Krenev, as well as those presented in section 2.1 of this work. He reported a BP melting temperature at 1 atm of approximately 2200 °C, with reported BP decomposition to $B_{13}P_2$ at any temperature.

Despite the enormous possibilities resulting from the recent calculations that indicate cubic boron nitride is the stable phase at low temperature and pressure, the author knows of only 2 BN phase diagrams that have been calculated for specific chemistries. Bohr et al. examined the B-N-H and B-N-X (X=F or Cl) as a function of temperature for a single pressure and initial reactant ratio [481]. In low pressure diamond synthesis graphite (sp^2 hybridized carbon) is preferentially etched in relation to diamond (sp^3 hybridized carbon) in the presence of atomic hydrogen at elevated temperature and the diamond surface is stabilized [484,485]. Bohr et al., however, showed in their equilibrium calculations that unlike diamond CVD, atomic hydrogen preferentially etches c-BN at higher temperatures. A similar effect was seen in separate calculations, when the influence of molecular fluorine and chlorine was examined while molecular hydrogen did not react quantitatively. On the other hand, when the system of boron nitride and molecular chlorine (without BCl_3 formation) was examined it was noted that c-BN is much more stable than h-BN up to 675 K. This can be accomplished experimentally by supplying an excess amount of BCl_3 to the CVD reactor. The current calculations do this by examining the thermodynamic equilibrium of the B-N-Cl-H system using BCl_3, NH3, and H_2 as precursors in realistic CVD molar ratios over a 1200 K temperature range.

This section presents the results of complex chemical equilibrium calculations in both the homogeneous and heterogeneous equilibrium compositions of the BCl_3-NH_3-H_2 system and subsystems as a function of both the initial BCl_3 and NH_3 partial pressures as well as temperature at a total pressure of one atm. When the H_2 equilibrium partial pressure is not shown, it can assumed to be ≈ 1 atm. All species partial pressures are given in atmospheres. In preliminary calculations, several ion species and the electron gas were considered but their influence on the overall equilibrium was negligible; hence they were not included in subsequent calculations. The thermodynamics of three separate systems have been examined in this work:

NH_3 - H_2	-	homogeneous equilibrium
BCl_3 - NH_3 - H_2	-	homogeneous equilibrium
BCl_3 - NH_3 - H_2	-	heterogeneous equilibrium

Thermodynamic equilibrium in the BCl_3-H_2 homogeneous and heterogeneous systems as well as the BCl_3-H_2-excess HCl homogeneous system were examined in section 2.1.2. Each molecule considered in this work can be grouped into one of six classes - molecules containing hydrogen (BH_x and NH_x), containing boron, hydrogen, and chlorine (BH_xCl_y), containing chlorine (BCl_x and HCl_x), containing only boron and nitrogen (c-BN, h-BN, and BN(g)), containing boron, nitrogen, and hydrogen ($B_xN_yH_z$), and pure species (H_x, Cl_x, N_x, and B_x).

Values of the standard enthalpy of formation, standard entropy of formation, and heat capacity for each species are summarized in Table 2.2. All heat capacity expressions taken from the work of Allendorf and Melius [458] were entered directly into the Meyers FORTRAN equilibrium program. For reasons discussed in section 1.3.1, predicted thermochemical properties for several BH_mCl_n species using the G-2 level of theory and BAC-MP4 theory have been used in these calculations. Equilibrium in the N-H and B-N-H-Cl homogeneous systems was calculated using the Meyers FORTRAN program; the heterogeneous system was determined using ThermoCalc.

2.2.2 Results and Discussion

In this section the thermodynamics of the 3 different systems will be discussed in order.

NH_3 - H_2 - homogeneous system

Thermodynamic equilibrium in the N-H system using NH_3 and H_2 as precursors was examined over the 800 to 1800 K temperature range and initial NH_3 partial pressures ranging from 1×10^{-5} to 0.10 atm. The main gas phase species were found to be H_2, H, N_2,

Table 2.2 Selected Thermochemical Data of the B-N-H-Cl System

Species	$\Delta H^o_{f,298}$ (kcal/mol)	$\Delta S^o_{f,298}$ (kcal/K•mol)	A *	B *	C *	D *	E *	Ref.
$H_3B:NH_3$ (v)	-19.9	-5.96999E-02	1.94870E+00	2.00933E-02	-5.06347E-06	-3.34936E-09	1.74629E-12	458
			2.20712E+00	2.15259E-02	-1.06964E-05	2.58490E-09	-2.46123E-13	
H_2BNH_2 (v)	-23.02	-3.19868E-02	4.19363E-01	2.31209E-02	-1.84913E-05	8.47169E-09	-1.69981E-12	458
			3.04384E+00	1.41031E-02	-6.78182E-06	1.60854E-09	-1.52698E-13	
H_2BNH (v)	44.6	-1.11603E-02	2.48122E+00	1.54748E-02	-1.41289E-05	7.99117E-09	-2.03194E-12	458
			3.94647E+00	9.51661E-03	-4.71399E-06	1.13490E-09	-1.07642E-13	
$HBNH_2$ (v)	31.2	-1.46003E-02	1.29696E+00	1.88733E-02	-1.81027E-04	1.01816E-08	-2.40434E-12	458
			3.49424E+00	9.86320E-03	-4.34465E-05	9.06537E-10	-7.45745E-14	
HBNH (v)	11.0	-2.95303E-02	2.31933E+00	1.53231E-02	-2.10111E-05	1.60446E-08	-4.82767E-11	458
			4.21456E+00	5.56145E-03	-2.38773E-06	5.01863E-10	-4.19158E-14	
BNH_2 (v)	48.8	-2.35382E-03	3.02648E+00	1.05516E-02	-1.07574E-05	6.53597E-09	-1.62551E-12	458
			4.18469E+00	5.31324E-03	-2.16397E-06	4.31377E-10	-3.41950E-14	
BNH (v)	70.0	1.02227E-02	2.92552E+00	8.96653E-03	-1.22844E-05	9.32881E-09	-2.78730E-12	458
			4.15297E+00	2.94187E-03	-1.14619E-06	2.16617E-10	-1.60799E-14	
HBN (v)	94.3	9.99270E-03	2.16787E+00	1.02992E-02	-1.17182E-05	7.85090E-09	-2.24671E-12	458
			3.46763E+00	4.85777E-02	-2.55066E-06	6.41151E-10	-6.27952E-14	
BN (v)	140.3	2.27292E-02	3.77761E+00	-2.72795E-03	8.25962E-06	-7.49158E-09	2.30742E-12	458
			2.90238E+00	2.16314E-03	-1.23852E-06	3.32371E-10	-3.42364E-14	
$B_3N_3H_6$ (v)	-122.0	-9.69615E-02	-5.99443E+00	8.24596E-02	-8.89599E-05	5.12924E-08	-1.23332E-11	458
			8.10915E+00	3.09558E-02	-1.63419E-05	4.15356E-09	-4.12099E-12	
$Cl_3B:NH_3$ (v)	-133.0	-7.14961E-02	3.30041E+00	4.39218E-02	-6.13163E-05	4.45618E-08	-1.27607E-11	458
			1.06724E+01	1.10790E-02	-5.08886E-06	1.14731E-09	-1.02844E-13	
$H_3N:BCl_2NH_2$ (v)	-119.1	-9.49884E-02	4.33198E+00	4.35041E-02	-5.35880E-05	3.69482E-08	-1.02794E-11	458
			1.04306E+01	1.61856E-02	-7.09917E-06	1.53182E-09	-1.31861E-13	
$HClBNH_2$ (v)	-63.0	-3.33789E-02	4.41868E-01	3.20255E-02	-3.82602E-05	2.49914E-08	-6.67050E-12	458
			5.48141E+00	1.13579E-02	-5.49621E-06	1.30801E-09	-1.23071E-13	
Cl_2BNH_2 (v)	-99.3	-3.82410E-02	1.61114E+00	3.61738E-02	-4.99194E-05	3.53977E-08	-9.89790E-12	458
			8.34120E+00	7.66660E-03	-3.25174E-05	6.63814E-10	-5.45275E-14	

Table 2.2 Continued

Species	$\Delta H^o_{f,298}$ (kcal/mol)	$\Delta S^o_{f,298}$ (kcal/K•mol)	A *	B *	C *	D *	E *	Ref.
$ClB(NH_2)_2$ (v)	-91.3	-6.36033E-02	1.91051E+00	4.18471E-02	-5.19640E-05	3.56463E-08	-1.00562E-11	458
			8.05877E+00	1.56547E-02	-8.16481E-06	2.03184E-09	-1.96949E-13	
$HB(NH_2)_2$ (v)	-52.4	-6.17512E-02	7.07459E-01	3.75463E-02	-4.04007E-05	2.51771E-08	-6.53732E-12	458
			5.33132E+00	1.76858E-02	-8.17173E-06	1.80506E-09	-1.57684E-13	
$B(NH_2)_3$ (v)	-74.6	-8.64055E-02	3.65310E+00	4.14823E-02	-4.69434E-05	3.09138E-08	-8.38906E-12	458
			8.41271E+00	1.94698E-02	-8.98165E-06	1.98918E-09	-1.73390E-13	
Cl_2BNH (v)	-25.7	-2.01445E-02	3.10375E+00	2.59309E-02	-3.87299E-05	2.84898E-08	-8.14158E-12	458
			8.18555E+00	3.89885E-03	-1.80739E-06	4.13605E-10	-3.77217E-14	
$ClBNH_2$ (v)	-8.1	-1.70124E-02	1.81712E+00	2.41644E-02	-3.04085E-05	2.04280E-08	-5.47127E-12	458
			5.90027E+00	6.97058E-03	-2.83845E-06	5.36899E-10	-3.95450E-14	
ClBNH (v)	-18.9	-8.23588E-03	2.59186E+00	2.27364E-02	-3.63935E-05	2.87647E-08	-8.70216E-12	458
			6.59952E+00	3.61316E-03	-1.49179E-06	3.00310E-10	-2.38909E-13	
ClBN (v)	59.7	7.44063E-03	3.40537E+00	1.09084E-02	-1.47066E-04	1.04538E-08	-3.03560E-12	458
			5.41064E+00	2.86702E-03	-1.64946E-06	4.42742E-10	-4.55050E-14	

Species	$\Delta H^o_{f,298}$ (kcal/mol)	$\Delta S^o_{f,298}$ (kcal/K•mol)	A	B	C	D	C_P^o † Model	Ref.
N_2 (v)	0	0	5.73865E-03	2.62070E-06	-6.02447E-10	4.49099E+01	3	454
N (v)	11.30	1.37418E-02	4.96797E-03	0	0	0	1	454
NH (v)	85.67	4.79924E-03	7.12744E-03	-1.06417E-06	1.92188E-09	-5.25062E-13	2	454
NH_2 (v)	45.41	-7.52689E-03	5.79233E-03	5.56869E-06	-1.01799E-09	6.59094E+01	3	454
NH_3 (v)	-10.98	-2.36747E-02	5.65946E-03	9.73705E-06	-1.99124E-09	1.00134E+01	3	454
N_2H_2 (v)	50.64	-2.48470E-02	4.03721E-03	1.39516E-05	-2.97976E-09	3.64393E+01	3	454

Table 2.2 Continued

Species	$\Delta H^{o}_{f,298}$ (kcal/mol)	$\Delta S^{o}_{f,298}$ (kcal/K•mol)	A	B	C	D	C_P^{o} † Model	Ref.
N_2H_4 (v)	22.75	-5.12672E-02	-5.96040E-02	-3.13222E-06	2.02908E+02	1.22554E-02	1	454
BN (s,hexagonal)	-59.89	-2.077E-02	2.390E-04	9.541E-06	-4.235E-09	1.951E+02	3	481
BN (s, cubic)	-63.77	-2.273E-02	8.499E-03	3.090E-06	-5.750E+02	0	1	481

† (1) $C_P^{o}(T) = A + BT + CT^{-2} + D\ln(T)$; (2) $C_P^{o}(T) = A + BT + CT^{2} + DT^{3}$; (3) $C_P^{o}(T) = A + BT + CT^{2} + DT^{-2}$; in kcal/mol

* $C_P^{o}(T) = A + BT + CT^{2} + DT^{3} + ET^{4}$; in kcal/mol; First row for $300 \leq T \leq 1000$ K; second row for $1000 < T \leq 3000$ K

Note: Values for all other B,N,H, and/or Cl containing species (i.e. H_2, $BHCl_2$, Cl_2, etc.) were identical to those shown in Table 2.1

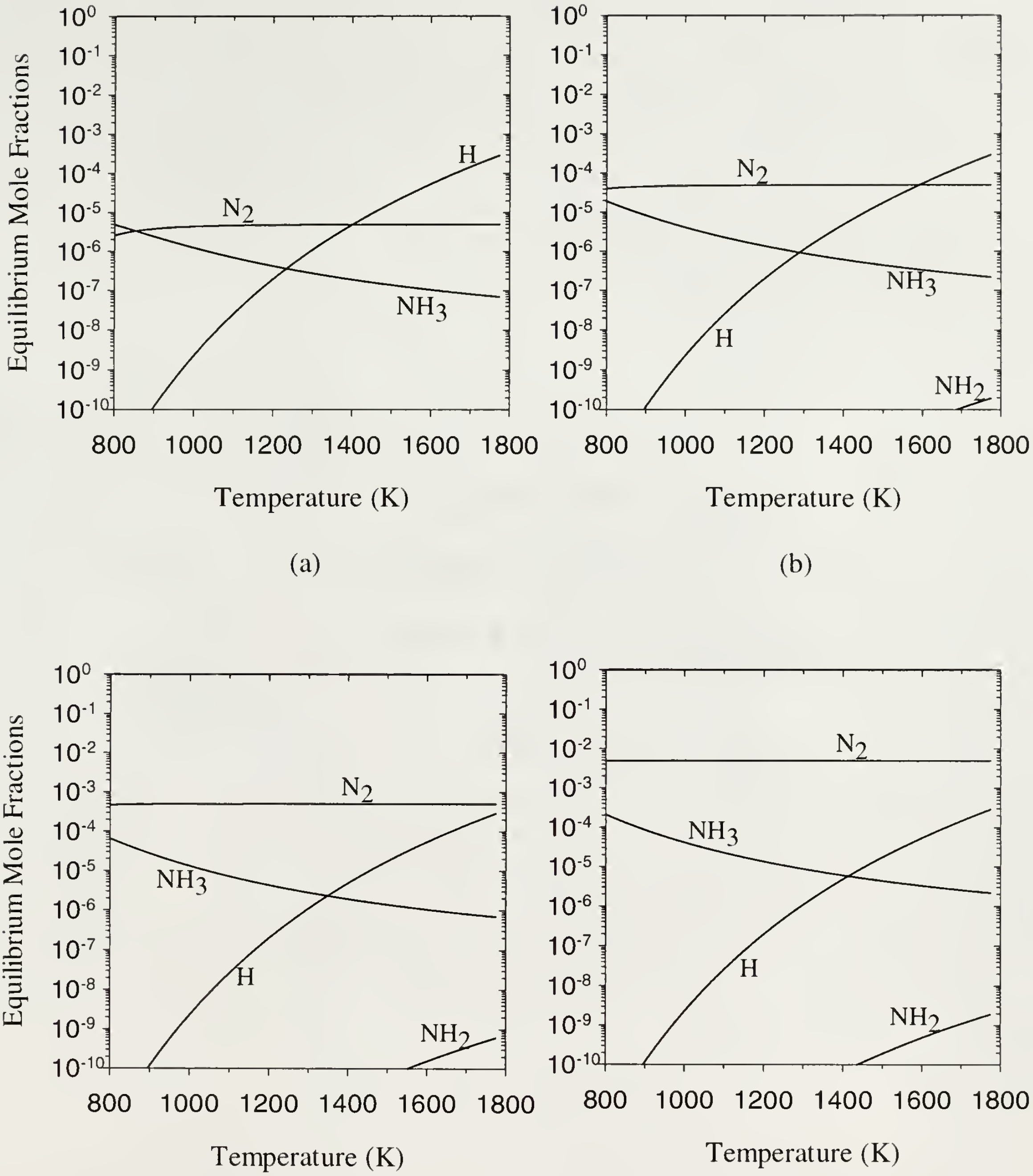

(a)

(b)

(c)

(d)

Figure 2.17: Equilibrium partial pressure (atm) in the homogeneous system NH_3-H_2 as a function of temperature at constant NH_3 initial partial pressures a) $p^o(NH_3)=10^{-4}$; b) $p^o(NH_3)=10^{-3}$; c) $p^o(NH_3)=10^{-2}$; d) $p^o(NH_3)=10^{-1}$.

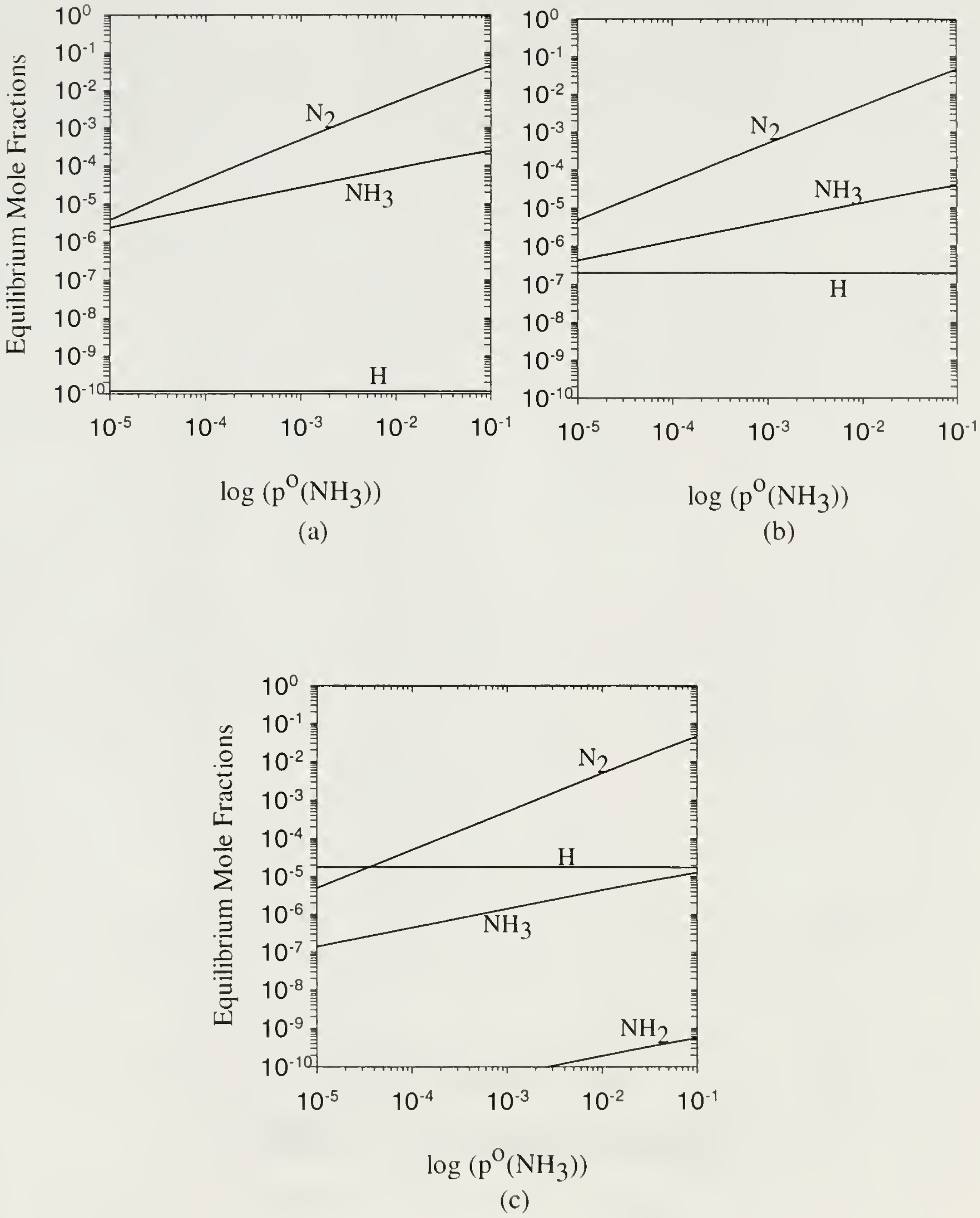

(a)

(b)

(c)

Figure 2.18: Equilibrium partial pressure (atm) in the homogeneous system NH_3-H_2 as a function of NH_3 initial partial pressure at constant temperature
a) T=900 K; b) T=1200 K; c) T=1500 K.

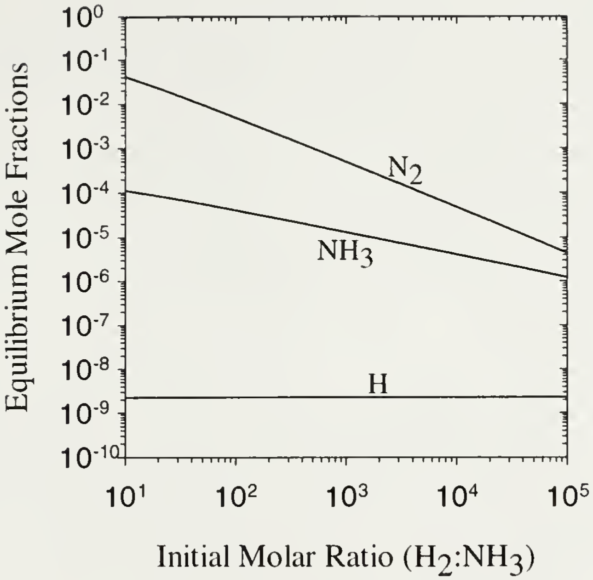

Figure 2.19: Equilibrium partial pressure (atm) in the homogeneous system NH_3-H_2 as a function of the initial H_2:NH_3 molar ratio at constant temperature (T=1000 K).

and NH_3 for all calculated equilibrium states. From Figure 2.17 it is evident that as the initial NH_3 partial pressure increases the equilibrium partial pressures of each major nitrogen containing species increase for a given temperature. The elemental hydrogen partial pressure is found to be nearly independent of the initial NH_3 partial pressure. This is a direct result of the constant large excess of molecular hydrogen. Thus the small additional amount of hydrogen contained in the NH_3 precursor is inconsequential. The elemental hydrogen partial pressure also increases with temperature as expected from previously calculated equilibrium of the H_2 system. The N_2 partial pressure was found to be independent of temperature at each initial NH_3 partial pressure due to its high chemical stability over the entire temperature range considered.

Figure 2.18 shows equilibrium partial pressures as a function of the input NH_3 partial pressure. It is interesting to note that each of the nitrogen containing species equilibrium partial pressures are nearly linear with respect to the log of the initial NH_3 partial pressure. As before the elemental hydrogen partial pressure is only dependent on the equilibrium temperature. Also, at higher temperature, the NH_3 equilibrium partial pressure for a given initial NH_3 partial pressure decreases due to its lower chemical stability at higher temperatures.

Analysis of the initial H_2:NH_3 molar ratio shows that there are only three species whose equilibrium partial pressures exceed 10^{-10} atm over the 10 to 100,000 molar ratio examined. The monatomic hydrogen partial pressure was independent of the molar ratio due to the large initial H_2 partial pressure, even for the lowest molar ratio considered. The major nitrogen containing species, N_2 and NH_3, decreased as the molar ratio increased since less nitrogen was introduced into the system initially.

Therefore, the main equilibria in the NH_3-H_2 homogeneous system are:

$$2NH_3 \Leftrightarrow N_2 + 3H_2 \qquad \text{Equation 2.8}$$

$$H_2 \Leftrightarrow 2H \qquad \text{Equation 2.9}$$

BCl_3 - NH_3 - H_2 - homogeneous system

The BCl_3 - NH_3 - H_2 homogeneous system was constrained to prohibit the formation of solid boron at equilibrium. Analysis of the B-N-H-Cl homogeneous system indicated that the final equilibrium partial pressures of the main boron containing species are dependent on the initial NH_3 partial pressure. Similarly, the main nitrogen containing species were found to be dependent on the initial BCl_3 partial pressures. This is in contrast to the B-P-H-Cl system, where the main phosphorus containing species were

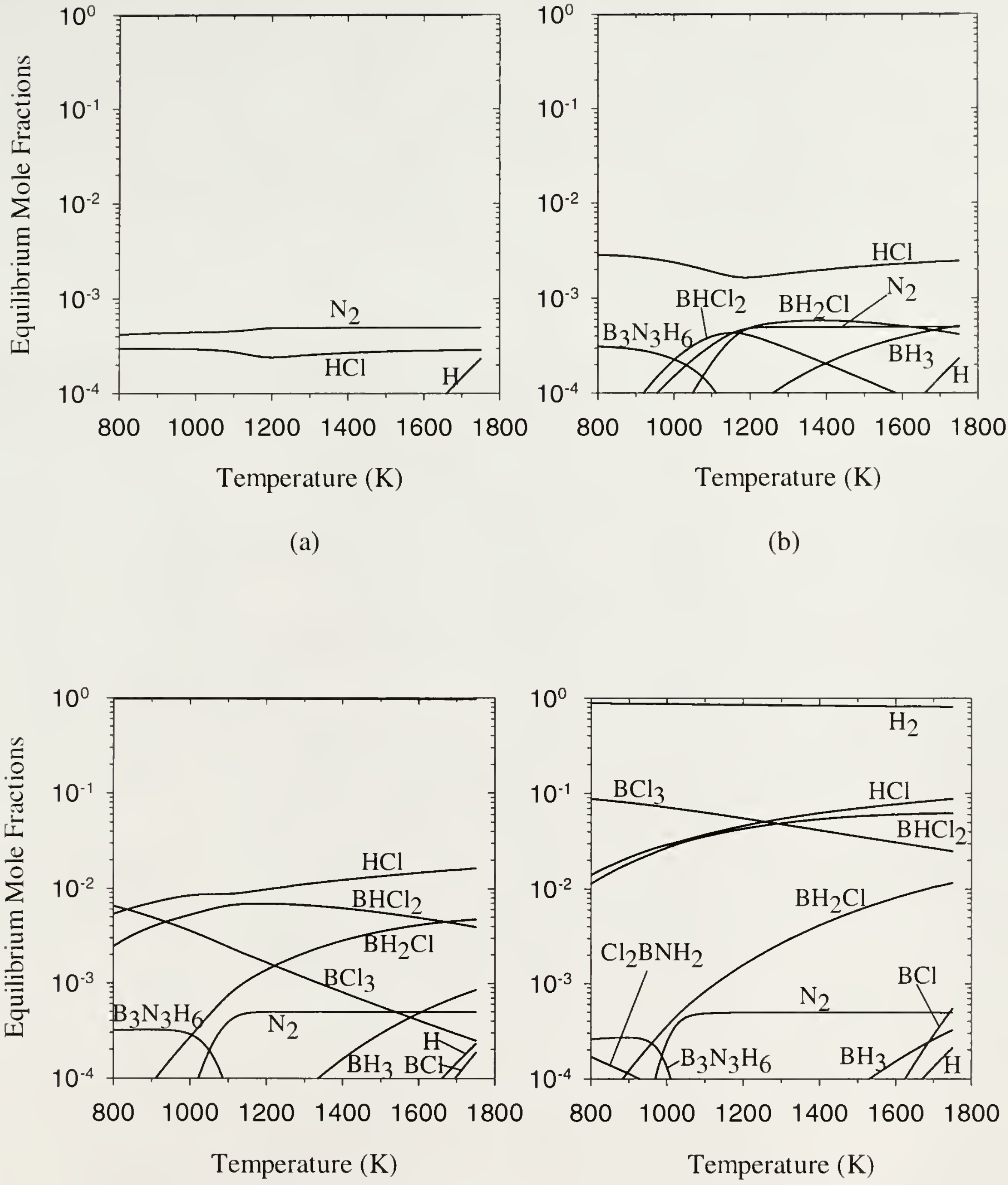

(a)

(b)

(c)

(d)

Figure 2.20: Equilibrium partial pressure (atm) in the homogeneous system BCl_3-NH_3-H_2 as a function of temperature at constant NH_3 initial partial pressures ($p^o(NH_3)=10^{-3}$)
a) $p^o(BCl_3)=10^{-4}$; b) $p^o(BCl_3)=10^{-3}$; c) $p^o(BCl_3)=10^{-2}$; d) $p^o(BCl_3)=10^{-1}$.

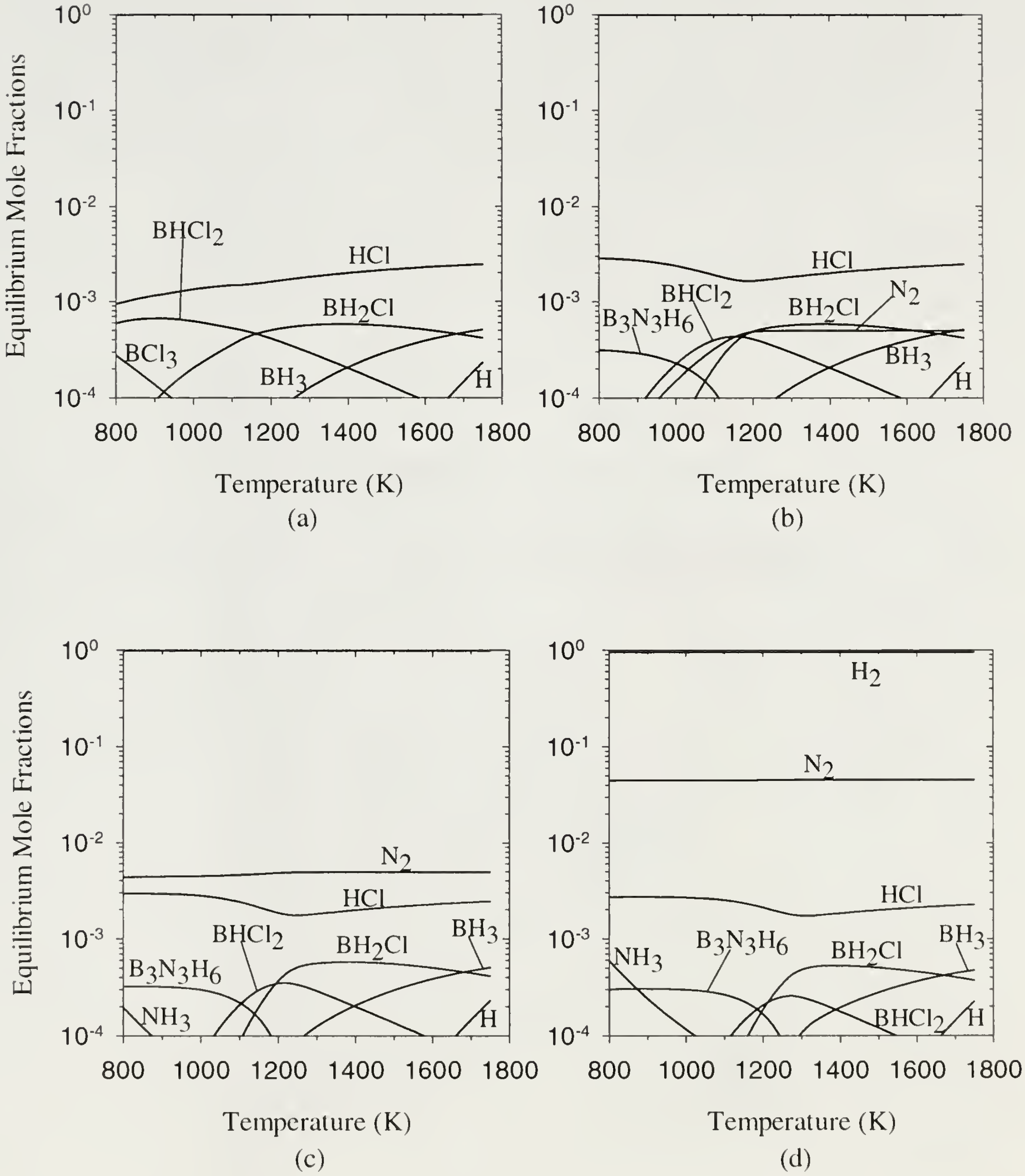

Figure 2.21: Equilibrium partial pressure (atm) in the homogeneous system BCl_3-NH_3-H_2 as a function of temperature at constant NH_3 initial partial pressures ($p^o(BCl_3)=10^{-3}$)
a) $p^o(NH_3)=10^{-4}$; b) $p^o(NH_3)=10^{-3}$; c) $p^o(NH_3)=10^{-2}$; d) $p^o(NH_3)=10^{-1}$.

independent of the initial BCl_3 partial pressure while the main boron containing species were dependent on the initial PCl_3 partial pressure.

The main boron containing species at low temperatures were found to be $B_3N_3H_6$, BCl_3, and $BHCl_2$ while at high temperatures they were $BHCl_2$, BH_2Cl, and BH_3. The major nitrogen containing species at low temperatures include $B_3N_3H_6$, N_2, NH_3 and at high temperatures, N_2. HCl was present at significant equilibrium partial pressures over the entire range of temperatures and initial partial pressures considered. Figures 2.20 and 2.21 show the equilibrium partial pressures of all major species as a function of temperature at constant initial NH_3 and BCl_3 partial pressures, respectively. Various similarities arise when comparing the individual graphs of each figure to its respective counterpart. For instance, the equilibrium H and HCl partial pressures are nearly identical for the same lower initial BCl_3 and NH_3 partial pressures. Also, the $B_3N_3H_6$ equilibrium partial pressure decreases rapidly near 1200 K for both constant initial NH_3 and BCl_3 partial pressures.

Therefore, in addition to the reactions shown in 2.8 and 2.9 the main equilibria in the BCl_3-NH_3-H_2 system are:

$$3BCl_3 + 3NH_3 + 3H_2 \Leftrightarrow B_3N_3H_6 + 9HCl \qquad \text{Equation 2.10}$$

$$BCl_3 + H_2 \Leftrightarrow BHCl_2 + HCl \qquad \text{Equation 2.11}$$

$$BCl_3 + 2H_2 \Leftrightarrow BH_2Cl + 2HCl \qquad \text{Equation 2.12}$$

$$BCl_3 + 3H_2 \Leftrightarrow BH_3 + 3HCl \qquad \text{Equation 2.13}$$

BCl_3 - NH_3 - H_2 - heterogeneous system

By far the most interesting results were found in the heterogeneous equilibrium examination of the B-N-H-Cl system using BCl_3, NH_3, and H_2 as precursors. Six different solid phase regimes were identified that were highly dependent on the input precursor ratio and the deposition temperature. Four regions exist as pure phases: c-BN, h-BN, B, and an area where no solid phase deposition occurs. Two solid phase mixtures regimes that are also present are c-BN+B and h-BN+B. For graphical clarity the initial BCl_3:NH_3 precursor ratio was normalized as:

$$Beta = \frac{p^o(BCl_3)}{p^o(BCl_3)+p^o(NH_3)} \qquad \text{Equation 2.14}$$

It was found for all solid phase diagrams that the transition temperature from c-BN to h-BN (or their respective solid phase mixtures with boron) was 1576 K (i.e., G_{cBN}-G_{hBN} = 0 at T=1576K). Cubic boron nitride was found to be the stable phase at a temperature below 1576 K and as a pure phase at lower BCl_3:NH_3 (β) molar ratios. CVD phase diagrams were generated over a 1200 K temperature range and a variety of initial reactant conditions. These include variable initial BCl_3 partial pressures, variable initial H_2 partial pressures, replacement of the H_2 precursor with an inert gas, and addition of HCl to act as an etchant.

The influence of increasing the input BCl_3 partial pressure on the solid deposition is shown in Figure 2.22. In these graphs the input BCl_3 partial pressure was held constant and the input NH_3 partial pressure was varied to correspond to a given β value. As a result the B/N molar ratio varies with β. Thus at low β values the input NH_3 partial pressure is high while at high β values the NH_3 partial pressure is low. As the initial

BCl_3 partial pressure is increased, the region of pure cubic BN deposition increases at low temperature. This is consistent with the idea proposed by Bohr et *al.* that the hindrance of BCl_3 product formation will enhance the thermodynamic stability of the cubic BN phase over its hexagonal counterpart. The opposite occurs for h-BN, where its pure phase deposition region decreases with increasing BCl_3 partial pressure. Also, the region of pure B deposition greatly decreases with an increase in the BCl_3 partial pressure.

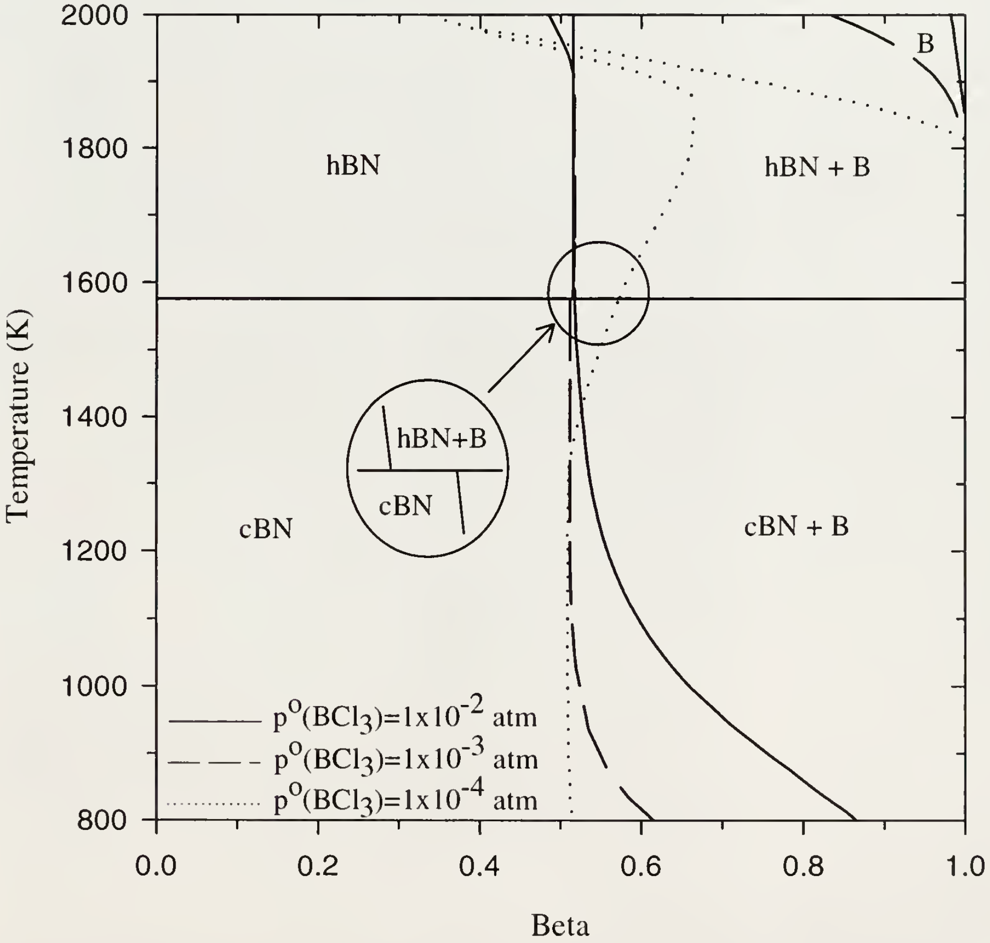

Figure 2.22: Solid CVD phase diagram for the heterogeneous system BCl_3-NH_3-H_2 as a function of temperature and BCl_3 fraction beta as defined by equation 2.14.

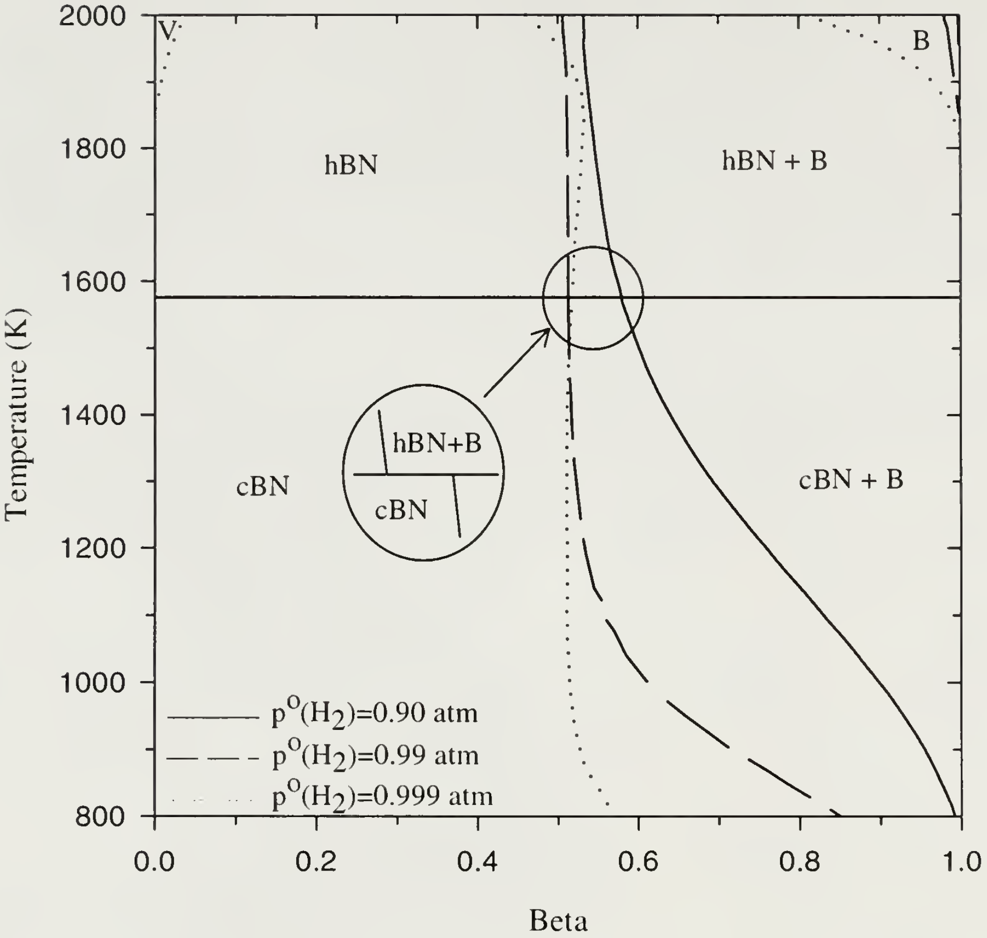

Figure 2.23: Solid CVD phase diagram for the heterogeneous system BCl_3-NH_3-H_2 as a function of temperature and BCl_3 fraction beta as defined by equation 2.14.

Equilibrium was also calculated at constant initial H_2 partial pressures. Results are graphically shown in Figure 2.23. As the initial H_2 partial pressure was varied from 0.90 to 0.999 atm., the domain of cubic boron nitride stability was shifted to lower β values (lower initial BCl_3 partial pressures). This is consistent with the previous results where a constant initial BCl_3 partial pressure was used (Figure 2.22). A slight shift in the hBN - hBN+B boundary was observed as the H_2 partial pressure was increased, though no definitive trend can be noted. Furthermore, when the H_2 partial pressure is increased, a region where no solids were deposited is evident at very low β values and high temperature. Finally, the region of pure solid boron deposition increases with increasing H_2 partial pressure. This could be a result of the increased initial H_2 partial pressure preventing the significant decomposition of the NH_3 precursor. This would in turn lead to a diminished amount of N available for the formation of BN.

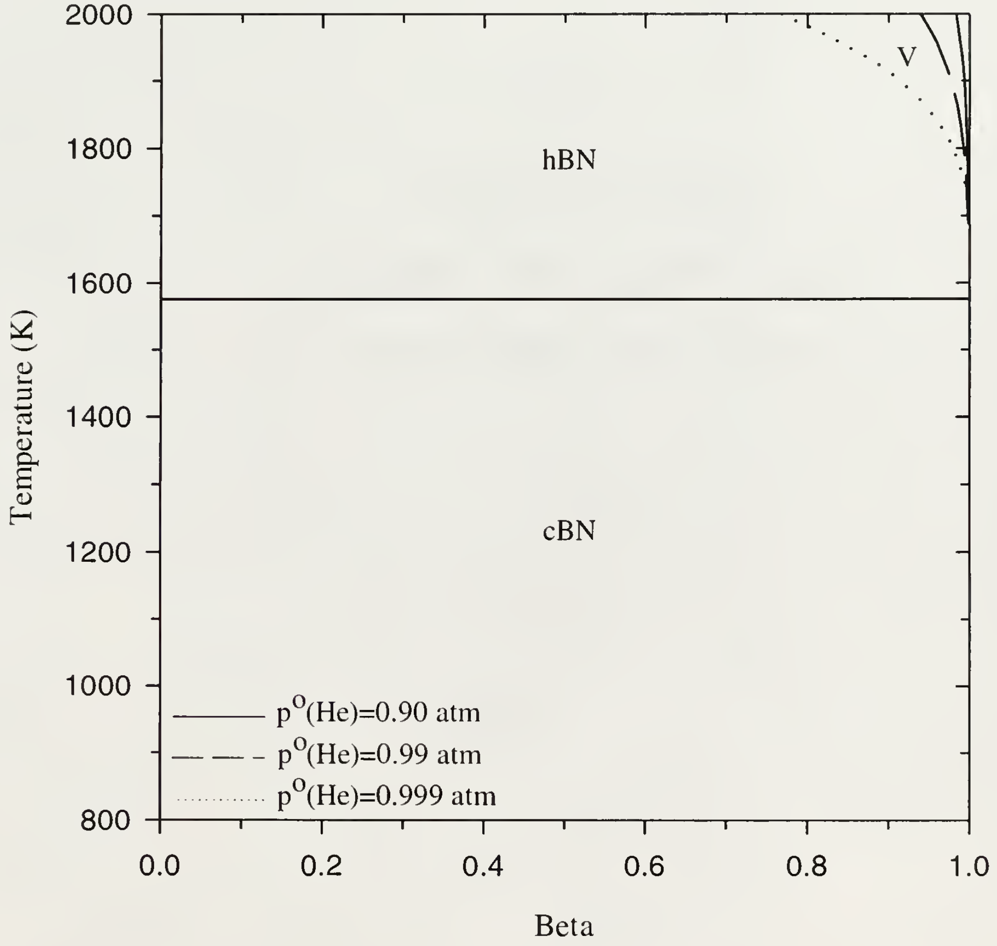

Figure 2.24: Solid phase diagram for the heterogeneous system BCl_3-NH_3-H_2-He as a function of temperature and BCl_3 fraction beta as defined by equation 2.14.

The effect of substituting an inert gas (He) in place of hydrogen, was examined to determine the effect of reducing the dissociation of the BCl_3 precursor by limiting the amount of hydrogen available to form the necessary HCl byproduct. Therefore, any of the required hydrogen must result from the thermal dissociation of the NH_3 precursor. In contrast to helium use as the carrier gas in the calculations of boron phosphide equilibrium, solid deposition occurs in the boron nitride system over the entire range of initial helium partial pressures, even with no initial H_2. This is due to decomposition of the NH_3 precursor and the subsequent availability of hydrogen to reduce the BCl_3 precursor. This contrasts with the BCl_3-PCl_3-inert system, where no hydrogen was available from any of the precursors. As shown in Figure 2.24, changes in the initial inert gas partial pressure had very little effect on the solid deposition boundaries. As in the BCl_3-NH_3-H_2 system, the phase transition from cBN to hBN occurs at 1576 K and the region of no solid formation increases with an increase in the inert gas partial pressure. The most striking difference between the two systems is that neither solid phase mixtures were formed in the He diluted system.

The final equilibrium calculations involved the study of the etching effect due to HCl addition to the system. Note that in Figure 2.25, when the initial HCl partial pressure was zero, this corresponded to the case where the H_2 partial pressure was 0.99 in Figure 2.23. Analysis of the etching effect of HCl revealed that as the initial HCl partial pressure was increased, the region of pure cBN deposition increased significantly. In fact, at high HCl partial pressures and temperatures below 1000 K, cubic boron nitride is the only stable phase at equilibrium. Thus the domain of cBN deposition may possibly be extended experimentally by simultaneously injecting HCl into the carrier gas and depositing films at low temperatures.

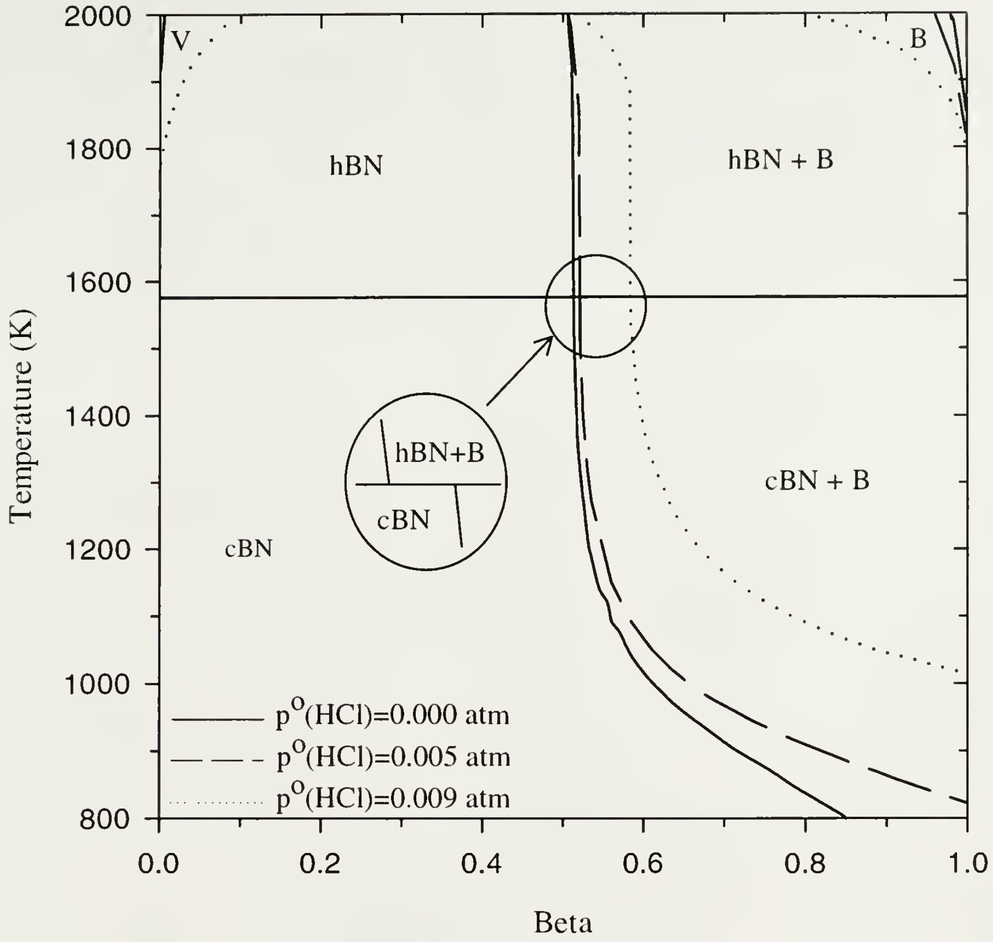

Figure 2.25: Solid phase diagram for the heterogeneous system BCl_3-NH_3-H_2-HCl as a function of temperature and BCl_3 fraction beta as defined by equation 2.14.

Addition of HCl also shifts the hBN / hBN+B phase boundary to slightly higher beta values and results in the formation of a region at very low beta values where no solid deposition occurs. HCl addition also has the effect of increasing the region of pure boron deposition at high temperatures and beta values. The increase in the region of hBN deposition as well as that of pure solid boron as the initial HCl partial pressure increases has the effect of decreasing the deposition region of the hBN+B solid mixture. This indicates that the hBN+B solid mixture is preferentially etched by the addition of HCl.

There is no change in the cBN-hBN solid phase boundary, however, regardless of the initial HCl partial pressure.

2.2.3 Conclusions

Thermodynamic equilibrium calculations were performed on the homogeneous NH_3-H_2 system and the homogeneous and heterogeneous BCl_3-NH_3-H_2 systems. In the NH_3-H_2 system important species are N_2 and NH_3 over the temperature and initial NH_3 partial pressure ranges considered. In the BCl_3-NH_3-H_2 homogeneous system the equilibrium of all species was determined to be dependent on both the initial BCl_3 and NH_3 partial pressures.

Calculations for the BCl_3-NH_3-H_2 heterogeneous system revealed the stability of cubic boron nitride at one atm pressure over a wide range of temperature and initial partial pressures. This is in direct contradiction to the experimentally determined stability of cubic boron nitride at only high temperatures and pressures. The thermochemical data for BN used in the calculations presented in this dissertation utilizes experimental data on the formation enthalpy of cBN that was unavailable until 1988. Furthermore, Solozhenko obtained and comprehensively studied four BN crystalline modifications (cBN, hBN, wBN, and rBN) using a wide range of modern experimental methods [107]. The availability of this new data explains the contradiction between the calculated results and the experimentally determined "catalyst" influenced BN phase diagram.

Five regions of deposition were observed: three pure phases of hexagonal boron nitride, cubic boron nitride, and boron and two solid mixture phases of cubic boron nitride+boron and hexagonal boron nitride+boron. The transition from cBN to hBN stability always occurred at 1576 K. It was determined that the domain of cBN deposition increased with an increase in the initial BCl_3 partial pressure, a decrease in the initial H_2 partial pressure, and with the addition of HCl as an etchant. While yields were not considered, the maximum cBN deposition region occurred when the H_2 dilutant was replaced with He. In this system cBN deposition was thermodynamically favorable over the entire beta value range and from 800 to 1576 K.

2.3 Gallium Nitride

2.3.1 Introduction

The increased interest in heteroepitaxy of semiconductor films has motivated the development of a reliable method of calculating the strain energy due to the mismatch between the epitaxial growth layer and the underlying substrate. This lattice mismatch and subsequent strain can influence the rate of reaction and the extent of dislocation generation during growth, as well as the equilibrium phase diagram. While cubic film/cubic substrate combinations have been analyzed previously [486], systems involving hexagonally oriented material as either the film or substrate have not been thoroughly investigated to date. Examples of important semiconductor materials that exist in the hexagonal crystal structure include the wide band gap compound semiconductors GaN, SiC, BN and II-VI semiconductors such as CdS. These materials are promising candidates for use in optoelectronic applications including blue wavelength LEDs and ultraviolet laser diodes, high power-high temperature electronics, and in the case of cBN as an abrasive [487,488]. The lack of large area bulk crystals for most of these hexagonal compounds has necessitated the use of alternative substrates with different lattice parameters and thermal expansion coefficients. Furthermore, device applications often require alloying that introduces additional stress in the film. As an example, alloying GaN with InN to lower the band gap energy increases the value of the lattice parameter.

The strain energy stored in a film grown on a mismatched substrate increases the Gibbs energy of the material. This strain energy contribution modifies such equilibrium quantities as melting temperature, vapor pressure, and miscibility limits. While the growth of hexagonal materials has been extensively studied experimentally, quantitative calculation of the inherent strain energy has not been fully performed [489]. Furthermore, the effect of the strain energy on the resulting equilibrium has not been addressed. In this work, elastic compliance equations are developed and their relationship to the overall strain energy of a hexagonally oriented film and substrate are presented. These general relations are then applied to the growth of GaN on different substrates.

2.3.2 Strain Energy Formula Derivation

The development of the general equations necessary to calculate the strain energy of a hexagonal film on either a hexagonal or rhombohedral substrate is shown below.

The general form of strain energy for an elastic body can be written as:

$$U = \frac{1}{2}(\sigma_x \varepsilon_x + \sigma_y \varepsilon_y + \sigma_z \varepsilon_z + \tau_{xy}\gamma_{xy} + \tau_{yz}\gamma_{yz} + \tau_{zx}\gamma_{zx}) \qquad \text{Equation 2.15}$$

where U is the strain energy per unit volume, σ_x ,σ_y and σ_z are the normal stresses, τ_{xy} τ_{yz} and τ_{zx} are the shear stresses, ε_x, ε_y and ε_z are normal strain and γ_{xy}, γ_{yz} and γ_{zx} are the shear strain. Generally, only the normal strain and stress in two perpendicular axes are considered due to lattice mismatch in epitaxial growth. Hooke's law can be written as

$$\varepsilon_x = s'_{11}\sigma_x + s'_{12}\sigma_y$$ Equation 2.16

$$\varepsilon_y = s'_{22}\sigma_y + s'_{12}\sigma_x$$ Equation 2.17

where s'_{ij} are the elastic compliances of the ij plane. These values can be obtained from the fourth-rank transform of the s_{ij} values in the principle plane. S_{ij} values can be calculated from the elastic stiffness coefficients or taken directly from the available literature. The fourth-rank transform of the s_{ij} values is:

$$s'_{ijkl} = \sum_{m=1}^{3}\sum_{n=1}^{3}\sum_{p=1}^{3}\sum_{q=1}^{3} a_{im}a_{jn}a_{kp}a_{lq}s_{mnpq}$$ Equation 2.18

where a_{im}, a_{jn}, a_{kp}, and a_{lq} are the direction cosines of the axes of the plane studied with respect to those of the principle plane. It should be noted that s_{ij} is actually the reduced representation of the fourth tensor s_{ijkl} according to Voigt's notation [490]. In the case where the elastic compliances are unknown but the elastic stiffness coefficients, c_{ij}, are available, the s_{ij} values can be calculated from c_{ij} since the matrix of s_{ij} and that for c_{ij} are mutually inverted.

The matrix of s_{ij} for the hexagonal crystal lattice is given by Lekhnitskii [490] as:

$$\begin{bmatrix} s_{11} & s_{12} & s_{13} & 0 & 0 & 0 \\ s_{12} & s_{11} & s_{13} & 0 & 0 & 0 \\ s_{13} & s_{13} & s_{33} & 0 & 0 & 0 \\ 0 & 0 & 0 & s_{44} & 0 & 0 \\ 0 & 0 & 0 & 0 & s_{44} & 0 \\ 0 & 0 & 0 & 0 & 0 & 2(s_{11} - s_{12}) \end{bmatrix} \qquad \text{Equation 2.19}$$

For the hexagonal lattice, the elastic compliances in the plane of interest can be written as:

$$s'_{11} = (1 - l_3^2)^2 s_{11} + l_3^4 s_{33} + l_3^2 (1 - l_3^2)(2s_{13} + s_{44}) \qquad \text{Equation 2.20}$$

$$s'_{12} = s_{11}(l_1 m_1 - l_2 m_2)^2 + s_{12}(l_1 m_2 - l_2 m_1)^2 + s_{33}[(1 - l_3^2) m_3^2 + l_3^2 (1 - m_3^2)] + s_{33} l_3^2 m_3^2 + s_{44} l_3 m_3 (l_2 m_2 - l_1 m_1) \qquad \text{Equation 2.21}$$

$$s'_{22} = (1 - m_3^2)^2 s_{11} + m_3^4 s_{33} + m_3^2 (1 - m_3^2)(2s_{13} + s_{44}) \qquad \text{Equation 2.22}$$

where l_1, l_2 and l_3 are the direction cosines of the x′ axis of the plane studied with respect to the x, y, and z axes of the principal plane. Similarly m_1, m_2, and m_3 are that of the y′ axis. The relationship between s_{ij} and c_{ij} in the principal plane can be written as:

$$s_{11} = \frac{c_{11}c_{33} - c_{13}^2}{(c_{11} - c_{12})(c_{11}c_{33} + c_{12}c_{33} - 2c_{13}^2)} \qquad \text{Equation 2.23}$$

$$s_{12} = \frac{c_{13}^2 - c_{12}c_{33}}{(c_{11} - c_{12})(c_{11}c_{33} + c_{12}c_{33} - 2c_{13}^2)} \qquad \text{Equation 2.24}$$

$$s_{13} = \frac{-c_{13}}{c_{11}c_{33} + c_{12}c_{33} - 2c_{13}^2} \qquad \text{Equation 2.25}$$

$$s_{33} = \frac{c_{11} + c_{12}}{c_{11}c_{33} + c_{12}c_{33} - 2c_{13}^2} \qquad \text{Equation 2.26}$$

$$s_{44} = \frac{1}{c_{44}}$$ Equation 2.27

Once these relationships are known calculation of a meaningful elastic energy term can made. Two different planes of film growth were considered, the (0001) basal plane and the $(10\bar{1}0)$ prism plane (see Figure 2.26). Since the (0001) basal plane of a hexagonal crystal is isotropic, the x and y axes can be chosen coincident with those of the principal plane. Therefore,

$$\varepsilon_x = s_{11}\sigma_x + s_{12}\sigma_y$$ Equation 2.28

$$\varepsilon_y = s_{22}\sigma_y + s_{12}\sigma_x$$ Equation 2.29

For growth on the (0001) basal plane there are two possible film/substrate crystallographic relationships. The first is that the planes of film growth and the underlying substrate are both hexagonal. The second is when either the film growth plane or the substrate are not hexagonal (e.g., zincblende, rhombohedral). Each case was analyzed.

When both the film and substrate are hexagonal and the basal plane of each is used in deposition, the strain in the x and y directions are equal due to symmetry and can be written as:

$$\varepsilon_x = \varepsilon_y = \frac{a - a_0}{a_0}$$ Equation 2.30

where a and a_0 are the lattice parameters of the growth layer and the substrate in the basal plane, respectively. Using equations 2.28 and 2.29, the normal stresses to the film/substrate interface can then be written as:

$$\sigma_x = \sigma_y = \frac{1}{s_{11} + s_{12}} \frac{a - a_0}{a_0} \qquad \text{Equation 2.31}$$

Thus from equation 2.15 the strain energy per unit volume is simply:

$$U = \frac{1}{s_{11} + s_{12}} \left(\frac{a - a_0}{a_0}\right)^2 \qquad \text{Equation 2.32}$$

In the second case, when either the growth layer or substrate are not hexagonal, the strain in the x and y directions will not be equal ($\varepsilon_x \neq \varepsilon_y$) due to departure from symmetry. From equation 2.28 and 2.29, it can be obtained that:

$$\sigma_x = \frac{s_{11}\varepsilon_x - s_{12}\varepsilon_y}{s_{11}^2 - s_{12}^2} \qquad \text{Equation 2.33}$$

$$\sigma_y = \frac{s_{11}\varepsilon_y - s_{12}\varepsilon_x}{s_{11}^2 - s_{12}^2} \qquad \text{Equation 2.34}$$

with a resulting strain energy expression of:

$$U = \frac{s_{11}(\varepsilon_x^2 + \varepsilon_y^2) - 2\varepsilon_x\varepsilon_y s_{12}}{2(s_{11}^2 - s_{12}^2)} \qquad \text{Equation 2.35}$$

Deposition on the $[10\bar{1}0]$ prism plane in the $[\bar{1}2\bar{1}0]$ and [0001] directions (defined as x′ and y′ direction of the plane studied, see Figure 2.26) were also considered. On this plane the direction cosines of the x′ and y′ axis are $l_1=0$, $l_2=1$, $l_3=0$, $m_1=0$, $m_2=0$, and $m_3=1$. Therefore the elastic compliances can be transformed from the plane of interest to the principal plane using:

$$s'_{11}=s_{11} \qquad \text{Equation 2.36}$$

$$s'_{12}=s_{13} \qquad \text{Equation 2.37}$$

$$s'_{22}=s_{33} \qquad \text{Equation 2.38}$$

The strains in the [$\bar{1}2\bar{1}0$] and [0001] directions are thus:

$$\varepsilon_{x'} = \sigma_{x'}s'_{11}+\sigma_{y'}s'_{12} = \sigma_{x'}s_{11}+\sigma_{y'}s_{13}$$ Equation 2.39

$$\varepsilon_{y'} = \sigma_{y'}s'_{22}+\sigma_{x'}s'_{12} = \sigma_{y'}s_{33}+\sigma_{x'}s_{13}$$ Equation 2.40

and the normal stresses are:

$$\sigma_{x'} = \frac{\varepsilon_{x'}s_{33}-\varepsilon_{y'}s_{13}}{s_{11}s_{33}-s_{13}^2}$$ Equation 2.41

$$\sigma_{y'} = \frac{\varepsilon_{y'}s_{11}-\varepsilon_{x'}s_{13}}{s_{11}s_{33}-s_{13}^2}$$ Equation 2.42

It directly follows as before that the strain energy per unit volume is:

$$U = \frac{\varepsilon_{x'}^2 s_{33}+\varepsilon_{y'}^2 s_{11}-2\varepsilon_{x'}\varepsilon_{y'}s_{13}}{2(s_{11}s_{33}-s_{13}^2)}$$ Equation 2.43

If a hexagonal lattice structured film with lattice parameters a and c is grown with its prism plane on a rectangular face of a substrate with lattice parameters a_0 and c_0, then the system's strain is $\varepsilon_{x'}=(a-a_0)/a_0$, $\varepsilon_{y'}=(c-c_0)/c_0$, and its resulting strain energy is:

$$U = \frac{(\frac{a-a_0}{a_0})^2 s_{33}+(\frac{c-c_0}{c_0})^2 s_{11}-2(\frac{a-a_0}{a_0})(\frac{c-c_0}{c_0})s_{13}}{2(s_{11}s_{33}-s_{13}^2)}$$ Equation 2.44

Equation 2.44 is generalized and can thus be used for all the other prism planes as well as "internal" planes such as (1 $\bar{2}$10) because of the isotropic nature of the basal plane.

2.3.3 Lattice Mismatch and Strain Energy Calculation

Three independent sets of calculations were performed to demonstrate the strain energy calculation of a GaN film grown on Al_2O_3 and $LiGaO_2$ substrates, using the fundamental data of tables 2.3 and 2.4 [491]. Table 2.5 summarizes the lattice mismatch and strain energy calculated for three different film/substrate orientations. It is clearly evident from both the equations presented above and the data in table 2.5 that as the lattice mismatch increases there is a corresponding increase in the system's strain energy. The minimum lattice mismatch in the GaN/Al_2O_3 system occurs when the GaN film is rotated 30° with respect to the sapphire substrate so that the (0001)//(0001), [$\bar{1}$010]//[1 $\bar{2}$10] GaN/Al_2O_3 interface is formed and a 3:1 film/substrate unit cell ratio is used. For instance, the lattice mismatch for no rotation and 30° rotation with a 3:1 GaN/Al_2O_3 unit cell ratio are 33% and 16.1%, respectively. Rotation of GaN films on Al_2O_3 has been observed experimentally [492] and is illustrated in Figure 2.27. The strain energy of the 16.1% mismatched system is 11.755 GPa or 161.49 kJ/mole. It must be noted that this lattice mismatch exceeds the limits to maintain elastic deformation in the growth layer. Therefore, experimentally, a relaxation of the strain energy and a high dislocation density formation would be inevitable without the use of a buffer layer.

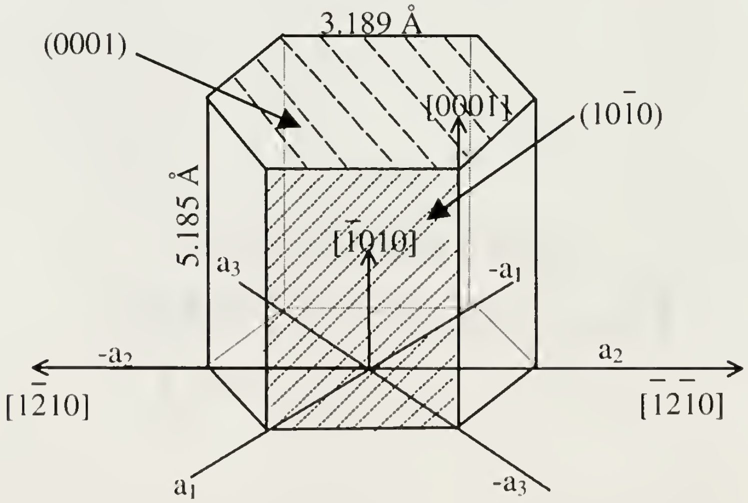

Figure 2.26: Basal plane (0001) and prism plane (10 $\bar{1}$0) of a hexagonal crystal. The [$\bar{1}$010] direction is parallel to the lower basal plane.

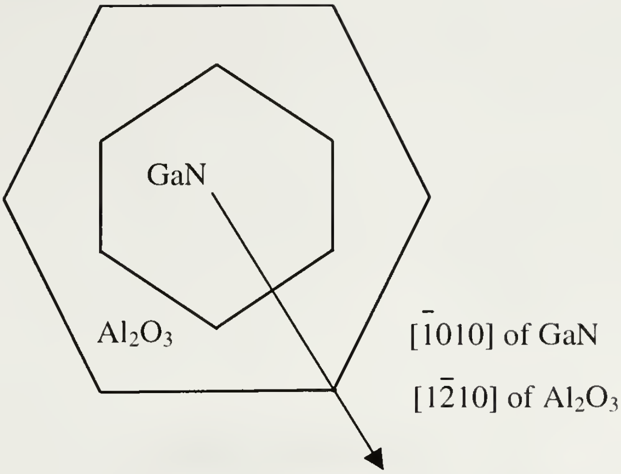
GaN
Al$_2$O$_3$
[$\bar{1}$010] of GaN
[1$\bar{2}$10] of Al$_2$O$_3$

Figure 2.27: Scheme for the deposition of (0001)//(0001), [$\bar{1}$010]//[1$\bar{2}$10] GaN/Al$_2$O$_3$ system

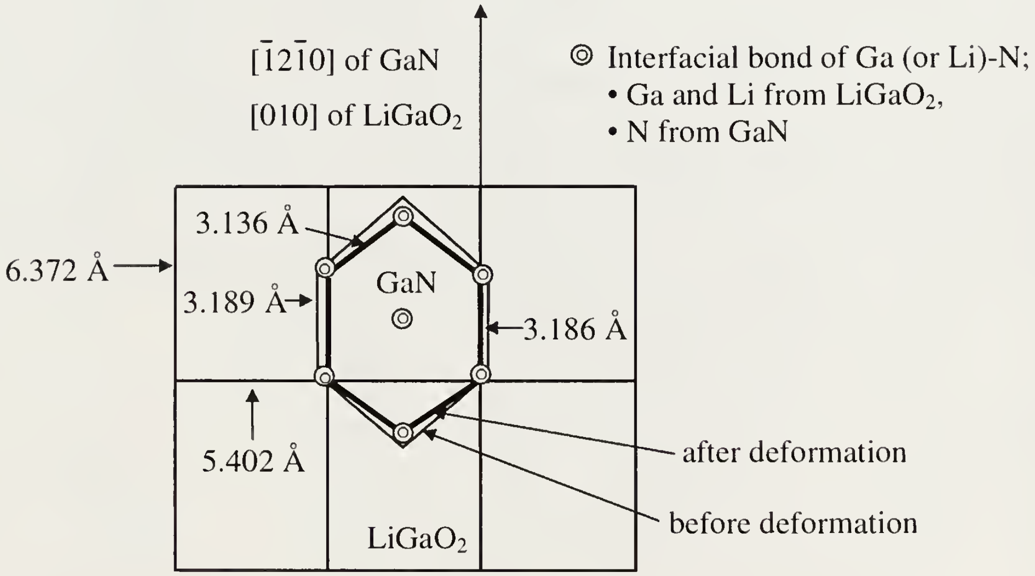
[$\bar{1}$2$\bar{1}$0] of GaN
[010] of LiGaO$_2$
◎ Interfacial bond of Ga (or Li)-N;
• Ga and Li from LiGaO$_2$,
• N from GaN
3.136 Å
6.372 Å
3.189 Å
GaN
3.186 Å
5.402 Å
after deformation
before deformation
LiGaO$_2$

Figure 2.28: Scheme for the deposition of (0001)//(001), [$\bar{1}$2$\bar{1}$0]//[010] GaN/LiGaO$_2$ system

Deposition of the (0001)//(001), [$\bar{1}$2$\bar{1}$0]//[010] GaN/LiGaO$_2$ system (Figure 2.28) is an attractive alternative due to its lower mismatch [493]. LiGaO$_2$ has an orthorhombic structure consisting of an alternate stacking of two-dimensional arrays made of oxygen tetrahedra centered Ga and Li ions. Therefore it can be deduced that LGO has a wurtzitic superstructure with a small departure from hexagonal symmetry due to the need to accommodate metallic atoms of different size. When GaN is grown on $LiGaO_2$ in this orientation, the normal strains are

$$\varepsilon_x = (\sqrt{3}*3.189-5.402)/5.402 = 2.25\% \qquad \text{Equation 2.45}$$

$$\varepsilon_y = (2*3.189-6.372)/6.372 = 0.09\%\,. \qquad \text{Equation 2.46}$$

Thus the strain energy is reduced by equation 2.35 to 0.094 GPa or 1.29 kJ/mole.

Another possible film/substrate orientation of prism plane growth shown in Figure 2.29 is the $(1\bar{2}10)//(010)$, $[10\bar{1}0]//[100]$ GaN/$LiGaO_2$ system. The normal strain can then be calculated as:

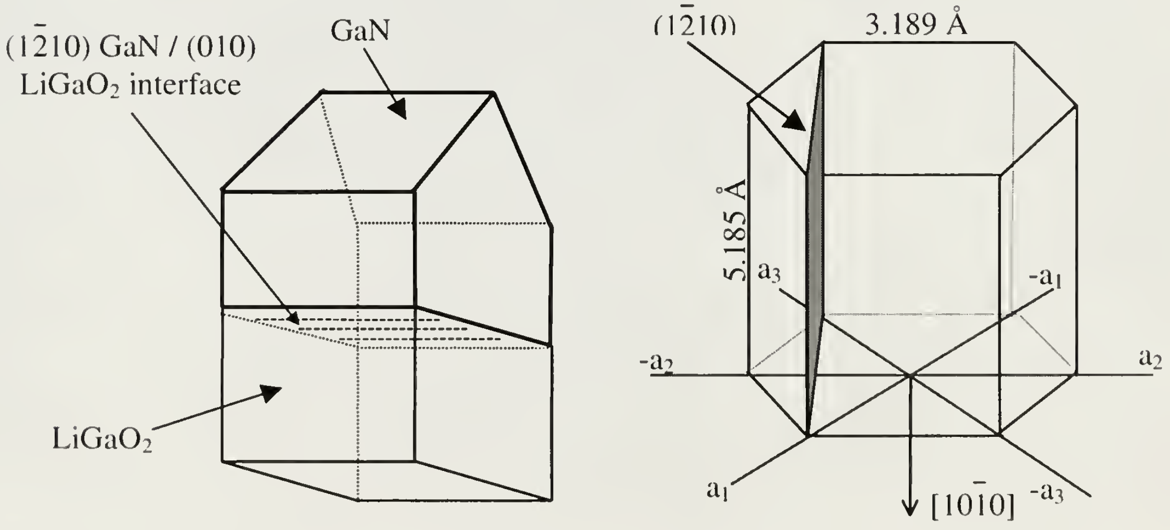
$(1\bar{2}10)$ GaN / (010) $LiGaO_2$ interface
GaN
$LiGaO_2$
$(1\bar{2}10)$
3.189 Å
5.185 Å
a_3
$-a_1$
$-a_2$
a_2
a_1
$[10\bar{1}0]$
$-a_3$

Figure 2.29: Scheme for the deposition of $(1\bar{2}10)//(010)$, $[10\bar{1}0]//[100]$ GaN/$LiGaO_2$ system

$$\varepsilon_x = (\sqrt{3} * 3.189 - 5.402)/5.402 = 2.25\% \qquad \text{Equation 2.47}$$

$$\varepsilon_y = (5.185 - 5.007)/5.007 = 3.56\% \qquad \text{Equation 2.48}$$

The strain energy for this orientation can then be calculated using equation 2.43 to be 0.359 GPa or 4.94 kJ/mole.

Table 2.3 Lattice constant (Å) of GaN, Al_2O_3, and $LiGaO_2$

	a	b	c
GaN(wurtzite)	3.189		5.185
Al_2O_3(wurtzite)	4.758		12.991
$LiGaO_2$(Orthorhombic)	5.402	6.372	5.007

Table 2.4 Elastic stiffness coefficients c_{ij} and compliances s_{ij} of GaN

c_{ij} (GPa)	c_{11}	c_{12}	c_{13}	c_{33}	c_{44}
	374	106	70	379	101
s_{ij} (1/GPa)	s_{11}	s_{12}	s_{13}	s_{33}	s_{44}
	0.00297	-0.00077	-0.00041	0.00279	0.00990

Table 2.5 Strain energy due to lattice mismatch

Growth layer/Substrate	Growth Orientation	Lattice Mismatch(%)		Strain Energy	
		ε_x	ε_y	GPa	kJ/mol
wGaN / wAl_2O_3	(0001)//(0001) $[\bar{1}010]//[1\bar{2}10]$	16.1		11.76	161.5
wGaN / $oLiGaO_2$	(0001)//(001), $[\bar{1}2\bar{1}0]//[010]$	2.25	0.09	0.094	1.3
wGaN / $oLiGaO_2$	$(1\bar{2}10)//(010)$ $[10\bar{1}0]//[100]$	2.25	3.56	0.36	4.9

wGaN = wurtzite
$oLiGaO_2$ = orthorhombic

2.3.4 Results and Discussion

Thermodynamic equilibrium calculations were carried out on the strained Ga-N system to demonstrate the importance of strain energy on a system's final equilibrium state. Thermochemical data for all species except for GaN(s) were taken from the ThermoCalc version K sub94 database [451]. GaN(s) data that were reassessed by

Davydov and Anderson [459] were incorporated. A strain energy term calculated from equations 2.32, 2.35, or 2.44 was added to the $G-H^{ser}$ GaN(s) term. $G-H^{ser}$ energy expressions for each species considered are shown in Table 2.6.

From Figures 2.30 and 2.31 the effect of strain energy on the strained Ga-N equilibrium binary system is evident. Figure 2.30 depicts equilibrium in the unstrained Ga-N heterogeneous system at 0.1 MPa and will be used as a basepoint for the strained GaN/$LiGaO_2$ and GaN/Al_2O_3 equilibrium systems. Figure 2.31 illustrates the effect of strain energy on the resulting Ga-N equilibrium. A decrease in the GaN thermodynamic stability (i.e. its melting point temperature) is due to the addition of a positive term in the Gibbs energy expression for solid GaN. As Figure 2.31 shows, at a system pressure of 0.1 MPa, the melting temperature of GaN will decrease by 11 and 43 K with the addition of strain energies of the (0001)//(001), $[\bar{1}2\bar{1}0]$//[010] GaN/$LiGaO_2$ and $(1\bar{2}10)$//(010), $[10\bar{1}0]$//[100] GaN/$LiGaO_2$ systems, respectively. The smaller change in the melting temperature corresponds to the less strained GaN basal plane deposition (Figure 2.28) while the larger melting temperature represents GaN prism plane growth (Figure 2.29). Due to the decrease in the GaN melting point temperature the liquid + gas stability domain will increase as the film/substrate strain energy is increased.

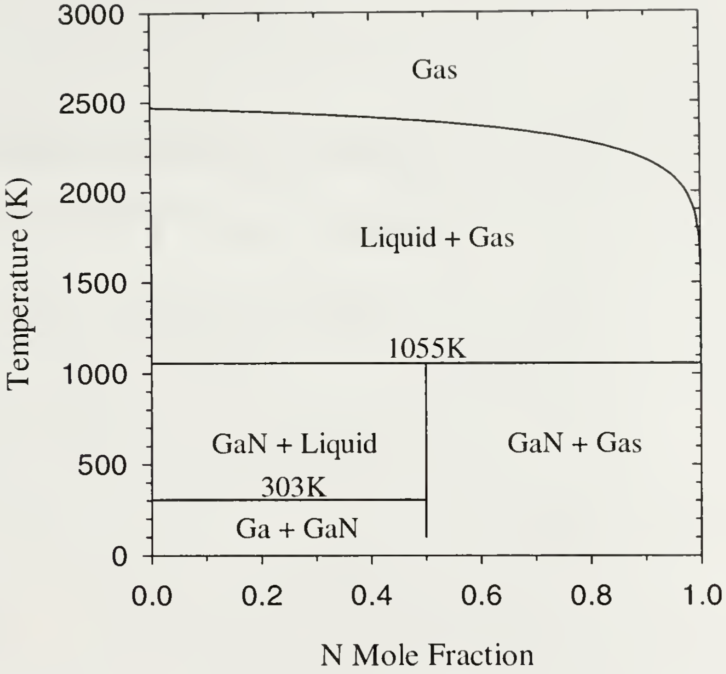

Figure 2.30: T-x diagram of the unstrained heterogeneous system Ga-N as a function of temperature and N mole fraction at 0.1 MPa

It is desirable in most semiconductor deposition techniques including CVD, MOCVD, and MBE to have only solid and gas phases present. Thus, from a thermodynamic viewpoint, deposition of GaN on LGO at near atmospheric conditions must occur below 1012 or 1044 K (1055 K in the unstrained case) and Ga:N molar ratios less than unity.

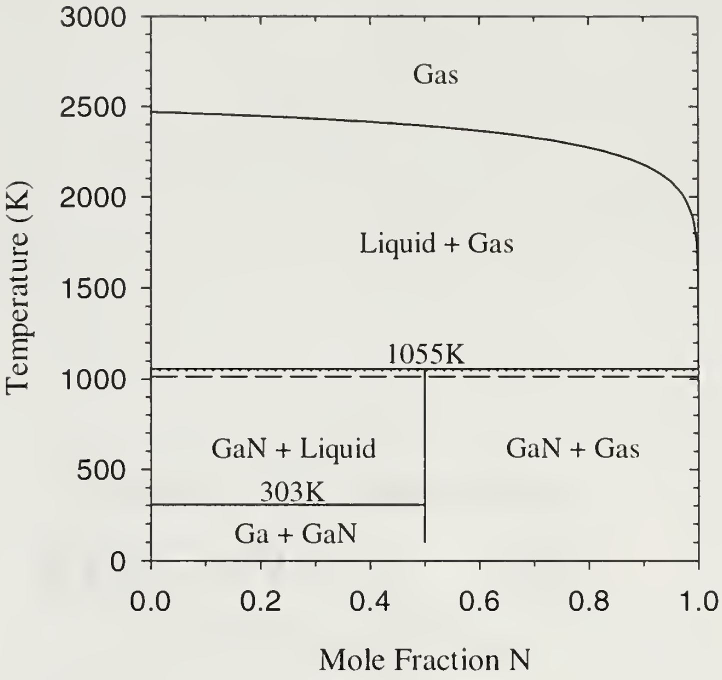

(a)

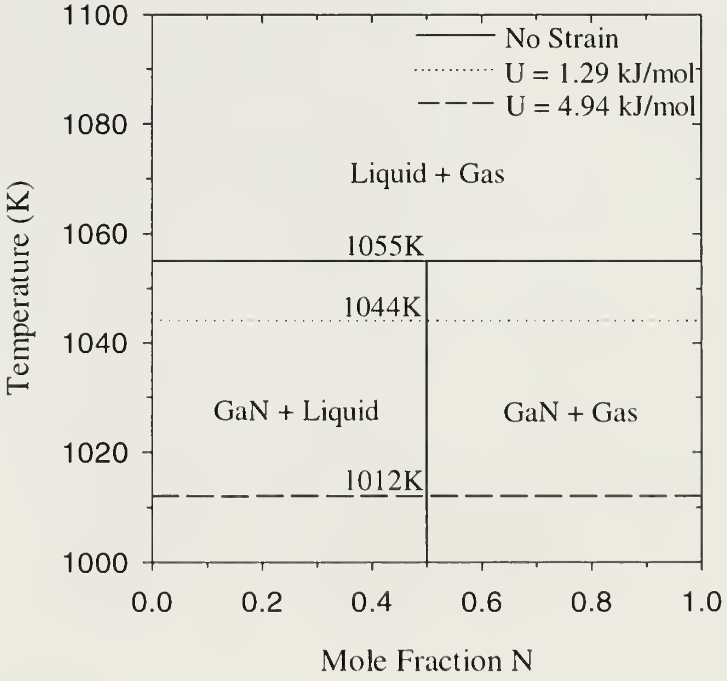

(b)

Figure 2.31: T-x diagram of the strained heterogeneous system Ga-N on $LiGaO_2$ at 0.1 MPa system pressure
a) Overall diagram; b) Enlarged view of change of melting temperature

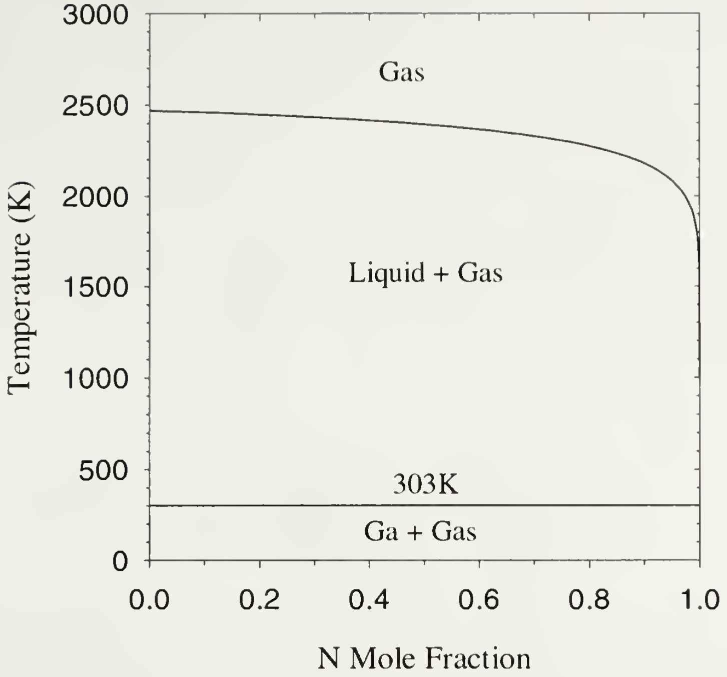

Figure 2.32: T-x diagram of the strained heterogeneous system Ga-N on Al_2O_3 at 0.1 MPa system pressure

Figure 2.32 shows the thermodynamic equilibrium deposition of GaN on Al_2O_3. A striking difference between Figures 2.30 and 2.32 can be seen immediately. The strain energy of the GaN film deposited on Al_2O_3, 161.5 kJ/mol, is so large that it prevents GaN from being a stable solid equilibrium phase at any temperature or mole fraction. This exemplifies one of the reasons why a buffer layer must be used to experimentally grow GaN on sapphire. Other calculations revealed that the maximum allowable strain energy still resulting in GaN stability was approximately 89 kJ/mol. Hence the strain energy present when GaN is deposited on sapphire is over 80% too large for solid GaN stability.

It must be clearly emphasized that these thermodynamic calculations assume a perfectly adhered GaN film with complete transfer of the lattice mismatch induced strain energy to the GaN film. The influence of dislocation formation, surface and interface energy terms have also been neglected. Thus, thermodynamically GaN is unstable on a sapphire substrate. Experimentally though, due to kinetic influences, it is possible to deposit a GaN film on a sapphire substrate.

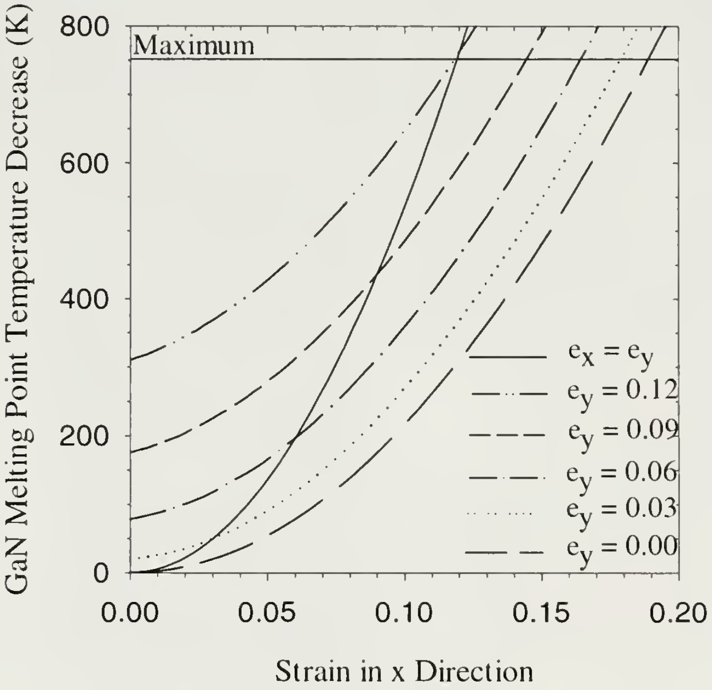

Figure 2.33: Generalized T-x diagram of the strained heterogeneous system Ga-N at 0.1 MPa system pressure

A general relationship between the decrease of the GaN melting point temperature and the lattice mismatch at 0.1 MPa system pressure is presented in Figure 2.33. As shown in Figure 2.30, the maximum possible change in the melting temperature, and thus the limit of GaN stability, is 752 K (1055 to 303 K). Therefore, the maximum symmetric strain the Ga-N system can possess and still have solid GaN stability is when ε_x and ε_y equal 0.12. When asymmetric strain in the y direction is considered, GaN can remain stable at higher x-direction strain values. For instance, when no strain is presented in the y direction the maximum strain in the x direction is 0.189. A similar relationship is noted if strain in the y direction is plotted on the x-axis.

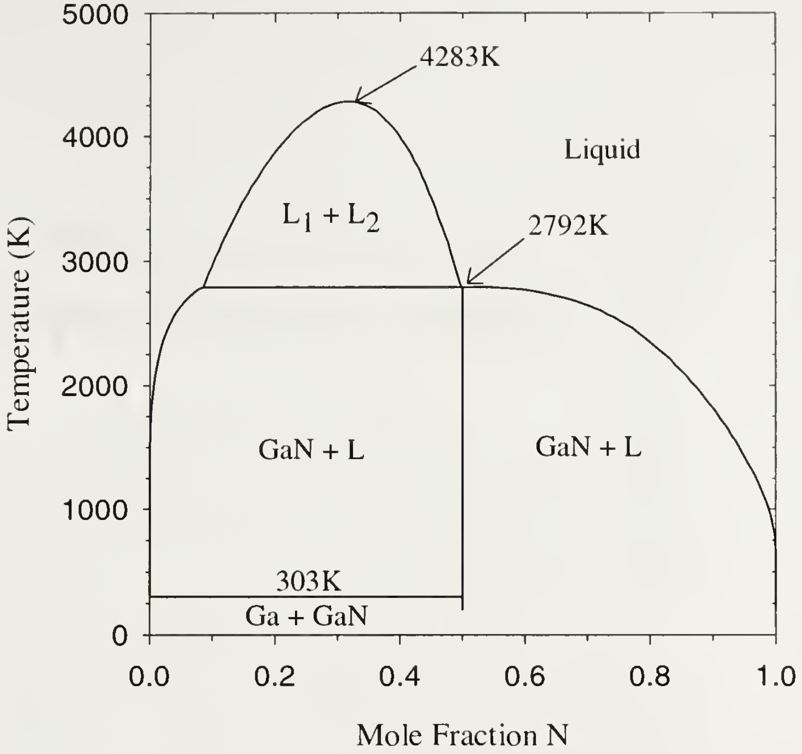

Figure 2.34: T-x diagram of the unstrained heterogeneous system Ga-N as a function of temperature and N mole fraction at equilibrium N_2 partial pressures

Calculations were also conducted at equilibrium N_2 partial pressures. N_2 partial pressures were examined since the gas phase of the Ga-N system would consist nearly exclusively of diatomic nitrogen gas. Deposition using the (0001)//(001), $[\bar{1}2\bar{1}0]//[010]$ and $(1\bar{2}10)//(010)$, $[10\bar{1}0]//[100]$ GaN/$LiGaO_2$ systems at this condition show that once again strain energy decreases the melting temperature of solid GaN. Figure 2.34, previously calculated by Davydov and Anderson [459] and verified in the present work, depicts the unstrained Ga-N heterogeneous system. Figure 2.35 illustrates that strained deposition of both the basal and prism planes of GaN on LGO at equilibrium N_2 partial pressures. Deposition under these conditions results in a much

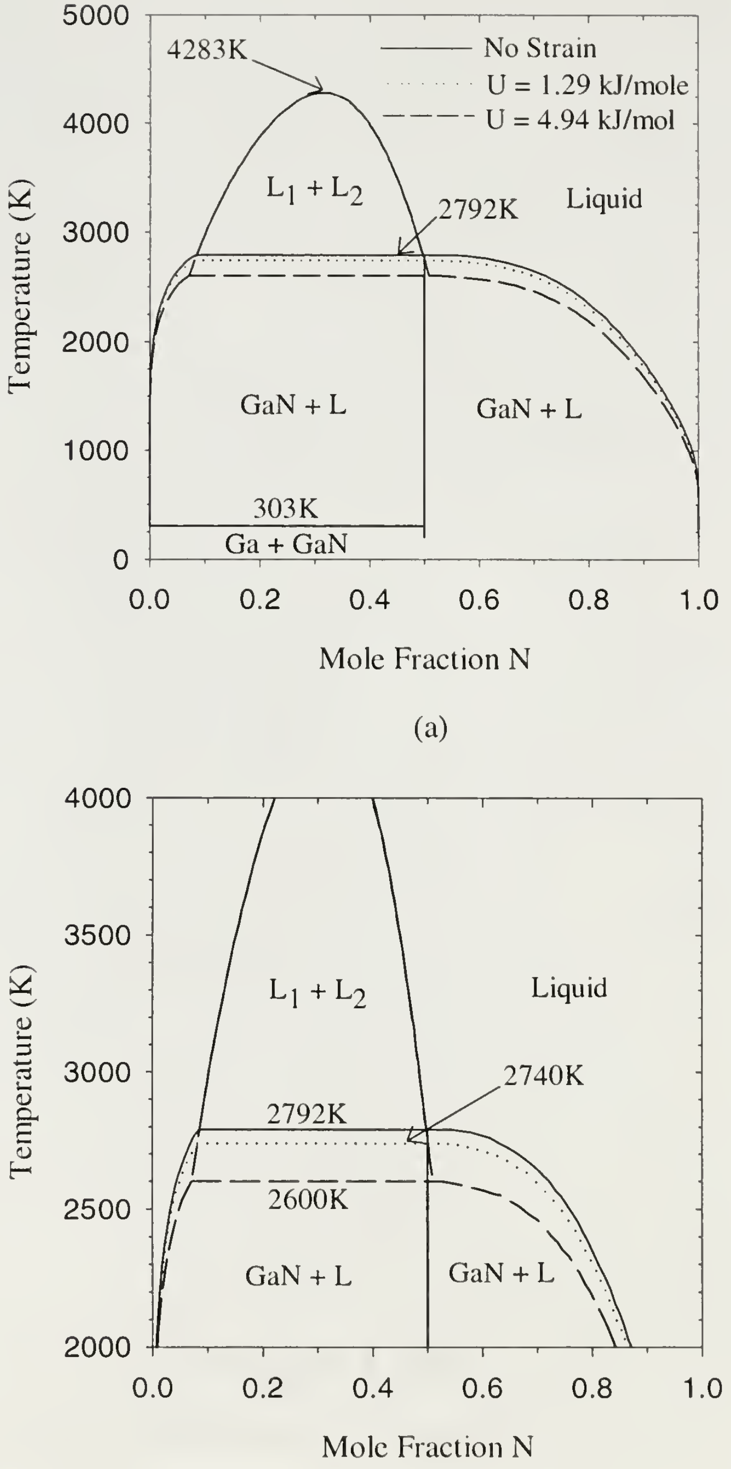

(a)

(b)

Figure 2.35: T-x diagram of the strained heterogeneous system Ga-N on $LiGaO_2$ at equilibrium N_2 partial pressures
a) Overall diagram; b) Enlarged view of change of melting temperature

larger decrease in the GaN melting temperature compared to that at 0.1 MPa system pressure (Figure 2.31). Nevertheless a large thermodynamically stable GaN (+liquid) phase is present with a temperature stability range up to at least 2600 K. It must be noted that there is no region where there is a GaN+gas phase as required by CVD.

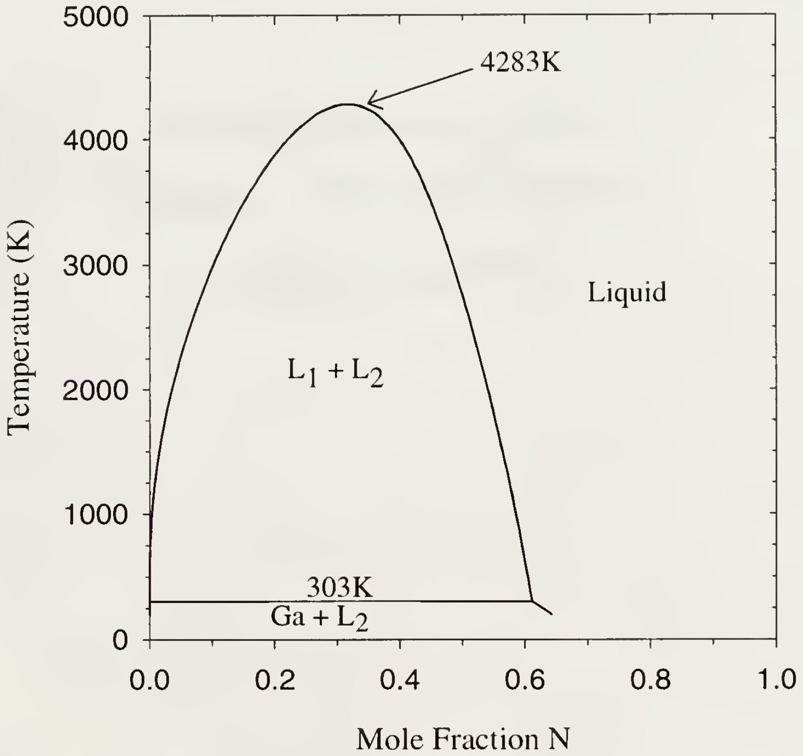

Figure 2.36: T-x diagram of the strained heterogeneous system Ga-N on Al_2O_3 at equilibrium N_2 partial pressures

When the significantly strained GaN/sapphire system at equilibrium nitrogen partial pressures was examined (Figure 2.36), solid GaN was not found to be thermodynamically stable at any temperature. Since a pure solid GaN phase or a GaN+gas phase is not thermodynamically stable, these results confirm near atmospheric calculations where solid GaN deposited on sapphire was not stable in any manner. The extremely large N_2 overpressure (≥ 10,000 atmospheres) did not prevent complete GaN decomposition to Ga by the loss of N atoms to the gas phase.

As mentioned above, a buffer layer of AlN is routinely used in GaN thin film deposition to decrease the film's dislocation density. GaN deposition (a=3.189 Å) on both an unstrained AlN substrate (a=3.111Å) and a 40Å AlN buffer layer on sapphire (a=3.088Å) were examined. Figure 2.37 shows the effect of each material combination on equilibrium in the Ga-N system. As the lattice mismatch between the GaN and its underlying material increases, the GaN melting point temperature decreases in a manner similar to GaN deposition on $LiGaO_2$. The GaN equilibrium melting temperature is decreased by 34 and 59 K for deposition on the unstrained AlN substrate and AlN buffer layer/sapphire substrate systems, respectively.

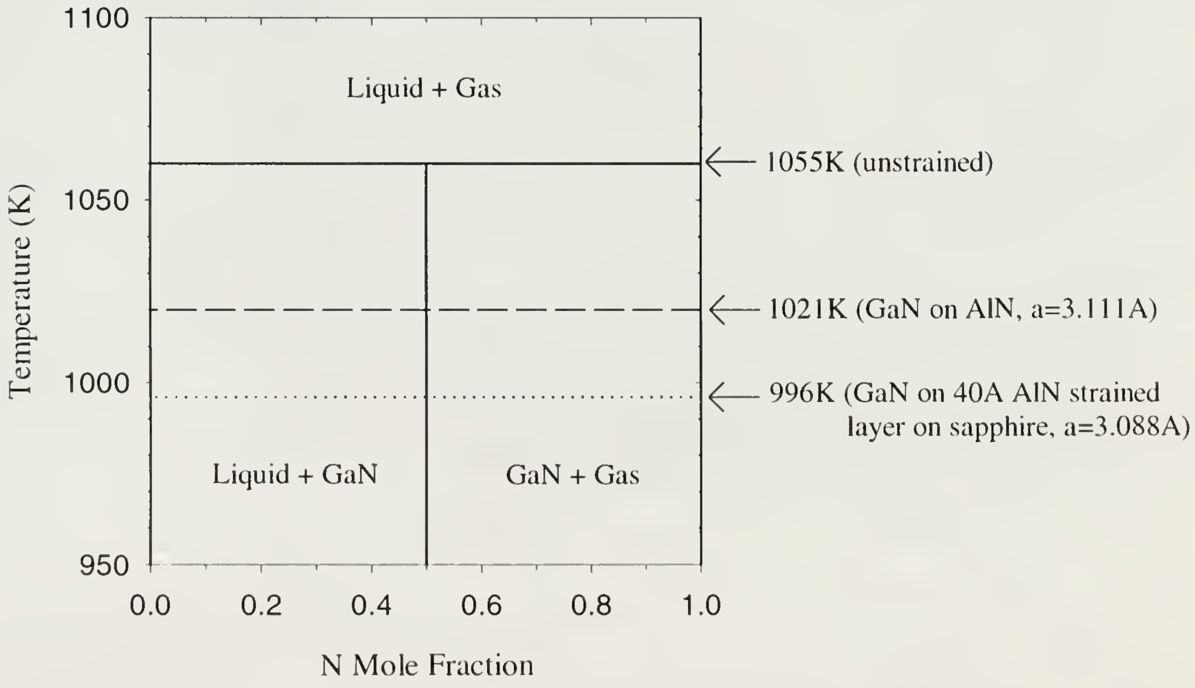

Figure 2.37: T-x diagram of the strained heterogeneous system Ga-N on AlN/Al_2O_3 at equilibrium N_2 partial pressures

Table 2.6 Thermochemical Data of the Ga-N System

Species	Temp. (K)	A	B	C	D	E	F	J
Ga (v)	298-600	2.59072E+05	8.01307E+01	-3.87106E+01	1.05378E-02	-9.86909E-07	0	0
	600-1400	2.63812E+05	3.34871E+01	-3.07501E+01	5.37745E-03	-5.46534E-07	-1.50943E+05	0
	1400-2700	2.70293E+05	-2.81811E+01	-2.19834E+01	3.19242E-04	-1.46299E-08	-9.92093E+05	0
Ga_2 (v)	298-1100	4.22882E+05	-3.60788E+01	-3.37286E+01	-9.36853E-03	6.27752E-07	-1.95204E+04	0
	1100-2500	4.19324E+05	8.33966E+00	-4.03356E+01	-4.18541E-03	2.67957E-08	3.12119E+05	0
N (v)	298-2950	4.66446E+05	-1.33753E+01	-2.08939E+01	8.45521E-05	-1.00187E-08	2.78879E+03	0
	2950-6000	4.81259E+05	-5.25441E+01	-1.63761E+01	-2.28374E-04	-2.78997E-08	-7.55911E+05	0
N_2 (v)	298-950	-7.50135E+03	1.89085E+01	-2.55638E+01	-3.53372E-03	5.36147E-09	-6.4745E+04	0
	950-2900	-1.47177E+04	3.44006E+01	-3.27398E+01	-1.30214E+03	6.0194E-08	1.12614E+06	0
N_3 (v)	298-800	4.03756E+05	-1.44341E+01	-2.95595E+01	-2.41312E-02	3.61560E-06	5.57142E+04	0
	800-2000	3.88937E+05	1.58670E+02	-5.54045E+01	-2.65705E-03	1.93657E-07	1.53645E+06	0
	2000-6000	3.80897E+05	2.10098E+02	-6.22956E+01	6.57265E-06	-7.868012E-10	3.33695E+06	0
Ga (l)	298-4000	5.66646E+03	-1.86811E+01	0	0	0	0	1.645E+23
N (l)	298-900	-4.4617E+03	6.07458E+01	-1.27819E+01	-1.76686E-03	2.68074E-09	-3.2374E+04	0
	900-2900	-8.06985E+03	8.74003E+01	-1.63699E+01	-6.5107E-04	3.0097E-08	5.63070E+05	0
GaN_1 (l)	298-6000	-2.16263E+04	1.82852E+01	0	0	0	0	0
GaN_2 (l)	298-6000	4.16673E+04	-4.29528E+00	0	0	0	0	0
Ga (s)	298-302.92	-2.13123E+04	5.85264E+02	-1.08229E+02	2.27156E-01	-1.18575E-04	4.39954E+05	0
	303-4000	-7.05564E+03	1.32730E+02	-2.60693E+01	1.506E-04	-4.0173E-08	-1.18332E+05	1.645E+23
GaN (s)	298-1773	-1.37112E+05	2.72388E+02	-4.43769E+01	-6.3011E-03	0	5.86387E+05	0

$G\text{-}H^{ser} = A + BT + CT\ln(T) + DT^2 + ET^3 + FT^{-1} + JT^{-9}$; in J/mol

For Ga-N (l): $G\text{-}H^{ser} = x_{Ga}x_N[GaN_1(l) + GaN_2(l)(x_{Ga} - x_N)]$; in J/mol

2.3.5 Conclusions

A series of generalized equations has been developed from fundamental stress/strain principles to calculate the lattice mismatch induced strain energy of a hexagonal film on hexagonal and rhombohedral substrates. Addition of strain energies to the thermodynamic equilibrium calculations of the Ga-N phase diagram shows dramatic differences between the strained and unstrained cases. At 0.1 MPa system pressure the GaN melting point decreased 11 and 43 K depending on the film/substrate orientation when GaN was deposited on $LiGaO_2$. Even more interesting was the disappearance of a GaN stability regime when the strain energy arising from its deposition on Al_2O_3 was included. At equilibrium N_2 partial pressures, deposition on LGO again decreased the GaN melting point temperature though a large GaN+liquid phase remained. Similar to near atmospheric pressures GaN is not stable at elevated N_2 partial pressures and temperatures below 303 K. The profound effect of strain energy in a lattice mismatched system indicates that the predicted equilibrium behavior of epitaxial thin films may differ greatly from that of unstrained thermodynamic systems. These calculations suggest that strain energy has significant influence on both the experimental and equilibrium deposition processes of semiconductor materials. In contrast these thermodynamic results, CVD of GaN on sapphire is experimentally possible due to kinetic influences.

CHAPTER 3
GROWTH OF BP BY CVD

3.1 Introduction

Boron phosphide (BP) thin film depositions were conducted as a forerunner to boron nitride (BN) growths to determine the effect of growth conditions on the BP morphological and structural properties and the process growth rate. An in-depth understanding of these effects was paramount since the as-grown BP film would subsequently be used as a template for nitridation. As noted in section 1.2.1, CVD of boron phosphide films has been conducted using a wide variety of precursors, typically diluted in a H_2 carrier gas stream. While a hydride based chemistry of B_2H_6 and PH_3 has been reported more often in the literature, a halide based system of BCl_3 and PCl_3 was used in these studies both for safety reasons and because of previous experience with halide compounds.

3.2 Experimental

CVD of boron phosphide was carried out with boron trichloride (BCl_3, 99.5% purity, Matheson) and phosphorus trichloride (PCl_3, 99.999% purity, Johnson-Matthey) precursors, diluted in hydrogen (H_2, 99.999% purity, Linde). BCl_3 was in the form of a compressed gas, and its flow was metered by means of a mass-flow controller. PCl_3 was in liquid form, and was delivered to the reactor by a bubbler system. The streams of BCl_3 and PCl_3 were introduced separately into the reactor to avoid adduct formation. A final diluting

H_2 stream was added and divided to ensure equal flowrates in both the BCl_3 and PCl_3 lines. The S-type thermocouple was housed in an alumina sheath to protect it from the chlorine environment. Additional information and a schematic of the deposition system can be found in section 1.4.2 of this work.

At the start of every run, UHP-argon gas was used to flush the system, after it was under vacuum for 20 min. The system was then switched to hydrogen. Pressure was increased to the desired deposition pressure via a computer controlled throttling valve, and the graphite susceptor was brought to the desired deposition temperature. To prevent the formation of HCl and subsequent etching of the substrate, the BCl_3 and PCl_3 were introduced simultaneously into the reactor at the immediate start of the run. Once the desired deposition time had passed, both precursors were turned off simultaneously to prevent etching of the deposited BP or uncoated substrate. A 5 min post-deposition flush period in hydrogen was performed at the end of each run to flush residual precursors in the reactor and inlet lines.

The deposition temperature typically did not exceed 1100 ^{o}C due to the reported decomposition of BP into its subphosphide, $B_{13}P_2$, at 1130 ^{o}C, although samples were grown in a temperature range spanning 850 to 1200 ^{o}C. The reactor pressure was varied from 10 Torr to atmospheric pressure. Flowrates of the precursors were varied from 0.25 to 2 sccm and 0.5 to 4 sccm for BCl_3 and PCl_3, respectively, while total flowrates were varied from 250 to 1000 sccm. A variety of carrier gases were used including H_2, N_2, He, and Ar. Typical deposition times were 30 min, although longer runs (up to 4 h) were conducted to investigate and characterize the growth of thick BP films, while very short runs (5 to 10 sec) were conducted in an attempt to examine the nucleation of the first BP monolayers. A total of 214 BP films were deposited of which 83 were subsequently nitrided to form boron nitride.

The BP films were characterized with scanning electron microscopy (SEM) and atomic force microscopy (AFM) to determine surface morphology. Elemental analysis and film identification was performed using X-ray photoelectron spectroscopy (XPS), Auger electron spectroscopy (AES), Fourier transform infrared spectroscopy (FTIR), and Raman spectroscopy. To determine the crystallinity and film quality, the films were also analyzed by transmission electron microscopy (TEM).

To identify and determine the crystallinity and preferred orientation of the BP films X-ray diffraction (XRD) analysis was employed. Furthermore, the Vickers microhardness of these films was measured using an Instron identor, while the type of majority carriers were determined using conductivity measurements.

3.3 Results and Discussions

3.3.1 Growth Rate

A study of growth rate as a function of temperature, pressure, total gas flowrate, and III/V ratio was conducted using Si(100) and Si(111) substrates. Standard deposition parameters were T=1000 °C, P=760 Torr, F_{BCl3}=1 sccm, F_{PCl3}=1 sccm, and time of deposition=30 min. BP films on Si(100) and Si(111) substrates were grown simultaneously as were growths on maacle and off-cut diamond substrates. BP films on β-SiC, sapphire, and other substrates were grown separately from each other. The activation energy for the deposition of BP was calculated and the deposition reaction was determined to be kinetically controlled. Growth rates were measured using FTIR by taking the difference between the interference peaks of a given sample. This approach is valid for wavenumbers between those of the phonon peak of interest and the band gap of the material. The equation:

$$T = \frac{1}{2*\Delta v*(n^2 - \sin^2 \Theta)^{0.5}} \qquad \text{Equation 3.1}$$

was used to estimate film thickness where Δv is the difference between interference peaks, n is the complex index of refraction ($n=n_o+ik$ where k is assumed to equal 0), and Θ is the angle of incidence.

Growth Rate vs. Temperature

As evident from Figure 3.1, the growth rate of boron phosphide on silicon decreases with a corresponding decrease in temperature for all temperatures below 1100 °C. At the highest deposition temperature (1200 °C), however, there is a dramatic decrease in the thickness of the BP film. This phenomenon is attributed to the decomposition of much of the deposited BP into $B_{13}P_2$ and was confirmed using X-ray diffraction. The estimated activation energy of BP deposition on Si(100) and Si(111) is 26.5 kJ/mol and 53.2 kJ/mol, respectively, indicating a heterogeneous reaction limited growth process.

Growth Rate vs. Total Flow Rate

Figure 3.2 depicts the growth rate of BP as a function of the total gas flow rate into the reactor. A constant deposition temperature of 1000 °C, reactor pressure of 1 atmosphere, and III/V ratio of 0.5 was used. There is no significant change in the growth rate of BP as the total flow rate increases. Also, the orientation of the substrate does not appear to affect the growth rate versus total flow rate lines. Given the linear increase in the growth rate versus 1/T, the effect of substrate orientation on the growth rate, and the lack of dependence of the growth rate on the total flow rate, it is evident that the growth of boron phosphide is kinetically controlled within the operating regime examined.

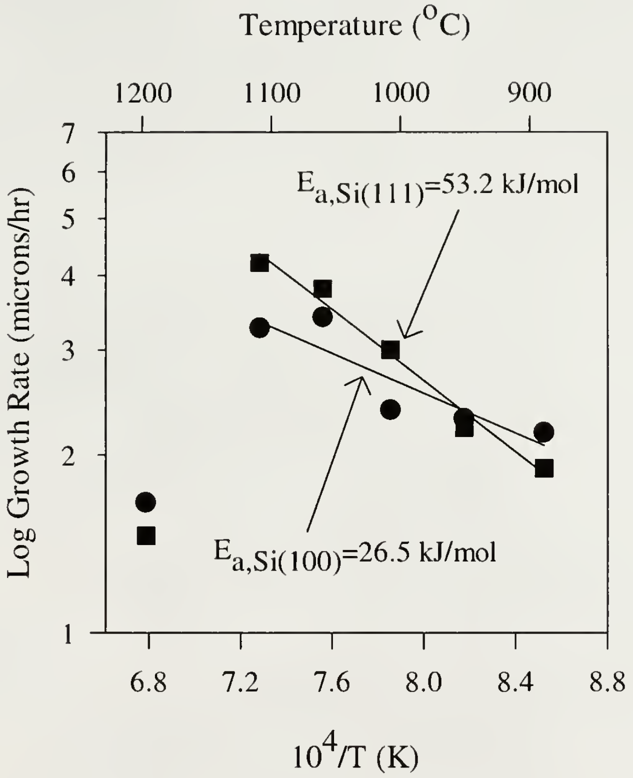

Figure 3.1 Arrhenius plot of the growth rate of BP on single crystal silicon

Growth Rate vs. III/V Ratio

As expected, there is no impact of silicon substrate orientation when the growth rate of BP is plotted against the III/V (BCl_3/PCl_3) ratio as shown in Figure 3.3. It was observed that the growth rate increases as the III/V ratio increases with an average slope of 1.3. There also exists a high degree of linear correlation of the data points for both substrate orientations.

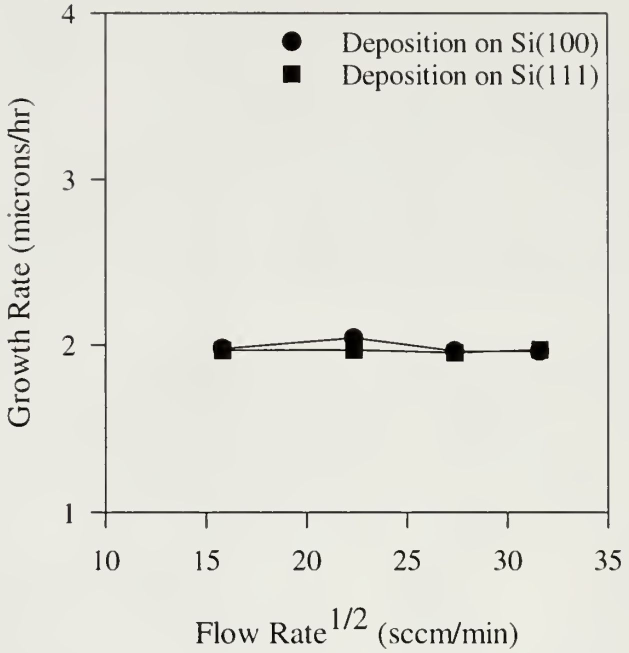

Figure 3.2 Effect of the total gas flow rate on the growth rate of BP on single crystal silicon

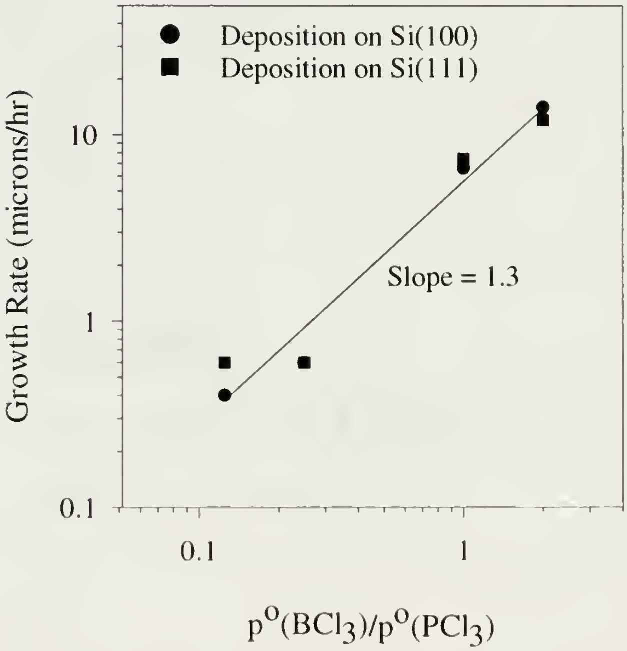

Figure 3.3 Effect of the input III/V molar ratio on the growth rate of BP on single crystal silicon

3.3.2 Microhardness

A series of microhardness tests was conducted on several Si(100) and Si(111) substrates with the results summarized in Table 3.1. The average Vickers hardness was 19 GPa for the thin BP film grown on the Si(100) substrate. Using a 0.2kg load, a slightly higher Vickers hardness of 24 GPa was observed for the BP thin film grown on the Si(111) substrate. The harder BP film on the Si(111) substrate was not unexpected given the close packed nature of the (111) plane. Both values, however, are considerably lower than previously published BP hardness values, which are around 34.3 GPa [4]. This difference is attributed to the fact that only a thin film of BP was grown on the silicon substrates. For comparison, silicon's microhardness is reported to be approximately 12.2 GPa [4]. Thus, it is believed that the indentor pierced through the BP film layer. As a result, the hardness of both the BP film layer and the silicon substrate were being measured.

Table 3.1 Microhardness of BP on Si(100) and Si(111)

Si(100)	Hardness (GPa)
	24.8
	20.1
	19.6
	18.6
	25.0
	16.0
	23.2
	15.9
	15.1
	19.4
	14.6
	Average = 19.3

Si(111)	Hardness (GPa)
	23.5
	24.8
	23.9
	26.5
	23.1
	22.3
	27.1
	25.0
	19.8
	20.9
	Average = 23.7

3.3.3 Conductivity

Both n and p-type conductivities were measured for several samples grown on silicon. The conductivity did not vary with respect to temperature, although for a given temperature there were variations between the two different orientations of silicon substrates. N-type films were deposited using III/V (BCl_3/PCl_3) ratios of 0.25, 1, 2, and 4. P-type films resulted from III/V ratios of 0.5 and 0.125. Thus, a general trend in film conductivity versus III/V ratio could be observed with a possible outlying data point at a III/V ratio of 0.25.

3.3.4 Surface Morphology

Scanning electron microscopy (SEM) was performed to note surface features and growth characteristics of each sample. Figure 3.4 illustrates the variation of surface morphology with growth temperature for BP films grown on silicon substrates. Three different films were grown at deposition temperatures of 950, 1000, and 1050 °C. A similar trend is found as the time of deposition is increased from approximately 15 to 45 min to 1 h of growth. Figure 3.4a depicts the beginnings of coalescence for BP on a Si(111) substrate at 950 °C. Incomplete substrate wetting is observed with a significant fraction of the islands beginning to coalesce. Figure 3.4b is a micrograph of a BP thin film deposited on Si(111) at 1000 °C. It shows a much more uniform film coating with only isolated regions of substrate visible. Figure 3.4c, reveals that at 1050 °C the BP film has complete surface coverage with an apparent high uniformity. Thus an increase in substrate coverage due to island coalescence is seen both as the deposition temperature and the time of deposition is

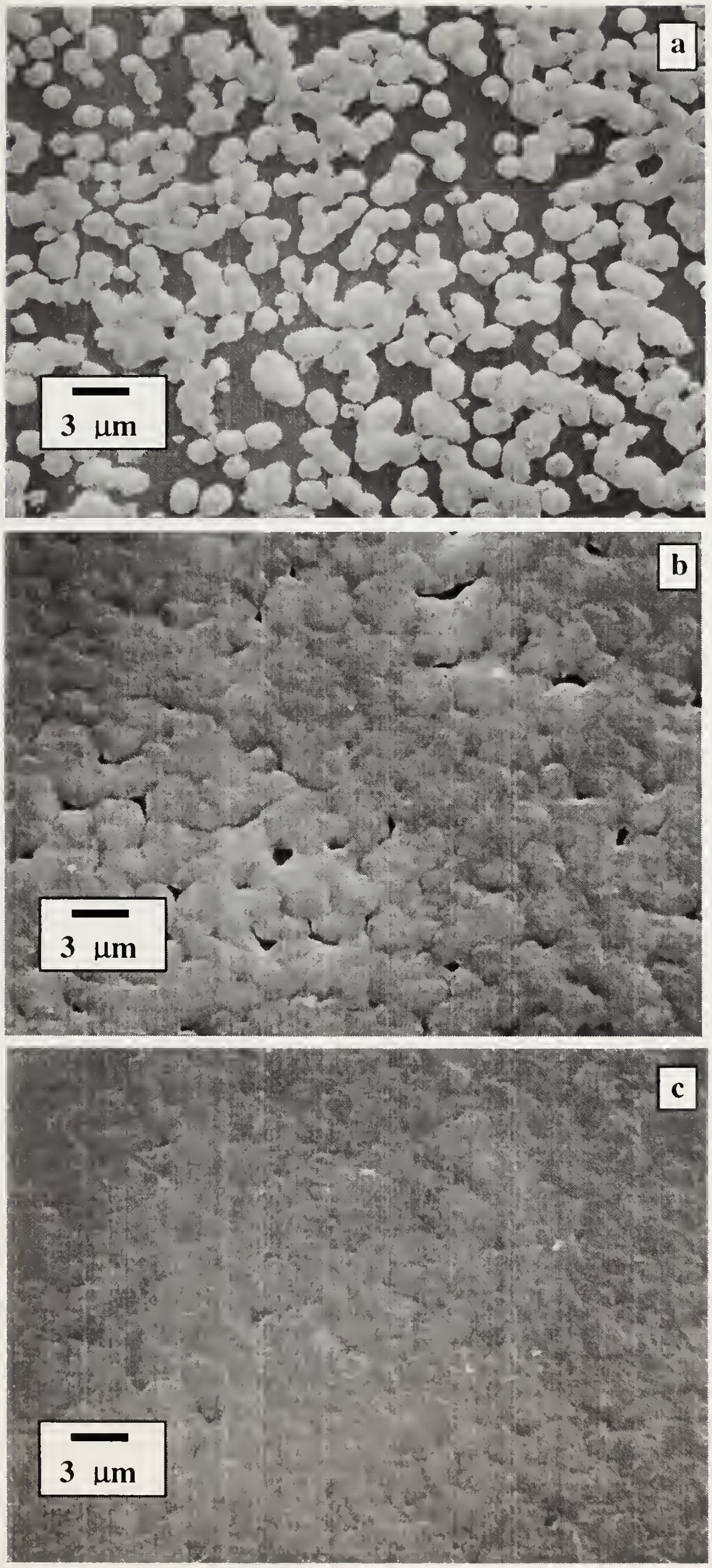
a
3 μm
b
3 μm
c
3 μm

Figure 3.4 Surface morphology of BP growth on Si(111) (island coalescence)
a) T_D=950 °C; b) T_D=1000 °C; c) T_D=1050 °C

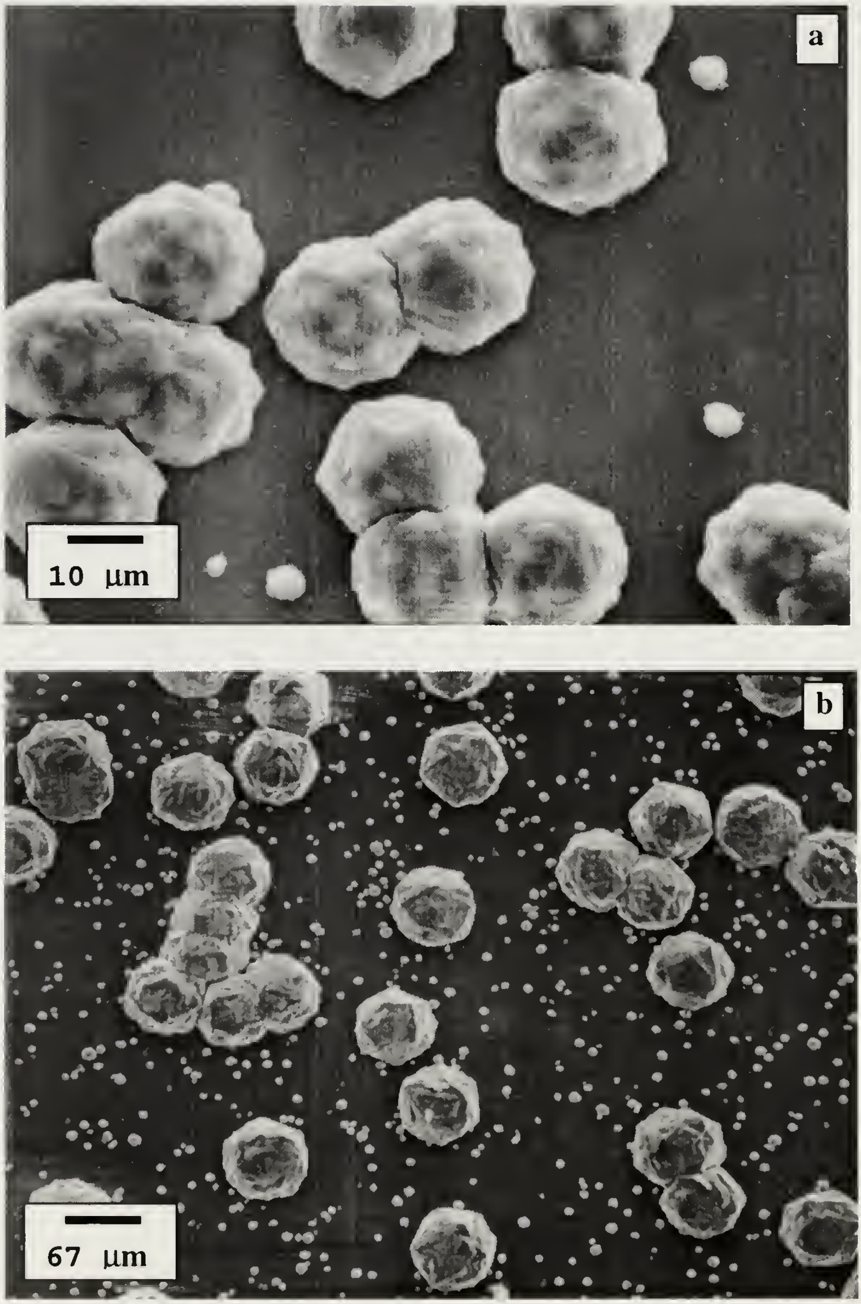
a
10 µm
b
67 µm

Figure 3.5 Surface morphology of BP growth on a) Si(100); b) β-SiC

increased. The island coalescence growth is most probably related to the large lattice mismatch between the BP film and the underlying Si substrate.

Figure 3.5a illustrates the growth of BP in the form of three dimensional ball structures. These ball like structures are similar to those observed by other researchers [58, 74]. Si(100) was the substrate, while the flowrate of PCl_3 was reduced to 1 sccm from the normal 2 sccm used in Figure 3.4 to reduce the amount of BP deposited. Each BP ball-like deposit on Si is approximately 25 μm in diameter. It is unclear whether the smaller particles shown are simply surface contaminants, such as dust, or the beginnings of nucleation sites. It was observed that the Si(111) substrate was more conducive to BP film growth at growth temperatures greater than 950 °C. This is illustrated in Figure 3.1. Due to the lower film growth rate, deposition on Si(100) substrates resulted in smoother films. Figure 3.5b shows similar ball-like BP deposits on β-SiC. The average diameter of these structures, however, is over 60 μm. Deposition conditions were similar to those of Figure 3.5a. A noticeable decrease in the growth rate of BP is observed on the β-SiC substrate, even at the lower magnification of Figure 3.5b. As before, the BP balls coalesce in a manner similar to those on silicon substrates but at a slower rate.

Figure 3.6 depicts the growth of BP on a sapphire (0001) substrate. Figure 3.6 shows slightly elongated BP balls with a substrate coverage of roughly 25%. If the time and temperature of deposition is increased, the BP balls again coalesce to form a uniform film. Figure 3.6b shows the beginnings of a uniform film formation on sapphire (1000) at a longer time and higher temperature of deposition.

BP film growths on diamond exhibited a similar BP ball-like microstructure for short deposition times (Figure 3.7a). Figure 3.7a indicates that the BP film tended to grow

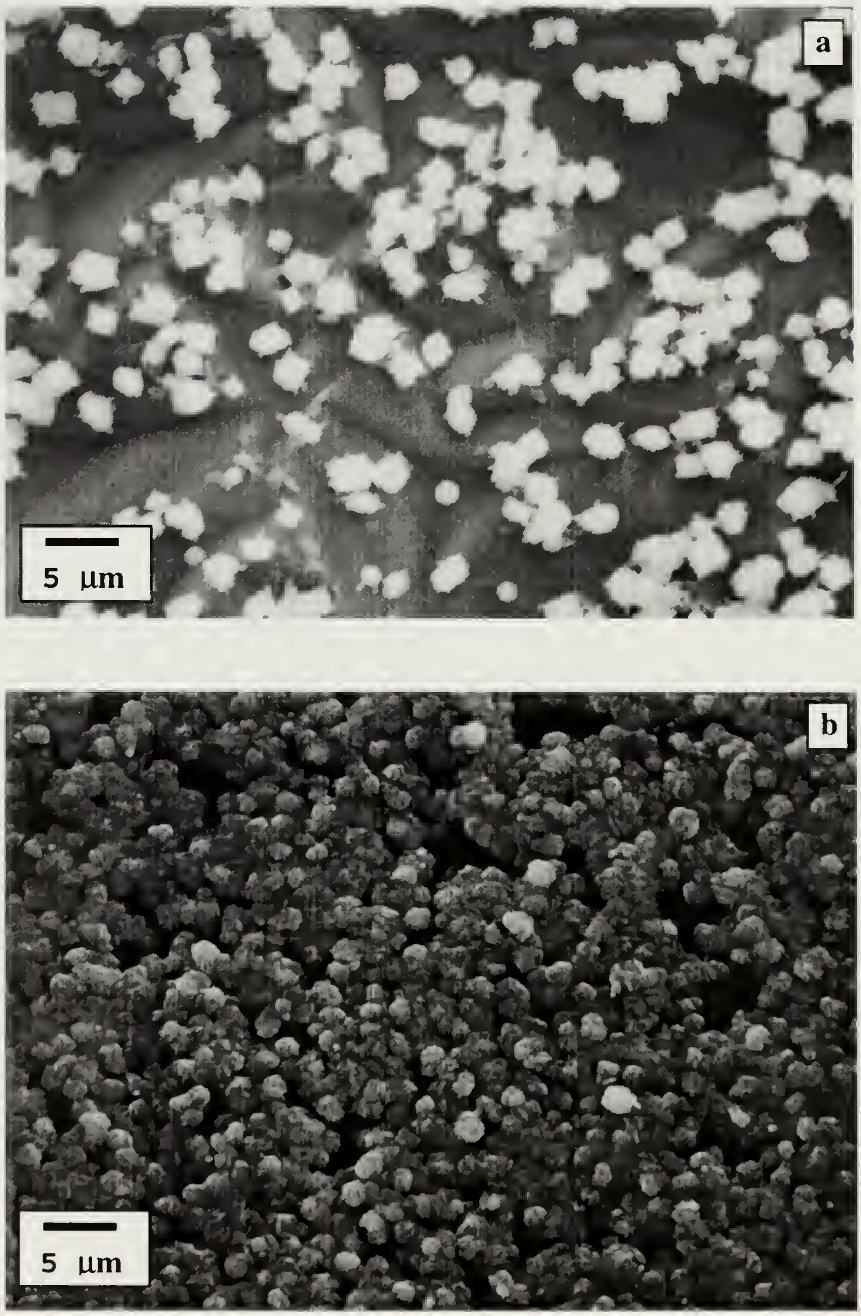

Figure 3.6 Surface morphology of BP growth on Al_2O_3 (0001)

a) T_D= 1000 °C for 30 minutes

b) T_D= 1000 °C for 30 minutes, T_D= 1132 °C for 1 h

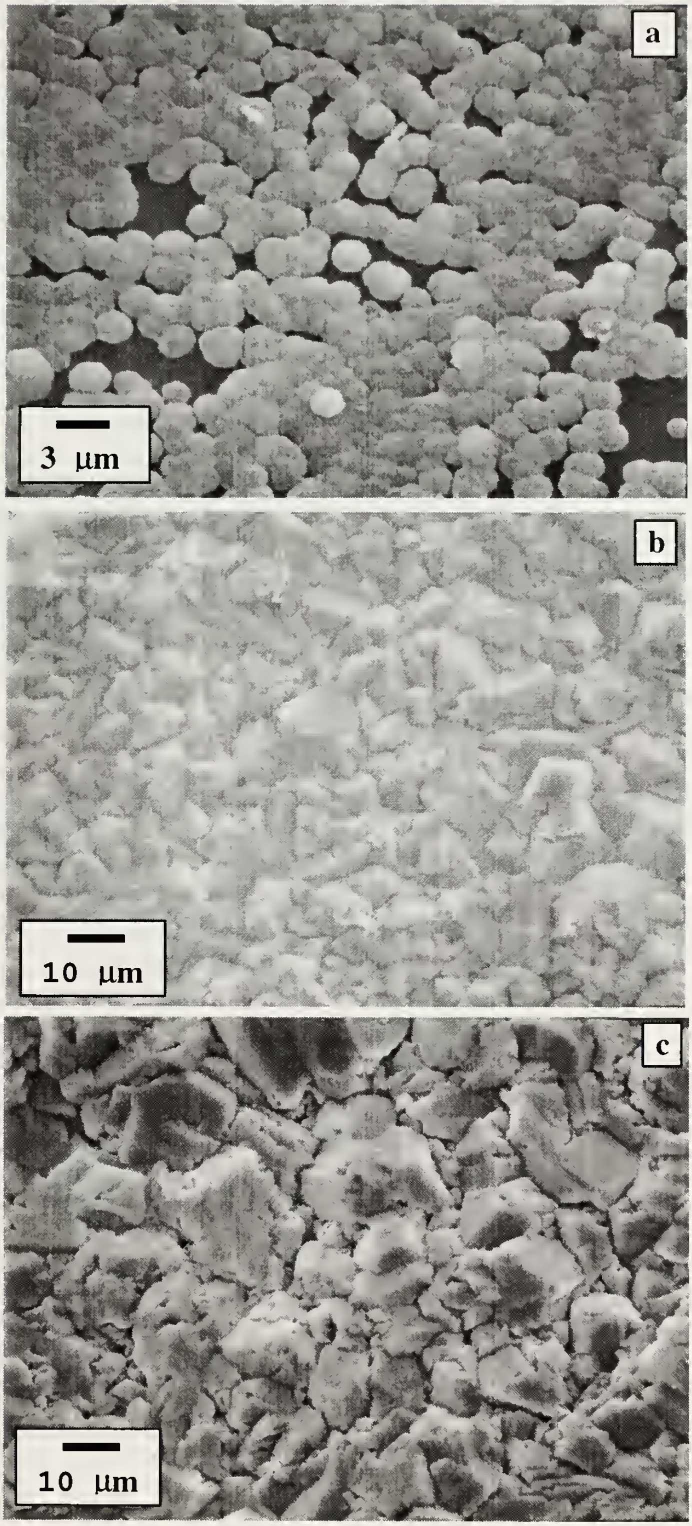
a
3 µm
b
10 µm
c
10 µm

Figure 3.7 Surface morphology of BP growth on diamond

a) maacle – T_D= 1132 °C for 30 min
b) maacle – T_D= 1050 °C for 1 h
c) off-cut – T_D= 1050 °C for 1 h

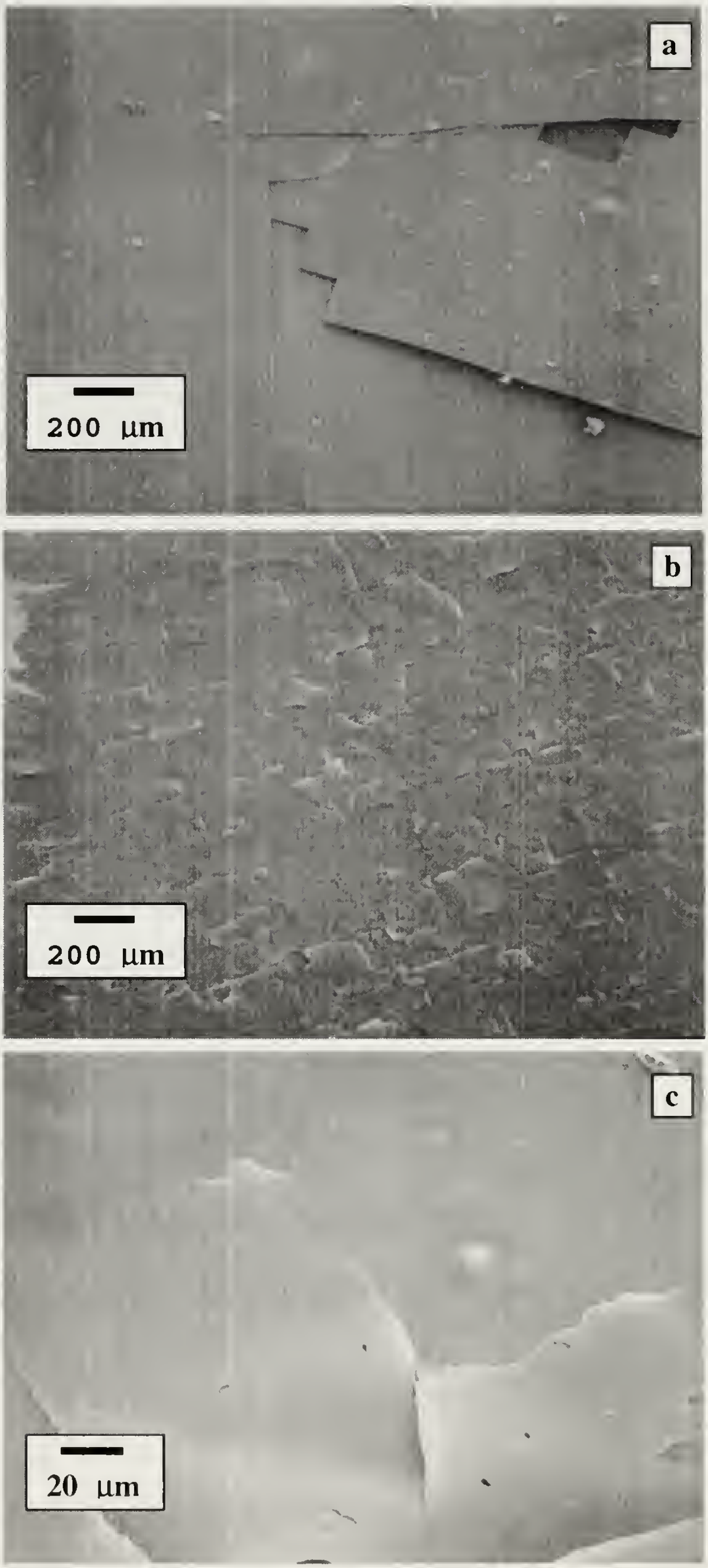
a
200 μm
b
200 μm
c
20 μm

Figure 3.8 Surface morphology of BP film cracking on Si(100)

in a uniform single layer initially. Complete substrate coverage was achieved with longer deposition times. As the time of deposition was increased, however, the film became very polycrystalline, as shown in Figures 3.7b and 3.7c, for the maacle and offcut diamond substrates, respectively.

As mentioned before, the large lattice mismatch between BP and Si (-16.4%) results in large film stresses. Furthermore, the thermal expansion coefficient of each is quite different (4.03 and 3.20×10^{-6} K^{-1} at 300K and 6.12 and 4.05×10^{-6} K^{-1} at 800 K for BP and Si, respectively [4]). The combination of these two effects produced film cracking in several samples as shown in Figure 3.8. If a thick BP film was deposited, film cracking usually resulted. A cross-section visual inspection of the substrate revealed an inward bowing due to the compressive stresses exerted on the Si substrate by the harder, smaller latticed BP film.

Atomic force microscopy (AFM) has been performed on a few BP samples, which yield results similar to SEM. A fairly smooth coating is observed for samples where the deposition time exceeded 1 hour (Figure 3.9). The large object at the top edge of the AFM micrograph is believed to be dust contamination.

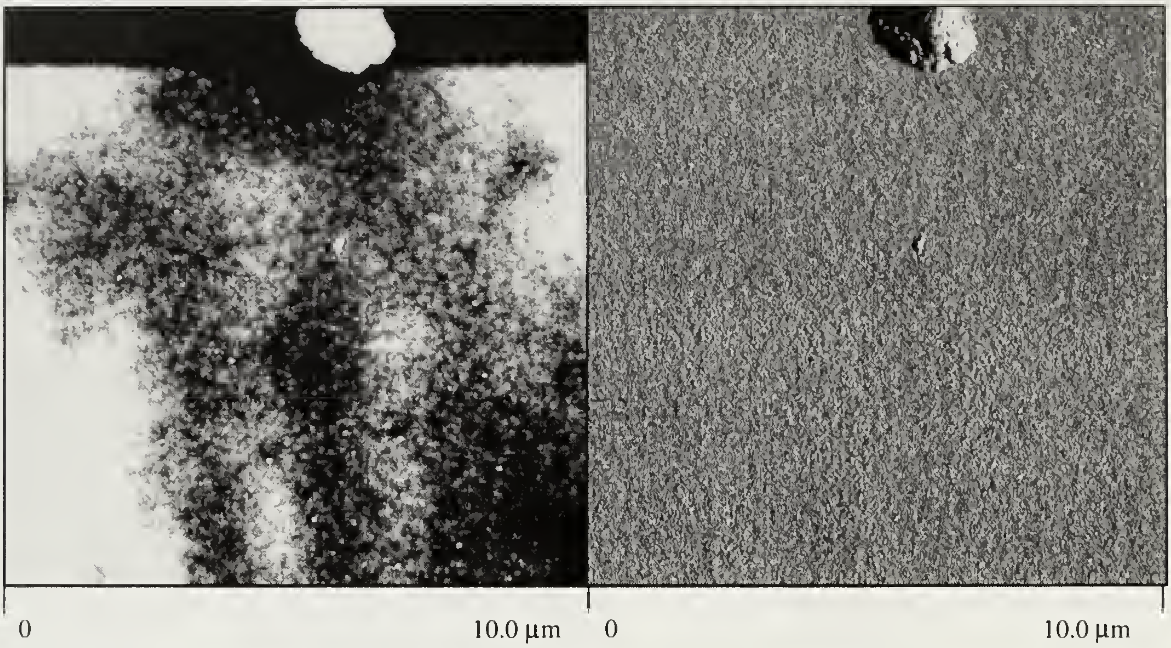

Data type - Height
Z range - 20.0 nm

Data type - Amplitude
Z range - 28.1 nm

Figure 3.9 AFM micrograph of BP growth on Si(100)

3.3.5 X-ray Diffraction

Diffraction spectra of BP films on Si(100) at 30 min growth time are shown in Figure 3.10. The standard powder diffraction pattern is shown in Figure 3.10c for reference. It is evident that deposition on a Si(100) substrate yields a polycrystalline film as indicated by both the (200) and (311) reflections of Figure 3.10a. The large Si(100) reflection relative to either BP reflection indicates that either a very thin BP film was deposited or that the film's substrate coverage is incomplete. In Figure 3.10b, deposition on Si(111) appears to be greater given the higher intensity of the BP(111) reflection relative to the Si(111) reflection. This is also supported by the data shown in Figure 3.1, which depicts a higher growth rate on Si(111) than Si(100) at a temperature > 1000 °C. There is also a lack of reflections in directions other than the plane of the substrate, indicating that single crystal growth is occurring.

As the deposition time is increased to 2 h at the same growth conditions, a more varied diffraction pattern is generated with widespread polycrystalline growth observed on both substrate orientations. Highly preferentially oriented BP growth is observed on the Si(100) substrate with the BP(200) reflection intensity much greater than any of the other BP reflections shown. Thus, as the growth process proceeds from Figure 3.10a to 3.11a, growth is dominant in the substrate plane and not the (311) plane. Deposition on Si(111) substrates yields a much more polycrystalline film with nearly equal reflection intensities for BP(111) and BP(220). The BP(222) reflection is simply an internal reflection of ½ the lattice spacing of BP(111) and thus is not considered to be a polycrystalline peak. Given the higher growth rates of BP on Si(111) and a large film-substrate lattice mismatch (>16%), the emergence of widespread polycrystalline film growth is expected. The lower growth rate of BP on a Si(100) substrate presumably allows for more lattice mismatch accommodation and surface reconstructions which lead to more epitaxial film growth.

3.3.6 FTIR and Raman Spectroscopy

Fourier transform infrared spectroscopy (FTIR) was used in conjunction with X-ray diffraction and Raman spectroscopy to confirm the presence of BP in each of the films and, as described in section 3.3.1, to measure film thickness. Figure 3.12a is an example of a typical FTIR for a BP film on Si(100). It has been reported in the literature that boron phosphide exhibits two distinct phonon peaks: a main longitudinal optical phonon peak (ν_{lo})

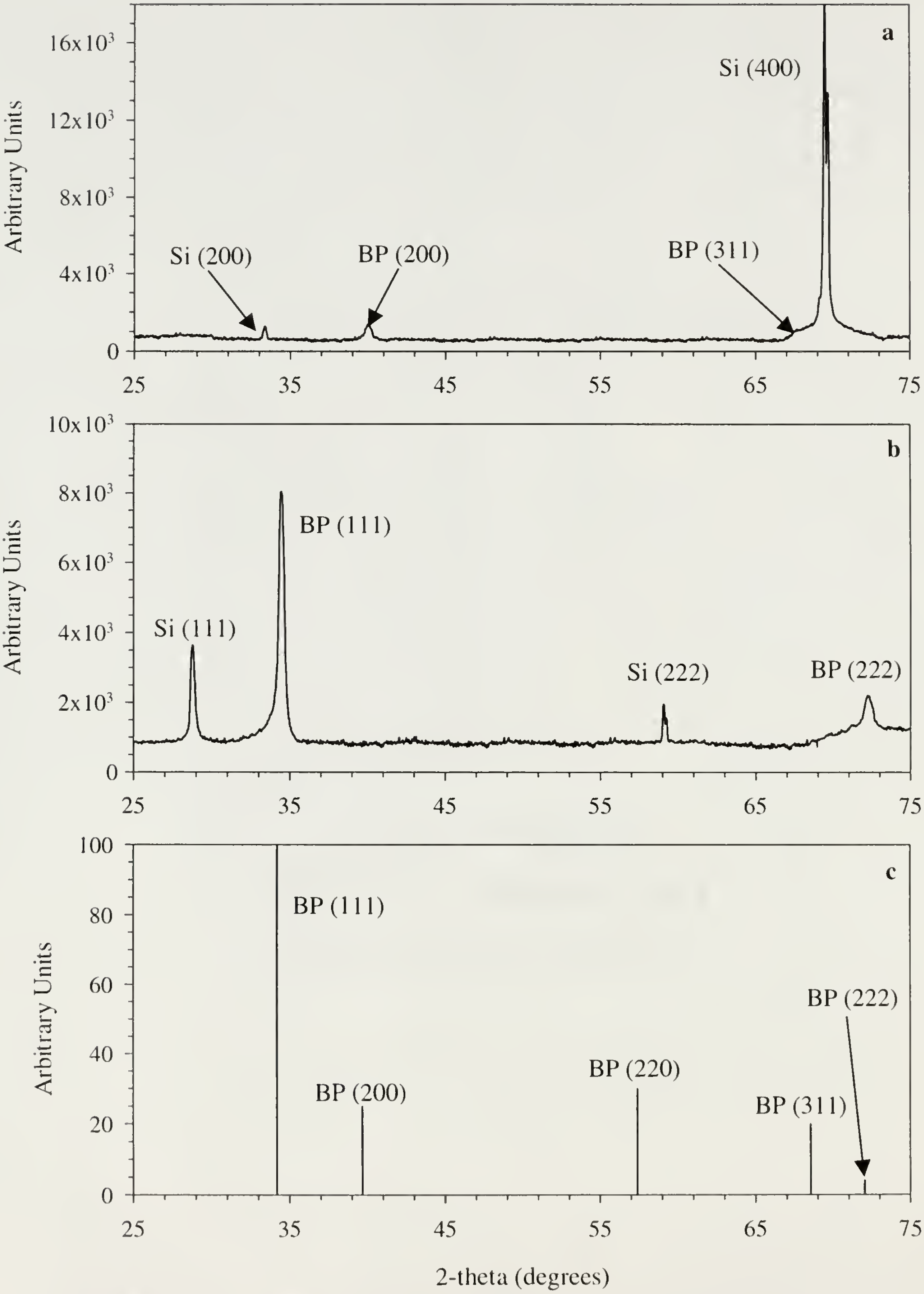

Figure 3.10 XRD patterns of BP deposited on a) Si(100) and b) Si(111) for 30 min c) standard powder pattern

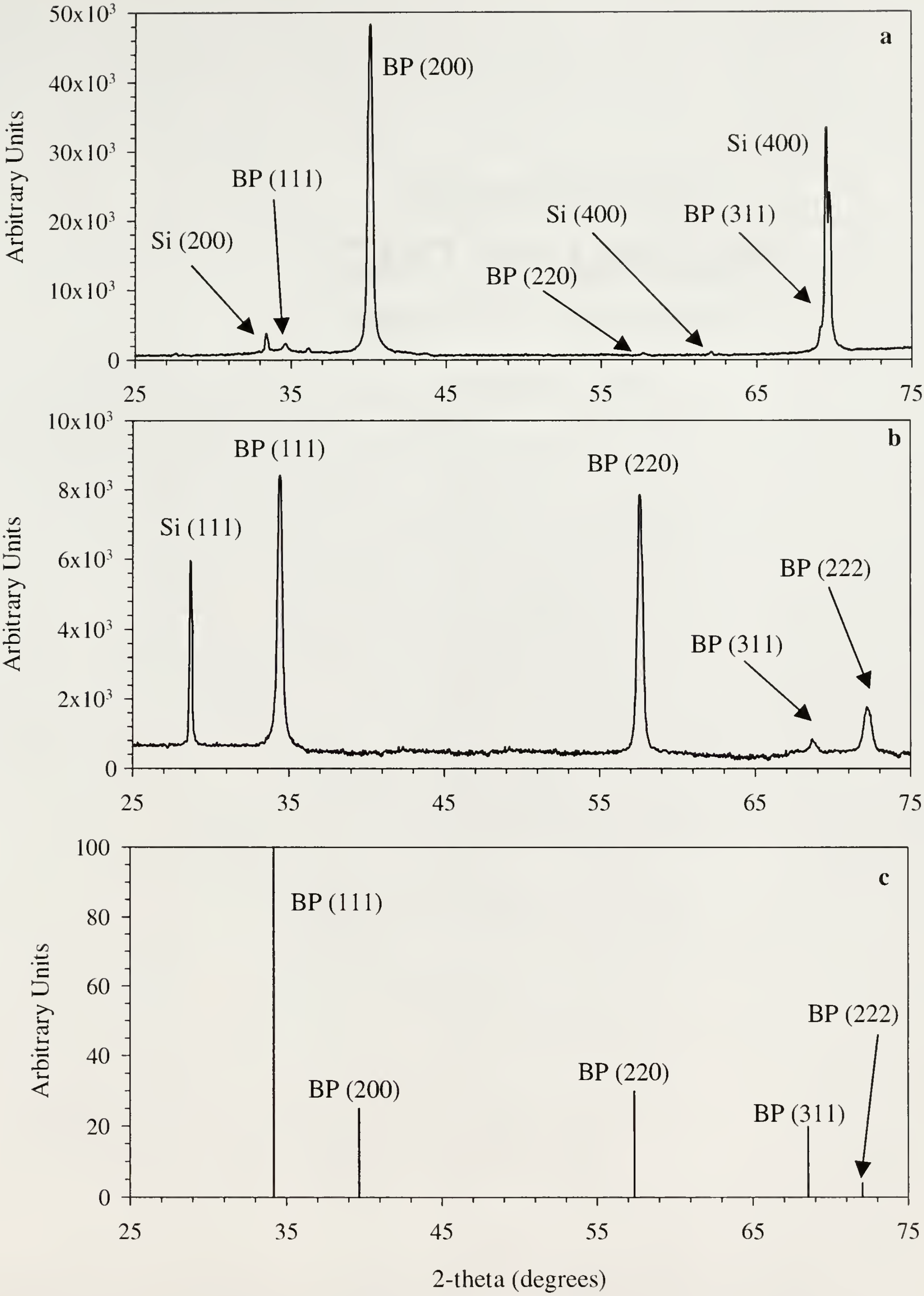

Figure 3.11 XRD patterns of BP deposited on a) Si(100) and b) Si(111) for 2 h c) standard powder pattern

centered at 828.9 cm^{-1} and a smaller transverse optical phonon peak (ν_{to}) located at 799 cm^{-1} [153]. These values coincide with the phonon peaks shown in Figure 3.12a, thus confirming the presence of a BP film. Similar FTIR results of BP film growth on Si(111) are shown in Figure 3.12b. FTIR results for growth on a nickel substrate also exhibited a major peak at 828 cm^{-1}, confirming the presence of a BP film. FTIR was not performed on the sapphire substrate growths due to poor film adhesion and the formation of ribbon-like film flakes after the substrates were removed from the reactor. Thus, the sapphire substrates could not be inverted in the FTIR unit. FTIR analysis of all growths on diamond substrates was inconclusive, possibly due to the very small substrate size and substrate curvature.

Raman spectroscopy was also used to confirm the presence of a BP film on both Si(100) and Si(111) substrates. Figure 3.13a was generated from Raman analysis of a BP film on Si(100). Again, the major peak (ν_{lo}) is located at 826 cm^{-1} while a smaller peak(ν_{to}) is located at 797 cm^{-1}. Likewise, the BP ν_{lo} peak is centered at 824 cm^{-1} for growth on the Si(111) substrate with the ν_{to} peak at 797 cm^{-1}. A boron phosphide film was identified on sapphire substrates using Raman spectroscopy. A narrower ν_{lo} peak than those for silicon substrates was detected at 827 cm^{-1} with the ν_{lo} peak centered at 798 cm^{-1}. Raman analysis of BP growth on both the maacle and offcut diamond substrates yielded phonon peaks at 828 and 799 cm^{-1}, as shown in Figure 3.13b. Raman spectroscopy was possible on diamond substrates, while FTIR spectroscopy was not for two reasons. First, as mentioned above, the samples must be inverted in FTIR. The small substrates used would have fallen through the sample analysis opening of the unit, even if the smallest mask were used. The second reason is that Raman spectroscopy analysis can be focused to a more localized area, thus

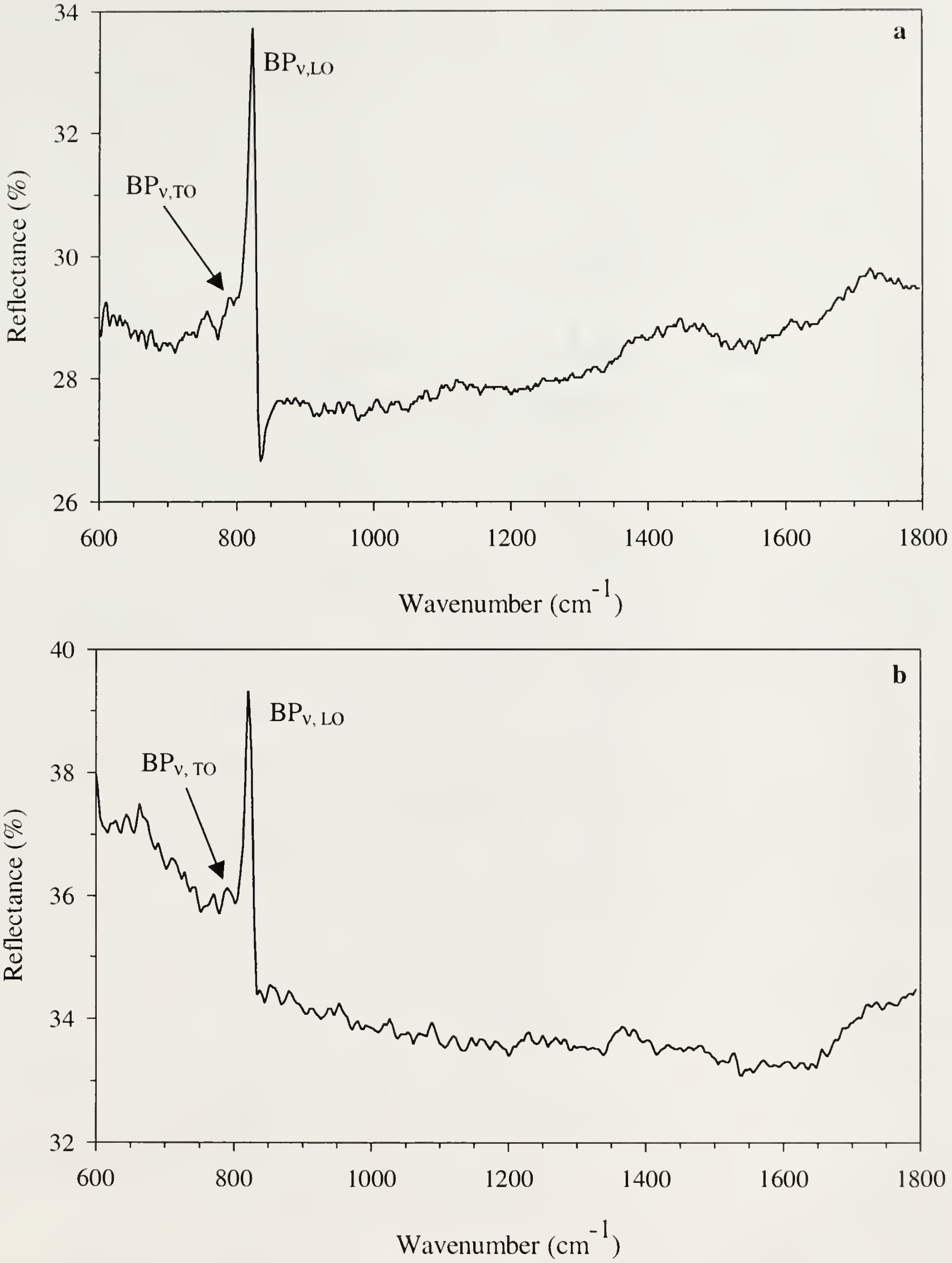

Figure 3.12 FTIR spectra of BP deposited on a) Si(100) and b) Si(111)

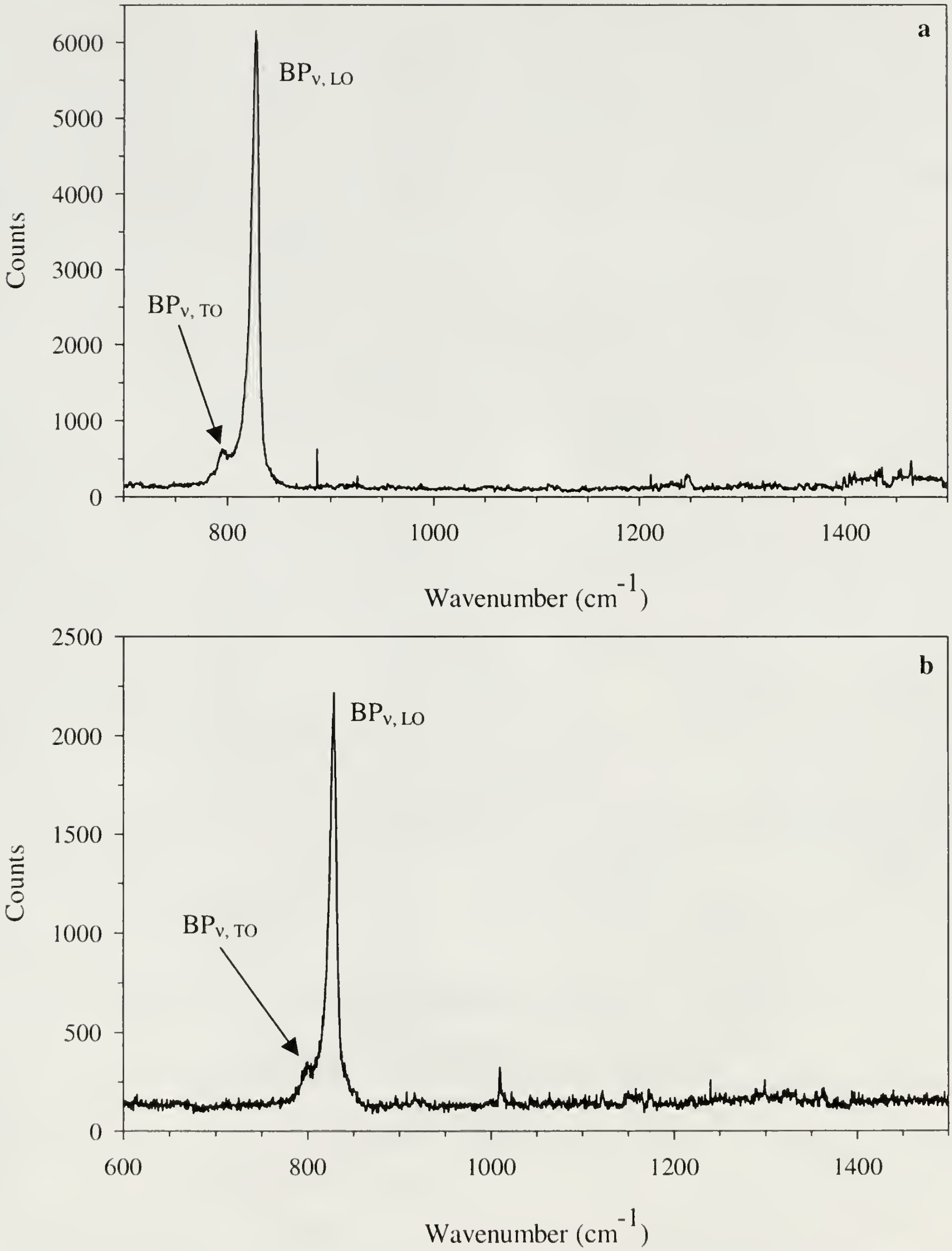

Figure 3.13 Raman spectra of BP deposited on a) Si(100) and b) diamond (maacle)

permitting analysis of much smaller samples than FTIR. BP film growths on β-SiC were not analyzed by either FTIR or Raman because of the interference of the BP ν_{lo} phonon peak with that of the β-SiC substrate.

3.3.7 AES and TEM

Auger electron spectroscopy (AES) was also used to confirm the presence of a boron monophosphide film on a limited number of samples. The excitation energy of boron and phosphorus (B-KVV and N-KVV) are 179 and 120 eV, respectively [503]. As seen in Figure 3.14, significant peaks occur at both 120 and 179 eV, thus confirming the presence of boron phosphide on the silicon substrate. After sputtering for 30 sec (which would remove approximately 30 Å of material), only a slight carbon and oxygen contamination of the film is evident. Quantification of the spectra was performed using sensitivity factors for each element and the relative peak to peak heights detected. Figure 3.15 exhibits even less contamination in the bulk film, with no carbon and only 2% oxygen contamination. Thus, the error associated with the elemental compositions is roughly ± 5 to 7 percent. Regardless, the level of contamination is low and, in the case of carbon in Figure 3.15, below the detectable limit of the unit.

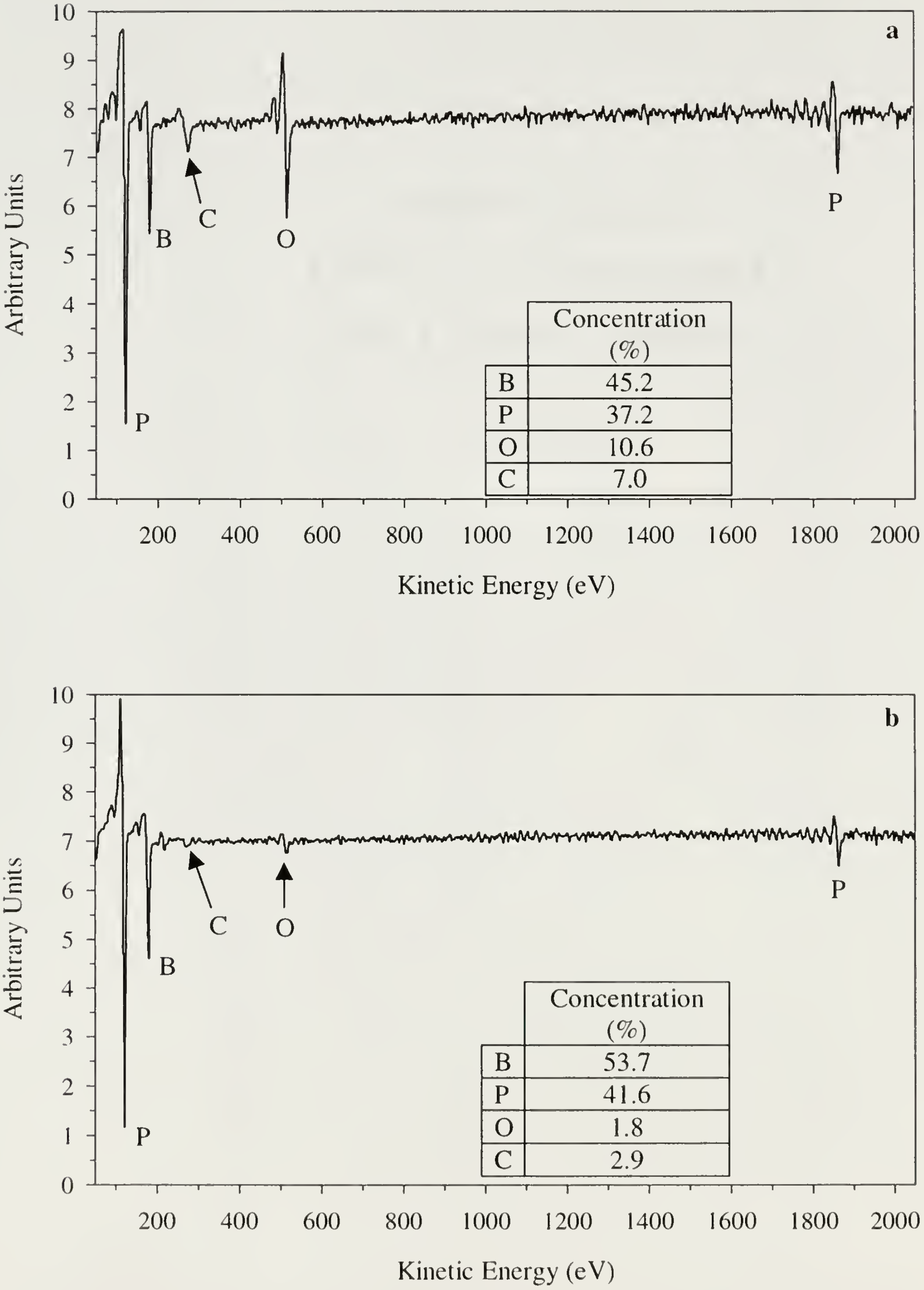

	Concentration (%)
B	45.2
P	37.2
O	10.6
C	7.0

	Concentration (%)
B	53.7
P	41.6
O	1.8
C	2.9

Figure 3.14 AES spectra of BP deposited on Si(100)
a) As received; b) 0.5 minute 3 keV Ar^+ sputter

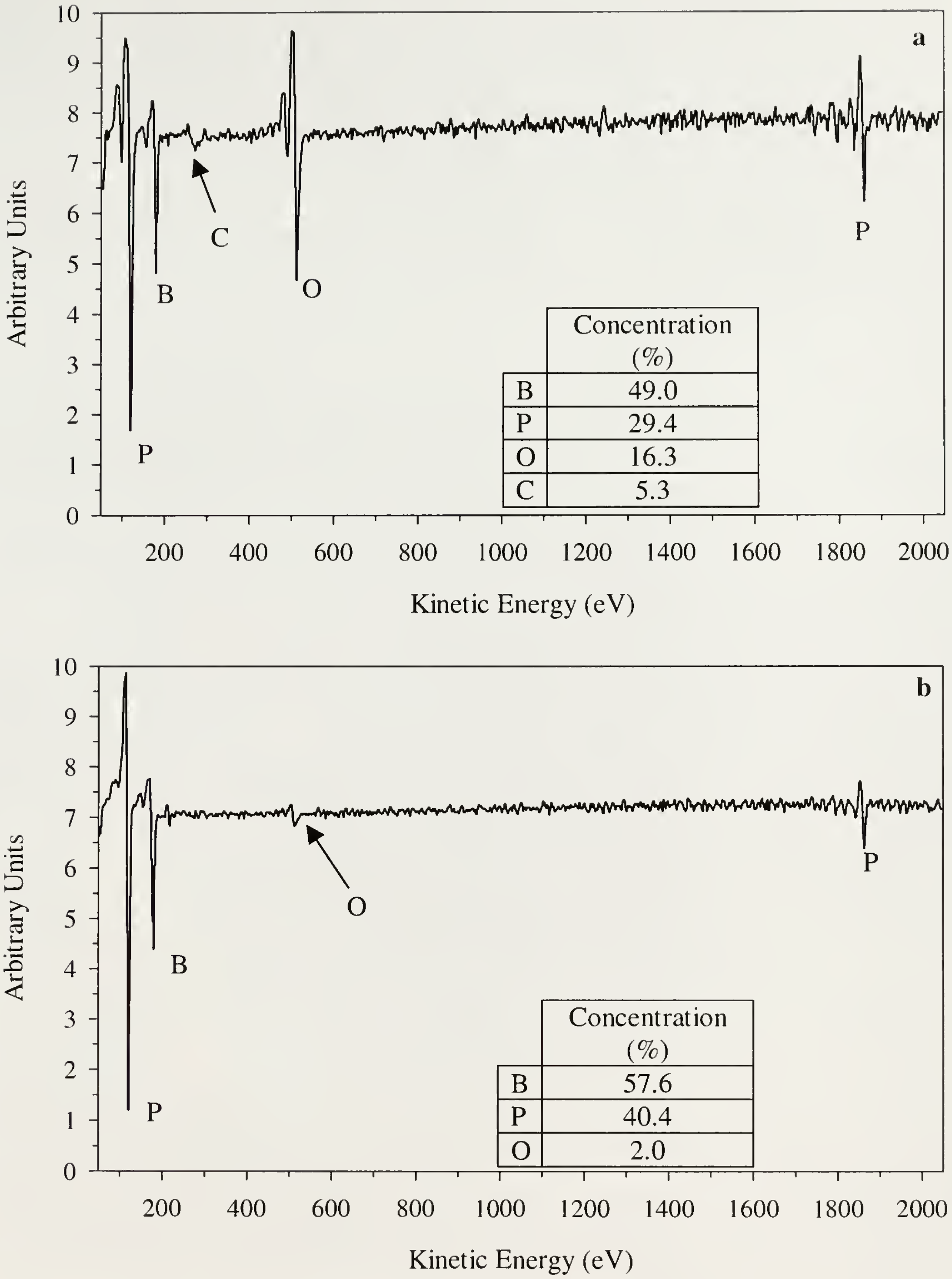

	Concentration (%)
B	49.0
P	29.4
O	16.3
C	5.3

	Concentration (%)
B	57.6
P	40.4
O	2.0

Figure 3.15 AES spectra of BP deposited on Si(100)
a) As received; b) 0.5 minute 3 keV Ar$^+$ sputter

Transmission electron microscopy (TEM) was also performed on one sample to observe features such as the Si/BP interface and approximate thickness of the BP film deposited under normal operating conditions. Figure 3.16 illustrates both clearly. Three sequentially deposited material layers can be seen: the silicon substrate, the deposited epitaxial BP, and a thin gold film that was sputtered onto the sample to reduce charging during SEM characterization. The Si/BP and BP/Au interfaces are rough, with roughnesses of approximately 100 Å each. In many runs, PCl_3 was introduced into the reactor during the preheating phase. This may have caused the formation of HCl and subsequent etching of the silicon substrate's surface prior to BP deposition. The thickness of the epitaxial BP was measured to be approximately 675Å with a lattice parameter of 4.6Å.

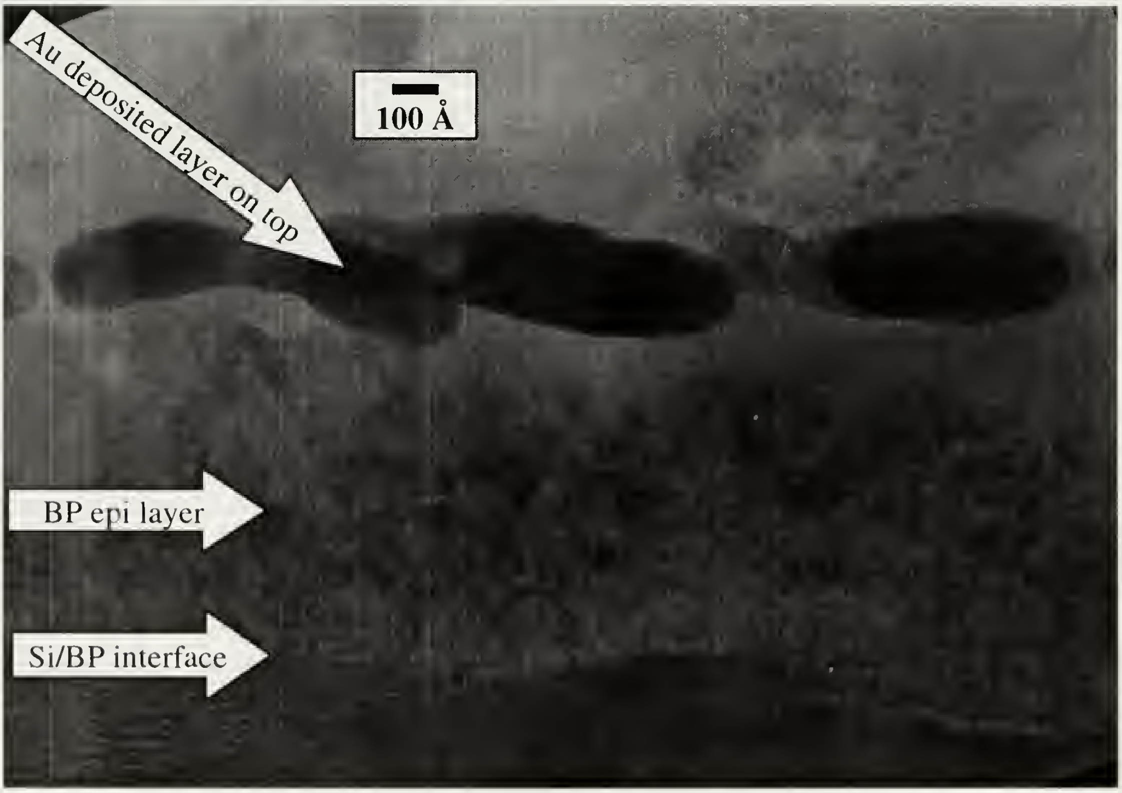

Figure 3.16 TEM micrograph of BN/BP/Si system

3.4 Conclusions

Films of boron monophosphide were grown on Si(100) and Si(111). The films are polycrystalline, but exhibit a strongly preferred orientation relative to the underlying substrate. Films were also grown on sapphire (1000), diamond (maacle and off-cut samples), and β-SiC. Adhesion was poor on all sapphire substrates, with growth rates and characteristics similar to those of films grown on silicon. Both diamond substrates exhibited strong polycrystalline BP growth, with slower growth rates than those observed on silicon. Growths on β-SiC, as well as sapphire, produced similar BP ball-like microstructures that coalesced to form uniform BP films. Growth was slower on β-SiC due to the increased size of the nucleating BP balls.

BP deposition on Si(100) had an apparent activation energy of 26.5 kJ/mol that was roughly half the 53.2 kJ/mol value for BP deposited on Si(111). The lack of dependence of the growth rate on the total gas flowrate and the differences in the activation energies indicates that deposition is heterogeneous reaction limited. Both n and p-type conductivities were observed for BP films grown on silicon, with the III/V ratio affecting which conductivity is predominant. Finally, the Vickers hardness of the films were on the average 20 GPa. This value is lower than that reported by previous researchers and indicates the possibility that the indentor+0.2kg load penetrated through the film. Thus a BP/Si system was instead analyzed. Regardless, BP films grown on Si(111) had a slightly higher hardness than those grown on Si(100).

X-ray diffraction, FTIR, and Raman spectroscopy were the primary means to confirm BP film growth, crystal structure, and crystallinity. Good agreement with previously published peak values was observed. Film elemental analyses by AES determined that impurity contamination was less than 3% in the bulk of the film. TEM was also used to examine a cross-section of the film/substrate structure. A fairly rough interface (≈ 100 Å) was observed for both the BP/Si and Au/BP interfaces. One likely reason for the interface roughness was the formation of HCl vapors prior to film deposition, which etched portions of the exposed silicon surface. Surface morphology analysis using AFM revealed a smooth film surface in good agreement with SEM micrographs at longer deposition times and higher deposition temperatures.

CHAPTER 4
GROWTH OF BN BY IN-SITU NITRIDATION OF BP FILMS

4.1 Introduction

As noted in section 1.2.2, boron nitride is a III/V indirect energy gap semiconductor whose two primary crystal structures are an sp^3 bonded cubic phase (cBN) and an sp^2 bonded hexagonal one (hBN). These forms parallel similar modifications of carbon, namely diamond and graphite, respectively. Research and commercial interest has focused heavily on the cubic phase for its use primarily in the ultra-hard coatings industry and in high temperature-high power devices. A more detailed review of both cBN and hBN properties, attempted and successful deposition techniques, and characterization of these films is given in section 1.2.2.

In this study boron nitride thin film synthesis was performed by in-situ nitridation of previously grown boron phosphide thin films using NH_3, and by thermal CVD from BCl_3 and NH_3 precursors. BP nitridation conditions and BN thin film deposition on a nitrided template were examined in terms of the BN morphological and structural properties. It was hypothesized that the cubic structure of the BP films would be retained after nitridation and thus a multilayered cBN/cBP/substrate system formed. As noted in section 1.2.2, previous research on cBP nitridation has been limited to six publications with significant uncertainty in identifying the resulting BN phase [56,249-253]. Characterization of the resulting BN films was limited to X-ray diffraction (XRD), with the one exception of inconclusive FTIR spectroscopic analysis reported by Davis et al. [255]. Non-energized BN CVD using a variety of hydride and halide precursors has yielded only hBN. Similar thermal nitridation of cGaP and cAlP films has revealed that nitridation and retention of at least a cubic/hexagonal crystal structure mixture, if not a pure cubic film [504-508].

As discussed in literature review presented in section 2.2.1 and based on the work of this dissertation in section 2.2.2, it has recently been shown that from a strictly thermodynamic viewpoint, the cubic phase of boron nitride should be stable at lower temperature and pressure [256-258]. This is in contradiction to the experimentally observed hBN phase stability at lower temperature and pressure. In thermodynamic calculations at one atmosphere pressure, Solozhenko has calculated that the cubic phase is the most stable BN phase to approximately 1576 K. This was confirmed in section 2.2.2 of this work for the B-N-H-Cl (e.g., BCl_3-PCl_3-H_2) system. Thus, depositing cBN without the use of energized particles is thermodynamically favored and lends credence to the ongoing research into thermal CVD of cubic boron nitride, particularly the nitridation of a cubic template (e.g. boron phosphide).

4.2 Experimental

The growth of BN films was accomplished using a two step process. First, a cubic boron phosphide template film was grown on a variety of substrates including Si(100), Si(111), diamond (maacle and off-cut), Al_2O_3 (0001), β-SiC (100), and nickel. In the second step, the phosphorus in the BP lattice structure was substituted by in-situ nitridation using NH_3.

The CVD of boron phosphide was carried out as described in Chapter 3. In-situ nitridation of the grown cBP films was performed using anhydrous ammonia (99.999% purity, Matheson) diluted in hydrogen. Typical nitridation times were from 30 minutes to 2 hours. The nitridation temperature and pressure were varied from 850 to 1132 ^{o}C and 200 to 760 Torr, respectively. The ammonia flow rates varied from 2 to 10 sccm. cBP nitridation was also attempted using N_2 and Ar as carrier gases. Two other types of in-situ nitridation experiments were conducted. The first involved cyclical cBP growth and nitridation for a total of three cycles, resulting in a BN/cBP/BN/cBP/BN/cBP/substrate material system. The second method involved CVD growth of BN with BCl_3 and NH_3 on a template of previously nitrided cBP.

The nitrided films were characterized with scanning electron microscopy (SEM) and atomic force microscopy (AFM) to determine surface morphology. To differentiate between hexagonal and cubic modifications of BN, the films were also analyzed by X-ray photoelectron spectroscopy (XPS), auger electron spectroscopy (AES), Fourier transform infrared spectroscopy (FTIR), and Raman spectroscopy. In addition, to determine the crystallinity and film quality, the films were analyzed by transmission electron microscopy (TEM). Due to film charging, all SEM samples had to be sputter coated with gold-palladium.

4.3 Results and Discussion

4.3.1. Surface Morphology

SEM analysis of the nitrided samples grown on Si (100) and (111) revealed two different types of surface morphology. For films grown at a temperature above 1050 °C (Figure 4.1a), a fairly smooth, fine grain structure was observed. The continuity of these films was occasionally disrupted by cracks that developed due to lattice mismatch and cooling stresses between the underlying cBP films and Si substrates (Figure 3.8). Upon closer examination, these films appeared to be composed of elongated grains (see Figure 4.1b). At a temperature below 1050 °C, the grain structure changed to a round, equiaxed shape and the degree of substrate coverage appears to decrease (Figure 4.2). This change in grain structure can be attributed to changes in the wettability of Si by cBP as temperature increases. It is important to emphasize that the observed surface morphologies are primarily a reflection of the underlying cBP structure, since the BN films were not expected to be thick and, except for the case of direct BN growth using BCl_3 and NH_3, the overall film thickness was not expected to change. For films grown on β-SiC, diamond, and sapphire, only the round, equiaxed structure was observed even at 1132 °C. This is consistent with the fact that the refractory nature of these substrates prevents as much substrate relaxation as in the case of Si at elevated temperatures.

Atomic force microscopy (AFM) was performed on several samples for which previous spectroscopic analysis had detected the presence of cBN grown on Si(100). A much rougher suface morphology is seen using AFM as compared to that seen using SEM due to the smaller film area analyzed by AFM. Small spherical growth structures are seen

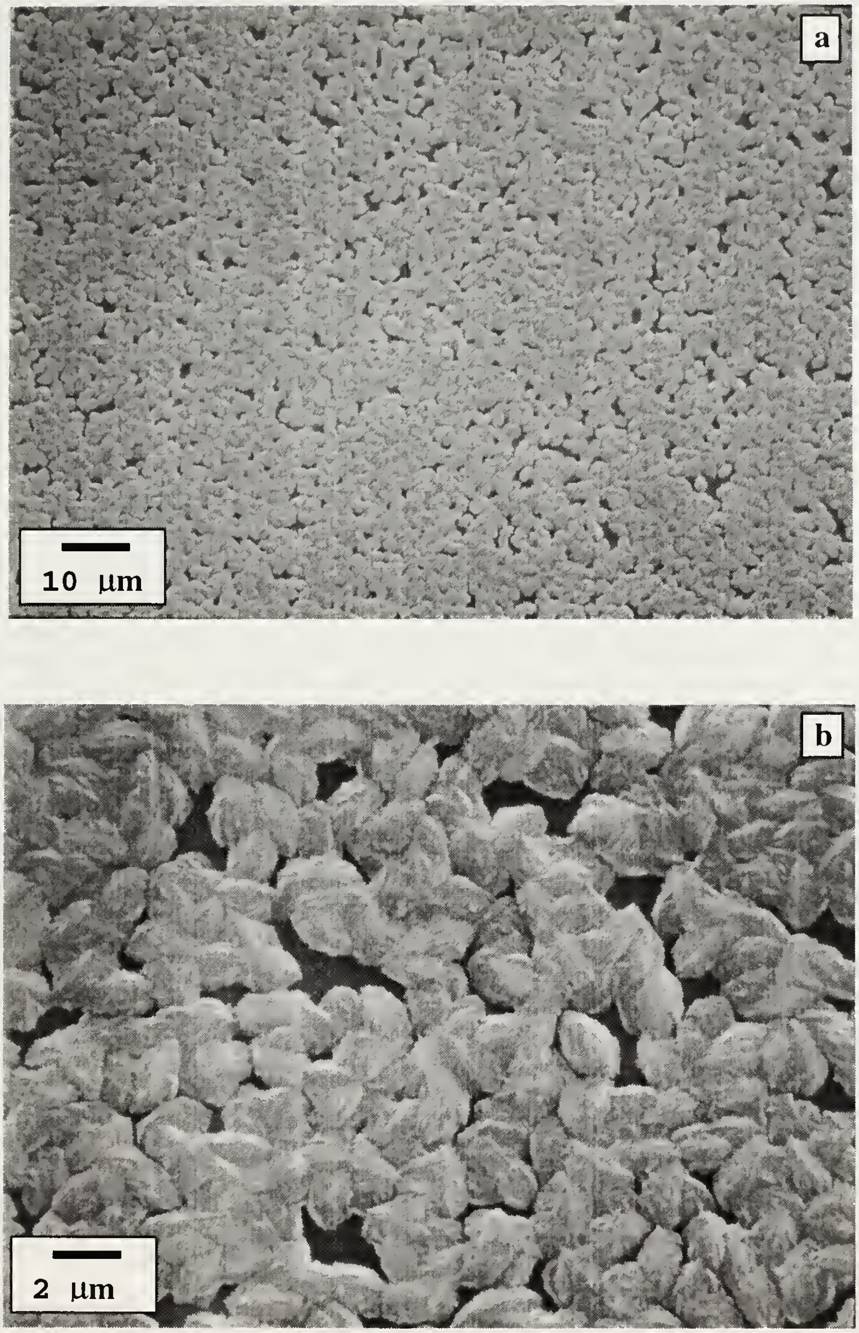

Figure 4.1 Microstructure of BN/BP growth on a) Si (111); b) Si(111) at $T_D=T_N=1075$ °C

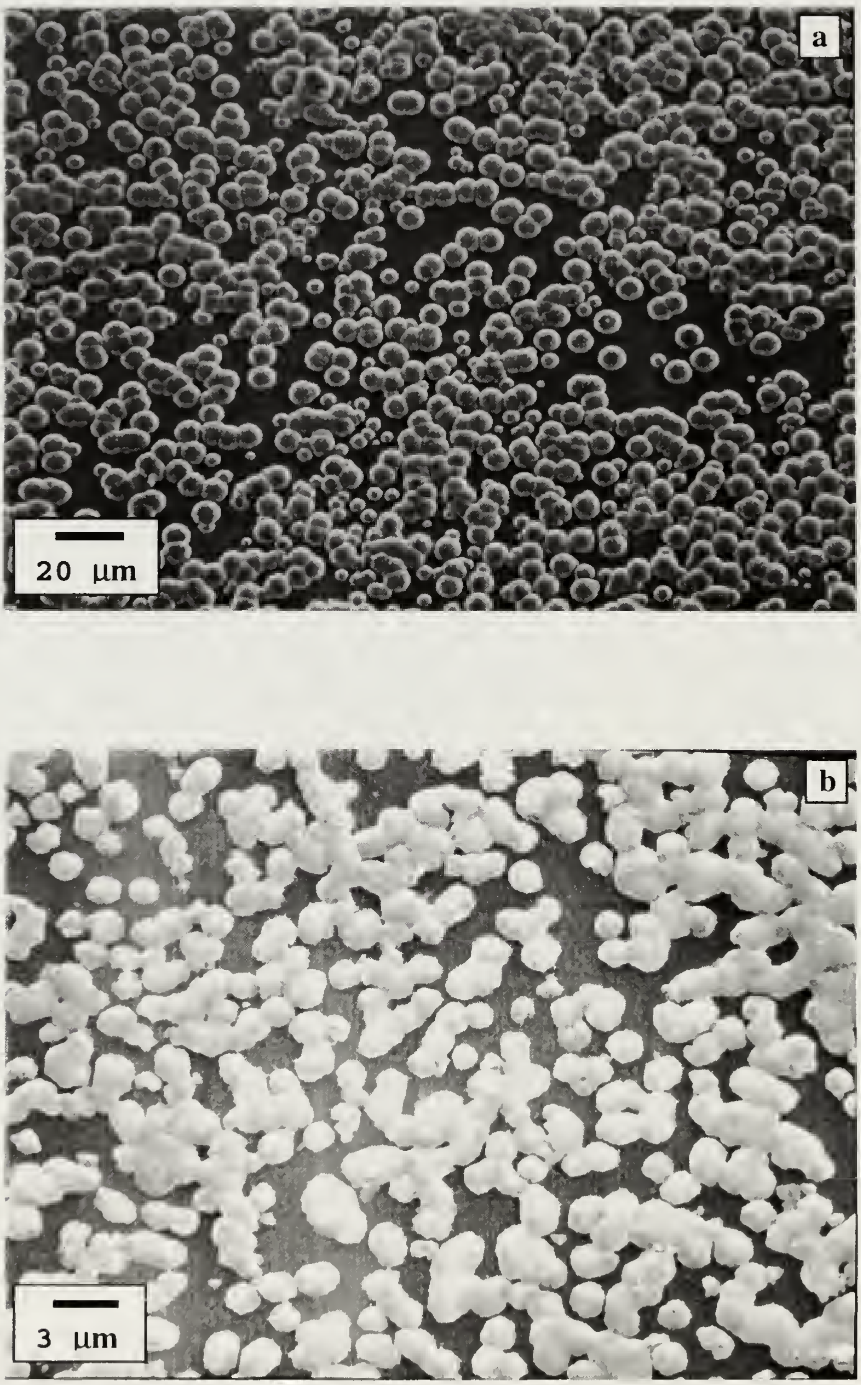

Figure 4.2 Microstructure of BN/BP growth on a) Si (111); b) Si(111) at T_D=T_N=1000 °C

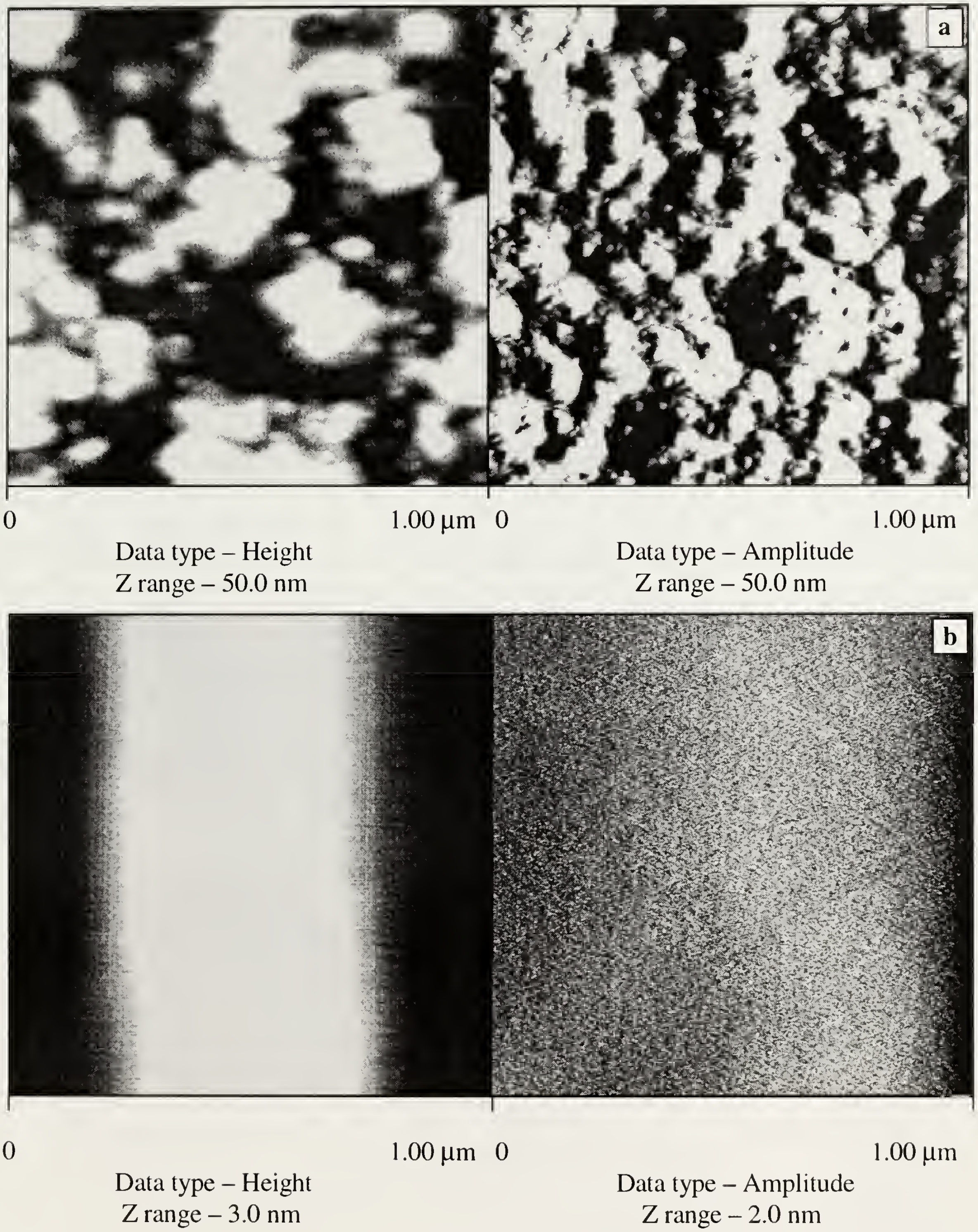
a
0
1.00 µm
0
1.00 µm
Data type – Height
Z range – 50.0 nm
Data type – Amplitude
Z range – 50.0 nm
b
0
1.00 µm
0
1.00 µm
Data type – Height
Z range – 3.0 nm
Data type – Amplitude
Z range – 2.0 nm

Figure 4.3 AFM micrograph of BN/BP on Si (100)

a) $T_{\text{Deposition}} = T_{\text{Nitridation}} = 1000\ ^{\circ}\text{C}$, $P_{\text{Deposition}} = P_{\text{Nitridation}} = 760$ Torr

b) $T_{\text{Deposition}} = T_{\text{Nitridation}} = 1132\ ^{\circ}\text{C}$, $P_{\text{Deposition}} = P_{\text{Nitridation}} = 200$ Torr

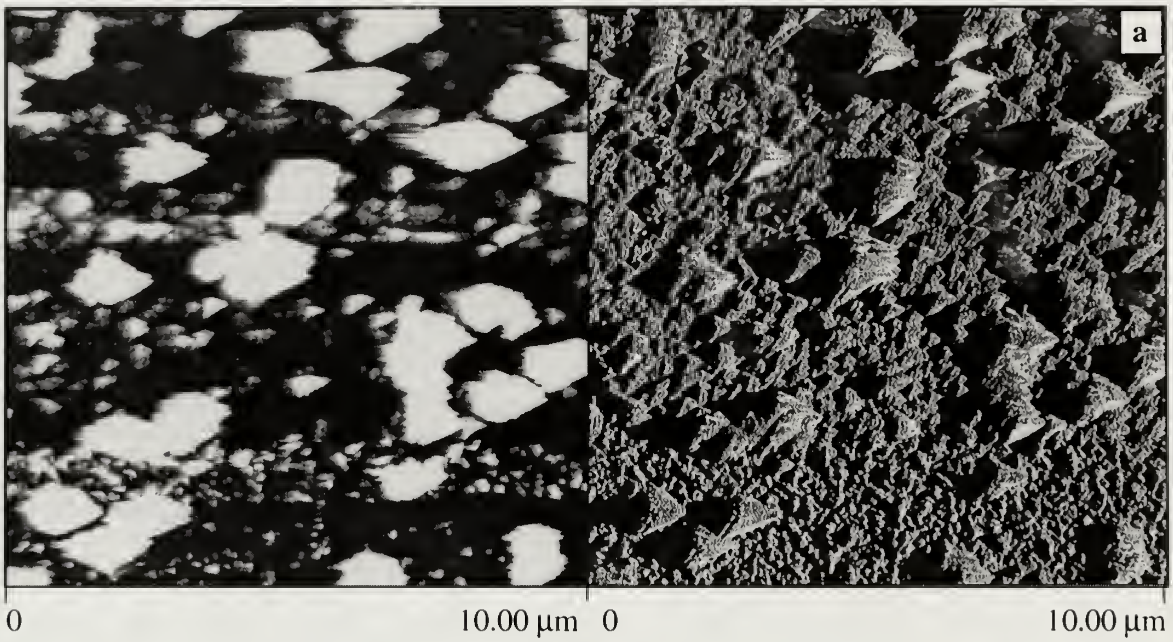
a
0
10.00 μm
0
10.00 μm

Data type – Height
Z range – 175.0 nm

Data type – Amplitude
Z range – 100.0 nm

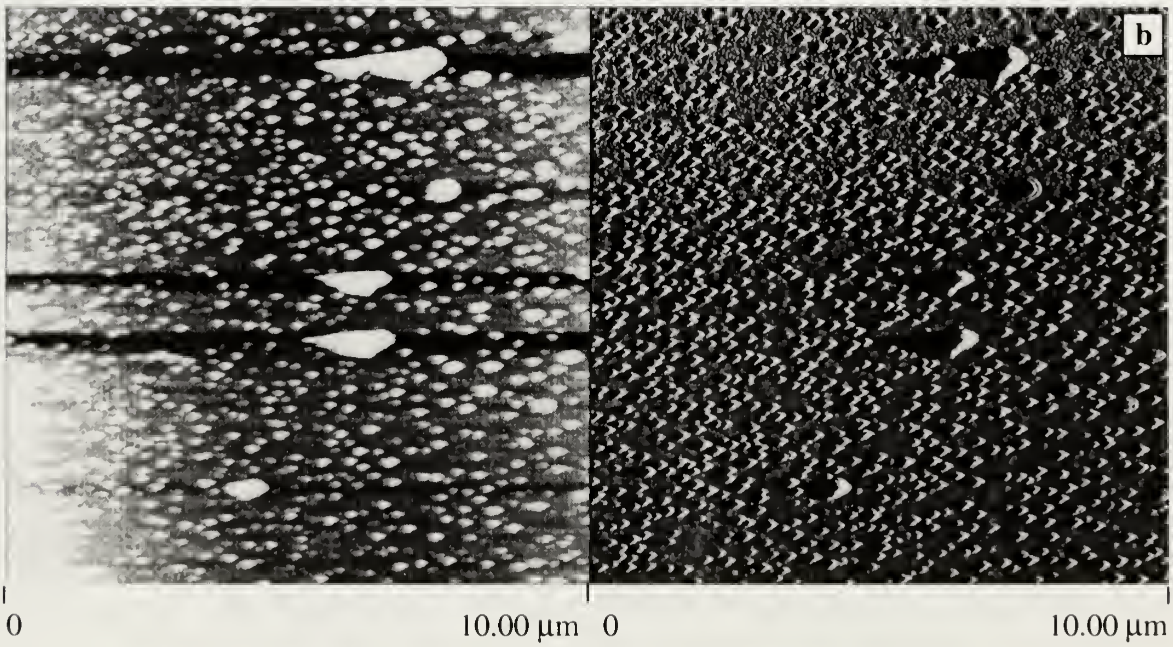
b
0
10.00 μm
0
10.00 μm

Data type – Height
Z range – 35.0 nm

Data type – Amplitude
Z range – 50.0 nm

Figure 4.4 AFM micrograph of BN/BP on Si (111)
a) $T_{Deposition} = T_{Nitridation} = 1132\ ^{o}C$, $P_{Deposition} = P_{Nitridation} = 400$ Torr
b) $T_{Deposition} = T_{Nitridation} = 1050\ ^{o}C$, $P_{Deposition} = P_{Nitridation} = 760$ Torr

on top of the rough underlying surface. On Si(100), at higher temperature, a smoother surface is observed presumably due to the ability of the atoms to reconstruct and the higher surface coverage achieved (Figure 4.3). In Figure 4.4, the nitrided film's surface deposited on Si(111) is much rougher than that on Si(100) due in part to the increased BP growth rate on Si(100) as compared to Si(111) (see Figure 3.1). Depositions in the shape of triangles are evident, particularly at the higher growth temperature of 1132 °C. These depositions mimic the triangular crystal plane of the underlying (111) oriented silicon substrate.

4.3.2 FTIR and Raman

Because of the difference in bond coordination between cBN (sp^3) and hBN (sp^2), it is possible to identify BN modifications by FTIR and Raman spectroscopy. cBN has characteristic infrared and Raman peaks at 1065 and 1340 cm^{-1} for the transverse and longitudinal optical modes, respectively. In contrast, hBN has one active infrared mode at 1366 cm^{-1} and two active Raman modes at 783 and 1367 cm^{-1}. Due to the close proximity of the longitudinal cBN (1340 cm^{-1}) and transverse hBN (1367 cm^{-1}) characteristic peaks, phase identification is often made using the presence or absence of the 1065 cm^{-1} cBN peak.

Figure 4.5 shows an IR reflectance spectra for BN/BP on Si(100) and Si(111) (Sample BP-74). These samples were grown by the single step in-situ cBP nitridation method using NH_3. Evidence of cubic boron nitride is present for both samples as indicated by the peak at 1065 cm^{-1}. A smaller hexagonal boron nitride peak is also present at 1360 cm^{-1} for both oriented substrates, thus indicating a mixture of both the hexagonal and cubic phases. The upward shift in the cBN transverse optical mode from 1065 to approximately 1100 cm^{-1} is a result of the large strain inherent to the BN/BP film as a result of its lattice

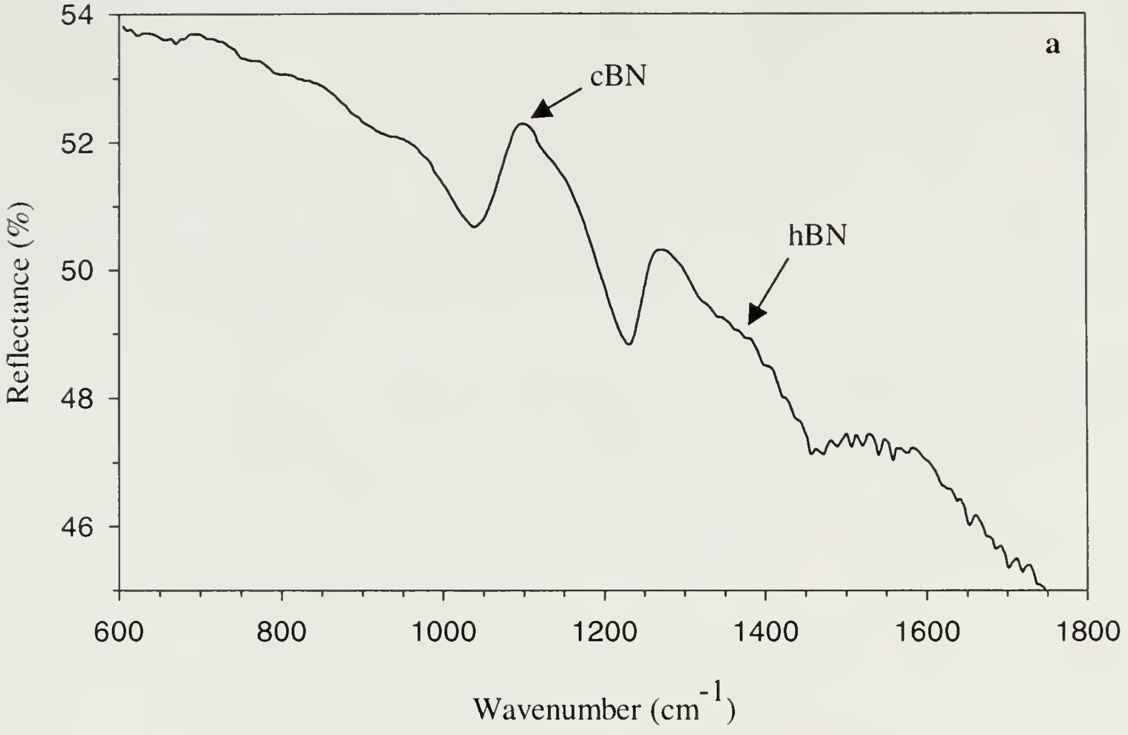

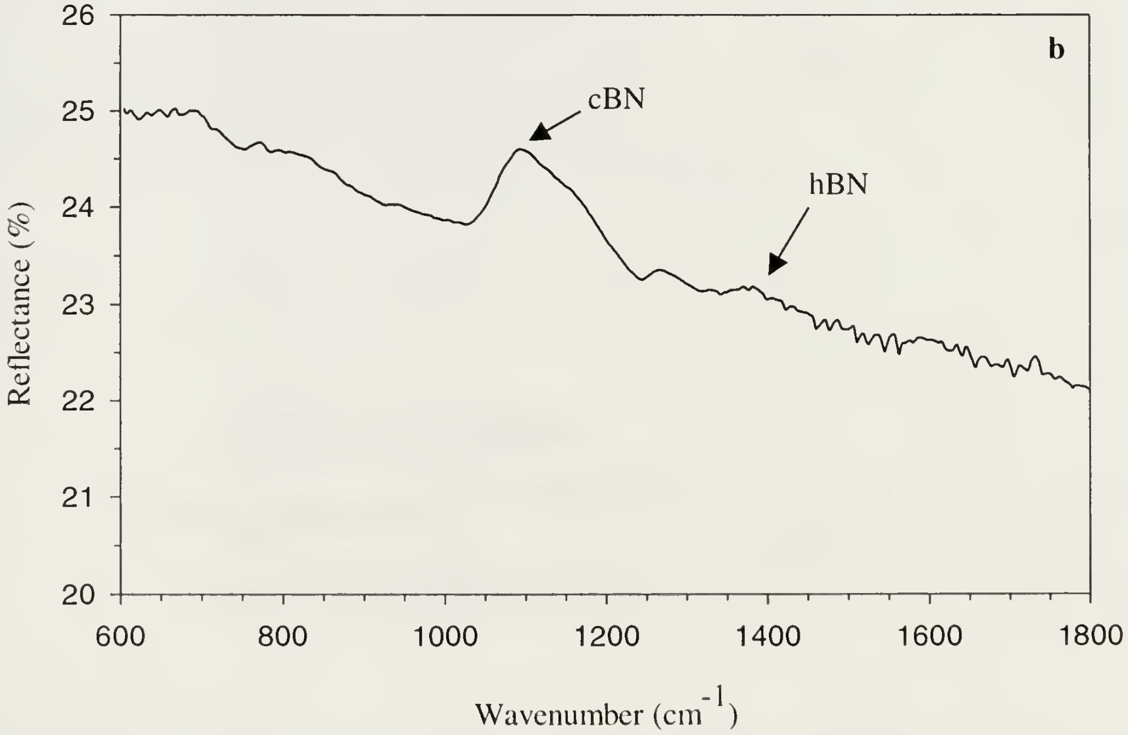

Figure 4.5 FTIR spectra of BN/BP deposited on a) Si(100) and b) Si(111) (Sample BP-74)

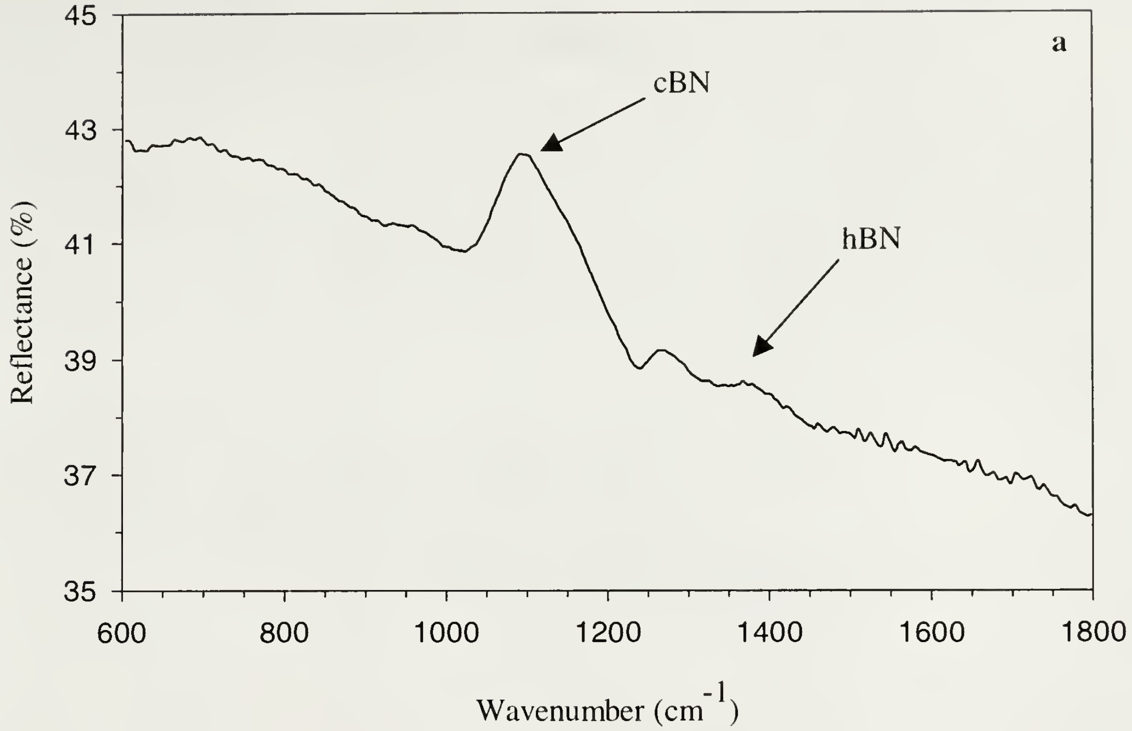

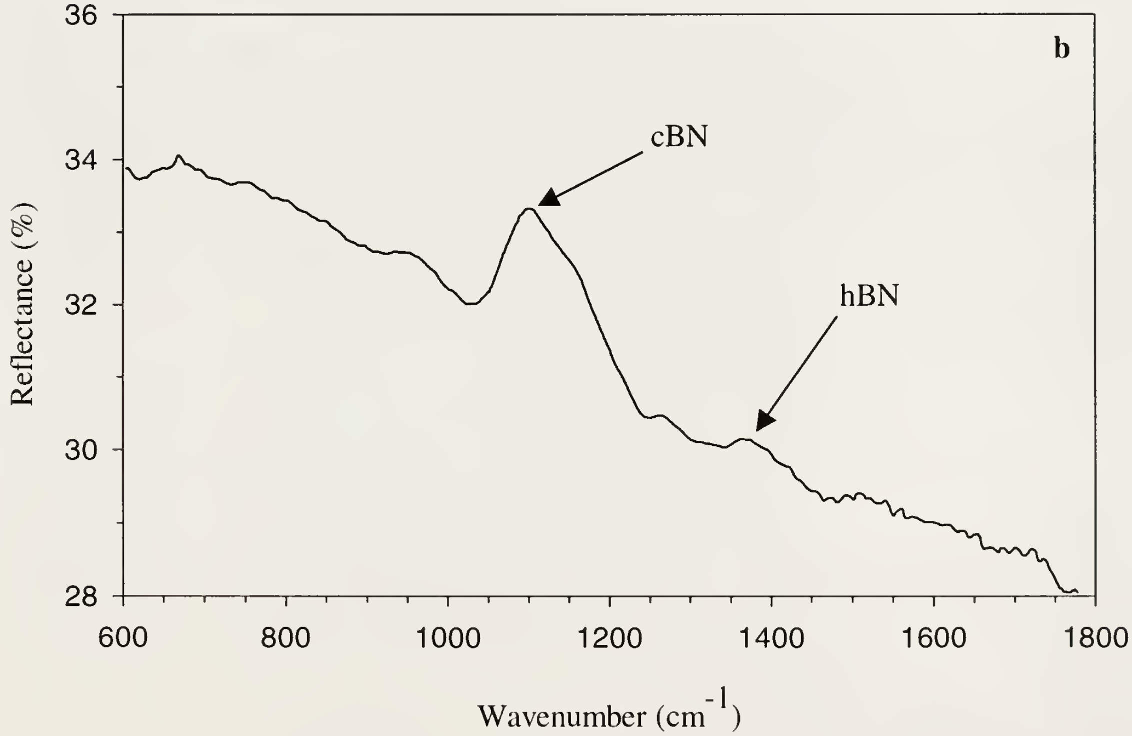

Figure 4.6 FTIR spectra of BN/BP deposited on a) Si(100) and b) Si(111)
(Sample BP-95)

mismatch with the substrate. According to Mirkarimi et al., an approximate cBN/hBN ratio can be obtained by comparing the peak heights of the two crystal structures since their extinction coefficients are similar [220]. From Figure 4.5, it appears that deposition on Si(100) and Si(111) yielded films with cBN contents in excess of 50% and 80%, respectively. Similar results are shown in Figure 4.6.

The IR reflectance spectrum of CVD growth for BN (BCl_3+NH_3) on a nitrided cBP/Si film is shown in Figure 4.7 (Sample BP-138). Although previous research has indicated that CVD of BN results in only the growth of hexagonal boron nitride, the intention of growing CVD BN on a nitrided cBP template was to attempt to utilize the underlying nitrided template as a guide for continued growth of cBN. The characteristic cBN IR peak is again present at 1060 cm^{-1}. As before, the spectrum indicates that a mixture of the hexagonal and cubic structures for boron nitride is present. It is known from critical thickness calculations performed as part of this work that the critical thickness for accommodation of dislocations for defect-free cBN growth on silicon is less than one monolayer. Thus, the presence of a mixture of hexagonal and cubic BN could result from localized film relaxation and transformation of a percentage of the cBN to the kinetically favored hBN crystal structure. Alternatively, the kinetics of straight BN growth by CVD could govern to such an extent that deposition on an underlying cubic template does not completely control growth. Such is the case for BN CVD growth on silicon where only hBN has been reported.

As mentioned in the experimental section of this chapter, a cyclical process was also used to nitride CVD films of cubic boron phosphide. The boron phosphide films were nitrided first, followed by additional CVD growth of boron phosphide that was again nitrided. Three cycles were performed.

Figure 4.8 shows IR transmittance spectra for the samples resulting from this cyclical process (Sample BP-139). A cBN peak is observed at 1065cm^{-1}, thus indicating a mixed phase film was again deposited on both Si(100) and Si(111) substrates. The smaller ratio of the cBN to hBN peak heights relative to those of Figure 4.7 could be a result of greater film relaxation or decreased impurity incorporation. Since it is believed that the stabilization of cubic BN can be enhanced by stress due to lattice mismatch between BP and Si, it is important to try to minimize dislocation formation and film cracking. It is proposed that thicker BP films will result in film relaxation and a transition from cBN to hBN.

Evidence of cBN stabilization as characterized by FTIR and Raman spectroscopy proved to be difficult to obtain. Although results were repeatable for a limited number of samples, a large majority of the in-situ nitridation experiments yielded spectra indicating only the hBN crystal structure. A typical FTIR spectra indicating only hBN formation is shown in Figure 4.9. Approximately 8% of the in-situ nitridation experiments conducted yielded spectra characteristic of cBN stabilization. There are two reasonable explanations for the limited repeatability of these experiments. The first, which will be discussed in greater detail in section 4.3.3 of this dissertation, is that the general surface scan produced by FTIR and Raman spectroscopy was not sufficiently sensitive enough to detect the cBN if it grows in isolated island formation, due to localized areas favorable for stabilization. Unlike other techniques that will be described later, FTIR and Raman spectroscopy do allow bulk composition analysis and thus ability to detect cBN in layers removed from the

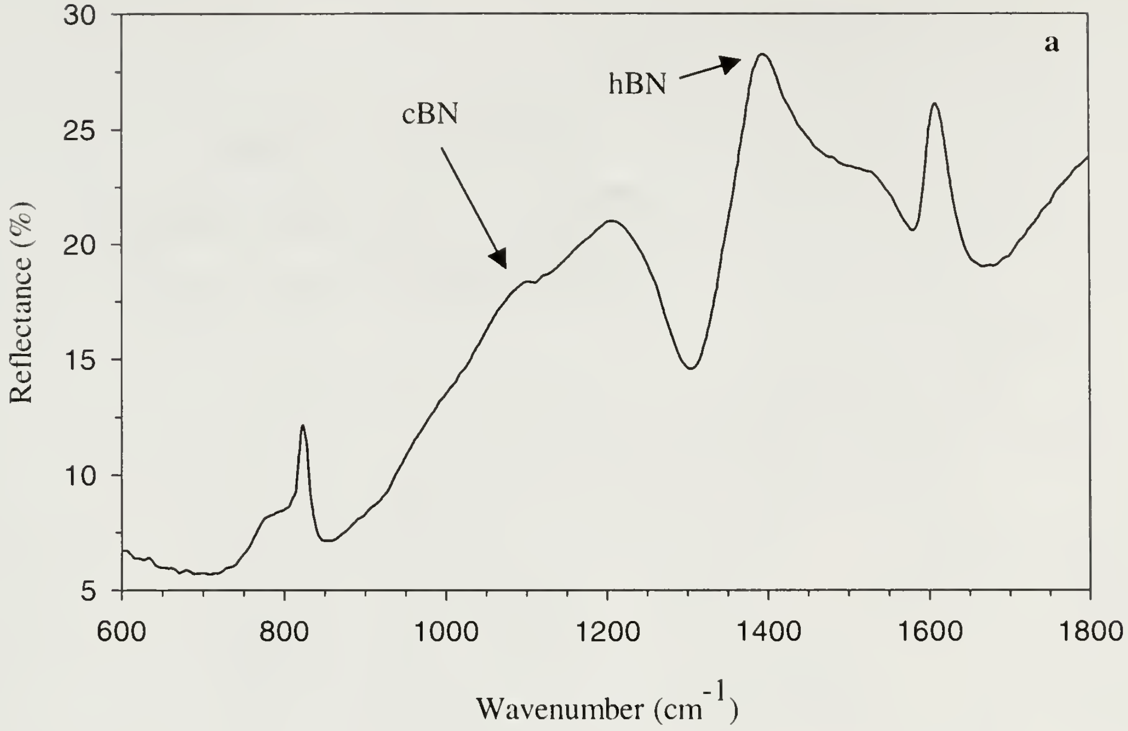

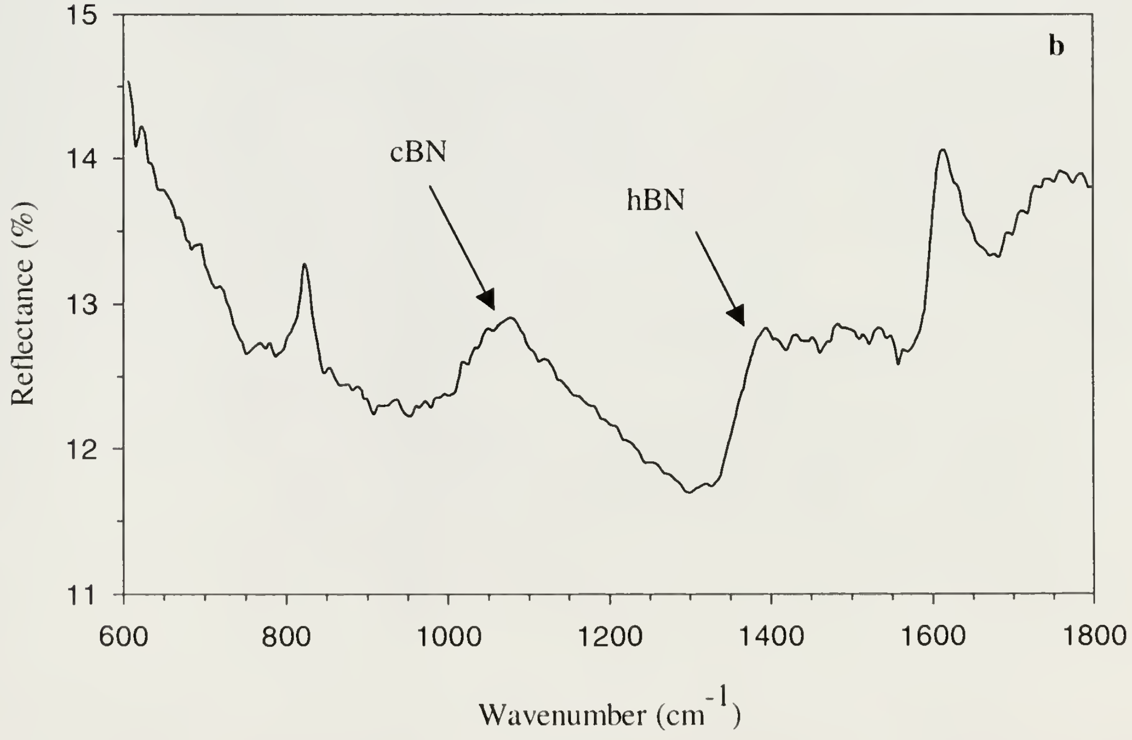

Figure 4.7 FTIR spectra of BN/BP deposited on a) Si(100) and b) Si(111) (Sample BP-138)

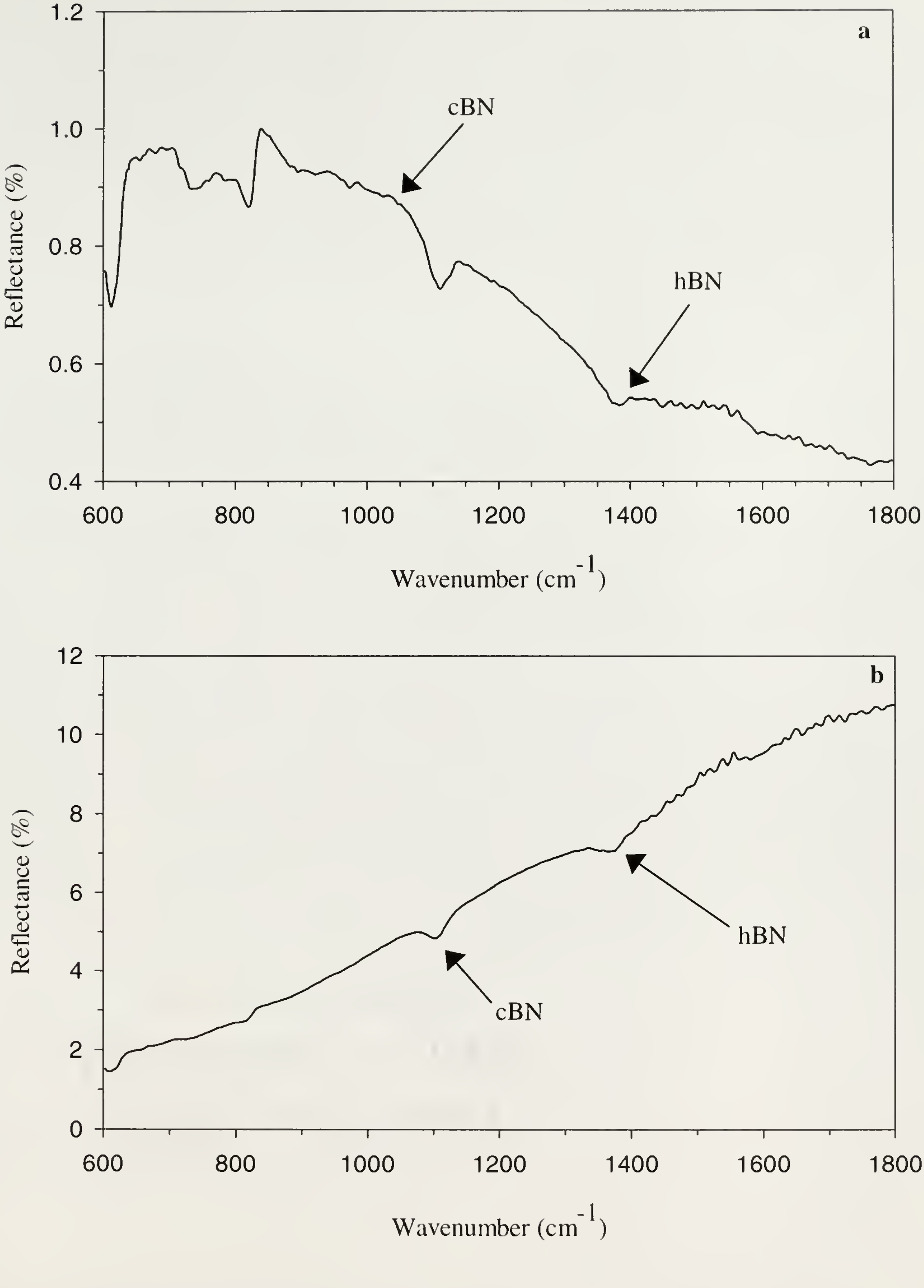

Figure 4.8 FTIR spectra of BN/BP deposited on a) Si(100) and b) Si(111) (Sample BP-139)

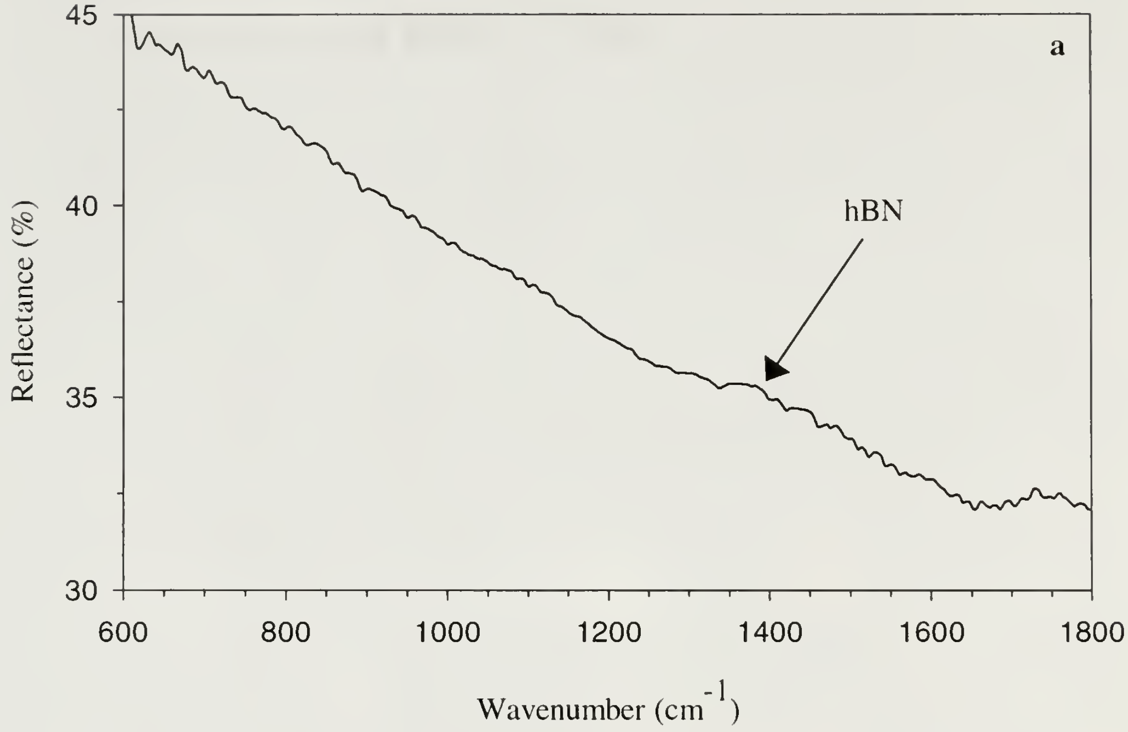

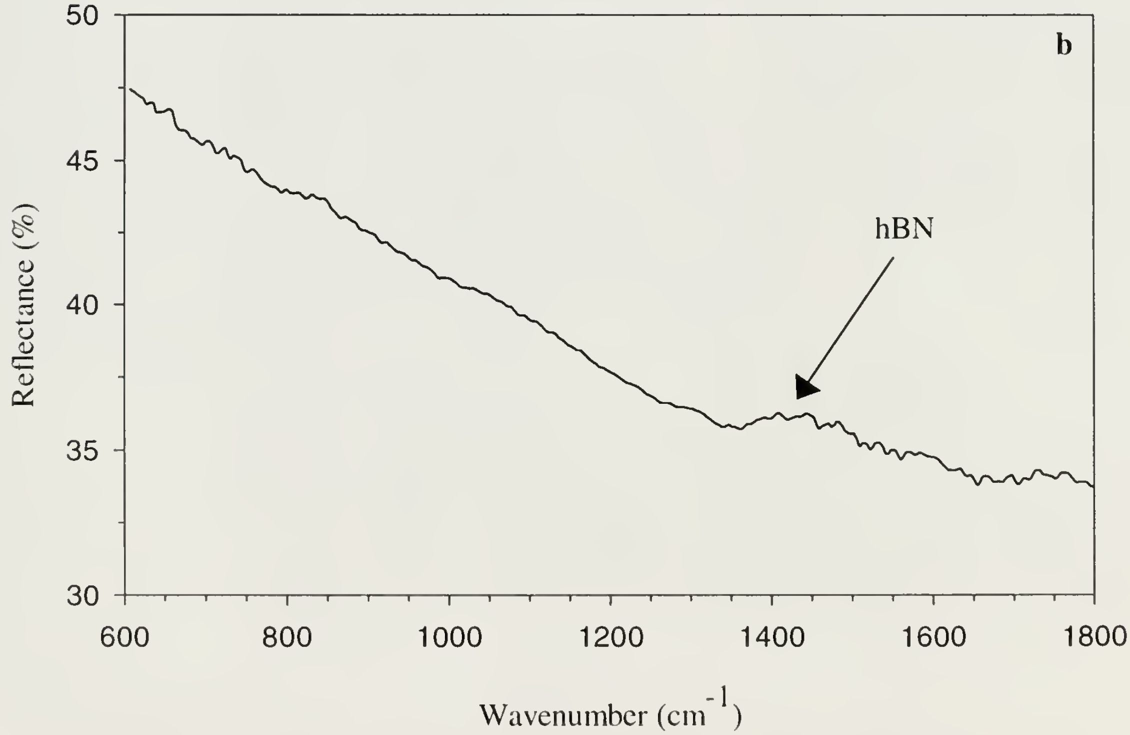

Figure 4.9 FTIR spectra of BN/BP deposited on a) Si(100) and b) Si(111) (Sample BP-75)

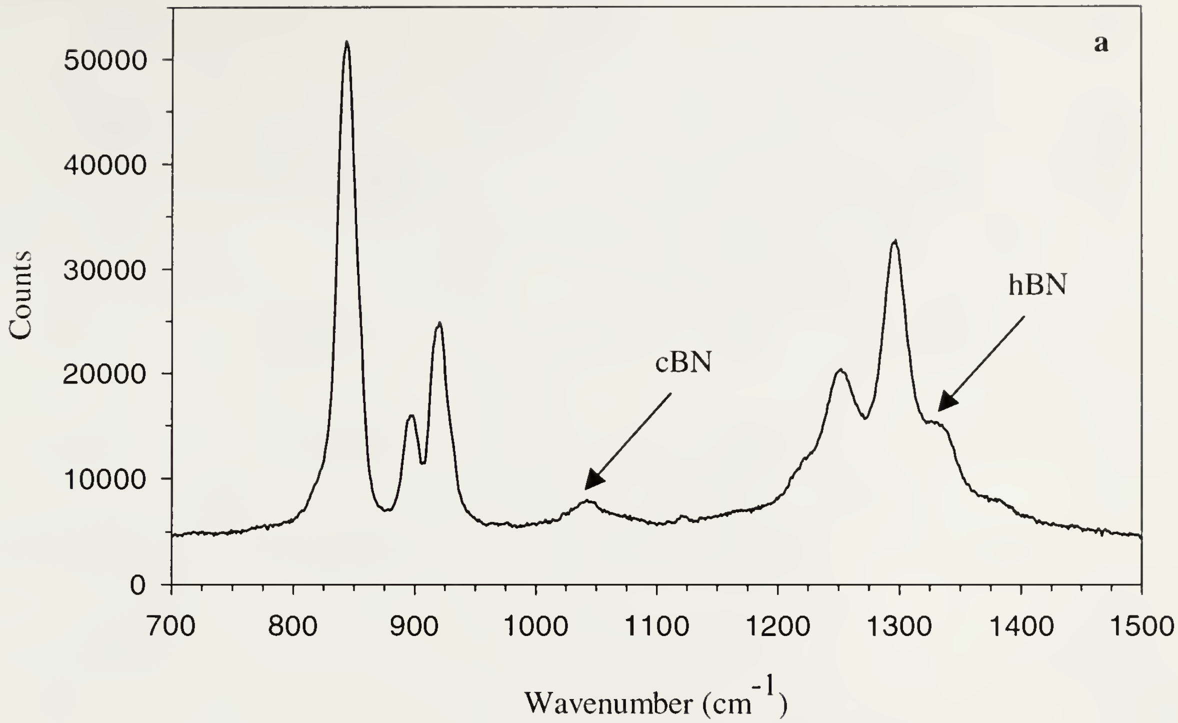

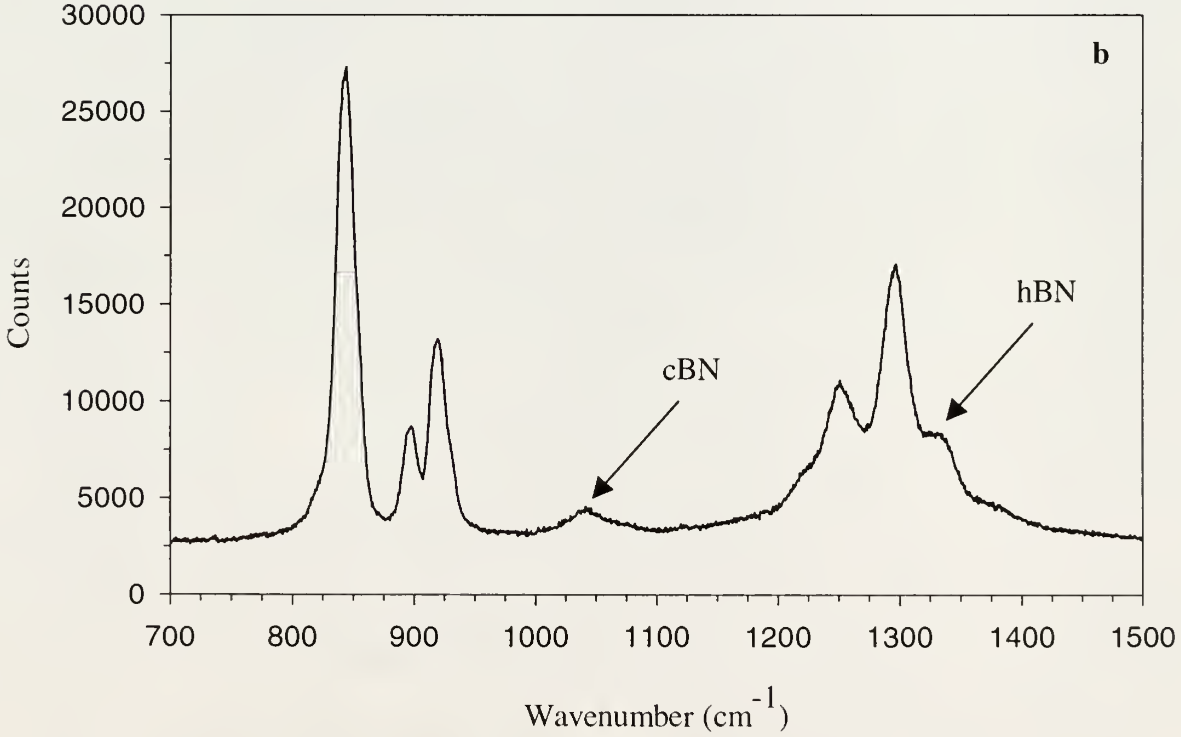

Figure 4.10 Raman spectra of BN/BP deposited on a) Si(100) and b) Si(111) (Samples BP-95 and BP-138)

film surface. The second explanation is that the lack of a load-lock system coupled with reactor leaks permitted oxygen introduction prior to and during film growth, resulting in non-repeatable experimental conditions. Oxygen uptake on the sides of the reactor during sample loading, and its subsequent release under vacuum, and/or elevated temperature during growth, and the oxidation of the silicon substrate and growing/nitriding film prior to and during growth/nitridation, respectively, could each play significant roles. The reactor seals and associated tubing have been subsequently modified as part of this work to eliminate vacuum leaks from the atmosphere.

Raman spectroscopy of sample BP-95 (Figure 4.10) clearly indicates the presence of cBN at 1060 cm^{-1}. A faint hBN peak is seen at 1360 cm^{-1} corroborating the FTIR results discussed above. Similar Raman characterization of samples BP-138 and BP-139, however, indicate the presence of only hexagonal BN. This corroborates the FTIR results of BP-139 but conflicts with that of BP-138. It is not clear whether BN formation occurs in a continuous film or as islands. It is reasonable to believe that the underlying BP structure influences the subsequent growth of BN. Furthermore SEM of nitrided samples has shown the formation of isolated structures (see Figures 4.1, 4.2). Even continuous films appear to grow in a polycrystalline manner with varying orientations that influence the final nitrided structure differently. Thus the increased aerial sensitivity of Raman spectroscopy as compared to FTIR may overlook these differences and therefore may account for the difference in cBN detection by Raman and FTIR in sample BP-138.

4.3.3 AES and XPS

Auger electron spectroscopy (AES) can also be used to identify the crystal structure of boron nitride. The differences in coordination bonding for cBN and hBN (sp^3 and sp^2, respectively) influences the binding energies of the core electrons, resulting in contrasting characteristic B and N spectra. In previous reports, the N-KVV and B-KVV characteristic peaks have been used for this purpose [509]. The difference in coordination bonding of cBN and hBN results in the presence of hBN plasmon peaks at 387 and 188 eV for N-KVV and B-KVV, respectively. These standard AES spectra are shown in Figure 4.11.

AES of sample BP-95 indicated the presence of a N-KVV plasmon peak at 387 eV and also a B-KVV plasmon peak at 188 eV (Figure 4.12). This is obviously inconsistent with FTIR and Raman spectroscopy results of this sample. There are two possible explanations as to why a cubic sample could exhibit an AES spectrum characteristic of a hexagonal one. There have been reports in the literature that an incident ion beam can graphitize a known diamond surface at relatively low accelerating voltage [510]. Given the similarity between the cubic and hexagonal phases of BN and carbon a similar phenomenon could be occurring particularly given the expected thin nature of the formed BN film and sputtering to remove post-growth impurities. The second possibility is that the very limited surface area probed by the incident electron beam is insufficient to detect the cubic BN if it is forming in isolated islands. The greater spatial scan area and penetration depth of FTIR and Raman spectroscopy enable these techniques to “see” a far larger area and volume and thus detect cBN in regions significantly beneath the film surface. AES was also performed on samples BP-138 and BP-139 with only the detection of hBN. AES results also indicate that oxygen contamination levels, resulting from both vacuum system leaks during growth

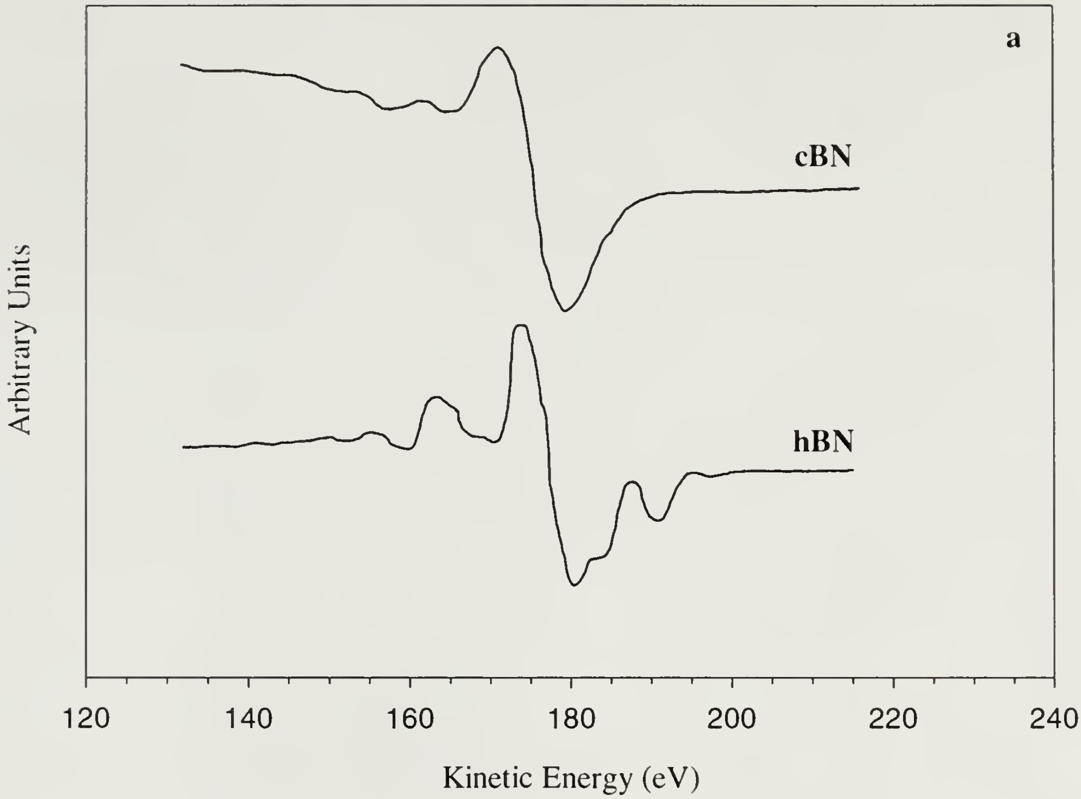

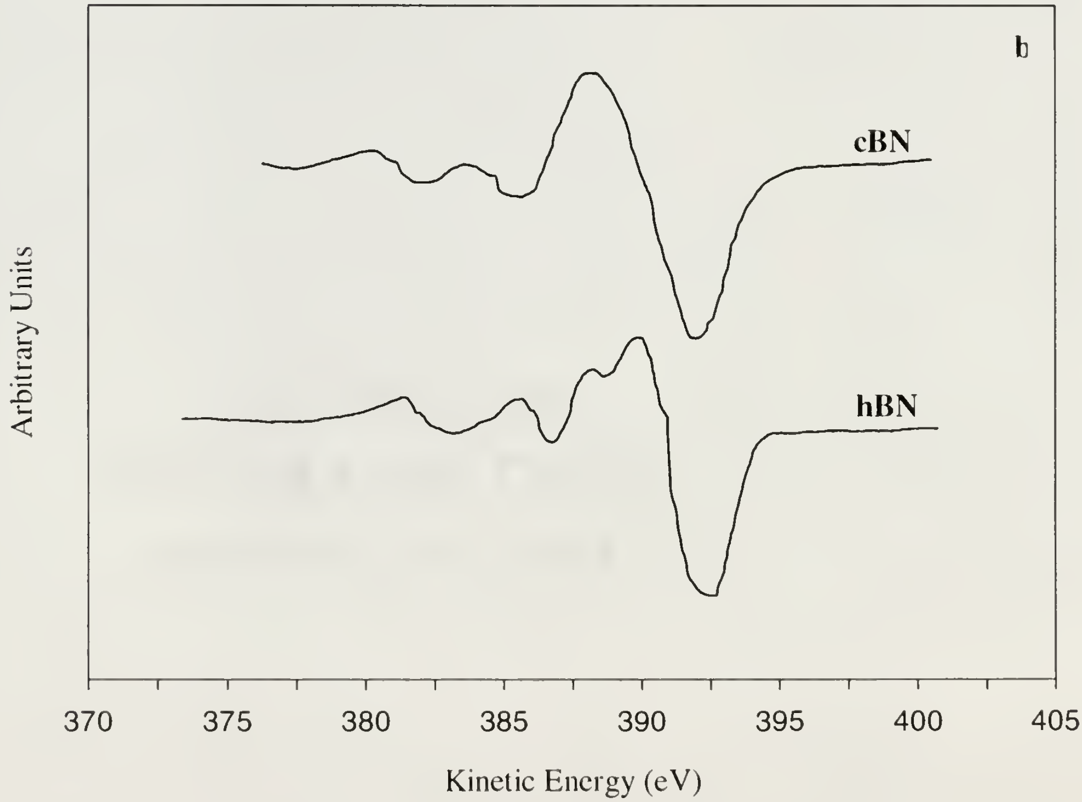

Figure 4.11 AES standard spectra for cBN and hBN: a) B-KVV and b) N-KVV (From reference 509)

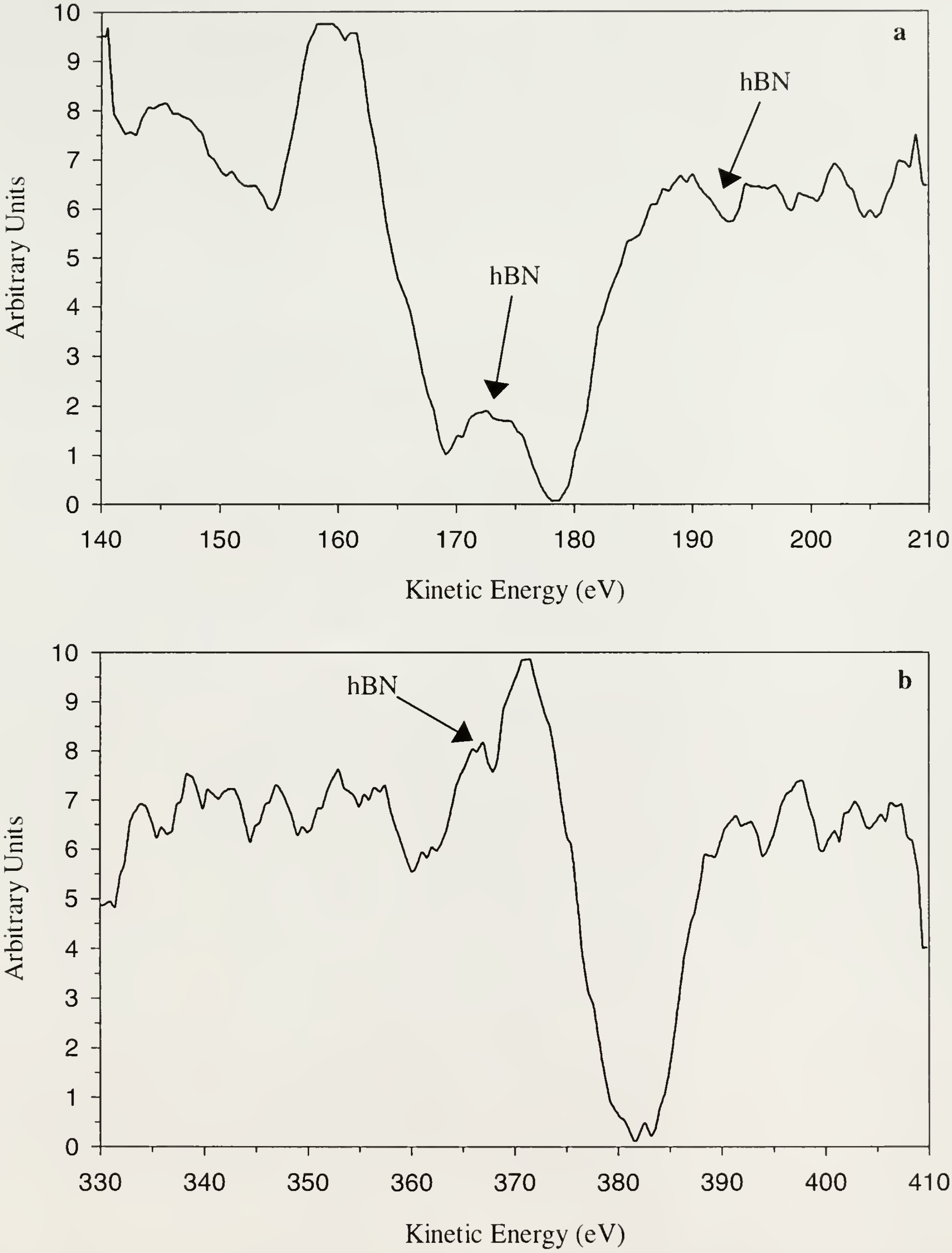

Figure 4.12 AES spectra for BN/BP deposited on Si(100): a) B-KVV and b) N-KVV

and post-growth incorporation in the first several monolayers, are quite low (≤ 5 atomic %). Thus the possible error of reporting FTIR and Raman spectroscopy wavelength positions of SiO_x compounds to that of cBN can be discounted given the extremely large cBN peaks shown in Figures 4.5-4.7 and 4.10. There is much more credibility to the claim in this work that cBN may in fact have been stabilized via a non-energized in-situ nitridation technique.

X-ray photoelectron spectroscopy (XPS) was also used to characterize the crystal structure by noting the presence or absence of a π plasmon peak at ≈ 9 eV from the main B 1s and N 1s core level peaks at 191 and 398 eV, respectively. The presence of a π plasmon peak indicates sp^2 bonding and thus hexagonal crystal structure. Analysis of the nitrided cBP films, for which FTIR and Raman spectroscopy showed cBN while Auger spectroscopy indicated hBN, indicated the possible presence of cBN (Figure 4.13) in the N-KVV spectra by the small and questionable existence of a π plasmon peak. The B-KVV spectra, however, shows a noticeable π plasmon peak far above the background noise. Thus the two spectra for the same sample appear to contradict. The belief proposed in this work and by other researchers, however, support that islands of cBN coexist with hBN ones, thus mixed spectra for a single sample is easily explainable. In fact, a film of pure cBN has never been reported using any thermal or ion/plasma assisted CVD technique. The maximum cBN content reported to date is approximately 85%.

After sputtering at 3.0 eV for 30 seconds the appearance of a π plasmon peak is clearly seen for the N-KVV spectra but, curiously absent for the B-KVV spectra (Figure 4.14). Thus, as supported by the FTIR and Raman spectroscopic data, a mixed cBN/hBN film appears to be detected by XPS. Previous literature has also reported that BN grows in a layered structure where a hBN layer underlies a mixed cBN/hBN top layer. Thus, after

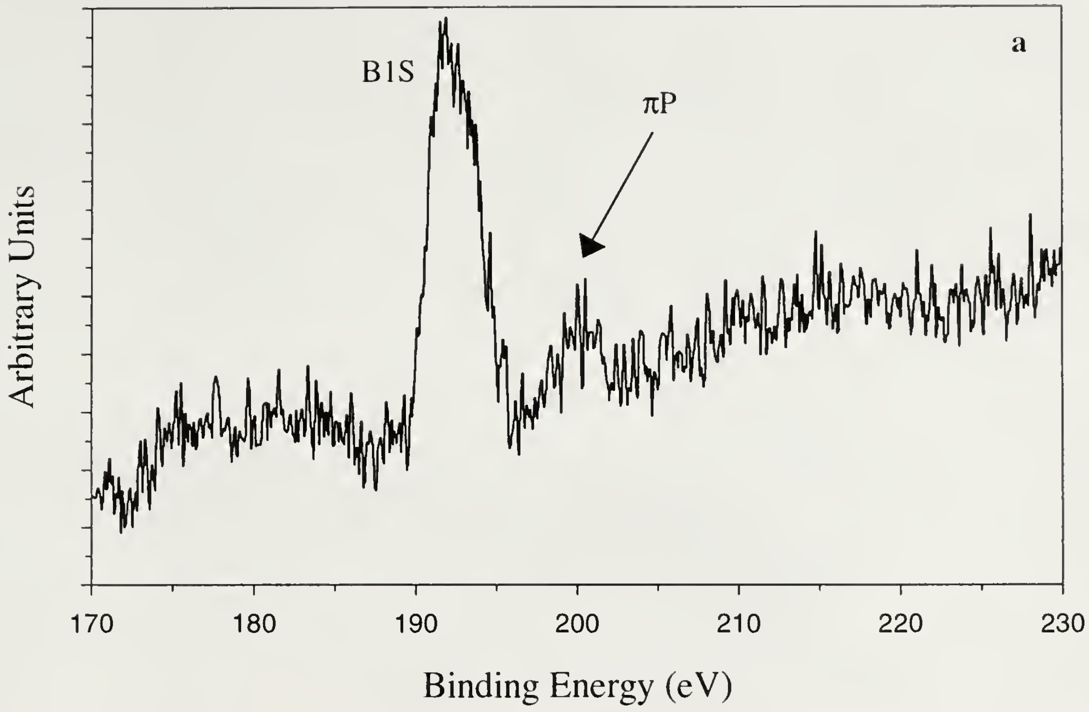

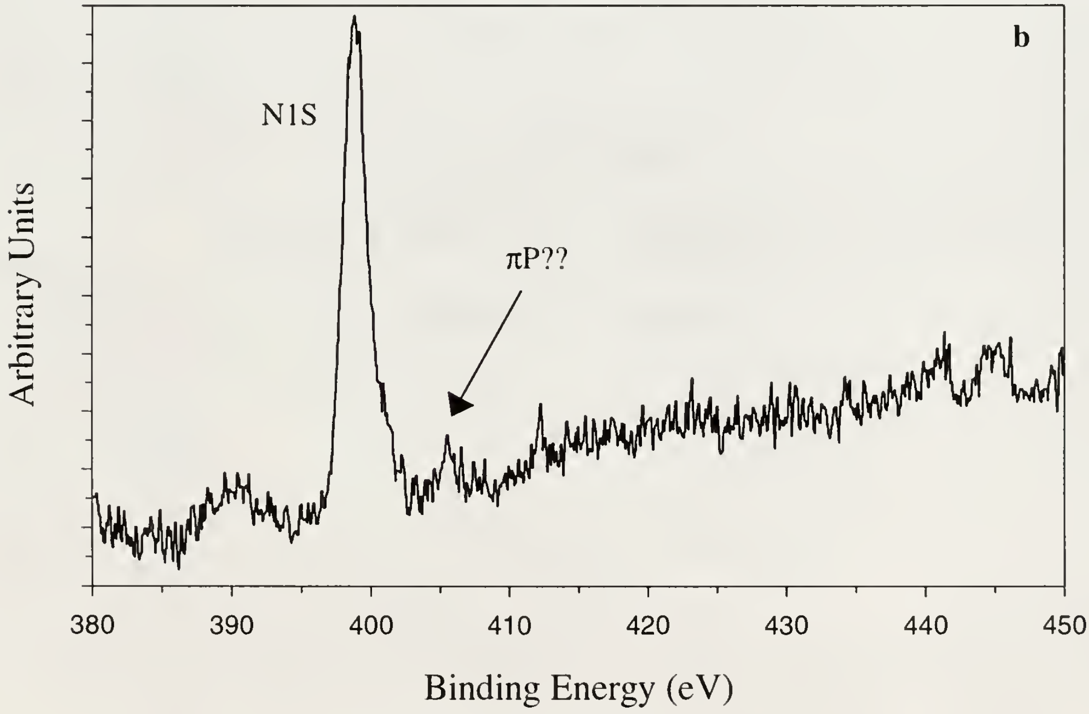

Figure 4.13 XPS spectra for BN/BP deposited on Si(100): a) B1S and b) N1S (As-received)

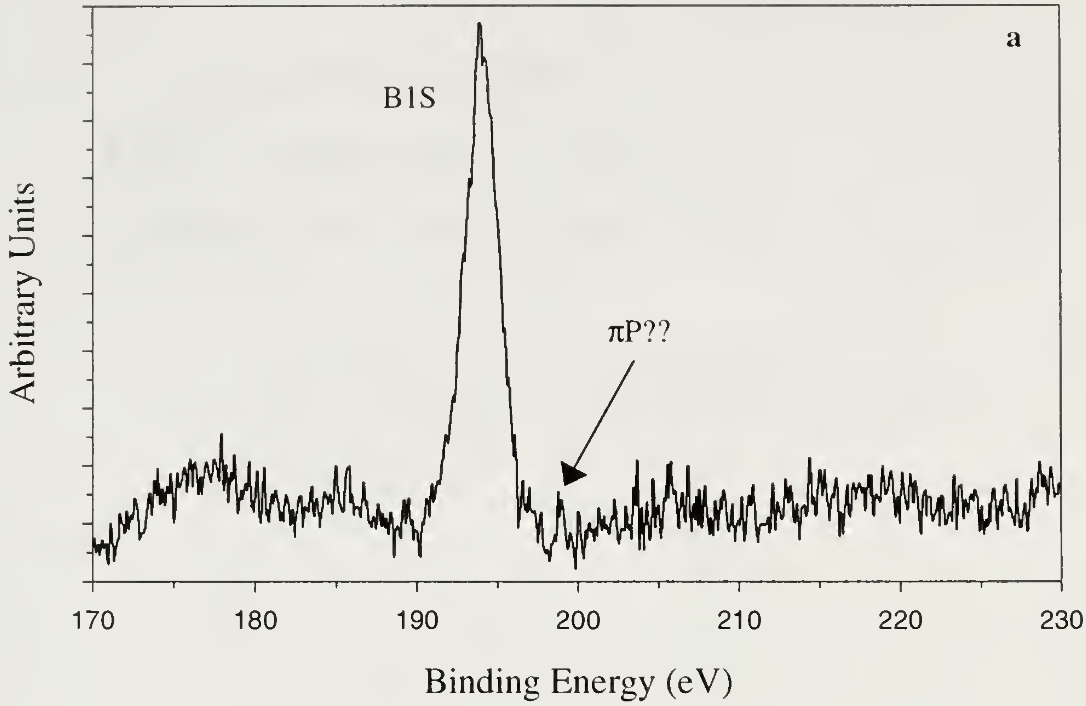

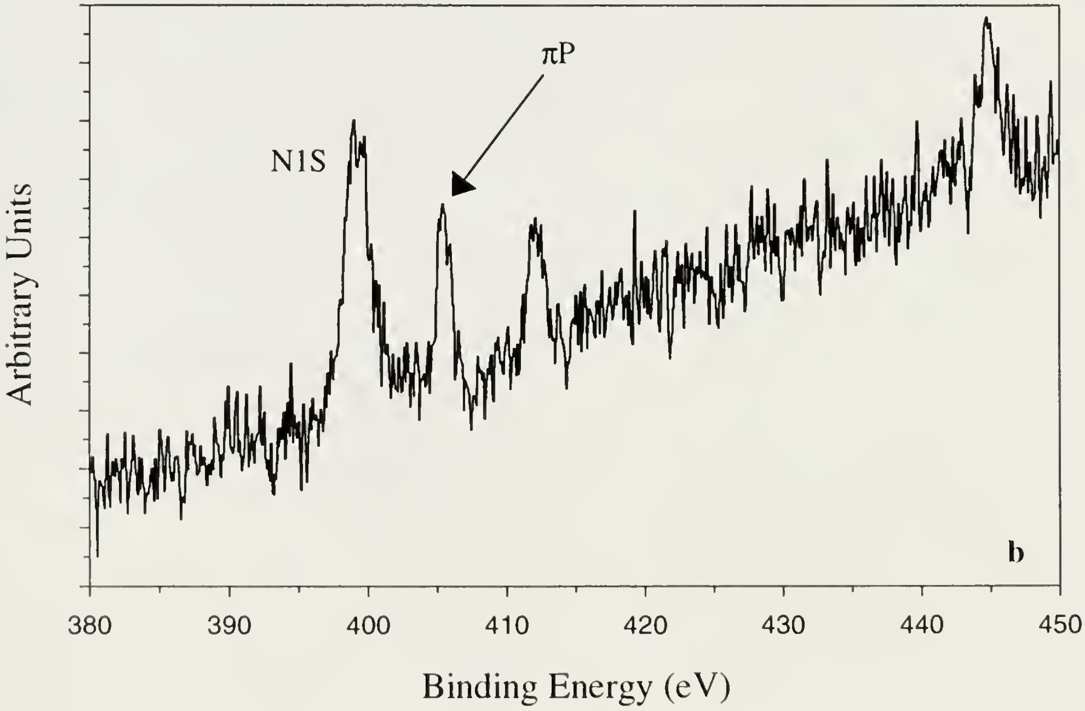

Figure 4.14 XPS spectra for BN/BP deposited on Si(100): a) B1S and b) N1S (0.5 min sputter)

sputtering, XPS may very well be detecting more signal from this underlying hBN layer. It is uncertain if the peaks at 413 and 445eV in the N1S spectra are artifacts or impurities.

4.3.4 TEM

High-resolution transmission electron microscopy (TEM) analysis of sample BP-95 is shown in Figure 3.16. Cross-sectional analysis showed only the presence of a BP film on a Si substrate. An amorphous layer approximately 100 Å thick was detected that may be attributable to BN. In addition a Au-Pd film is observed at the surface. This film was previously deposited for SEM analysis and could mask the presence of additional BN. The BP/Si interface exhibits significant roughness (approximately 200 Å). This is presumably due to the silicon wafer etching procedure or exposure of the cleaned Si wafer to the highly corrosive chlorine chemistry used (6 HCl molecules produced for every 1 molecule of BP film deposited).

Lack of detection of BN could result from several factors. As shown in the SEM analysis, island formation in the growth of BP and the subsequent nitridation is likely. Because of the extremely small substrate area observed using TEM, the detection of BN domains could at best be coincidental. It is also possible that the TEM sample preparation may have resulted in the loss of material containing BN.

4.4 Conclusions

BN films were deposited by in-situ nitridation of CVD grown BP films, by a cyclical process of BP growth and NH_3 nitridation and by the CVD of BN on templates of nitrided BP films. FTIR and Raman characterization of multiple films indicates the presence of a cubic BN layer. It is not clear whether the BN material is grown as a continuous film or as islands on the BP film. SEM analysis, however, is more consistent with island formation. Other characterization techniques (AES) seem to indicate the presence of only hexagonal BN. Previous research has stated that care must be taken in distinguishing between cBN and silicon oxide spectrographic peaks in FTIR and Raman. This is not the case in this work, where the oxygen contamination levels are too low to account for the size of the spectra peaks attributed to cBN. One plausible explanation is that a “graphitization” process similar to that reported for AES analysis of known diamond films is occurring. XPS analysis is inconclusive with the B-KVV and N-KVV spectra conflicting on both the as-received and sputtered samples. A table summarizing the BN results using each of these techniques is shown below.

Table 4.1 Summary of BN in-situ nitridation results

Characterization Technique	**cBN**	**hBN**
FTIR Spectroscopy	YES	
Raman Spectroscopy	YES	
Auger Electron Spectrometry (AES)		YES
X-ray Photoelectron Spectroscopy (XPS)	????	????

???? = Undetermined

CHAPTER 5
GROWTH OF WN_x BY MOCVD

5.1 Introduction

As the feature size in integrated circuits (ICs) has decreased, the necessity for thermally stable, high conformity interface diffusion barriers and gate electrodes has become more significant [267,338,358]. Traditionally, aluminum and its alloys have been used for thin film interconnections. The use of aluminum can create difficulties, however, including a low electromigration lifetime and chemical/electrical interaction with Si [511]. More recently copper has been investigated as an alternative to aluminum due to its lower electrical resistivity and higher resistance to electromigration. This would enable a decrease in the RC time constant of a transistor and increased device lifetime.

Unfortunately Cu, like Al, is quite mobile in metals and as well as silicon. Upon direct contact with Si, it diffuses and reacts rapidly. During subsequent thermal annealing shallow junctions and contacts can be destroyed, resulting in fatal device failure. Long-term reliability of a multi-layer metallization device can only occur if there is little to no interdiffusion between adjacent metallization layers. Any diffusion can result in an increase in contact resistance, a change in the barrier height, embrittlement of the contact layer, and destruction of the electrical connection to the chip [293]. Refractory metals have been investigated as potential diffusion barriers. Unfortunately, their reactivity and tendency to interdiffuse with the first level interconnect are significant at elevated temperature (>450

°C). Thus research has turned to refractory metal nitrides to minimize this interdiffusion and reactivity at the higher temperature used in post-processing and annealing (typically in the range 700 to 800 °C) [512]. Refractory metal nitrides generally fall into both the "stuffed" and "sacrificial" diffusion barrier categories: "stuffed", where the nitrogen atoms prevent rapid diffusion through the grain boundaries, and "sacrificial," where the entire barrier slowly reacts with the underlying film and/or overlying metallization layer until it is eventually short circuited [512,513]. Another possibility is the use of amorphous films where grain boundaries, by definition, should not exist. In fact, Kwon et al. have demonstrated the superiority of amorphous WN_X compared to its polycrystalline counterpart in blocking Cu diffusion into Si [374]. Research indicates that nitride barriers are indeed better candidates for reliable diffusion barriers from the interdiffusion standpoint [293].

5.2 Experimental

Novel single-source imido precursors were synthesized by Professor Lisa McElwee-White's research group in the Department of Chemistry at the University of Florida. These compounds were then analyzed to determine their vapor pressures, decomposition profiles versus temperature and time, and molecular decomposition using mass spectrometry. After this data were obtained, the MOCVD growths of WN_X thin films were attempted using each precursor compound. These growths fell into two separate categories: (1) determining whether WN_X films could be deposited using a particular novel imido single-source precursor and (2) if deposition was possible, then what were the resulting film's properties. This information could then be given to the organometallic synthetic chemists for precursor redesign and/or solvent reselection to optimize the thin film's properties. The film properties studied most often were surface morphology, elemental composition, and thin film resistivity. NH_3 was added to the carrier gas during some of the experiments to determine what assistance, if any, it would lend to film deposition.

Samples were examined for growth rate, crystal structure, elemental composition, electrical properties, and barrier integrity after annealing at elevated temperatures. Since WN_X is not a heavily studied material, spectroscopic patterns for use in FTIR and Raman spectroscopy were not available. Hence these techniques were not used to characterize the growths as they were in the BP and BN studies. XRD was utilized to confirm the presence of a WN_X film, to determine if the films exhibited preferred oriented growth, and to determine qualitatively the degree of the film's crystallinity. AES was used to determine the film's surface and bulk elemental composition. It and secondary ion mass spectrometry (SIMS) were used to examine the degree of copper interdiffusion after thermally annealing the $Cu/WN_X/Si$ structures at elevated temperature. Cross-sectional SEM was used to determine the film's surface uniformity and thickness. Thin film resistivity values were measured using a four-point probe.

As part of this project, two different delivery systems for transport of the solid precursors to the reactor were designed, built, and added to the existing CVD system. The first was a solid-source delivery system that used sublimation to volatilize the novel metal-organic precursors. A variable intensity 650 W halogen light source was focused through a 12.5 mm diameter fused silica disc. The precursor, tightly packed into a 3 mm ID/5 mm OD quartz tube, was slowly translated in the vertical downward direction using a stepping motor through this focused light source where the volume exposed to the light source was volatilized. The precursor or its fragments, now in the vapor state, exited the quartz tube through a vertical slit that was positioned 180° from the light source. The vaporized precursor was then transported to the reactor via a sweeping carrier gas flow in heated lines.

Unfortunately, the vapor pressure of the novel metal-organic precursors used in the initial studies (W (IV) carbonyls) was extremely low. Therefore, even though the tubing between the delivery system and reactor could be heated from room temperature to approximately 450 °C, nearly all of the sublimed precursor was simply redeposited on the tubing walls. Thus another type of delivery system was designed to circumvent this low vapor pressure problem.

The second delivery system employed in this work is based on the idea of transporting a near-saturated solution of solid precursor dissolved in a liquid solvent to the reactor. This system can best be described as an ultrasonic nebulizing delivery system. The solid precursors are dissolved in a solvent, typically benzonitrile, and injected slowly (≈ 4 ml/hr) via a syringe pump to the top of a circular quartz plate vibrating at 1.44 MHz due to the piezoelectric effect. Once this liquid stream contacts the quartz plate, it is immediately nebulized to an ultra-fine mist. This mist, composed of both the dissolved solid precursor and solvent, is then transported to the reactor via a sweeping carrier gas flow. Thus the problem of delivering low vapor pressure precursors is avoided, although careful choice of the solvent must be made to avoid its decomposition/reaction and subsequent impurity incorporation into the film. A picture of this system is shown in Figure 1.9.

WN_X growths were conducted exclusively on planar silicon (100) and (111) substrates prepared as described in chapter 3. Typical growth times were 2.5 h to ensure sufficient deposition thickness and to determine the initial suitability of each precursor for

MOCVD thin film growths. Once process parameters yielding suitable WN_X films were determined, the growth time was diminished to 30 min or less. It must be emphasized that the purpose of this work was, first and foremost, to determine if a WN_X thin film could be deposited. Once it was confirmed that precursor transport to the reactor was achievable and that a WN_X film was in fact being deposited, then the focus of the research shifted to performing parametric studies on the deposition process, deposition on patterned silicon substrates, impurity incorporation minimization through precursor redesign and/or solvent reselection, and deposition of thinner WN_X films whose post-annealing barrier capabilities were comparable to the thicker films first deposited. Each of these studies was just beginning at the completion of this dissertation.

5.3 Results and Discussion–Precursor Characterization

The novel metal-organic precursors synthesized by Professor Lisa McElwee-White's research group in the Department of Chemistry at the University of Florida were characterized by mass spectroscopy (MS), differential thermogravimetric analysis (DTA/TGA), and vapor pressure measurement. A general overview of the results are presented in this section. For a more thorough overview of the synthesis and characterization of the W(IV) carbonyl complexes, the reader is referred to the master's of science thesis of Jennifer Wilde and the doctor of philosophy dissertation of Jennifer McCusker [514,515].

Negative chemical ionization mass spectrometry was also performed on each potential precursor. As shown in Table 5.1, the W≡N fragment from the decomposed precursor was almost two orders of magnitude higher for the $L{=}CH_3CN$ compound than the other three precursors shown. In other words, it decomposes into the necessary W≡N fragment much more readily and completely than do the other potential precursors. This easier dissociation is attributed to the loosely coordinated bonding of the ligand to the central W metal atom. Thus, this ligand was used for each of the precursor complexes examined as part of this dissertation research.

Table 5.1 Negative Chemical Ionization Mass Spectral Data for $I_2(CO)_2(L)W{\equiv}NPh$ Complexes

Compound	Fragment	Mass (a.m.u.)	Intensity (%) vs. base peak
L=CH_3CN	W≡N	198.1	100
L=Pyridine	W≡N W(NPh)(Py)	198.1 353.9	1.26 5.8
L=NEt_3	W≡N NEt_3	198.1 101.1	1.52 100
L=Mesityl Amine	W≡N Mesityl Amine	198.1 135.1	1.52 100

DTA/TGA was used to determine sample weight loss versus temperature and time. Ideally a rapid weight loss (>80%) would be observed over a small temperature interval (10 to 20 °C). This would indicate near complete vaporization (or a rapid decomposition reaction) was accomplished at a given temperature and thus indicate a suitable delivery temperature. For use in a solid-source delivery system this "step" decrease is essential for choosing a sublimation temperature.

Results for each of the novel precursors revealed a gradual decrease in the sample weight versus temperature and time. A typical DTA/TGA decomposition profile for one of the precursors used in this study is shown in Figure 5.1. The increased weight loss at 115 °C is attributable to the loss of the weakly bonded CO group mentioned above in the mass spectrometry precursor characterization. Above this temperature, however, the decomposition profile is nearly linear. This gradual decrease in sample weight indicates that volatilization of these compounds by sublimation technique may be problematic for precursor transport to a CVD reactor. The sample weight percent change for each compound analyzed was between 41 to 50%. Thus, even after a linear temperature increase from room temperature to 600 °C over a 1 h time span only half of the sample had volatilized.

Vapor pressure measurements were taken over a 25 to 80 °C temperature range. A typical vapor pressure versus temperature plot is shown in Figure 5.2. It is obvious that the vapor pressures of each precursor compound are very low even at elevated temperature (0.025 mmHg at 80 °C). For comparison, trimethylgallium (TMG), a widely used metal-organic precursor used in gallium nitride thin film depositions, has a vapor pressure ranging from 68.5 to 283.5 mmHg in the temperature range 0 to 30 °C.

The combined results of the DTA/TGA and vapor pressure analyses indicated that transport of the precursor compounds using a sublimation technique such as a solid-source delivery system could be problematic. A solid-source delivery system, based on a design used to grow TiO_2 thin films at DuPont's research station in Wilmington, Delaware, was originally planned to be used as part of this project. Thus this system was constructed with certain design changes. This type of delivery system proved to be inadequate for precursor transport due to condensation/deposition of the sublimed precursor on the inner tubing walls between the delivery system and reactor. Hence the ultrasonic nebulizing system was constructed and installed. It was this system that enabled the far superior tungsten nitride thin film deposition reported in the following section.

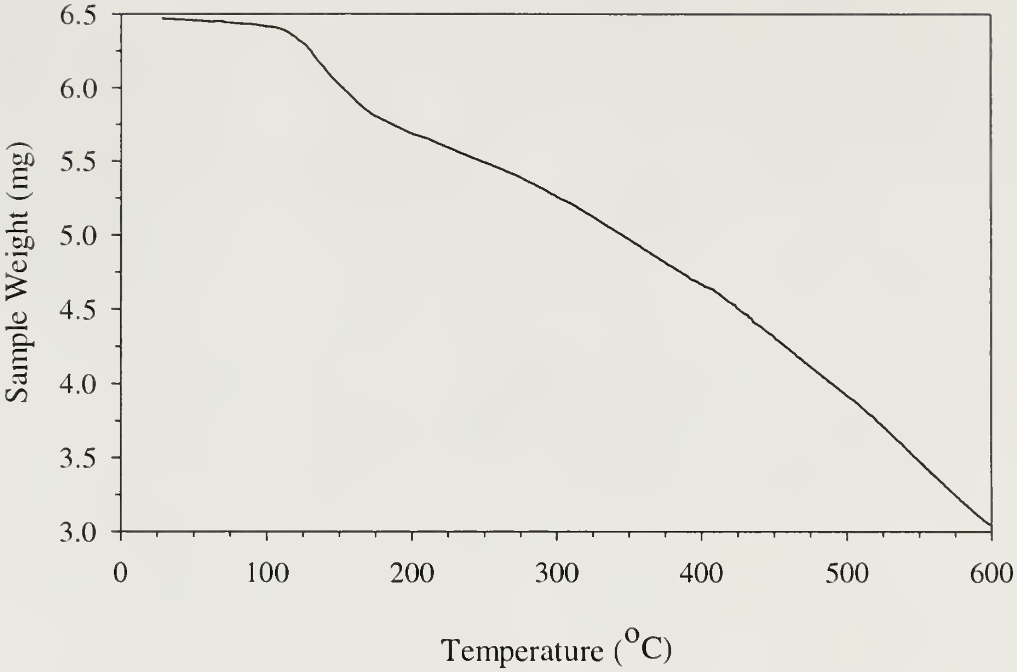

Figure 5.1 Thermal gravimetric analysis results for the $I_2(CO)_2(CH_3CN)W{\equiv}NPh$ complex

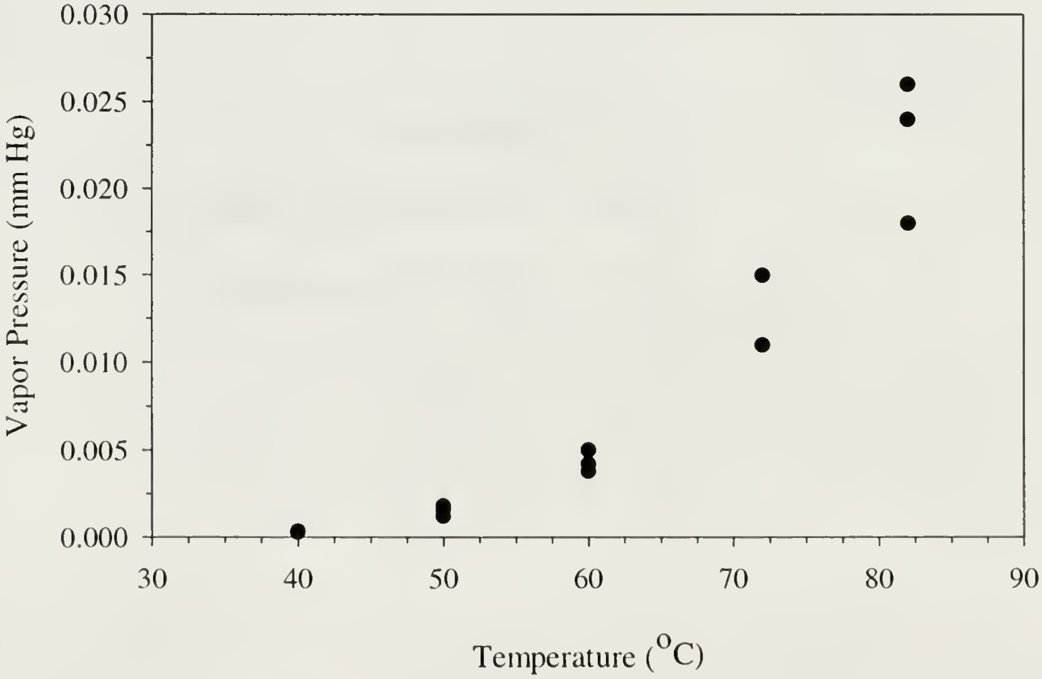

Figure 5.2 Vapor pressure measurements for the $I_2(CO)_2(CH_3CN)W{\equiv}NPh$ complex

5.4 Results and Discussion–Thin Film Growths

Growths using the solid-source delivery system were generally unsuccessful due to very low film growth rates. As explained above, this was attributed to the precursor's low vapor pressures and the inability to transport it to the reactor with this delivery system. Even after a 2 h growth time the silicon composition detected using AES was in excess of 75%. SEM analysis of grown films revealed whisker formation. This has been reported for other material systems, both CVD and electrochemical, as characteristic of films growing in a regime where they are starved for growth material.

Growths using the ultrasonic nebulizing system were much improved with AES and XRD confirmation of WN_X thin film deposition. SEM, 4-point probe, and AES depth profiling of annealed samples were also performed. The combination of these results are so promising that a patent application has been filed.

5.4.1 Surface Morphology

Scanning electron microscopy (SEM) analysis of the grown films revealed complete surface coverage as shown in Figure 5.3. A fairly rough surface morphology can be seen although chemical mechanical polishing could be used to planarize the surface. Films grown on both Si(100) and Si(111) reveal similar complete surface coverage. The secondary stage of WN_X film growth, shown in Figure 5.4, can be characterized as island coalescent similar to the growth observed for boron phosphide. For diffusion barrier applications, growth conditions should be selected to avoid the formation of a rough film due to the necessity to uniformly coat high aspect ratio trenches and vias with a very thin diffusion barrier layer.

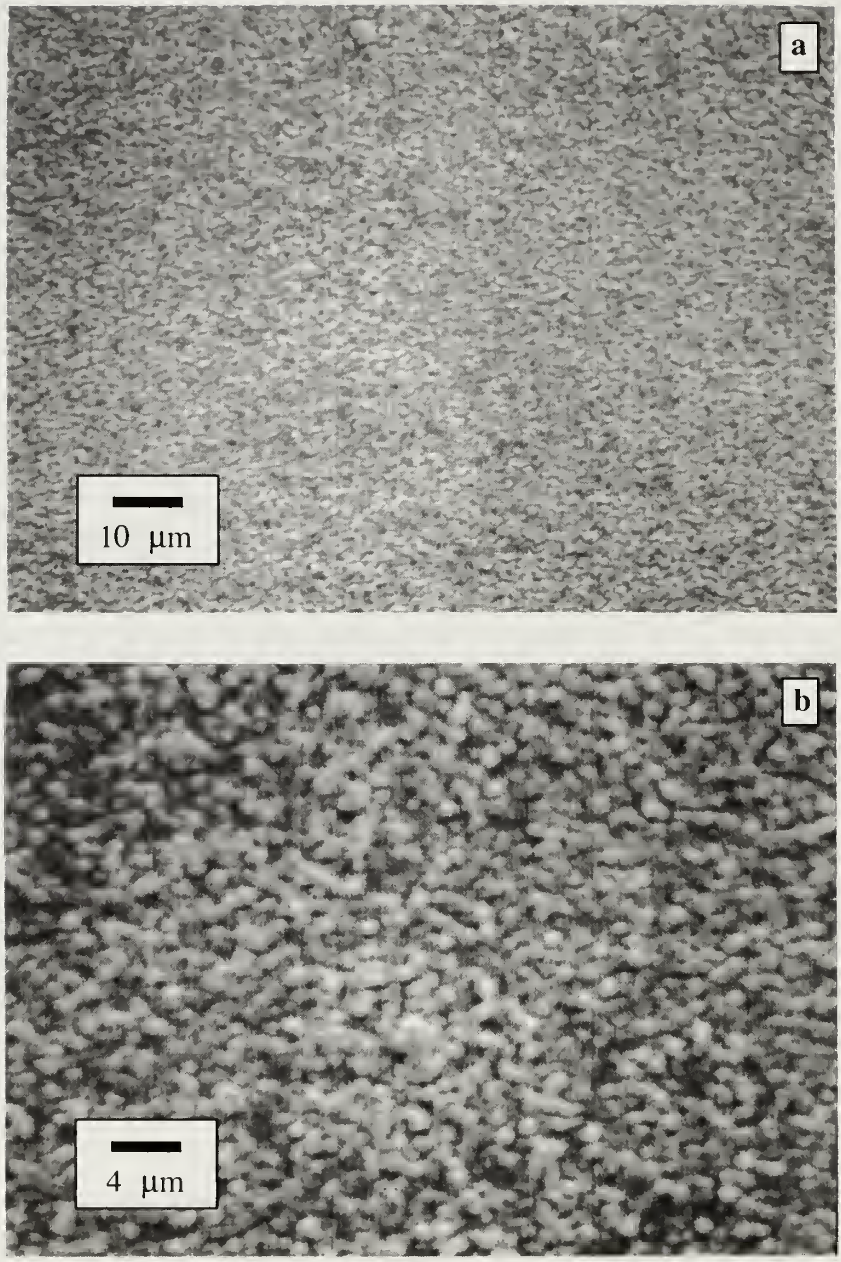

Figure 5.3 SEM micrograph of WN_X growth on Si(100) using $Cl_4(CH_3CN)WN$-*i*-Pr precursor dissolved in benzonitrile at:
a) 1,000 magnification; b) 2,500 magnification

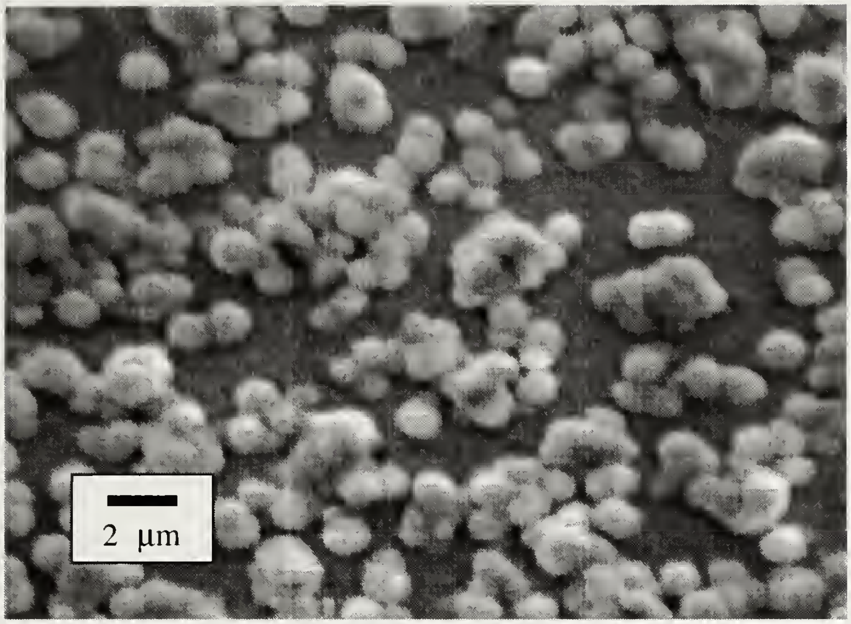

Figure 5.4 SEM micrograph of initial WN_X growth on Si(111) using $Cl_4(CH_3CN)WN$-*i*-Pr precusror

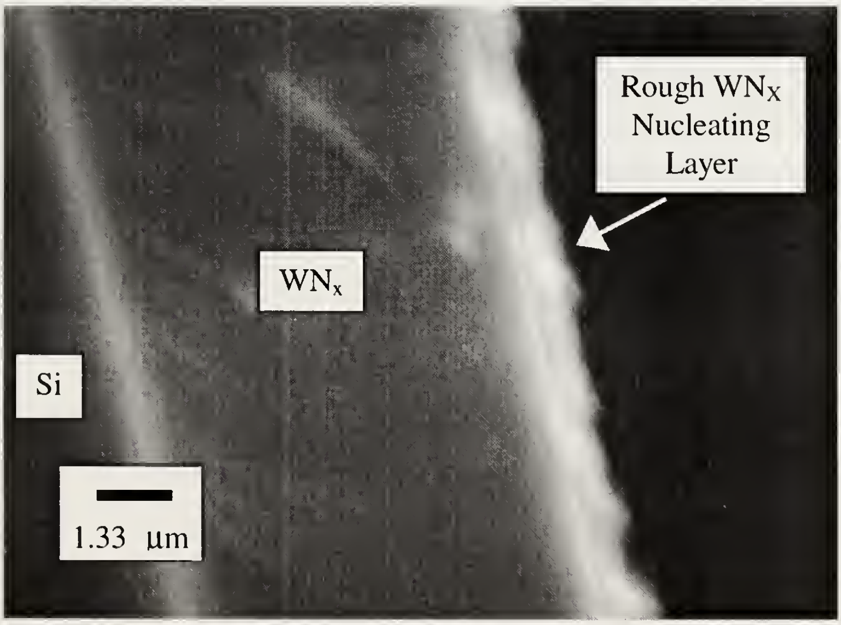
Rough WN_X
Nucleating
Layer
WN_x
Si
1.33 μm

Figure 5.5 SEM cross-sectional micrograph of WN_X growth on Si(100) using $Cl_4(CH_3CN)WN$-*i*-Pr precursor

Cross-sectional SEM revealed the rough film surface as seen by the out-of-focus structures on the top of Figure 5.5. The substrate is seen on the left side of the photo, the uniform film is in the center, and the coarse film surface morphology is on the right. SEM was also used to estimate film thickness. Thin film resistivity values were determined using this thickness and the resistance as measured by a 4-point probe. The thickness of the film shown below was approximated as 5.3 μm, inferring a 2.2 μm/hr growth rate. This is a rather high growth rate for a MOCVD process and quite sufficient for a diffusion barrier material. In fact, assuming adequate barrier integrity after annealing, this implies that the growth time can be significantly reduced to below 15 min.

5.4.2 X-ray Diffraction

X-ray diffraction (XRD) was the primary technique used to verify that the deposited film was tungsten nitride. Tungsten nitride (W_2N) exhibits two strong powder reflection peaks at 37.735 and 43.849 2-theta degrees for the (111) and (200) reflections, respectively. Smaller secondary reflections are seen at 63.736, 76.517, and 80.597 for the (220), (311), and (222) planes, respectively.

Figure 5.6 shows a typical XRD pattern for growth on both Si(100) and Si(111) using the $Cl_4(CH_3CN)WN$-*i*-Pr precursor complex. The primary tungsten nitride reflections seen on these and all other samples are (111) and (200). Polycrystalline growth is evident by the lack of preferentially oriented growth in the substrate growth plane. In fact, the broad

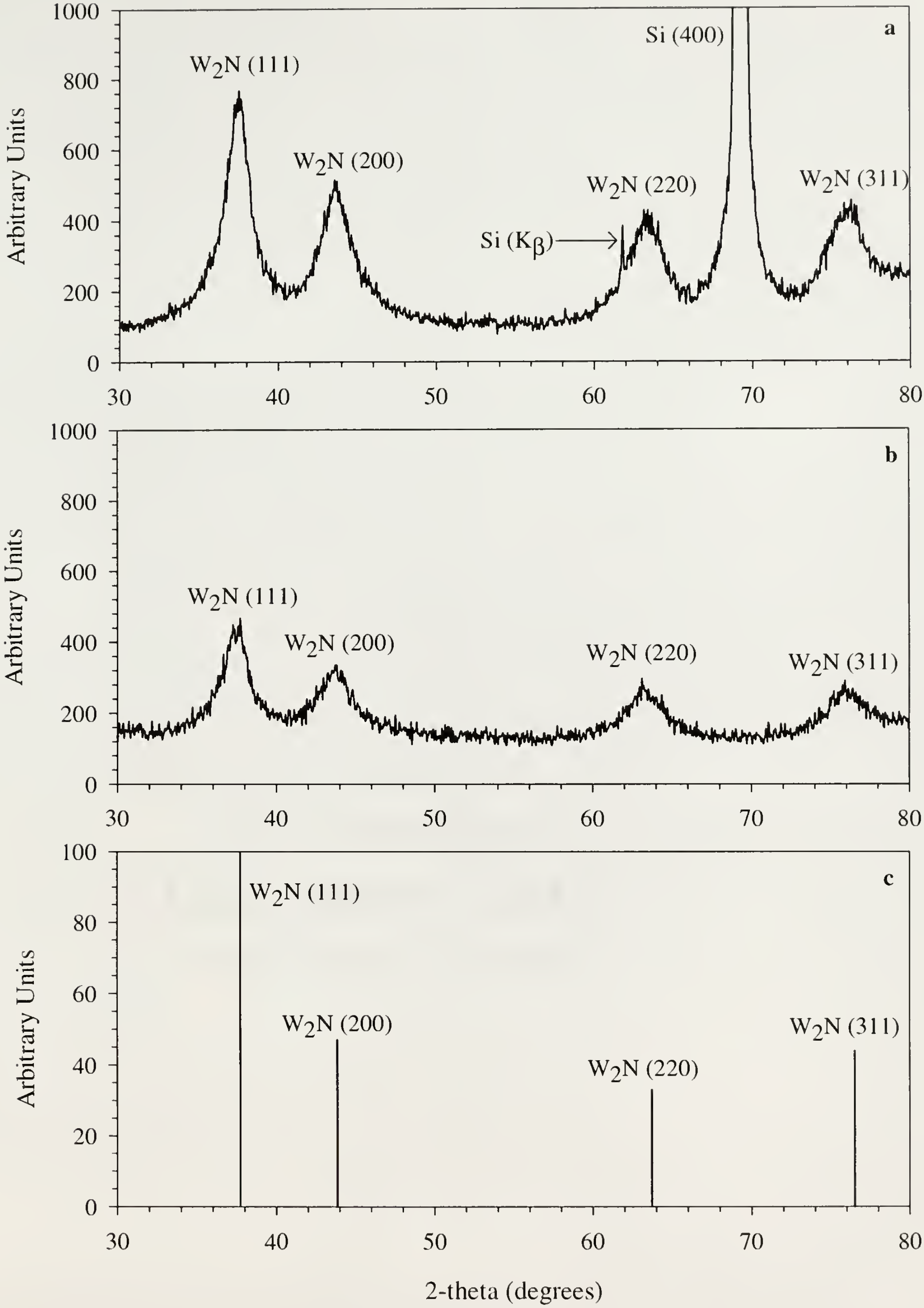

Figure 5.6 XRD patterns of WN$_X$ growth on a) Si(100);
b) Si(111); and c) standard powder pattern

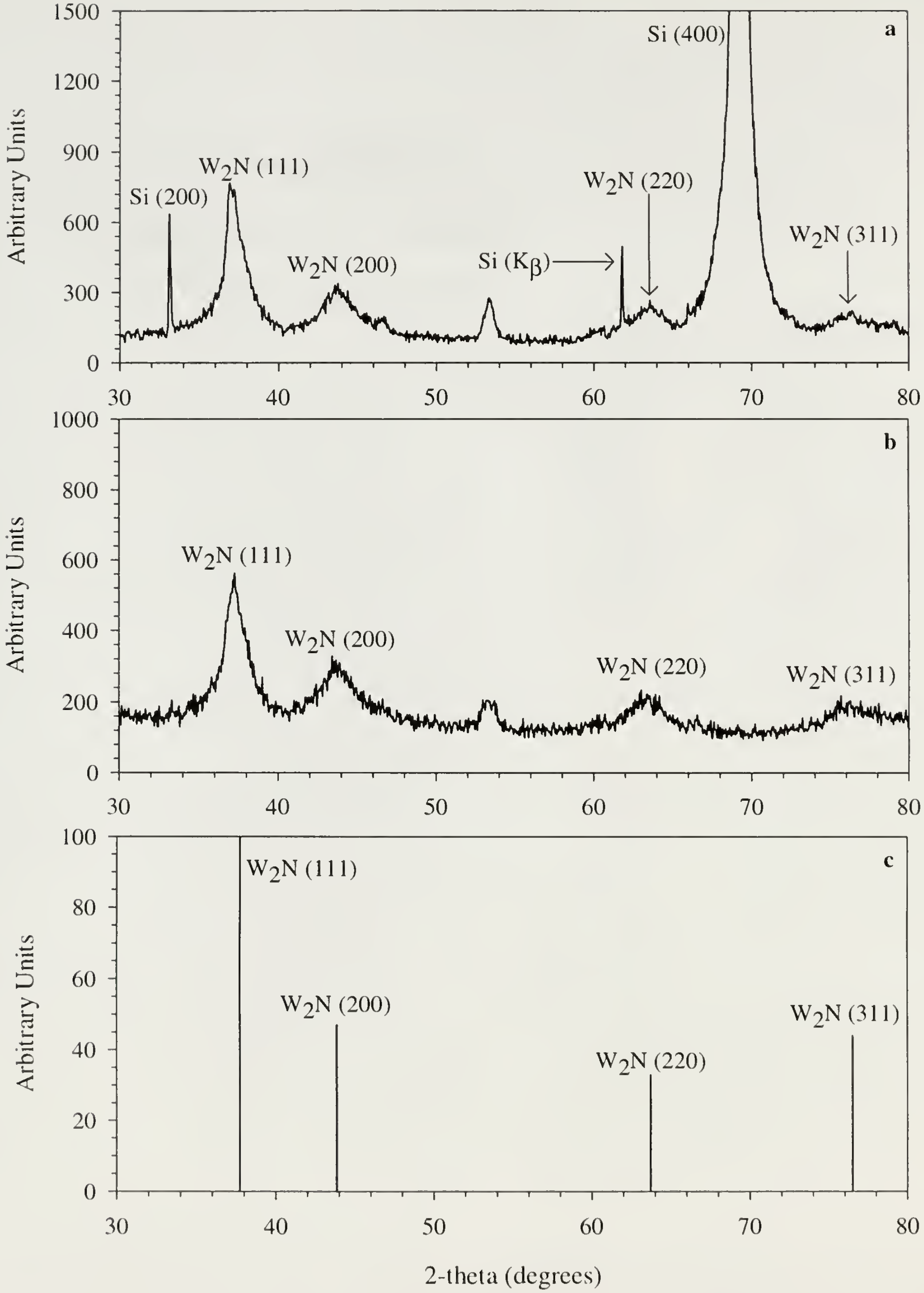

Figure 5.7 XRD patterns of WN_x growth on a) Si(100); b) Si(111); and c) standard powder pattern

peaks (i.e., large full width half max (FWHM)) values of each film indicate that microcrystalline thin films were deposited. While this is typically a very undesirable product for microelectronics devices, it is close to ideal for a diffusion barrier, since microcrystalline films are approaching an amorphous state. As discussed in section 5.1, an amorphous film by definition has no grain boundaries and thus would lack the pathways for fast copper interdiffusion. If either the nitrogen in tungsten nitride or the carbon contaminant can act to "stuff" the microcrystalline grain boundaries, then an adequate copper diffusion barrier is realized. Microcrystalline films are, themselves, not ideal due to the numerous grain boundaries they possess. Figure 5.7 shows a similar XRD spectra for another WN_x deposition. Both figures are representative of XRD data obtained using the ultrasonic nebulizing delivery system.

5.4.3 AES and SIMS

Auger electron spectroscopy (AES) revealed the presence of large-scale carbon contamination in excess of 30%. Exact N and C elemental levels are difficult to quantify due to the preferential removal of N atoms and incorporation of C atoms by Ar^+ sputtering as reported by Ingrey et al. [388]. Still, carbon contamination levels exceed those generally desired for high quality thin films and may act as electron scattering sites, thus raising the film's resistivity value.

Typical AES spectra for a WN_x film for both as-received and 0.5 min sputter time (using a 3keV Ar^+ ion source) are shown in Figures 5.8 and 5.9 for tungsten nitride deposited on Si(100) and Si(111) substrates, respectively. Included in each figure is an

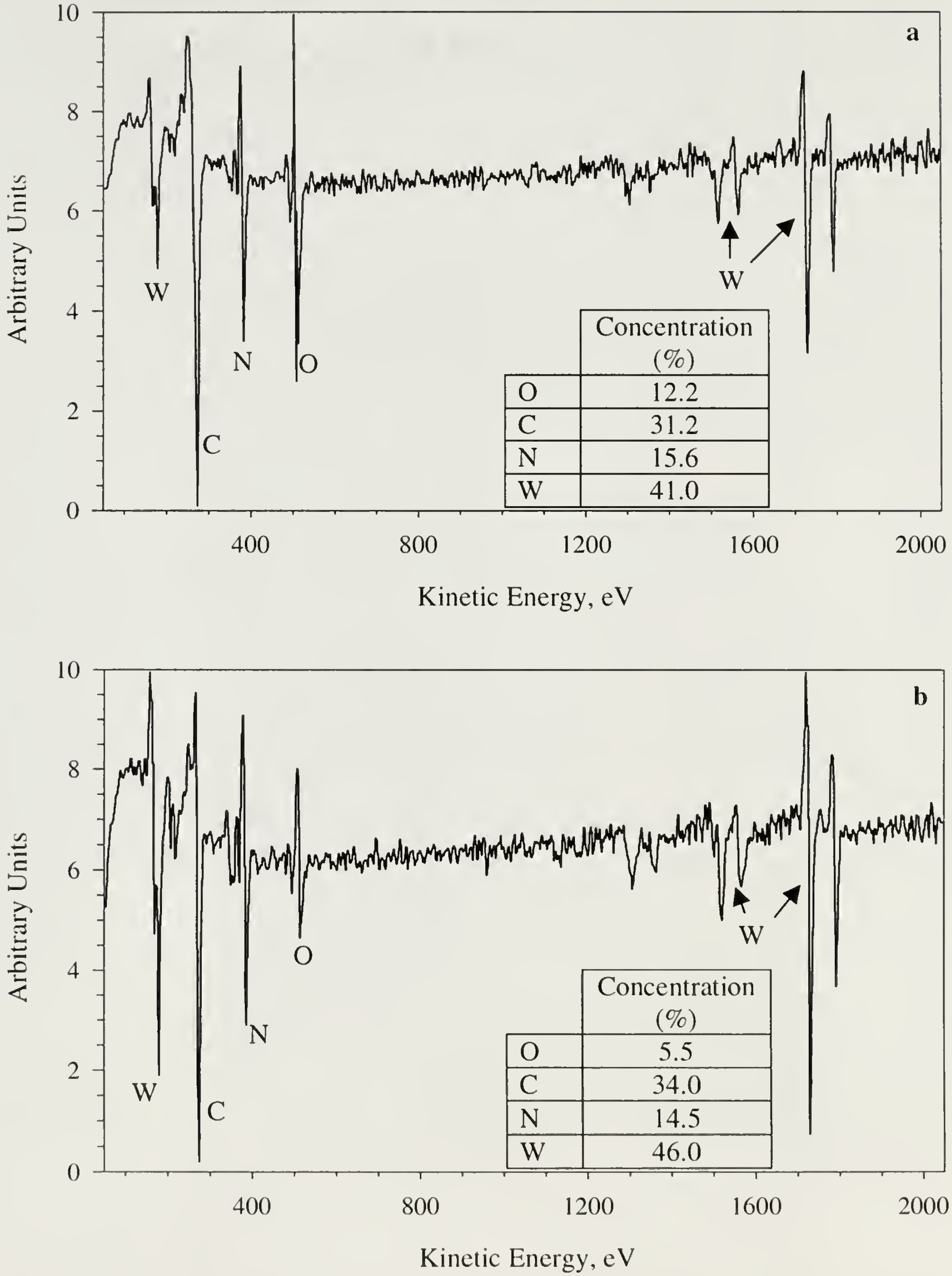

	Concentration (%)
O	12.2
C	31.2
N	15.6
W	41.0

	Concentration (%)
O	5.5
C	34.0
N	14.5
W	46.0

Figure 5.8 AES spectra of WN_X growth on Si(100)
a) As received; b) 0.5 minute sputter

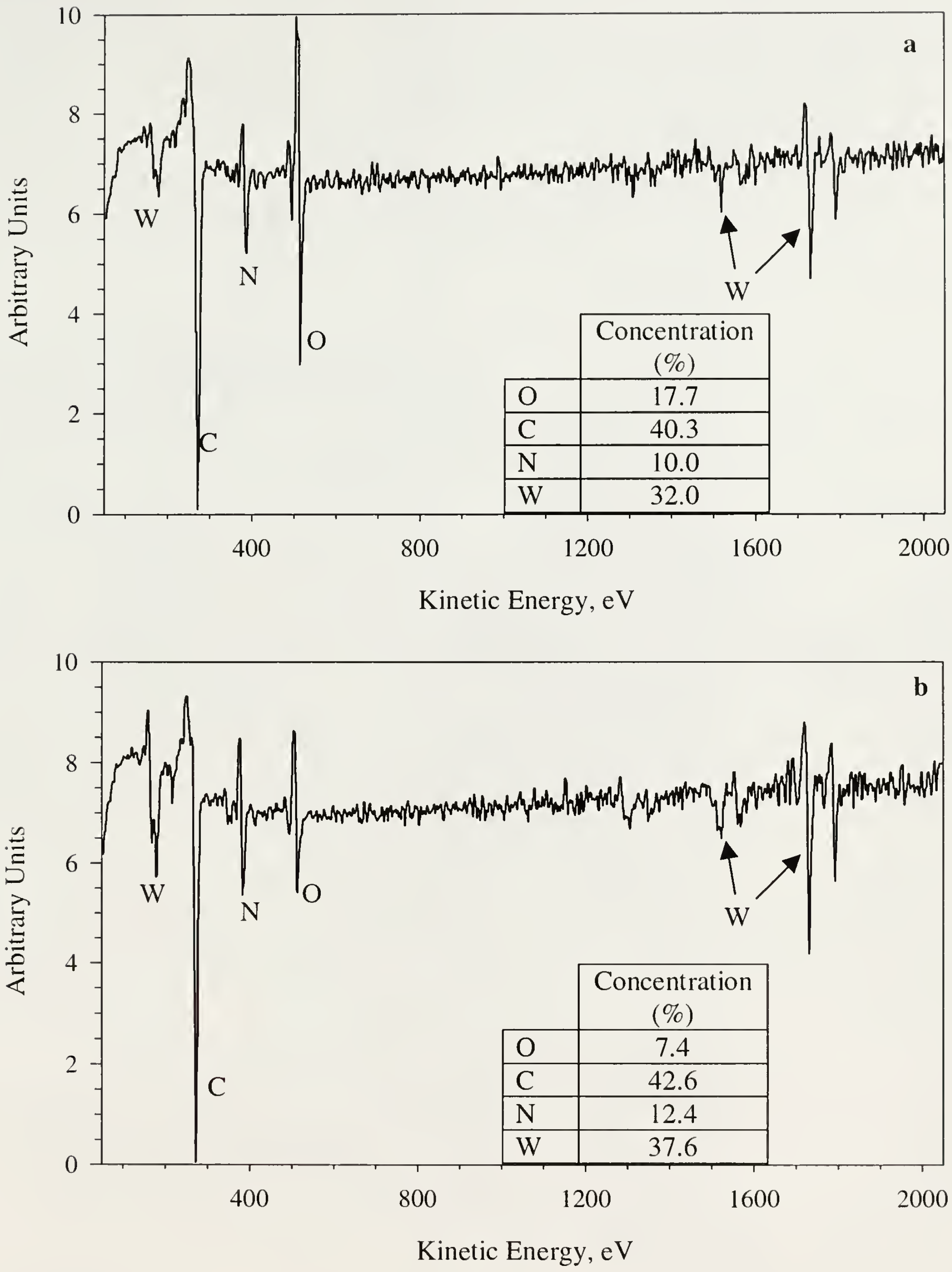

a)

	Concentration (%)
O	17.7
C	40.3
N	10.0
W	32.0

b)

	Concentration (%)
O	7.4
C	42.6
N	12.4
W	37.6

Figure 5.9 AES spectra of WN_X growth on Si(111)
a) As received; b) 0.5 minute sputter

approximate elemental composition analysis based on peak heights and sensitivity factors from [503]. After sputtering each sample, which would remove approximately 25Å of material, the approximate elemental composition of O, C, N, and W were 5, 34, 15, and 46%, respectively. Since the oxygen contribution from the precursor and reactor vacuum leakage are known to be negligible, the oxygen contamination is attributed to post-growth reaction of air with the tungsten lattice. This effect will be exacerbated by the rough surface morphology shown in the SEM cross-section picture shown in Figure 5.5. It is unclear at this point whether the carbon contamination originates from the precursor molecule, the organic solvent, or a combination of the two. Detailed mass spectrometry studies of the gases exiting the reactor are currently being analyzed to determine the exact contamination source.

Depth profiling was performed using AES and SIMS on three samples to determine copper interdiffusion after annealing at 700 °C for 30 minutes in an atmospheric pressure N_2 environment. Results indicate barrier failure at this temperature. The exact source is unknown at this time but is likely a result of either the aforementioned “pinholes” in the tungsten nitride film or copper deposition on the sides of the silicon substrate and subsequent side interdiffusion during annealing.

5.4.4 Four Point Probe

A 4-point probe was used to measure the resistivity of the tungsten nitride films and the backside resistivity of the silicon substrate before and after annealing. For deposition from $Cl_4(CH_3CN)WN$-*i*-Pr dissolved in benzonitrile, a thin film resistivity value of 447 μΩ-cm was obtained with a standard deviation of 130 μΩ-cm. This film had a 2.3 μm/hr film growth rate. Growth from $Cl_4(CH_3CN)WN$-*t*-Bu resulted in a higher thin film resistivity value of 1870 μΩ-cm and a standard deviation of 780 μΩ-cm. Its growth rate was measured at 22 μm/hr and a 55 μm film was deposited. The film thickness significantly raised the thin film resistivity value. Thus, if a thinner film was deposited (i.e., lower growth time), it is believed that a lower thin film resistivity value would be obtained.

These values correspond favorably to values reported by other researchers for both MOCVD of TiN and CVD/MOCVD of WN_X. For instance, recently Lu et al. at Texas Instruments reported that MOCVD of TiN using tetrakis(dimethylamino)-titanium (TDMAT) precursor yielded bulk resistivity values of approximately 3000 μΩ-cm, which are similar to that reported for TDMAT/NH_3 coreacted films (≈ 2400 μΩ-cm) [516]. Chiu et al. report resistivity values ranging from 620 to over 8000 μΩ-cm for film growth rates of 0.07 and 0.44 μm/hr, respectively, for WN_X grown from (*t*-BuNH)$_2$W(N-*t*-Bu)$_2$ [385]. Thus, the resistivity values measured in this work are much lower than each of these and the growth rates are significantly higher. Sputtered WN_X films typically possess resistivity values in the range 200 to 4600 μΩ-cm, which are at best equal to and typically much higher than our thin film values [259, 264, 517]. Hence, the carbon contamination reported above does not seem to greatly impact the film's resistivity for either complex. Efforts to reduce the carbon levels are ongoing. Table 5.2 shows the comparison between the current WN_X MOCVD results with those of other researchers.

5.5 Conclusions

Tungsten nitride thin films with significant carbon incorporation were successfully deposited using novel single-source metal-organic precursors. Low resistivity thin films deposited at relatively low temperature (<700 °C) were achieved. The lowest film resistance values were 447 and 1870 μΩ-cm for the $Cl_4(CH_3CN)WN$-*i*-Pr and $Cl_4(CH_3CN)WN$-*t*-Bu precursor complexes, respectively. These values are considerably lower than those reported by most other researchers. In addition, a microcrystalline film crystal structure was observed using X-ray diffraction. This is much closer to the ideal amorphous diffusion barrier film structure than the more porous crystalline films reported by others for deposition of TiN, TaN, and WN_X films using CVD and sputtering. AES indicates a W:N:C ratio of 3:1:2 for films deposited using $Cl_4(CH_3CN)WN$-*i*-Pr. Although the carbon composition is elevated due to either incomplete precursor decomposition or dissociated precursor/solvent incorporation in the tungsten nitride film, it does not appear to raise the overall thin film resistivity values to an unacceptably high level.

Table 5.2 Comparison of current work with that reported for WN_X and TiN

Precursor	Product Material	Resistivity (μΩ-cm)	Grain Structure	Growth Rate (μm/hr)	Reference
$Cl_4(CH_3CN)WN$-*i*-Pr	WN_X	447	Microcrystalline	2.2	This Work
$Cl_4(CH_3CN)WN$-*t*-Bu	WN_X	1870	Microcrystalline	21	This Work
$(t\text{-BuNH})_2W(N\text{-}t\text{-Bu})_2$	WN_X	620-2000	N/A	0.12 to 0.60	385
$Ti(NMe)_4$	TiN	2000-4000	Microcrystalline	2.4	516, 518
WF_6+NH_3	WN_X	1000-3000	Crystalline	6 to 27	358
$TiCl_4+NH_3$	TiN	120-2500	Crystalline	N/A	519
Sputtered WN_X	WN_X	180-750	Crystalline	1.4 to 3.5	264
Sputtered TiN	TiN	100-700	Columnar / Porous	0.6 to 6	518

CHAPTER 6
CONCLUSIONS AND RECOMMENDATIONS FOR FUTURE WORK

6.1 Conclusions

CVD of BP, BN, and WN_x thin films on a variety of substrates were examined. The purpose of this study was to learn fundamental and experimental aspects of the deposition of these materials and to determine the suitability of various growth techniques and precursors for desired film formation. Successful deposition of the desired phases and/or compositional and electrical properties of each could result in major breakthroughs in the microelectronics and coatings industries. The first step in the CVD of each material was to model the respective processes in order to corroborate a priori assumptions and guide subsequent experimental work.

Hence at the outset of each investigation, equilibrium modeling of each system was conducted over a wide range of temperature and inlet precursor compositions to simulate CVD conditions. The deposition domains of each desired product were noted. In the case of BP using BCl_3, PCl_3, and H_2 as precursors, the experimental data range investigated coincided well with the solid phase diagram generated through the equilibrium calculations. This is in spite of the fact that BP was experimentally deposited in a kinetically controlled fashion (see Figure 3.1). As expected, the model also revealed the existence of $B_{13}P_2$ stability at elevated temperature, although the exact $BP/B_{13}P_2$ decomposition temperature depended heavily on the initial precursor ratios. Gradual replacement of H_2 with an inert gas drastically shifted the solid phase diagram boundaries, resulting in a very large increase in the region of no solid deposition. This is a result of the inability of the BCl_3 and PCl_3 precursors to react and form the necessary HCl byproduct. Addition of HCl had an etching effect on both BP and $B_{13}P_2$ at lower initial BCl_3:PCl_3 ratios. The domain of BP solid phase formation, however, was increased significantly at higher initial BCl_3:PCl_3 ratios.

BN thermodynamic equilibrium was analyzed over a 1200 K temperature range using BCl_3, NH_3, and H_2 as precursors. cBN or its solid phase mixture with boron was found to be the stable phase at low temperatures over the entire precursor range studied. This is in direct contrast to the previously accepted Bundy-Wentorf "equilibrium phase diagram" and the results of experimental deposition of BN. The cBN/hBN transition temperature was 1576 K over the entire precursor range. The domain of cBN stability increased as the initial BCl_3:NH_3 ratio increased and as the initial H_2 partial pressure decreased. This is believed to be a result of the production of more HCl from the BCl_3 decomposition that preferentially etched the cBN+B region. This is supported by calculations showing that the addition of HCl into the system preferentially etches this region. Analysis indicates that the most favored deposition condition to grow cBN would be using an inert gas as a replacement for H_2. cBN was the only stable phase at temperatures below 1576 K over the entire precursor range studied.

Equilibrium in the Ga-N system concentrated on developing a series of generalized equations to account for lattice mismatch induced strain energy and then incorporating these equations in the resulting equilibrium analysis. Calculations were performed at equilibrium and one atm N_2 partial pressures. Examination of GaN growth on sapphire (0001) showed that the strain energy, resulting from the large lattice mismatch of 16.1%. incorporated in the growing GaN film, exceeds the critical limit for GaN stability for both N_2 partial pressures considered. GaN growth on Al_2O_3 results in a much smaller lattice mismatch (<1% in the y direction) and hence greatly reduced strain energy incorporation. For deposition on $LiGaO_2$, one atm N_2 partial pressure the GaN melting point was only reduced by 11 and 43 K for GaN basal and prism plane deposition, respectively. A large GaN + gas domain, a fundamental requirement for CVD thin film growth, is thus still present.

Boron phosphide experimental depositions were successfully conducted on Si(100), Si(111), Al_2O_3 (0001), maacle diamond, off-cut diamond substrates using BCl_3, PCl_3, and H_2 as precursors. Growth on nickel substrates was unsuccessful due to the melting of the impure substrate below the growth temperature. Growth was determined to be kinetically controlled throughout the temperature and flowrate ranges considered. An Arrhenius dependence of the deposition rate with temperature was found for the Si(100) and Si(111) substrates, with apparent activation energies of 26.5 and 53.2 kJ/mol, respectively. Microstructure revealed ball-like island formation growth that nucleated to form uniform films as the deposition time was increased. This is consistent with the results of other researchers using a bromine-based chemistry. The presence and physical properties of BP films was confirmed by FTIR and Raman spectroscopy, XRD, AES, XPS, XTEM, conductivity typing, and Vicker's microhardness testing. SEM and AFM were used for surface morphology characterization.

Dispute has existed in the literature since 1959 as to whether the possibility of stabilizing cBN by simple cBP nitridation is possible or if the conventionally observed hBN phase would instead formed. Although the idea has been previously investigated by other researchers, only XRD was used to characterize the film crystal structure (in one report FTIR spectroscopy was also attempted but results were inconclusive). Due to its far superior physical properties, the cubic phase is desired over its hexagonal counterpart. In an attempt to finally answer this looming question, in-situ nitridation of boron phosphide films was conducted and analyzed by SEM, AFM, FTIR and Raman spectroscopy, XRD, AES, XPS, and XTEM. FTIR and Raman analysis of the films first revealed the possible presence of cBN. Auger spectroscopy detected only hBN on the same samples. These spectra obviously conflicted with those of FTIR and Raman. XPS was inconclusive, with apparent indications of both c-BN and h-BN crystal structures present on the same sample. It is believed that the limited volume sampling of Auger spectroscopy compared to FTIR and Raman spectroscopy, coupled with the possible graphitization of a cubic BN sample during sputtering, accounts for the apparent conflicting data.

MOCVD of tungsten nitride thin films from novel imido metalorganic precursors was attempted using two separate delivery systems. Both systems were utilized as part of this project. The first delivery system was a solid-source system designed to volatilize the precursor by slowly lowering it through a concentrated high powered light source and transporting the sublimed precursor via a carrier gas stream to the reactor. Depositions utilizing this system were largely unsuccessful due to significant film contaminants and extremely low growth rates. It is believed that the precursor vapor pressures were too low to permit their successful transport to the reactor. Furthermore, it is believed that oxygen and carbon, present in two of the precursors examined and subsequently liberated after precursor decomposition, were incorporated into the resulting film and thus accounted for a significant fraction of the film contamination.

As a result of the inability to grow tungsten nitride films utilizing the novel imido precursors, an ultrasonic delivery system was constructed in conjunction with Dr. Roy Gordon of Harvard University. In this system, the precursor is dissolved in a solvent, the solution is injected via a syringe pump into a carrier gas stream, and subsequently it is transported to the reactor. Thus, the low vapor pressure problem was circumvented. MOCVD growths were vastly improved using the $Cl_4(CH_3CN)WN$-*i*-Pr and $Cl_4(CH_3CN)WN$-*t*-Bu precursor complexes. Confirmation of WN_x films was made using XRD and AES. Four point probe analysis yielded thin film resistivity values of 447 and 1870 μΩ-cm for growths using the $Cl_4(CH_3CN)WN$-*i*-Pr and $Cl_4(CH_3CN)WN$-*t*-Bu precursors, respectively. A 100 nm Cu film was e-beam deposited on several samples and these samples were subsequently annealed at 700 °C for 30 minutes in a N_2 environment. AES and SIMS depth profiling detected Cu in the Si substrate, though it is believed that the detected Cu may have originated from the sides of the Si substrate rather than by penetration of the WN_X barrier layer. Copper diffusion though pin holes in the film's surface is also a possibility.

6.2 Recommendations for Future Work

a) Improve vacuum capability of CVD system by installation of a reactor load-lock system. Perhaps the most limiting factor that the current CVD system encounters is contamination each time the reactor and surrounding tubing is completely opened to the atmosphere to load or remove samples. The addition of a load-lock system would minimize this contamination and should result in higher quality film growths. A design for such a system has already been made and is available to the student taking over the tungsten nitride project. Since a 2 ¾"gate valve has been added to the reactor top as part of this project, the construction and installation of a load-lock system utilizing the gate valve's existing exterior Del-Seal flange would be relatively simple. Coupled with the addition of the load-lock, a new motorized thermocouple translator must be constructed. This must be completely encapsulated to ensure vacuum system integrity. A rotary motion control can easily be added to this translator unit to improve film uniformity. As with the load-lock system, preliminary design of the translator system has already been performed.

b) Install and utilize mass spectrometry on the reactor outlet line. Use of mass spectrometry (MS) on the reactor outlet will allow a detailed analysis of several system parameters. During the course of film growths, gas phase by-products would be identified and their quantities estimated. This can be extremely useful in the postulation of film growth reaction kinetics as well as trace contaminant levels. During reactor down-time, the MS can be used to leak check the vacuum integrity of the system by noting oxygen, water vapor, CO, and CO_2 deviations from a baseline measurement. Finally, the source of carbon contamination may be determined by analysis of the integrity of each leaving group from the tungsten nitride central fragment.

c) Purchase of a new dual sensor H_2 leak detector. The H_2 leak detector currently used in the system is quite old and its calibration drifts daily. At times, a high or low level alarm sounds, even though no H_2 is being flowed at that time. This is currently the only safety component of the CVD system, which is in close proximity to other experimental equipment used by researchers that are unfamiliar with the CVD system. With this in mind, it is imperative that the H_2 detector operate correctly. A dual sensor is necessary in order to detect a H_2 leak in the reactor fume hood and the plexiglass valve control box simultaneously.

d) Installation of an automatic switching valve that will switch the H_2 carrier gas stream to an inert gas if sudden pressurization occurs. As mentioned in part c, although multiple researchers will be using equipment near the CVD reactor, the only safety equipment associated with the system is a H_2 leak detector. The addition of an automatic switching valve capable of switching the system from a H_2 to an inert carrier gas would greatly improve the safety of the system, its operator, and other researchers. Currently, a manual three-way ball valve is used to switch between carrier gas types.

e) If a video output connection is available, a small Pentium class computer should be connected to the research group's SEM. The use of a computer in conjunction with the SEM will allow the capture of digital SEM images in addition to the currently available paper pictures. These digital images, saved directly to the computer's hard drive, can then be easily manipulated for poster, conference, and thesis/dissertation presentations. In addition, brightness, contrast, and image size can all be easily manipulated in many commercially available programs. Poor image resolution could immediately be ascertained and photos retaken as well as avoidance of the time consuming picture development process. Finally, numerous images of a single sample could be taken and saved without cost concerns associated with printed film.

f) Selection of a new tungsten nitride precursor solvent. Benzonitrile is the current solvent of choice in the tungsten nitride MOCVD experiments. Unfortunately, significant liquid pooling occurs at the colder portions of the reactor (quartz viewport at the top of the reactor and bottom cooling water jacket) during the course of each run. This necessitates extensive cleaning after each experiment. A new solvent with a higher volatility may eliminate this problem. Any new solvent must: 1) not preferentially separate from the dissolved precursor material in the ultrasonic nebulizer aerosol unit, 2) have a viscosity low enough to permit easy transport to the aerosol unit via the 1/16” PTFE tubing, 3) be thermally stable at deposition temperatures to minimize contaminant incorporation in the tungsten nitride film, and 4) not react with the solid precursor compound.

REFERENCES

1. Diamond, Silicon Carbide and Related Wide Bandgap Semiconductors, edited by J.T. Glass, R. Messier, and N. Fujimori, Mater. Res. Soc. Symp. Proc., Pittsburgh, PA, 162 (1990)

2. R.F. Davis, Z. Sitar, B.E. Williams, H.S. Kong, H.J. Kim, J.W. Palmour, J.A. Edmond, J. Ryu, J.T. Glass, and C.H. Carter, Jr., Mater. Sci. Eng. B, 1, 77 (1988)

3. J. H. Edgar, Properties of Group III Nitrides, INSPEC, The Institution of Electrical Engineers, Short Run Press Ltd., Exeter, United Kingdom (1994)

4. Landolt-Bornstein, Semiconductors, Vol. III/22a

5. H. Welker and H. Weiss, Solid State Physics, 3, 1 (1956)

6. P. Popper and T.A. Ingles, Nature, 179, 1075 (1957)

7. J.A. Perri, S. LaPlace, and B. Post, Acta Cryst., 11, 310 (1958)

8. F.V. Williams and R.A. Ruehrwein, J. Amer. Chem. Soc., 82, 1330 (1960)

9. V.I. Matkovich, Acta Cryst., 14, 93 (1961)

10. L.H. Spinar and C.C. Wang, Acta Cryst., 15, 1048 (1962)

11. J.L. Peret, J. Amer. Ceram. Soc., 47, 44 (1964)

12. E.M. Kelder, A. Goossens, P.J. van der Put, and J. Schoonman, J. Physique, C5, 567 (1989)

13. A. Besson, C.R. Acad. Sci., 113, 78 (1891)

14. H. Park, Ph.D. Thesis, Duke University (1983)

15. P. Groot, J.H.F. Grondel, and P.J. van der Put, Solid State Ionics, 16, 95 (1985)

16. B. Stone and D. Hill, Phys. Rev. Letters, 4, 282 (1960)

17. N. Sclar, J. Appl. Phys., 33, 2999 (1962)

18. R.J. Archer, R.Y. Koyoma. E.E. Loebner, and R.C. Lucas, Phys. Rev. Lett., 12, 538 (1964)

19. C.C. Wang, M. Cardona, and A.G. Fischer, RCA Rev., 25, 159, (1964)

20. J. Lidstrom, K. Fundell, and A. Lind, Proc. 4th Intern. Conf. On CVD, 547 (1973)

21. T. Takenaka, M. Takigawa, and K. Shohno, Jpn. J. Appl. Phys., 15, 2235 (1976)

22. T. Mizutani, H. Asano, T. Nishiniga, and S. Uchiyama, Jpn. J. Appl. Phys., 16, 1629 (1977)

23. M. Takigawa, M. Hiriyama, and K. Shohno, Jpn. J. Appl. Phys., 13, 411 (1974)

24. D.E. Hill and A.S. Epstein, U.S. Patent 3,077,506 (1963)

25. D.E. Hill, U.S. Patent 3,071,715 (1963)

26. F.V. Williams, R.A. Ruehrwein, and D.E. Hill, U.S. Patent 3,054,936 (1962)

27. Y. Kumashiro, Y. Okada, S. Misawa, and T. Koshiro, Abstract 1092, p. 1520, The Electro. Soc. Ext. Abstr., Vol.87-2, Honolulu, HI, Oct. 18-23, 1987

28. F.V. Williams, R.A. Ruehrwein, and D.E. Hill, U.S. Patent 3,022,452 (1962)

29. R.A. Ruehrwein, U.S. Patent 3,069,604 (1962)

30. Y. Kumashiro and Y. Okada, Appl. Phys. Lett., 47, 64 (1985)

31. Y. Kumashiro, T. Koshiro, and Y. Okada, J. Electro. Soc., 136, 1830 (1989)

32. T. Takenaka, M. Takigawa, and K. Shohno, Jpn. J. Appl. Phys., 15, 2021 (1976)

33. T. Takenaka, M. Takigawa, and K. Shohno, J. Electro. Soc., 125, 633 (1978)

34. B.A. Gruber, U.S. Patent 3,009,230 (1961)

35. S. Motojima, Y. Ohtsuka, S. Kawajiri, Y. Takahashi, and Y. Sugiyama, J. Mater. Sci., 14, 496 (1979)

36. D.H. Grantham, U.S. Patent 4,227,977 (1980)

37. Anon. Photonics Spectra, October 1984, 30

38. A. Goossens, E.M. Kelder, J. Schoonman, Proc. Electro. Soc., 90-12, Proc. Int. Conf. Chem. Vap. Deposition, 11th, 567 (1990)

39. A. Goossens, Ph.D. thesis, Delft University of Technology, 1991

40. D.C. Harris, Proc. SPIE-Int. Soc. Opt. Eng., 2552, 325 (1995)

41. H. Moisson, C.R. Acad. Sci., 113, 624 (1891)

42. H. Moisson, C.R. Acad. Sci., 113, 726 (1891)

43. H. Moisson, C.R. Acad. Sci., 113, 787 (1891)

44. T. Kobayashi, K. Susa, and S. Taniguchi, Mat. Res. Bull., 9, 625-632 (1974)

45. K.P. Ananthanarayanan, C. Mohanty, and P.J. Gielisse, J. Cryst. Growth, 20, 63 (1973)

46. B.D. Stone, US Patent, No. 3009780 (1959)

47. R.A. Burmeister and P.E. Greene, Bull. Amer. Phys. Soc., 10, 1184 (1965)

48. M. Iwami, N. Fujita, and K. Kawabe, Jpn. J. Appl. Phys., 10, 1746 (1971)

49. M. Iwami, T. Tohda, and K. Kawabe, Electr. Eng. Jpn., 95, 19 (1975)

50. R.I. Stearns and P.E. Greene, J. Electro. Soc., 112, 1239 (1965)

51. R.A. Burmeister and P.E. Greene, Trans. Met. Soc. AIME, 239, 408 (1967)

52. T.L. Chu, M. Gill, and R.K. Smeltzer, J. Cryst. Growth, 33, 53 (1976)

53. T.L. Chu, J.M. Jackson, and R.K. Smeltzer, J. Electro. Soc., 120, 802 (1973)

54. N. Kato, W. Kammura, M. Iwami, and K. Kawabe, Jpn. J. Appl. Phys., 16, 1623 (1977)

55. Y. Kumashiro, T. Yao, and S. Smeltzer, J. Cryst. Growth, 33, 53 (1976)

56. R.C. Vickery, Nature, 184, 268 (1959)

57. G.V. Samsonov and Y.B. Titkov, Rus. J. Appl. Chem., 36, 636 (1963)

58. E. Schroten, A. Goossens, and J. Schoonman, J. Appl. Phys., 79, 4465 (1996)

59. H.M. Mansevit, W.B. Hewitt, A.J. Nelson, and A.R. Mason, J. Electro. Soc., 136, 3070 (1989)

60. R.J. Baughman and D.S. Ginley, J. Solid State Chem., 50, 189 (1983)

61. T.L. Chu, J.M. Jackson, A.E. Hyslop, and S.C. Chu, J. Appl. Phys., 42, 420 (1971)

62. M. Takigawa, M. Hirayama, and K. Shohno, Jpn. J. Appl. Phys., 13, 411 (1974)

63. K. Shohno, H. Ohtake, and J. Bloem, J. Cryst. Growth, 45, 187 (1978)

64. K. Shohno, M. Takigawa, and T. Nakada, J. Cryst. Growth, 24/25, 193 (1974)

65. Y. Hirai and K. Shohno, J. Cryst. Growth, 41, 124 (1977)

66. K. Nohaka, C.J. Kim, and K. Shohno, J. Cryst. Growth, 50, 549 (1980)

67. Y. Kumashiro, T. Yao, and S. Gonda, J. Cryst. Growth, 70, 515 (1984)

68. T. Takenaka, M. Takigawa, and K. Shohno, Jpn. J. Appl. Phys., 14, 549 (1975)

69. T.L. Chu, J.M. Jackson, and R.K. Smeltzer, J. Cryst. Growth, 15, 254 (1973)

70. T. Nishinaga, H. Ogawa, H. Watanabe, and T. Arizumi, J. Cryst. Growth, 13/14, 346 (1972)

71. T. Nishinaga and T. Mizutani, Jpn. J. Appl, Phys., 14, 753 (1975)

72. A. Goossens and J. Schoonman, J. Electro. Soc., 139, 893 (1992)

73. E.M. Kelder, Ph.D. thesis, Delft University of Technology, 1991

74. E. Schroten, A. Goossens, and J. Schoonman, J. Appl. Phys., 83, 1660 (1998)

75. E. Schroten, A. Goossens, and J. Schoonman, Mater. Res. Soc. Symp. Proc., 451, 209 (1997)

76. S. Motojima, S. Yokoe, and K. Sugiyama, J. Cryst. Growth, 49, 1 (1980)

77. Y.K. Grinberg, Z.S. Medvedeva, A.A. Eliseev, and E.G. Zhukov, Sov. Phys. Dok., 10, 6 (1965)

78. A.F. Armington, J. Cryst. Growth, 1, 47 (1967)

79. R.H. Wentorf, Jr., J. Chem. Phys., 36, 1990 (1962)

80. R.H. Wentorf, Jr., J. Chem. Phys., 26, 956 (1957)

81. F.P. Bundy and R.H. Wentorf, J. Chem. Phys., 38, 1144 (1963)

82. R.S. Pease, Acta Cryst., 5, 356 (1952)

83. A. Herold, B. Marzluf, and P. Perio, C. R. Acad. Sci., 246, 1866 (1958)

84. T. Matsuda, N. Uno, H. Nakai, and T. Hirai, J. Mater. Sci., 21, 649 (1986)

85. J. Thomas, Jr., N.E. Weston, and T.E. O'Connor, J. Am. Chem. Soc., 84, 4619 (1963)

86. R. F. Corrigan and F. P. Bundy, J. Chem. Phys, 63, 3812 (1975)

87. R.C. DeVries, General Electric Company Corporate Research and Development Report No. 72CRD178, 1972

88. L. Vel, G. Demazeau, and J. Etourneau, Mat. Sci. Eng., B10, 149 (1991)

89. H. Ehrhardt, Surf. Coat. Tech. 74/75, 29 (1995)

90. M. Murakawa and S. Watanabe, Proc. 1st Int. Conf. Appl. Diamond and Related Materials, Auburn, AL, Elsevier, 641 (1990)

91. J.C. Angus, Y. Wang, and M. Sunkara, Annu. Rev. Mater. Sci., 21, 221 (1991)

92. W.A. Yarbrough, J. Vac. Sci. Technol. A, 9, 1145 (1991)

93. H. Holleck, J. Vac. Sci. Technol. A, 4, 2661 (1986)

94. R.C. DeVries, Diamond and Diamond-Like Films and Coatings, R.E. Clausing (ed.), Plenum Press, New York, NY, 151 (1991)

95. M.J. Powers, M.C. Benjamin, L.M. Porter, R.J. Nemanich, R.F. Davis, J.J. Cuomo, G.L. Doll, and S.J. Harris, Appl. Phys. Lett., 67, 3912 (1995)

96. O. Mishima, Synthesis and Properties of Boron Nitride, J.J. Pouch and S.A. Alterovitz (eds.), Materials Science Forum, Trans Tech Publications, Brookfield, 54/55, 313 (1990)

97. K. Era, O. Mishima, Y. Wada, J. Tanaka, and S. Yamaoka, Springer Proc. In Phys., 38, 386 (1989)

98. O. Mishima, K. Era, J. Tanaka, and S. Yamaoka, Appl. Phys. Lett., 53, 962 (1988)

99. J.H. Edgar, J. Mater. Res., 7, No.1 (1992)

100. O Mishima, J. Tanaka, S. Yamaoka, and O. Fukunaga, Science, 238, 181 (1987)

101. Y. Ichinose, H. Ssitoh, and Y. Hirotsu, Surf. Coat. Tech., 43/44, 116 (1990)

102. R. Habner and B. Lux, Diamond Relat. Mater., 2, 1277 (1993)

103. R. Westergard, Proc. Insti. Mech. Eng., Part J, J. Eng. Tribology, 212, 5, 381 (1998)

104. T. Funahashi, Kawasaki Steel Tech. Rep., 28, 17 (1993)

105. R.H. Wentorf, Jr., J. Chem. Phys., 34, 809 (1961)

106. O. Mishima, S. Yamaoka, and O. Fukunaga, J. Appl. Phys. 61, 2822 (1987)

107. V.L. Solozhenko, High Press. Res., 9, 140 (1992)

108. K. Kudaka, H. Konno and T. Matoba, J. Chem. Soc. Jpn., 63, 365 (1966)

109. L.I. Fel'dgun and V.N. Krylov, Trudy VNIIASh, 7, 13 (1968)

110. A.M. Mazurenko and A.A. Leusenko, Izv. AN BSSR, ser. fiz.-mat. Nauk, 6, 108 (1978)

111. N.N. Sirota and A.M. Mazurenko, Dokl. AN SSSR, 241, 884 (1978)

112. L.F. Vereshchagin, I.S. Gladkay, G.A. Dubitski and V.N. Slesarev, Izv. An SSSR. Neorg. Mater., 15, 256 (1979)

113. M. Kagamida, H. Kanda, M. Akaishi et al., J. Cryst. Growth, 94, 261 (1989)

114. J. Maki, H. Iwata and O. Fukunaga, Proc. II Int. Conf. "New Diamond Science and Technology", ed. R. Messier, J.T. Glass, J.E. Batler, R. Roy, Material Research Society, Pittsburgh, PA, 1051 (1991)

115. R.C. DeVries and J.F. Fleischer, J. Cryst. Growth, 13/14, 88 (1972)

116. S. Yamaoka, O. Shimomura, M. Akaishi et al., Physica, 139/140B, 668 (1986)

117. A.S. Balchan and H.G. Drickamer, Rev. Sci. Instr., 32, 308 (1961)

118. J. Kouvetakis, V. V. Patel, C.W. Miller, and D.B. Beach, J. Vac. Sci. Technol. A, 8, 3929 (1990)

119. F. Meyer and R. Zappner, Ber. Dt. Chem. Ges., 54, 560 (1921)

120. M.J. Rand and J.F. Roberts, J. Electro. Soc., 115, 423 (1968)

121. S.P. Murarka, C.C. Chang, D.N.K. Wang, and T.E. Smith, J. Electro. Soc., 126, 1951 (1979)

122. M. Hirayama and K. Shohno, J. Electro. Soc., 122, 1671 (1975)

123. I.E. Campbell, C.F. Powell, D.H. Nowicki, and B.W. Gonser, J. Electro. Soc., 96, 318 (1948)

124. V.T. Renner, Z. Anorg. Allegem. Chem., 298, 22 (1959)

125. S. Motojima, Y. Tamura, and K. Sugiyama, Thin Solid Films, 88, 269 (1982)

126. W. Boronian, Mater. Res. Bull., 7, 119 (1972)

127. M. Sano and M. Aoki, Thin Solid Films, 83, 247 (1981)

128. W. Schmolla and H.L. Hartnagel, J. Phys. D., 15, L95 (1982)

129. T.H. Yuzuriha and D.W. Hess, Thin Solid Films, 140, 199 (1986)

130. B. Rother and C. Weissmantel, Phys. Stat. Sol. A, 87, k119 (1985)

131. K. Yasuda, A. Yoshida, M. Takeda, H. Masuda, and I. Akasaki, Phys. Stat. Sol. A, 90 (1985)

132. J. J. Gebhardt, Proc. 4th Int. Conf. On CVD, Boston, MA, Electro. Soc., Princeton, NH, 460 (1973)

133. G. Constant and R. Feurer, J. Less-Comm. Met., 82, 113 (1981)

134. W. Schmolla and H.L. Hartnagel, Solid State Electr., 26, 931 (1983)

135. K. Nakamura, J. Electro. Soc., 132, 1757 (1985)

136. "ESCA Spectrometer System 5950 Manual", Section IV, Hewlett-Packard Co (1972)

137. D.J. Joyner and D.M. Hercules, J. Chem. Phys., 72, 1095 (1980)

138. H.E. Bishop and J.C. Riviere, Appl. Phys. Lett., 16, 21 (1970)

139. H.O. Pierson, J. Compos. Mater., 9, 228 (1975)

140. K. Nakamura, J. Electro. Soc., 133, 1120 (1986)

141. K. Nakamura, Mat. Sci. Forum 54/55, 111 (1990)

142. M.S. Nakhmanson and V.P. Simirnov, Sov. Phys. Solid State, 13, 2763 (1972)

143. F.C. Brown, P.Z. Bachrach, and M. Skibowski, Phys. Rev. B, 13, 2663 (1976)

144. J. Williams, R.L. Williams, and J.C. Wright, J. Chem. Soc., 5816 (1963)

145. M. Grasserbauer, Microchim. Acta, 1, 145 (1975)

146. A. Zunger, Phys. Rev. B, 13, 5560 (1976)

147. W.C. Price, R.D.B. Fraser, T.S. Robinson, and H.C. Longuet-Higgins, Discuss. Farady Soc., 9, 131 (1950)

148. S.P.S. Arya and A. D'Amico, Thin Solid Films, 157, 267 (1988)

149. S. Manorama, GN. Chaudhari, and V.J. Rao, J. Phys. D, 26, 1793 (1993)

150. A.R. Phani, G.N. Chaudhari, and S. Manorama, J. Solid State Chem., 118, 99 (1995)

151. G. Sarala Devi, S. Roy, and V.J. Rao, Solid State Comm., 87, 67 (1993)

152. A.R. Phani, S. Roy, and V.J. Rao, Thin Solid Films, 258, 21 (1995)

153. G.L. Doll, J.A. Sell, C.A. Taylor II, and R. Clarke, Phys. Rev. B, 43, 6816 (1991)

154. R. Clarke, C.A. Taylor II, G.L. Doll, and T.A. Perry, Diamond Relat. Mater., 1, 93 (1992)

155. T.A. Friedman, K.F. McCarty, E.J. Klaus, D. Boehme, W.M. Clift, H.A. Johnsen, M.J. Mills, and D.K. Ottesen, Appl. Phys. Lett., 61, 2406 (1992)

156. R.W. Pryor, Z.L. Wu, K.R. Padmanabhan, S. Villanueva, and R.L. Thomas, Thin Solid Films, 253, 243 (1994)

157. R.W. Pryor, K.R. Padmanabhan, and K. Chawla, Diamond Relat. Mater., 4, 128 (1995)

158. F. Qian, V. Nagabushnam, and R.K. Singh, Appl. Phys. Lett., 63, 317 (1993)

159. P. A. Molian, J. Mater. Sci., 29, 5646 (1994)

160. T.A. Friedmann, K.F. McCarty, E.J. Klaus, J.C. Barbour, W.M. Clift, H.A. Johnsen, D.L. Medlin, M.J. Mills, and D.K. Ottesen, Thin Solid Films, 237, 48 (1993)

161. P.B. Mirkarimi, K.F. McCarty, and D.L. Medlin, Mater. Sci. Eng., R21, 47 (1997)

162. T.A. Friedmann, P.B. Mirkarimi, D.L. Medlin, K.F. McCarty, E.J. Klaus, D.R. Boehme, H.A. Johnsen, M.J. Mills, D.K. Ottesen, and J.C. Barbour, J. Appl. Phys., 76, 3088 (1994)

163. M. Okamato, H. Yokoyama, and Y. Osaka, Jpn. J. Appl. Phys., 29, 930 (1990)

164. A. Chayahara, H. Yokoyama, T. Imura, and Y. Osaka, Jpn. J. Appl. Phys., 26, L1435 (1987)

165. A. Chayahara, H. Yokoyama, T. Imura, and Y. Osaka, Appl. Surf. Sci., 33/34, 561 (1988)

166. H. Saitoh, T. Hirose, H. Matsui, Y. Hirotsu, and Y. Ichinose, Surf. Coat. Technol. 39/40, 265 (1989)

167. Y. Osaka, A. Chayahara, H. Yokoyama, M. Okamoto, T. Hamada, T. Imura, and M. Fujisawa, Synthesis and Properties of Boron Nitride, J.J. Pouch and S.A. Alterovitz (eds.), Materials Science Forum, 54/55, Trans Tech. Publications, Brookfield, (1990)

168. W. Dworschak, K. Jung, and H. Ehrhardt, Thin Solid Films, 254, 65 (1995)

169. W. Dworschak, K. Jung, and H. Ehrhardt, Diamond Relat. Mater., 3, 337 (1994)

170. T. Ichiki, T. Momose, and T. Yoshida, J. Appl. Phys., 75, 1330 (1994)

171. M. Okamoto, Y. Utsumi, and Y. Osaka, Plasma Sources Sci. Technol., 2, 1, (1993)

172. A. Weber, U. Bringmann, R. Nikulski, and C.P. Klages, Diamond Relat. Mater., 2, 201 (1993)

173. H. Saitoh, T. Hirose, H. Matsui, Y. Hirotsu, and Y. Ichinose, Surf. Coat. Technol., 39/40, 265 (1989)

174. H. Saitoh and W.A. Yarbrough, Appl. Phys. Lett., 58, 2230 (1991)

175. M. Kuhr, S. Reinke, and W. Kulisch, Surf. Coat. Technol., 74/75, 806 (1995)

176. A. Weber, U. Bringmann, R. Nikulski, and C.P. Klages, Diamond Relat. Mater., 2, 201 (1993)

177. C.R. Aita, Synthesis and Properties of Boron Nitride, J.J. Pouch and s.A. Alterovitz (eds.), Materials Science Forum, 54/55, Trans Tech Publications, Brookfield, 1 (1990)

178. M.D. Wiggins, C.R. Aita, and F.S. Hickernell, J. Vac. Sci. Technol. A, 2, 322 (1984)

179. W. Gissler, J. Haupt, A. Hoffmann, P.N. Gibson, and D.G. Rickerby, Thin Solid Films, 199, 113 (1991)

180. H. Ohkawa, N. Ozawa, K. Ichihara, and N. Yasuda, Jpn. J. Appl. Phys., 33, 4486 (1994)

181. S. Ulrich, J. Scherer, J. Schwan, I. Barzen, K. Jung, M. Scheib, and H. Ehrhardt, Appl. Phys. Lett., 68, 909 (1996)

182. A.J. Noreika and M.H. Francombe, J. Vac. Sci. Technol., 6, 722 (1969)

183. K. Tanaka, Y. Uemura, and M. Iwata, Oyo Butsari, 46, 120 (1977)

184. G. Petrocoo, S.P.S. Arya, A. Bearzotti, M. Gentili, A. Paoletti, and A. D'Amico, Symp. On Sputtering, Spitz a.d. Donau/Vienna, June 2-6 (1986)

185. V.N. Gashtold, S.A. Kutol'n, L.M. Shakarian, L.F. Bielova, and G.M. Komarova, Electron. Tekh., 12, 58 (1970)

186. P.D. Davidse, and L.I. Maissel, J. Appl. Phys., 37, 574 (1966)

187. M. Friedrich, J. Hahn, S. Laufer, F. Richter, H.-J. Hinneberg, and D.R.T. Zahn, Diamond Materials IV Electro. Soc. Proc., 94/95, The Electrochemical Society, Pennington, NH (1995)

188. V.Y. Kulikovsky, L.R. Shaginyan, V.M. Vereschaka, and N.G. Hatyenko, Diamond Relat. Mater., 4, 113 (1995)

189. S. Kidner, C.A. Taylor II, and R. Clarke, Appl. Phys. Lett., 64 1859 (1994)

190. R. Ganzetti and W. Gissler, Mater. Manuf. Processes, 9, 507 (1994)

191. M.P. Johansson, I. Ivanoz, L. Hultman, P. Munger, and A. Schutze, J. Vac. Sci. Technol A, 14, 3100 (1996)

192. D. Litvinov, C.A. Taylor II, R. Clarke, Diamond Relat. Mater., 7, 360 (1998)

193. K. Bewilogua, J. Buth, H. Hubsch, and M. Grischke, Diamond Relat. Mater., 2, 1206 (1993)

194. M. Mieno, and T. Yoshida, Jpn. J. Appl. Phys., 29, L1175 (1990)

195. P.B. Mirkarimi, D.L. Medlin, K.F. McCarty, D.C. Dibble, W.M. Clift, J.A. Knapp, and J.C. Barbour, J. Appl. Phys., 82, 1617 (1997)

196. H. Luthje, K. Bewilogua, S. Daaud, M. Johansson, and L. Hultman, Thin Solid Films, 257, 40 (1995)

197. M. Mieno and T. Yoshida, Surf. Coat. Technol, 52, 87 (1992)

198. J. Hahn, M. Friedrich, R. Pintaske, M. Schaller, N. Kahl, D.R.T. Zahn, and F. Richter, Diamond Relat. Mater., 5, 1103 (1996)

199. K. Inagawa, K. Watanabe, H. Ohsone, K. Saitoh, and A. Itoh, J. Vac. Sci. Technol A, 5, 2696 (1987)

200. D.J. Kester, K.S. Ailey, R.F. Davis, and K.L. More, J. Mater. Res., 8, 1213 (1993)

201. D.R. McKenzie, W.D. McFall, W.G. Sainty, C.A. Davis, and R.E. Collins, Diamond Relat. Mater., 2, 970 (1993)

202. L.B. Hackenberger, L.J. Pilione, R. Messier, and G.P. Lamaze, J. Vac. Sci. Technol A, 12, 1569 (1994)

203. T. Ikeda, Y. Kawate, and Y. Hirai, J. Vac. Sci. Technol A, 8, 3168 (1990)

204. D.J. Kester and R. Messier, J. Appl. Phys., 72, 504 (1992)

205. T. Ikeda, Appl. Phys. Lett., 61, 786 (1992)

206. D. Bouchier, G. Sene, M.A. Djouadi, and P. Moller, Nucl. Instrum. Meth. B, 89, 369 (1994)

207. D.R. McKenzie, W.D. McFall, H. Smith, B. Higgins, R.W. Boswell, A. Durandet, B.W. James, and I.S. Falconer, Nucl. Instrum. Meth. B, 106, 90 (1995)

208. M. Sueda, T. Kobayashi, H. Tsukamoto, T. Rokkaku, S. Morimoto, Y. Fukaya, N. Yamashita, and T. Wada, Thin Solid Films, 228, 97 (1993)

209. T. Wada and N. Yamashita, J. Vac. Sci. Technol. A, 10, 515 (1992)

210. D.J. Kester, K.S. Ailey, D.J. Lichtenwalner, and R.F. Davis, J. Vac. Sci. Technol. A, 12, 3074 (1994)

211. M. Murakawa and S. Watanabe, Surf. Coat. Technol., 43/44, 145 (1990)

212. T. Ikeda, T. Satou, and H. Satoh, Surf. Coat. Technol, 50, 33 (1991)

213. M. Murakawa and S. Watanabe, Surf. Coat. Technol., 43/44, 128 (1990)

214. S. Watanabe, S. Miyake, and M. Murakawa, Surf. Coat. Technol., 49, 406 (1991)

215. M. Lu, A. Bousetta, R. Sukach, A. Bensaoula, K. Walters, K. Eipers-Smith, and A. Schultz, Appl. Phys. Lett., 64, 1514 (1994)

216. K.L. Chopra, V. Agarwal, V.D. Vanker, C.V. Deshpandey, and R.F. Bunshah, Thin Solid Films, 126, 307 (1985)

217. P.B. Mirkarimi, K.F. McCarty, G.F. Cardinale, D.L. Medlin, D.K. Ottesen, and H.A. Johnsen, J. Vac. Sci. Technol. A, 14, 251 (1996)

218. G.F. Cardinale, P.B. Mirkarimi, K.F. McCarty, E.J. Klaus, D.L. Medlin, W.M. Clift, and D.G. Howitt, Thin Solid Films, 253, 130 (1994)

219. A.K. Ballal, L. Salamanca-Riba, C.A. Taylor II, and G.L. Doll, Thin Solid Films. 224, 46 (1993)

220. P.B. Mirkarimi, K.F. McCarty, D.L. Medlin, W.G. Wolfer, T.A. Friedman, E.J. Klaus, G.F. Cardinale, and D.G. Howitt, J. Mater. Res., 9, 2925 (1994)

221. P.B. Mirkarimi, D.L. Medlin, K.F. McCarty, and J.C. Barbour, Appl. Phys. Lett., 66, 2813 (1995)

222. A.K. Ballal, L. Salamanca-Riba, G.L. Doll, C.A. Taylor II, and R. Clarke, J. Mater. Res., 7, 1618 (1992)

223. S. Mineta, M. Kolrata, N. Yasunaga, and Y. Kikuta, Thin Solid Films, 189, 125 (1990)

224. C. Weissmantel, Thin Film Formation from Free Atoms and Particles, K.J. Klabunde (ed.), Academic Press, New York, NY, 1985

225. C. Weissmantel, K. Bewilogua, D. Dietrich, H.J. Erler, H.J. Hinnerberg, S. Klose, W. Nowich, and G. Reisse, Thin Solid Films, 72, 19 (1980)

226. C. Weissmantel, K. Bewilogua, K. Breuer, D. Dietrich, U. Ebersbach, H.J. Erler, B. Rau, and G. Reisse, Thin Solid Films, 96, 31 (1982)

227. B. Rother, H.D. Zscheile, C. Weissmantel, C. Heiser, G. Holzhuter, G. Leonhardt, and P. Reich, Thin Solid Films, 142, 83 (1986)

228. C. Weissmantel, J. Vac. Sci. Technol., 18, 179 (1981); S. Shanfield and R. Wolfson, J. Vac. Sci. Technol. A, 1, 323 (1983)

229. S. Shanfield and R. Wolfson, J. Vac. Sci. Technol. A, 1, 323 (1983)

230. K. Miyoshi, D.H. Buckley, and T. Spalvins, J. Vac. Sci. Technol. A, 3, 2340 (1985)

231. W. Halverson, and D.T. Quinto, J. Vac. Sci. Technol. A, 3, 2141 (1985)

232. M. Satou and F. Fujimoto, Jpn. J. Appl. Phys., 22, L171 (1983)

233. L. Guzman, F. Marchetti, L. Calliari, I. Scotoni, and F. Ferrari, Thin Solid Films, 117, L63 (1984)

234. L. Guzman, Ingegneria, 1, 3 (1985)

235. D.L. Medlin, T.A. Friedmann, P.B. Mirkarimi, G.F. Cardinale, and K.F. McCarty, J. Appl. Phys., 79, 3567 (1996)

236. M. Lu, A. Bousetta, A. Bensaoula, K. Waters, and J.A. Schultz, Appl. Phys. Lett., 68, 622 (1996)

237. N. Tanabe and M. Iwaki, Nucl. Instrum. Meth. Phys. Res., B80/81, 1349 (1993)

238. H. Yamashita, K. Kuroda, H. Saka, N. Yamashita, T. Watanabe, and T. Wada, Thin Solid Films, 253, 72 (1994)

239. O. Burat, D. Bouchier, V. Stambouli, and G. Gautherin, J. Appl. Phys., 68, 2780 (1990)

240. M.F. Plass, W. Fukarek, S. Mandl, and W. Moller, Appl. Phys. Lett., 69, 46 (1996)

241. M.F. Plass, W. Fukarek, A. Kolitsch, M. Mader, and W. Moller, Phys. Stat. Sol. A, 155, K1 (1996)

242. D.S. Zhou, C.L. Chen, T.E. Mitchell, L.B. Hackenberger, and R. Messier, Phil. Mag. Lett., 72, 163 (1995)

243. H. Hofsass, H. Feldermann, M. Sebastian, and C. Ronning, Phys. Rev. B, 55, 13230 (1997)

244. H. Hofsass, C. Ronning, U. Griesmeier, M. Gross, S. Reinko, and M. Kuhr, Appl. Phys. Lett., 67, 46 (1995)

245. D.H. Berns and M.A. Cappelli, Appl. Phys. Lett., 68, 2711 (1996)

246. T. Ichiki, S. Amagi, and T. Yoshida, J. Appl. Phys., 79, 4381 (1996)

247. G. Krannich, F. Richter, J. Hahn, R. Pintaske, V.B. Filippov, and Y. Paderno, Diamond Relat. Mater., 6, 1005 (1997)

248. F. Richter, G. Krannich, J. Hahn, R. Pintaske, M. Friedrich, S. Schmidbauer, and D.R.T. Zahn, Surf. Coat. Technol., 90, 178 (1996)

249. G.V. Samsonov, T.S. Bartnitskaya, S.V. Muchnik, and K.A. Lunchak, Akad Nauk UKrSSR Inst. Prob. Mater., 60 (1977)

250. T.S. Bartnitskaya, S.V. Muchnik, K.A. Lynchak, L.A. Ivanchenko, I.I. Timofeeva, and V.B. Chernogorenko, Izv. Akad. Nauk SSSR, Neorg. Mater., 14, 197 (1978)

251. C. Hauser, Swiss Patent CH 645,596; 10/15/84; filed 11/14/80

252. V.L. Solozhenko, V.A. Mukhanov, and N.V. Novikov, Dok. Akad. Nauk. SSSR, 312, 630 (1990)

253. R.F. Davis et al., Semiannual Report on Nitride Semiconductors, June 1993

254. D. R. McKenzie, W. D. McFall, W. G. Sainty, C. A. Davis, and R. E. Collins, Diamond and Related Materials, 2, 970 (1993)

255. C.A. Davis, Thin Solid Films, 226, 30 (1993)

256. V. Solozhenko, V. Turkevich, and G. Will, High Press. Res., 15, 135 (1996)

257. S. Bohr, R. Haubner, and B. Lux, Diamond and Related Materials, 4, 714 (1995)

258. J. Maki, H. Ikawa, and O. Fukanaga, Proc. 2nd Int. Conf. On New Diamond Science and Technology, 1990, Materials Research Society, Pittsburgh, PA, 1051 (1991)

259. F.C.T. So, E. Kolawa, X.-A. Zhao, E.T.-S. Pan, and M.-A. Nicolet, J. Appl. Phys., 64, 2787, (1988)

260. M. Nagai and K. Kishida, Appl. Surf. Sci., 70/71, 759, (1993)

261. P.J. Pokela, C.K. Kwok, E. Kolawa, S. Raud, and M.-A. Nicolet, Appl. Surf. Sci., 53, 364, (1991)

262. A. Bosseboeuf, A. Fourrier, F. Meyer, A. Benhocine, and G. Gautherin, Appl. Surf. Sci., 53, 353, (1991)

263. F.C.T. So, E. Kolawa, Z.-A. Zhao, and M.-A. Nicolet, Thin Solid Films, 153, 507, (1987)

264. H.P. Kattelus, E. Kolawa, K. Affolter, and M.-A. Nicolet, J. Vac. Sci. Technol. A, 3, 2246, (1985)

265. K. Iguchi, M. Urai, C. Shiga, and M. Koba, Jpn. Kokai Tokkyo Koho JP 01 05,014 Japanese Patent granted 10 Jan. 1989

266. A. Charai, S.E. Hornstrom, O. Thomas, P.M. Fryer, and J.M.E. Harper, J. Vac. Sci. Technol. A, 7, 784, (1989)

267. Y.T. Kim, C.W. Lee, and S.-K. Min, Jpn. J. Appl. Phys, 32, 6126, (1993)

268. C.J. Uchibori, J. Electr. Mater., 26, 410 (1997)

269. L. Boukhris, Le Vide Science and Technique and Applications, n284, 203 (1997)

270. S.C. Sun, Digest Tech. Papers – Symposium on VLSI Technology, IEEE, Piscataway, NJ, 46 (1996)

271. M. Uekubo, Thin Solid Films, 286 170 (1996)

272. M. Wittmer, J. Vac. Sci. Technol. A, 2, 273 (1984)

273. B. Pecz, A. Sulyok, G. Radnoczi, O. Noblanc, C. Arnodo, S. Cassette, and C. Brylinski, Microscopy of Semiconducting Materials 1997, Proc. Royal Micro. Soc. Conf., 519 (1997)

274. C.S. Park, J.S. Lee, J.W. Lee, J.Y. Kang, and J.Y. Lee, Mat. Res. Soc. Symp. Proc., 201, 99, (1991)

275. J.S. Lee, C.S. Park, J.Y. Kang, D.S. Ma, and J.Y. Lee, J. Vac. Sci. Technol. B, 8, 1117, (1990)

276. P. Boher, P. Houdy, P. Kaikati, and L.J. Van Ijzendoorn, J. Vac. Sci. Technol. A, 8, 846, (1990)

277. H. Yamagishi and Y. Yamamoto, Jpn. J. Appl. Phys., 26, 122, (1987)

278. S. Nakajima, T. Ehata, K. Fukuda, and S. Shikada, Jpn. Kokai Tokkyo Koho JP 62 95,823 Japanese Patent granted 02 May 1987

279. L. Zhang, Bandaoti Xuebao, 11, 348 (1990)

280. A.E. Geissberger, R.A. Sadler, F.A. Leyenaar, and M.L. Balzan, J. Vac. Sci. Technol. A, 4, 3091, (1986)

281. N. Uchitomi, M. Nagaoka, K. Shimada, T. Mizoguchi, and N. Toyoda, J. Vac. Sci. Technol. B, 4, 1392, (1986)

282. N. Uchitomi, T. Kitaura, T. Mizoguchi, Y. Ikawa, N. Toyoda, and A. Hojo, Extended Abstracts of the 16th International Conference on Solid State Devices and Materials, 383, (1984)

283. K.M. Yu, J.M. Jaklevic, E.E. Haller, S.K. Cheung, and S.P. Kwok, J. Appl. Phys., 64, 1284 (1988)

284. S.K. Cheung, S.P. Kwok, A. Kaleta, K.M. Yu, J.M. Jaklevic, C.L. Liang, N.W. Cheung, and E.E. Haller, J. Vac. Sci. Technol. B, 6, 1779 (1988)

285. C.J. Galewski, Micro. Engin., 37-38, 365 (1997)

286. M.T. Takagi, Tech. Digest – Int. Electron Devices Meeting, IEEE, Piscataway, NJ, 455 (1996)

287. K. Nishihor, Jpn. J. Appl. Phys. Part 1, 34, 1241 (1995)

288. Y. Kitaura, Micro. Rel., 35, 1515 (1995)

289. T. Seshita, IEEE J. Solid-State Circ., 29, 1583 (1994)

290. T. Seshita, Digest of Tech. Papers – IEEE Int. Solid-State Circ. Conf., IEEE, Piscataway, NJ, 172 (1994)

291. E.-G. Oh, GaAs IC Syposium Technical Digest – GaAs IC Symposium, IEEE, Piscataway, NJ, 93 (1995)

292. M. Nagaoka, Jpn. J. Appl. Phys., 33, 767 (1994)

293. M. Wittmer, Appl. Phys. Lett, 36, 456 (1980)

294. S.-Q. Wang, I. Raaijmakers, B.J. Burrow, S. Suthar, S. Redkar, and K.-B. Kim, J. Appl. Phys., 68, 5176, (1990)

295. A. Weber, R. Nikulski, and C.-P. Klages, Appl. Phys. Lett., 63, 325 (1993)

296. A. Intemann, H. Koerner, and F. Koch, J. Electro. Soc., 140, 3215 (1993)

297. S.-H. Kim, D.-S. Chung, K.-C. Park, K.-B. Kim, and S.-H. Min, J. Electro. Soc., 146, 1455 (1999)

298. F. Pintchovski, T. White, E. Travis, P.J. Tobin, and J.B. Price, Tungsten and Other Refractory Metals for VLSI Applications IV, Materials Research Society, Pittsburgh, PA, 275 (1989)

299. A. Sherman, J. Electro. Soc., 137, 1892 (1990)

300. J.T. Hillman, M.J. Rice Jr., D.W. Studiner, R.F. Foster, and R.W. Fiordalice, Proc. 9th Int. VLSI Multilevel Interconnection Conf., Santa Clara, CA, June 9-10, 1992, VMIC, 246 (1992)

301. C.G. Faltermeier, C. Goldberg, M. Jones, A. Upham, A. Knorr, A. Ivanova, G. Peterson, A. Kaloyeros, and B. Arkles, J. Electro. Soc., 145, 676 (1998)

302. C. Faltermeier, J. Electro. Soc., 144, 1002 (1997)

303. A. Weber, J. Electro. Soc., 144, 1131 (1997)

304. A. J. Toprac, Evol. Thin Films Surf. Struc. Morph., Materials Research Society Symposium Proceedings, Pittsburgh, PA, 355, 323 (1995)

305. Y.W. Bae, Chem. Vap. Dep. Refrac. Met. Ceram. III, Materials Research Society Symposium Proceedings, Pittsburgh, PA, 363, 245 (1995)

306. R.M. Fix, R.G. Gordon, and D.M. Hoffman, Chem. Mater., 3, 1138 (1991)

307. R.M. Fix, R.G. Gordon, and D.M. Hoffman, Materials Research Society Symp. Proc., Materials Research Society, Pittsburgh, PA, 168, 357 (1990)

308. T.S. Cale, M.B. Chaara, G.B. Raupp, and I.J. Raaijmakers, Thin Solid Films, 236, 294 (1993)

309. C.S. Whelan, J.M. Bulger, A. Dumont, J. Clark, and M. Kuhn, J. Vac. Sci. Tech. B, 17, 194 (1999)

310. I.J. Raaijmakers, R.N. Vrtis, G.S. Sandhu, J.Yang, E.K. Broadbent, D.A. Roberts, and A. Lagendijk, Proc. 9th Int. VLSI Multilevel Interconnection Conf., Santa Clara, CA, June 9-10, VMIC, 260 (1992)

311. I.J. Raaijmakers, R.N. Vrtis, J. Yang, S. Ramaswami, A. Lagendijk, D.A. Roberts, and E.K. Broadbent, Advanced Metallization and Processing for Semiconductor Devices and Circuits II, Materials Research Society, Pittsburgh, PA, 99 (1992)

312. I.J. Raaijmakers, Proc. Schumacher 4th Annual Dielectric and CVD Metallization Symp., Carlsbad, CA, February 10-11, 1992, Schumacher, Carlsbad, CA, 1992

313. S.R. Kurtz and R.G. Gordon, Thin Solid Films, 140, 277 (1986)

314. A. Intemann, H. Koerner, and F. Koch, J. Electro. Soc., 140, 3215 (1993)

315. C.K. Narula, Chem. Vap. Dep., 1, 51 (1995)

316. L.C. Zhang, S.K. Cheung, C.L. Liang, and N.W. Cheung, Appl. Phys. Lett., 50, 445 (1987)

317. J. Ding, Z. Liliental-Weber, E.R. Weber, J. Washburn, R.M. Fourkas, and N.W. Cheung, Appl. Phys. Lett., 52 (1998)

318. S.-Q. Wang, I. Raaijmakers, B. Burrow, S. Suthar, S. Redkar, and K.-B. Kim, J. Appl. Phys., 68, 5176 (1990)

319. M.A. George, Hard Coatings Based on Borides, Carbides & Nitrides: Synthesis, Characterization & Application, TMS Annual Meeting 1998, 203 (1998)

320. L.-J. Meng, Surf. Coat. Tech., 90, 64 (1997)

321. W.-H. Soe, Interfacial Engineering for Optimized Properties, Materials Research Society Symposium Proceedings, Pittsburgh, PA, 458, 379 (1997)

322. J.W. Gerlach, Surf. Coat. Tech., 103/104, 281 (1998)

323. K. Volz, Surf. Sci. Tech., 103/104, 257 (1998)

324. Y. Kasukabe, Jpn. J. Appl. Phys. Part 1, 36, 2323 (1997)

325. Y. Kasukabe, Thin Solid Films, 281/282, 32 (1996)

326. A. Koniger, Nuc. Instru. Meth. Phys. Res. Sect. B, 120, 282 (1996)

327. H.D. Gu, Surf. Coat. Tech., 110, 153 (1998)

328. G. Yu, Thin Solid Films, 335, 59 (1998)

329. N.A. Travitzky, J. Mater. Sci. Lett., 15, 1818 (1996)

330. Y.-M. Sun, J. Endle, J.G. Ekerdt, N.M. Russell, M.D. Healy, and J.M. White, Mat. Res. Soc. Symp. Proc., 495, 165 (1998)

331. F.M. Kilbane, and P.S. Habig, J. Vac. Sci. Technol., 12, 107 (1975)

332. K. Reichelt and G. Bergman, J. Appl. Phys., 46, 2747 (1975)

333. Huber, K.J., Aita, C.R., J. Vac. Sci. Technol. A, 6, 1717 (1988)

334. G. Eftekhari, Semicond. Sci. Tech., 10, 1408 (1995)

335. H. Yamagishi, Jpn. J. Appl. Phys., 23, L895 (1984)

336. E. Kolawa, F.C.T. So, M.-A. Nicolet, J. Electro. Soc., 134, 1759 (1987)

337. Y.T. Kim, C.W. Lee, and D.J. Kim, Appl. Phys. Lett., 72, 1507 (1998)

338. C.W. Lee, Y.T. Kim, C. Lee, J.Y. Lee, S.K. Min, and Y.W. Park, J. Vac. Sci. Technol. B, 12, 69 (1994)

339. M. Takeyama, K. Sasaki, and A. Noya, J. Appl. Phys., 31, 3424 (1992)

340. M. Takeyama, K. Sasaki, and A. Noya, J. Appl. Phys., 73, 185 (1993)

341. S.G. Galanin, G.D. Kuznetsov, A.B. Tolstoguzov, and E.Y. Chernyak, Tech. Phys. Lett., 19, 56 (1993)

342. L. Boukhris, Thin Solid Films, 310, 222 (1997)

343. W.-S. Lee, Y.-H. Chung, and N.-O. Kim, Proc. 5th Int. Conf. Prop. Appl. Dielectric Mater., IEEE, New York, NY, 674 (1997)

344. Z. Pang, Adv. Metall. Devices Circ. – Sci., Tech., Manuf. Mater. Res. Soc. Symp., Materials Research Society, Pittsburgh, PA, 337, 343 (1997)

345. C.J. Uchibori, Y. Ohtani, T. Oku, N. Ono, and M. Murakami, Appl. Surf. Sci., 117-118, 347 (1997)

346. C.J. Uchibori, Y. Ohtani, T. Oku, N. Ono, and M. Murakami, J. Electro. Mater., 26, 410 (1997)

347. K.Y. Ahn, S.B. Brodsky, C.Y. Ting, and J. Kim, J. Vac. Sci. Technol. A, 4, 3111 (1986)

348. J.S. Lee, C.S. Park, J.W. Yang, J.Y. Kang, and D.S. Ma, J. Appl. Phys., 67, 1134 (1990)

349. D. Gregusova, T. Lalinsky, Z. Mozolova, J. Breza, and P. Vogrincic, J. Mater. Sci.: Mater. Electr., 4, 197 (1993)

350. D. Gregusova, Thin Solid Films, 249, 250 (1994)

351. S.G. Galanin, Fiz. i. Khim. Obra. Mater., 5, 94 (1993)

352. A. Deneuville, M. Benyahya, M. Brunel, J.C. Oberlin, J. Torres, N. Bourhila, J. Paleau, and B. Canut, Appl. Surf. Sci., 38, 139 (1989)

353. S. Iwama, K. Hayakawa, and T. Arizumi, J. Cryst. Growth, 66, 189 (1984)

354. F. Tessier and R. Marchand, J. Alloys Compd., 262-263, 410 (1997)

355. F. Tessier, R. Marchand, and Y. Laurent, J. Eur. Ceram. Soc., 17, 15 (1997)

356. W.-K. Yeh, T.-T. Wu, M.-H. Tsai, S.-C. Sun, J.-C. Chuang, and M.-C. Chen, 1996 Proc. 13th Int. VLSI Multilevel Interconnection Conference, 628 (1996)

357. J.-S. Lee, C.-S. Park, J.-Y. Kang, and D.-S. Ma, Proc. of the 16th Intern. Symp., Gallium Arsenide and Related Compounds 1989, IOP, Bristol, UK, 824 (1990)

358. S.O. Marcus and R.F. Foster, Thin Solid Films, 236, 330 (1993)

359. C.W. Lee, Y.T. Kim, and S.K. Min, Appl. Phys. Lett., 62, 3312 (1993)

360. A. Koblhase, M. Mandl, and W. Pamler, J. Appl. Phys., 65, 2464 (1989)

361. A. Sherman, J. Electro. Soc., 137, 1892 (1990)

362. M.-A. Nicolet, I. Suni, and M. Finetti, Solid State Technol., 26, 129 (1983)

363. T. Nakajima, K. Watanabe, and N. Watanabe, J. Electro. Soc., 134, 3175 (1987)

364. M. Urai, K. Iguchi, C. Shiga, and M. Koba, Jpn. Kokai Tokkyo Koho JP 63 317,676 Japanese Patent granted 26 Dec 1988

365. T. Matsuda and R. Nakada, Jpn. Kokai Tokkyo Koho JP 63 72,881 Japanese Patent granted 02 Apr 1988

366. Y. Ikeda, Jpn. Kokai Tokkyo Koho JP 63 02,319 Japanese Patent granted 07 Jan 1988

367. M. Nagai, K. Kishida, and S. Omi, Nihon Kagakkai Shi, 4, 368 (1996)

368. M. Nagai, K. Kishida, and S. Omi, Nihon Kagakkai Shi, 10, 907 (1994)

369. L. Volpe and M. Boudart, J. Solid State Chem., 59, 332 (1985)

370. R.L. Landingham and J.H. Austin, J. Less-Comm. Met., 18, 229 (1969)

371. B.L. Park, J.M. Ha, D.-H. ko, B.Y. Yoo, S.I. Lee, H.-D. Lee, M.B. Lee, U.I. Chung, Y.G. Koh, and M.Y. Lee, Advanced Metallization and Interconnect Systems for ULSI Applications in 1996, 283 (1997)

372. Y.T. Kim and S.K. Min, Appl. Phys. Lett., 59, 929 (1991)

373. C. Meunier, C. Monteil, C. Savall, F. Palmino, J. Weber, R. Berjoan, and J. Durand, Appl. Surf. Sci., 125, 313 (1998)

374. C.S. Kwon, D.J. Kim, C.W. Lee, Y.T. Kim, and I.-H. Choi, Materi. Res. Soc. Symposium Proc., 355, 441 (1995)

375. C.W. Lee and Y.T. Kim, Solid-State Electr. 38, 679 (1995)

376. Y.T. Kim and C.W. Lee, J. Appl. Phys., 76, 542 (1994)

377. Y.T. Kim, C.W. Lee, and S.-K. Min, Appl. Phys. Lett., 61, 537 (1992)

378. C.W. Lee and Y.T. Kim, Appl. Phys. Lett., 65, 965 (1994)

379. B.L. Park, J. Electr. Mater., 26, 5 (1997)

380. C. Meunier, R. Berjoan, C. Savall, and J. Weber, Mater. Manuf. Proc., 13, 415 (1998)

381. J.P. Lu, W.Y. Hsu, J.D. Luttmer, L.K. Magel, and H.L. Tsai, J. Electro. Soc., 145, L21 (1998)

382. K.K. Lai, A.W. Mak, T.P.H.F. Wendling, P. Jian, and B. Hatcock, Thin Solid Films, 332, 329 (1998)

383. B.L. Park, D.-H. Ko, Y.S. Kim, J.M. Ha, Y.W. Park, S.I. Lee, H.-D. Lee, M.B. Lee, U.I. Chung, Y.B. Koh, and M.Y. Lee, J. Electro. Mater., 26, L1 (1997)

384. A.L. Currie and K.E. Howard, J. Mater. Sci., 27, 2739 (1992)

385. H.T. Chiu and S.H. Chuang, J. Mater. Res., 8, 1353 (1993)

386. M.H. Tsai, S.C. Sun, H.T. Chiu, and S.H. Chuang, Appl. Phys. Lett., 68, 1412 (1996)

387. S.C. Sun, M.H. Tsai, H.T. Chiu, and S.H. Chuang, 1996 Symp. On VLSI Tech., Digest of Tech. Papers, 46 (1996)

388. S. Ingrey, M.B. Johnson, and R.W. Streater, J. Vac. Sci. Technol. A, 20, 968 (1982)

389. J.E. Kelsey, C. Goldberg, G. Nuesca, G. Peterson, A.E. Kaloyeros, and B. Arkles, J. Vac. Sci. Technol. B, 17, 1101 (1999)

390. C.H. Winter, P.H. Sheridan, T.S. Lewkebandara, M.J. Heeg, and J.W. Proscia, J. Amer. Chem. Soc., 114, 1095 (1992)

391. R.M. Fix, R.G. Gordon, and D.M. Hoffman, Chem. Mater., 2, 235 (1990)

392. I.J. Raaijmakers and J. Yang, Appl. Surf. Sci., 73, 31 (1993)

393. M. J. Paisley, Z. Sitar, J. B. Posthill, R. F. Davis, J. Vac. Sci. Technol. A, 7, 701 (1989)

394. R. C. Powell, G. A. Tomasch, Y.-W. Kin, J. A. Thornton, J. E. Greene, Mat. Res. Soc. Symp. Proc., 162, 525 (1990)

395. H. Amano, M. Kito, K. Hiramatsu, and I. Akasaki, Jpn. J. Appl. Phys., 28, L2112 (1989)

396. S. Nakamura, T. Mukai, M. Senoh, and N. Iwasa, Jpn. J. Appl. Phys., 31, L139 (1992)

397. J. Hagen, R.D. Metcalfe, D. Wickenden, and W. Clark, J. Phys. C., 11, L143 (1978)

398. S. Yoshida, S. Misawa, and S. Gonda, J. Appl. Phys., 53, 6844 (1982)

399. M. A. Khan, R. A. Skogman, J. M. Van Hove, S. Krishnankutty, R. M. Kolbas, Appl. Phys. Lett., 56, 1257 (1990)

400. M.A. Khan, Q. Chen, C.J. Sun, J.W. Wang, and M.S. Shur, Proc. Mat. Res. Soc., Materials Research Society, Pittsburgh, PA, 1995

401. S.J. Pearton, C.R. Abernathy, and F. Ren, "Topics in Growth and Device Processing of III-V Semiconductors", World Scientific, Singapore (1996)

402. M.S. Shur and M.A. Khan, Proc. Symp. On Wide Band Gap Semiconductors and 23rd State of the Art Program on Compound Semiconductors" (SOTAPOCS), F.

Ren, D.N. Buckley, S.J. Pearton, P. Van Daele, G.C. Chi, T. Kamijoh, and F. Schuermeyer (eds.), The Electrochemical Society, Inc. (1995)

403. F. Ren and C. Abernathy, MIJ-NSR, 3, 41 (1998)

404. S.J. Pearton, C.R. Abernathy, and F. Ren, Topics in Growth and Device Processing of III-V Semiconductors, World Scientific, 1996

405. R. Nemanich, M.C. Benjamin, S.W. King, M.D. Bremser, R.F. Davis, B. Chen, Z. Zhang, and J. Bernholc, Proc. Mat. Res. Soc., Materials Research Society, Pittsburgh, PA, 1995

406. M.C. Benjamin, C. Wang, R.F. Davis, and R. Nemanich, Appl. Phys. Lett., 64, 3288 (1994)

407. Internet Website: http://www2.ncsu.edu/ncsu/pams/physics/Surf_Sci_Lab/wide/jc.html

408. J. I. Pancove, Mat. Res. Soc. Symp. Proc., 116, 515 (1990)

409. S. Nakamura, M. Senoh, S.-I. Nagahama, N. Iwasa, T. Yamada, T. Matsushita, Y. Sugimoto,H. Kiyoku, Jpn. J. Appl. Phys., 36, L1059 (1997)

410. S. Nakamura, M. Senoh, S.-I. Nagahama, N. Iwasa, T. Yamada, T. Matsushita, H. Kiyoku, Y. Sugimoto, T. Kozaki, H. Umemoto, M. Sano, K. Chocho, Jpn. J. Appl. Phys., 36, L1568 (1997)

411. S. Nakamura, M. Senoh, S.-I. Nagahama, N. Iwasa, T. Yamada, T. Matsushita, H. Kiyoku, Y. Sugimoto, T. Kozaki, H. Umemoto, M. Sano, K. Chocho, 37, L309 (1998)

412. K.S. Stevens, M. Kinniburgh, and R. Beresford, Appl. Phys. Lett., 66, 3518 (1995)

413. P. Kung, X. Zhang, D. Walker, A. Saxler, J. Piotrowski, A. Rogalski, and M. Razeghi, Appl. Phys. Lett., 67, 3792 (1995)

414. C.H. Qui, C. Hogatt, W. Melton, M.W. Leksono, and J.I. Pankove, Appl. Phys. Lett., 66, 2712 (1995)

415. D. Walker, P. Kung, A. Saxler, X.L. Zhang, M. Razeghi, and H. Jurgenson, Inst. Phys. Conf. Series, 145, 1133 (1996)

416. M. Asif Khan, Q. Chen, J. Yang, C.J. Sun, B. Lam, M.Z. Anwar, M.S. Shur, H. Temkin, B.T. Dermott, J.A. Higgins, J. Burm, W. Schaff, and L.F. Eastman, "The

Physics of Semiconductors", M. Scheffler and R. Zimmerman (eds.), World Scientific, Singapore (1996)

417. B. Lam, Q. Chen, M.A. Khan, C.J. Sun, and J. Yang, "High Responsivity Intrinsic Photoconductors Based on $Al_XGa_{1-X}N$", (unpublished manuscript), APA Optics, Inc., Blaine, Minnesota

418. Z. Fan, S.N. Mohammad, W. Kim, O. Aktas, A.E. Botchkarev, K. Suzue, and H. Morkoc, J. Electr. Mat., 25, 1703 (1996)

419. S. Nakamura, M. Senoh, S. Naghama, N. Iwasa, T. Yamada, T. Matsushita, H. Kiyoku, Y. Sugimoto, Jpn. J. Appl. Phys., 135, L217 (1996)

420. S. Nakamura, M. Senoh, S. Nagahama, N. Iwasa, T. Yamada, T. Matsushita, Y. Sugimoto, and H. Kiyoku, Appl. Phys. Lett., 72, 211 (1998)

421. E. D. Jungbluth, Solid State Tech., 38, 30 (1995)

422. H. Morkoc, S. Strite, G.B. Gao, M.E. Min, B. Sverdlov, and M. Burns, J. Appl. Phys., 76, 1363 (1994)

423. H.P. Maruska and J.J. Tietjen, Appl. Phys. Lett., 15, 327 (1969)

424. H.M. Manasevit, F.M. Erdmann, W.I. Simpson, J. Electro. Soc., 118, 1864 (1971)

425. O. Kryliouk, T. Dann, T. Anderson, et. al., Mat. Res. Soc. Proc., 493, 113 (1998)

426. O. Kryliouk, T. Dann, T. Anderson, A. Gaskov, K. Jones, J. H. Li, B. Chai, 8th Biannual Workshop on Organometallic Vapor Phase Epitaxy, Dana Point, CA, p.14 (1997)

427. O. Kryliouk, T. Dann, T. Anderson, A. Gaskov, K. Jones, J. H. Li, B. Chai, MRS Spring Meeting, San Francisco, Abstracts, p.86 (1997)

428. O. Kryliouk, T. Dann, T. Anderson, A. Gaskov, K. Jones, J. H. Li, B. Chai, E. Lamberg, CVD-XIV EVROCVD II, Paris, p. 2104 (1997)

429. T. P. Humphreys, C. A. Sukow, R. J. Nemanich, J. B. Posthill, R. A. Rudder, S. V. Hattangady, R. J. Markunas, Mat. Res. Soc. Symp. Proc., 162, 531 (1990)

430. M. A. Khan, J. N. Kuznia, J. M. Van Hove, D. T. Olson, S. Krishnankutty, R. M. Kolbas, Appl. Phys. Lett., 58, 536 (1991)

431. M. A. Khan, D. T. Olson, J. M. Van Hove, J. N. Kuznia, Appl. Phys. Lett., 58, 1515 (1991)

432. J.D. MacKenzie, C.R. Abernathy, J.D. Stewart, and R.G. Wilson, Mat. Res. Soc. Symp., 344 (1995)

433. T.D. Moustakas, R. Singh, R.J. Bennett, J.J. Gomes, and F.P. Dabkowski, Nitride Semiconductor Research, 3, 13 (1998)

434. Y.V. Melnik, I.P. Nikitina, A.S. Zubrilov, A.A. Sitnikova, Y.G. Misikhin, and V.A. Dmitriev, Inst. Phys. Conf. Series, 142, 863 (1996)

435. O. Kryliouk, M. Reed, T. Dann, T. Anderson, and B. Chai, MSE Journal, (1998)

436. A. Usui, H. Sunakawa, A. Sakai, and A. Yamaguchi, Jpn. J. Appl. Phys., 36, L899 (1997)

437. O.H. Nam, M.D. Bremser, T. Zheleva, and R.F. Davis, 39th Electr. Mater. Conf., D-5, June 25-27, Colorado State University, (1997)

438. W. Kim, A. Salvador, A.E. Botchkarev, S.N. Mohammad, and H. Morkoc, Appl. Phys. Lett., 69, 4 (1996)

439. M. Mizuta, S. Fujieda, Y. Matsumoto, T. Kawamara, Jpn. J. Appl. Phys., 25, L945 (1986)

440. S. Yoshida, S. Misawa, S. Gonda, Appl. Phys. Lett., 42, 427 (1983)

441. S. Yoshida, S. Misawa, S. Gonda, J. Vac. Sci. Technol. B, 1, 250 (1983)

442. H. Amano, N. Sawaki, I. Akasaki, Y. Toyoda, Appl. Phys. Lett., 48, 353 (1986)

443. I. Akasaki, H. Amano, Y. Koide, K. Hiramatsu, N. Sawaki, J. Cryst. Growth, 98, 209 (1989)

444. S. Nakamura, Jpn. J. Appl. Phys., 30, L1705 (1991)

445. M. Iwaya, T. Takeuchi, S. Yamaguchi, C. Wetzel, H. Amano, and I. Akasaki, Jpn. J. Appl. Phys., 37, L316 (1998)

446. R.A. Aparicio, Ph.D. Thesis, University of Florida, 1997

447. S.R. Brinkley, J. Chem. Phys., 14, 563 (1946)

448. W.B. White, W.M. Johnson, and G.B. Dantzig, J. Chem. Phys., 28, 751 (1958)

449. W.R. Smith and R.W. Missen, Chemical Reaction Equilibrium Analysis, John Wiley and Sons, Inc., New York, NY, 1982

450. D.J. Meyer, Ph.D. thesis, University of Florida, 1984

451. B. Sundman, B. Jansson, and J.O. Andersson, CALPHAD, 9, 153 (1985)

452. Computer Program "IvtanThermo", Ivtan, Thermocenter, Izhorskaya 13/19, Moscow, 127412, Russian Federation

453. T.M. Bessman, Surface Modification Technologies, The Metallurgical Society, 1988

454. L.V. Gurvich, I.V. Veyts, C.B. Alcock, Thermodynamic Properties of Individual Substances, v.3: The Elements B, Al, Ga, In, Tl, Be, Mg, Ca, Sr, Ba, and Their Compounds, Part Two: Tables, 4th ed., Hemisphere Publishing Corp.: New York, (1990)

455. M.W. Chase, C.A. Davies, J.R. Downey, D.J. Frurip, R.A. McDonald, and A.N. Szverud, JANAF Thermochemical Tables, 3rd ed., J. Phys. Chem. Ref. Data, 14 (1985)

456. I. Barin, Thermochemical Data of Pure Substances, 3rd ed., VCH, New York, (1995)

457. H.B. Schlegel and S.J. Harris, J. Phys. Chem., 98, 11178 (1994)

458. Personal communication with M.D. Allendorf. Information now available online at http://www.ca.sandia.gov/CRF/Research/Applied/ThermoKinData/thermo.cgi

459. A. Davydov and T. Anderson, University of Florida, Gainesville, FL, USA, Unpublished Work, 1997

460. M.E. Coltrin, R.J. Kee, and J.A. Miller, J. Electr. Soc., 131, 425 (1984)

461. R. Bird, W. Stewart, and E. Lightfoot, Transport Phenomena, John Wiley & Sons, New York, 1960

462. C.H.J. van den Brekel, Philips Res. Repts., 32, 118 (1977)

463. E. Weintraub, Trans. Amer. Electrochem. Soc., 16, 165 (1909)

464. Y. Kiyota, T. Nakamura, Muraki, Kazuhiko, Inada, T., J. Electro. Soc., 141, 2241 (1994)

465. J. Shan, Y. Wang, R.J. Hamers, J. Phys. Chem., 100, 4961 (1996)

466. H. Miura and N. Okamoto, J. Appl. Phys., 75, 4747 (1994)

467. C.S. Kwon, et. al., Mat. Res. Soc. Symp. Proc., 355, 441 (1995)

468. W.T. Tsang, R. Kapre, and P.F. Sciortine, Jr., J. Crystal Growth, 136, 42 (1994)

469. V.A.. Krenev and V.I. Evdokimov, Russ. J. Inorg. Chem., 14, 1966 (1969)

470. M.V. Milovanova and V.A. Krenev, Russ. J. Inorg. Chem., 21, 709 (1976)

471. M.V. Milovanova and V.A. Krenev, Russ. J. Inorg. Chem., 22, 1092 (1977)

472. M.V. Milovanova and V.A. Krenev, Izv. Akad. Nauk. SSSR Neorg. Mater., 13, 1704 (1977)

473. M.V. Milovanova and V.A. Krenev, Izv. Akad. Nauk. SSSR Neorg. Mater., 14, 2010 (1978)

474. L. Vandenbulcke and G. Vuillard, J. Electro. Soc., 123, 278 (1976)

475. L. Vandenbulcke and G. Vuillard, J. Electro. Soc., 124, 1937 (1977)

476. D.R. Stern and L. Lynds, J. Electro. Soc., 105, 676 (1958)

477. R.J. Starks and J.T. Buford, Electrochem. Tech., 1, 108 (1963)

478. E.T. Peters and W.D. Potter, Trans, AIME, 233, 473 (1965)

479. T. Mizutani, H. Asano, T. Nishiniga, and S. Uchiyama, Jap. J. Appl. Phys., 16, 1629 (1977)

480. A.F. Hollemann and E. Wiberg, Lehrbuch der anorganischen Chemie, 71-80th edn, Walter de Gruyter, Berlin, 1971

481. S. Bohr, R. Haubner, and B. Lux, Diamond and Related Materials, 4, 714 (1995)

482. V.L. Solozhenko, High Press. Res., 13, 199 (1995)

483. J.A. Van Vechten, Phys. Rev. B, 7, 1479 (1973)

484. A.R. Badzian and R.C. DeVries, Mater. Res. Bull., 23, 385 (1988)

485. T.R. Anthony, Vacuum, 41, 1356 (1990)

486. W.A. Brantly, J Appl. Phys., 44, 534 (1973)

487. H. Amano, T. Asahi, and I. Akasaki, Jpn. J. App. Phys. Lett., 28, L150 (1990)

488. S. N. Mohammad, A.A. Salvador, and H. Morkoc, Proc. of the IEEE, 83, 1306 (1995)

489. R. Thokala, and J. Chaudhuri, Thin Solid Films, 266, 189 (1995)

490. S. G. Lekhnitskii, Theory of Elasticity of an Anisotropic Elastic Body, Holden-Day, San Francisco, CA, (1963)

491. Y. Takagi, M. Ahart, T. Azuhata, T. Sota, K. Suzuki, and S. Nakamura, Physica B, 219-220, 547 (1996)

492. I. Akasaki, H. Amano, Y. Koide, K. Hiramatsu, and N. Sawaki, J. Crystal Growth, 98, 209 (1989)

493. Y. Tazou, T. Ishii, and S. Miyazawa, Jpn. J. Appl. Phys., 36, L746 (1997)

494. B. Neumann, C. Kroger, and H. Kunz, Z. Anorg. Allg. Chem., 218, 379 (1934)

495. G. Banik, P. Ettmayer, A. Vendl, and R. Kieffer, High Temp. High Press., 11, 349 (1979)

496. H.A. Wriedt, Bull. Alloy Phase Diag., 10, 358 (1989)

497. F.J. Norton and A.L. Marshall, Trans. AIME, 156, 351 (1944)

498. E. Fromm and H. Jehn, Z. Metallkd., 62, 378 (1971)

499. H. Jehn and P. Ettmayer, Monatsh. Chem., 111, 1437 (1980)

500. R.L. Wagner, Metall. Trans., 1, 3365 (1970)

501. R. Frauenfelder, J. Chem. Phys., 48, 3966 (1968)

502. Binary Alloy Phase Diagrams, 2nd ed., T.B. Massalski (ed.), ASM International, 1990

503. L.E. Davis, N.C. MacDonald, P.W. Palmberg, G.E. Riach, and R.E. Weber, Handbook of Auger Electron Spectroscopy, 2nd ed., Perkin-Elmer Corporation, 1978

504. M.E. Jones, J.R. Shealy, and J.R. Engstrom, Appl. Phys. Lett., 67, 542 (1995)

505. A.M. Zykov and G.K. Gaido, Izv. Akad. Nauk SSSR, Neorg. Mater., 9, 850 (1973)

506. H.I. Starnberg, P. Soukiassian, and T. Kendelewicz, Surf. Sci., 269/270, 915 (1992)

507. K. Kamimura, Y. Takase, Y. Onuma, and A. Kunioka, Appl. Surf. Sci., 41/42, 443 (1989)

508. T.L. Chu, S.S. Chu, C.L. Lin, Y.C. Tzeng, L.L. Kazmerski, and P.J. Ireland, J. Electrochem. Soc., 128, 855 (1981)

509. R. Trehan, Y. Lifshitz, and J.W. Rabalais, J. Vac. Sci. Technol. A, 8, 4026 (1990)

510. B.E. Williams and J.T. Glass, J. Mater. Res., 4, 373 (1989)

511. C.A. Ross, Mat. Res. Soc. Symp. Proc., 225, 35 (1991)

512. M.-A. Nicolet and M. Bartur, J. Vac. Sci. Technol. A, 19, 786 (1981)

513. F.M. d'Heurle and A. Gangulee, The Nature and Behavior of Grain Boundaries. edited by H. Hu (Plenum, New York), 339 (1972)

514. Jennifer Wilde, M.S. Thesis, University of Florida, 1996

515. Jennifer McCusker, Ph.D. Thesis, University of Florida, 1999

516. J.P. Lu, W.Y. Hsu, Q.Z. Hong, G.A. Dixit, J.D. Luttmer, R.H. Havemann, and L.K. Magel, Proc. ULSI XII, 269 (1997)

517. A. Noya, M. Takeyama, K. Sasaki, E. Aoyagi, and K. Hiraga, Jpn. J. Appl. Phys., 33, 1538 (1994)

518. K.-C. Park, K.-B. Kim, I.J.M.M. Raaijmakers, and K. Ngan, J. Appl. Phys., 80, 5674 (1996)

519. S.-H. Kim, D.-S. Chung, K.-C. Park, K.-B. Kim, and S.-H. Min, J. Electro. Soc., 146, 1455 (1999)

APPENDIX A
FORTRAN SOURCE CODE OF MODIFIED EQUILIBRIUM ALGORITHM

```
C  MCMPEC.STOIC .... MULTICOMPONENT MULTIPHASE EQUILIBRIUM CODE
C                  STOICIOMETRIC FORMULATION
C
C
      DIMENSION A(50,13),ACOEF(50),A0(50),A1(50),A2(50),A3(50),A4(50),
     &          COEFF(6),D(13,13),
     &          DINV(13,13),DD(13,13),DG(50),DH0(50),DS0(50),GNU(50,13),
     &          ICP(50),IDXBAS(13),INDEX(50),INERT(3),STDCP(50),
     &          TOTMC(50),WKA(50),ireac(13)
      INTEGER BSPCE(50,3),ISPCE(50,3),PHASE(50,3),SPECIE(50,3),
     &        STRING(6,4),TITLE(20),V,S,C,E,VP1,VPS,VPSP1,VSC,VSCE,
     &        BQUES(50),QUES(50),QUEST1/"?   '/,QUEST2/"??  '/,
     &        ELMNT(13)/13*' '/,VAPOR(3)/'  V','APO','R  '/,
     &        SOLN(3)/'SOL','UTI','ON '/,COND(3)/'CON','DEN','SED'/,
     &        RPSPS/') + '/,RPAS/')<= '/,RPBL/')   '/,SSPS/'  + '/,
     &        BLNKS/'    '/,LP/'('/,basis(50,3)
      REAL*8 DD,DINV,WKA,N(50),BESTN(50),NTEMP(50),DPRME(13,13),
     &       q(50),keq(50),frac(50),fracin(50),dzeta(50),lambda,
     &       rlxmin,b(13),bcalc(13),arg,chmpt(50),stp,chm,fraco(55)
C
C  A(I,J)   : ELEMENTAL ABUNDANCE MATRIX
C  B(J)     : TOTAL NUMBER OF GRAM-MOLES OF ELEMENT J
C  DH0(I)   : ENTHALPY OF FORMATION OF SPECIES I
C  DS0(I)   : ENTROPY OF FORMATION OF SPECIES I
C  STDCP(I) : STANDARD CHEMICAL POTENTIAL OF SPECIES I
C
C  **********  HEAT CAPACITY CORRELATIONS  **********
C  ICP(I)=0 : CP(I) = A0(I) + A1(I)*T + A2(I)/T**2 + A3(I)*ALOG(T)
C  ICP(I)=1 : CP(I) = A0(I) + A1(I)*T + A2(I)*T**2 + A3(I)*T**3
C  ICP(I)=2 : CP(I) = A0(I) + A1(I)*T + A2(I)*T**2 + A3(I)/T**2
C  ICP(I)=4 : CP(I) = A0(I) + A1(I)*T + A2(I)/T**2 + A3(I)*T**2 + A4(I)*T**-0.5
C
      OPEN(UNIT=5,FILE='CHOSPEC.DAT',STATUS='OLD')
      OPEN(UNIT=2,FILE='WRAPUP.DAT',STATUS='NEW')
      OPEN(UNIT=6,FILE='MCMOUT.DAT',STATUS='NEW')
      open(unit=9,file='gibb.dat',status='new')
      igib=9
      IRD=5
      IWRT=6
      IFILE=2
      IDIM1=50
      IDIM2=13
      FRCZIN=0.0
      DH0Z=0.0
      DS0Z=0.0
      A0Z=0.0
      A1Z=0.0
      A2Z=0.0
      A3Z=0.0
      TOTMV=0.0
C
C  READ TITLE
C
      READ(IRD,5) (TITLE(K),K=1,20)
    5 FORMAT(20A4)
C
C  NUMBER OF ELEMENTS, VAPOR SPECIES, SOLUTION SPECIES,
C  CONDENSED PURE PHASES, SYSTEM TEMPERATURE (K) AND PRESSURE (PA)
C
      READ(IRD,10) E,V,S,C,T,P,T0,P0,IX
   10 FORMAT(4I5,4F10.0,I5)
      VP1=V+1
      VPS=V+S
      VPSP1=V+S+1
      VSC=V+S+C
      VSCE=V+S+C+E
C
C  READ ELEMENTS
C
      READ(IRD,15) (ELMNT(J),J=1,E)
   15 FORMAT(13(1X,A2))
C
C  VAPOR SPECIES INFORMATION
C
      IF(V.EQ.0) GO TO 118
      DO 110 I=1,V
      READ(IRD,20) (SPECIE(I,K),K=1,3),DH0(I),DS0(I)
      READ(IRD,21) A0(I),A1(I),A2(I),A3(I),A4(I),ICP(I)
      READ(IRD,22) (A(I,J),J=1,13)
   20 FORMAT(3A4,2E12.5)
   21 FORMAT(5E12.5,I2)
   22 FORMAT(13(F5.0,1X))
      DO 110 J=1,3
      PHASE(I,J)=VAPOR(J)
  110 CONTINUE
C
C  INERT SPECIE
C
      READ(IRD,20) (INERT(K),K=1,3),DH0Z,DS0Z
      READ(IRD,21) A0Z,A1Z,A2Z,A3Z,A4Z,ICPZ
      READ(IRD,22) DUMMY
  118 CONTINUE
```

```
C
C  SOLUTION SPECIES INFORMATION
C
      IF(S.EQ.0) GO TO 125
      DO 120 I=VP1,VPS
      READ(IRD,20) (SPECIE(I,K),K=1,3),DH0(I),DS0(I)
      READ(IRD,21) A0(I),A1(I),A2(I),A3(I),A4(I),ICP(I)
      READ(IRD,22) (A(I,J),J=1,13)
      DO 120 J=1,3
      PHASE(I,J)=SOLN(J)
  120 CONTINUE
  125 CONTINUE
C
C  CONDENSED PHASE DATA
C
      IF(C.EQ.0) GO TO 135
      DO 130 I=VPSP1,VSC
      READ(IRD,20) (SPECIE(I,K),K=1,3),DH0(I),DS0(I)
      READ(IRD,21) A0(I),A1(I),A2(I),A3(I),A4(I),ICP(I)
      READ(IRD,22) (A(I,J),J=1,13)
      FRAC(I)=1.0
      FRACIN(I)=1.0
      DO 130 J=1,3
      PHASE(I,J)=COND(J)
  130 CONTINUE
  135 CONTINUE
c
c  read additional reference species to compute st. st. chem. pot.
c
      IF(ix.EQ.0) GO TO 131
      DO 132 I=vsc+1,vsc+ix
      READ(IRD,20) (SPECIE(I,K),K=1,3),DH0(I),DS0(I)
      READ(IRD,21) A0(I),A1(I),A2(I),A3(I),A4(I),ICP(I)
      READ(IRD,22) (A(I,J),J=1,13)
  132 CONTINUE
  131 CONTINUE
C
C  MAXIMUM NUMBER OF ITERATIONS, CONVERGENCE CRITERION AND OPTIONS
C
      READ(IRD,136) IDEBUG,IOPT,ISS,IWRAP,MAXIT,NMAX,CNVG,TINC,NCL,PINC,
     &              RLXMIN
  136 FORMAT(6I5,E10.1,F10.1,I5,F5.1,F10.1)
c-----------------------------------------------------------------
      READ(IRD,176) icoml,isp1,isp2,isp3,islv,islvi1,islvi2,ispl1,ispl2,
     &              ifcomp,cloop1,cloop2,slvf1,slvf2
  176 FORMAT(10I3,2E12.5,2f8.4)
c-----------------------------------------------------------------
      IF(IWRAP.EQ.3) IFILE=IWRT
C
C  CREATE A TABLE FILE IF LOOP OPTIONS ARE CHOSEN
C
```

```
      IF(IOPT.NE.0)OPEN(UNIT=7,FILE='TABLE.DAT',STATUS='NEW')
      ITAB=7
C
C  SET THE LOOP LIMITS FOR THE TEMPERATURE, PRESSURE AND COMPOSITION
C  LOOPS.  THE COMPOSITION LOOP STARTS HERE
C
      Tset=T
      NCMP=1
      NTP=1
      IF(IOPT.EQ.1.OR.IOPT.EQ.2) NTP=NMAX
      IF(IOPT.EQ.3) NCMP=NMAX
      IF(IOPT.EQ.4.OR.IOPT.EQ.5) NTP=NMAX
      IF(IOPT.EQ.4.OR.IOPT.EQ.5) NCMP=NCL
      DO 2000 ICMP=1,NCMP
      write(*,*) ' '
      if(ncmp.gt.1) write(*,*) 'Composition Loop #',ICMP
      write(*,*) ' '
C
C  TOTAL NUMBER OF MOLES OF VAPOR AND MOLE FRACTIONS
C
      IF(V.EQ.0) GO TO 138
      READ(IRD,137) TOTMV
      READ(IRD,137) (FRACIN(I),I=1,V),FRCZIN
  137 FORMAT(6E12.5)
C
C  TOTAL NUMBER OF MOLES OF SOLUTION SPECIES, MOLE FRACTIONS
C  AND EXCESS FREE ENERGY CORRELATION PARAMETERS
C
  138 CONTINUE
      IF(S.EQ.0) GO TO 140
      READ(IRD,137) TOTMS
      READ(IRD,137) (FRACIN(I),I=VP1,VPS)
      READ(IRD,139) IXSCOR,AXS,BXS
  139 FORMAT(I5,2E12.5)
  140 CONTINUE
C
C  TOTAL NUMBER OF MOLES IN PURE CONDENSED PHASES
C
      IF(C.EQ.0) GO TO 142
      READ(IRD,137) (TOTMC(I),I=VPSP1,VSC)
  142 CONTINUE
c---------------------------------------------------------------------
      do 163 i=1,vps
      fraco(i)=fracin(i)
  163 continue
      do 2000 icomp=1,ispl1
      do 2000 jcomp=1,ispl2
      if(ispl1.gt.1.or.ispl2.gt.1.and.icoml.eq.1) write(*,*)'Composition
     & Step',icomp,jcomp
      IDATA=0
      T=Tset
```

```
c--------------------------------------------------------------------
C
C  SAVE THE ORIGINAL SPECIE ORDER SO THE PROBLEM
C  CAN BE PLACED IN THIS ORDER AFTER THE ITERATIVE PROCEDURE
C
      DO 165 I=1,VSC
      DO 165 K=1,3
      ISPCE(I,K)=SPECIE(I,K)
  165 CONTINUE
c---------------------------------------------------------------------
      if(icoml.eq.0) go to 188
      if(ifcomp.eq.1)then
      fracin(isp1)=fraco(isp1)+(icomp-1)*cloop1
      fracin(isp2)=fraco(isp2)+(jcomp-1)*cloop2
      else
      icpo1=(icomp-1)
      icpo2=(jcomp-1)
      fracin(isp1)=fraco(isp1)*cloop1**icpo1
      fracin(isp2)=fraco(isp2)*cloop2**icpo2
      endif
      if(islv.gt.0) fracin(islv)=slvf1*fracin(islvi1)
     &                        +slvf2*fracin(islvi2)
      fracin(isp3)=1.0d+00-fracin(isp1)-fracin(isp2)-fracin(islv)
  188 continue
c----------------------------------------------------------------------
      IF(ICMP.GT.1.OR.IWRAP.EQ.3) GO TO 187
C
C  WRITE-OUT SOME OF THE INPUT DATA
C
      IPAGE=1
      WRITE(IWRT,400) (TITLE(K),K=1,20),IPAGE
      WRITE(IWRT,410) T,P
      IF(IWRAP.GT.1) GO TO 187
      WRITE(IWRT,170)
  170 FORMAT('0',/,1X,T55,'HEAT CAPACITY CORRELATION COEFFICIENTS',
     &/,1X,T16,'ENTHALPY OF',T33,'ENTROPY OF',T58,'ICP=0:  CP = A0',
     &' + A1*T + A2/T**2 + A3*LN(T)',/,1X,T17,'FORMATION',T33,'FORMAT',
     &'ION',T58,'ICP=1:  CP = A0 + A1*T + A2*T**2 + A3*T**3',/,1X,T58,
     &'ICP=2:  CP = A0 + A1*T + A2*T**2 + A3/T**2',/,1X,T4,
     &'SPECIE',T20,'DH0',T37,'DS0',T54,'A0',T73,'A1',T93,'A2',T113,
     &'A3',T122,'ICP',/,1X,T4,'SYMBOL',T15,'(KCAL/G-MOLE)',T30,
     &'(KCAL/G-MOLE-K)',T47,'(KCAL/G-MOLE-K)',T65,'(KCAL/G-MOLE-K**2)',
     &T86,'(.............)',T106,'(.............)',T122,'(-)',
     &/,'+',12('_'),T15,13('_'),T30,15('_'),T47,15('_'),
     &T65,18('_'),T86,15('_'),T106,15('_'),T122,3('_'))
      DO 180 I=1,VSC
      WRITE(IWRT,175) (SPECIE(I,K),K=1,3),DH0(I),DS0(I),A0(I),A1(I),
     &              A2(I),A3(I),ICP(I)
      IF(I.EQ.V) WRITE(IWRT,175) (INERT(K),K=1,3),DH0Z,DS0Z,A0Z,A1Z,
     &                      A2Z,A3Z,ICPZ
  175 FORMAT(1X,3A4,T17,F9.3,T33,F9.6,T50,F9.6,T68,E12.5,T88,E12.5,
     &T108,E12.5,T123,I1)
  180 CONTINUE
      WRITE(IWRT,184) T0,P0,MAXIT,CNVG,IDEBUG
  184 FORMAT('0',/,'0',T10,'THE ENTHALPY AND ENTROPY OF FORMATION ',
     &'REFERENCE TEMPERATURE AND PRESSURE ARE:',5X,'T0 = ',F6.1,' K',
     &5X,'P0 = ',F9.1,' PA',/,'0',T35,'MAXIMUM NUMBER OF ITERATIONS ',
     &'ALLOWED = ',I5,/,'0',T50,'CONVERGENCE CRITERION = ',E12.4,
     &/,'0',T48,'OUTPUT PARAMETER IDEBUG = ',I2)
      IF(S.GT.1) WRITE(IWRT,185) IXSCOR,AXS,BXS
  185 FORMAT('0','EXCESS FREE ENERGY CORRELATION DATA :',
     &      2X,'IXSCOR = ',I5,5X,'AXS = ',E12.5,5X,'BXS = ',E12.5)
      IF(ISS.GT.0) WRITE(IWRT,186) ISS
  186 FORMAT('0',T24,'ISS= ',I2,'  THE III-V LIQUID SOLUTION IS ',
     &      'AT EQUILIBRIUM WITH THE III-V STOICHIOMETRIC SOLID')
  187 CONTINUE
C
C  THE TEMPERATURE AND PRESSURE LOOPS BEGIN HERE
C
      DO 2000 ITP=1,NTP
      IF(IOPT.EQ.1.AND.ITP.GT.1) T=T+TINC
      IF(IOPT.EQ.2.AND.ITP.GT.1) P=P+PINC
      IF(IOPT.EQ.4.AND.ITP.GT.1) T=T+TINC
      IF(IOPT.EQ.5.AND.ITP.GT.1) P=P+PINC
      write(*,*) 'T= ',T
C
C  CALCULATE THE STANDARD STATE CHEMICAL POTENTIALS
C  AND AN INITIAL ESTIMATE OF THE EQUILIBRIUM COMPOSITIONS
C
      CALL STSTCP(A0,A1,A2,A3,A4,A0Z,A1Z,A2Z,A3Z,A4Z,DH0,DS0,DH0Z,DS0Z,
     &     STDCP,STDCPZ,ICP,ICPZ,T0,T,IDIM1,V,S,C,e,idim2,a,ireac,ix)
      IF(ITP.GT.1.AND.ISS.EQ.0) GO TO 195
      DO 190 I=1,VPS
      FRAC(I)=FRACIN(I)
  190 CONTINUE
      FRACZ=FRCZIN
      CALL ESTMTE(TOTMV,TOTMS,TOTMC,FRAC,N,FRACZ,ZV,
     &                  IDIM1,V,S,C)
  195 CONTINUE
C
C  SOURCE ZONE STEADY-STATE LIQUID COMPOSITION MODEL
C
      IF(ISS.GT.0) CALL STEADY(SPECIE,A,STDCP,ELMNT,XIII,T,T0,V,S,C,
     &                  IDIM1,IDIM2,ISS,IWRT)
C
C  CALCULATE THE TOTAL GRAM-MOLES OF EACH ELEMENT
C  BASED ON THE INITIAL COMPOSITION ESTIMATES IN THE PHASES
C
      write(igib,201)
  201 format(5x,'initial elemental abundances')
      write(igib,*) ' '
      DO 200 J=1,E
      BCALC(J)=0.
      DO 210 I=1,VSC
      BCALC(J)=A(I,J)*N(I)+BCALC(J)
      B(J)=BCALC(J)
  210 continue
      write(igib,202) elmnt(j),b(j)
  202 format(3x,a2,2x,e12.5)
  200 CONTINUE
      write(igib,*) ' '
      write(igib,*) ' '
      IF(IWRAP.GT.1) GO TO 476
      IF(ITP.GT.1) GO TO 472
C
C  WRITE-OUT THE INITIAL COMPOSITION ESTIMATES, STANDARD STATE
C  CHEMICAL POTENTIALS AND THE ELEMENTAL ABUNDANCE MATRIX
C
      IPAGE=IPAGE+1
      WRITE(IWRT,400) (TITLE(K),K=1,20),IPAGE
  400 FORMAT('1',/,'0',T34,'STOICIOMETRIC FORMULATION FOR DETERMINING',
     &      ' EQUILIBRIUM COMPOSITIONS',/,'0',T30,20A4,T120,
     &      'PAGE ',I2)
      WRITE(IWRT,410) T,P
  410 FORMAT('0',T43,'TEMPERATURE = ',F6.1,' K',5X,'PRESSURE = ',E12.5,
     &      ' PA')
      WRITE(IWRT,420) (ELMNT(K),K=1,13)
  420 FORMAT('0',/,T48,'INPUT DATA AND INITIAL COMPOSITION ESTIMATES',
     &/,'0',T29,'INITIAL',T43,'STANDARD',/,1X,T27,'COMPOSITION',
     &T43,'CHEMICAL',/,1X,T4,'SPECIE',T29,'ESTIMATE',T42,'POTENTIAL',
     &T72,'ELEMENTAL ABUNDANCE MATRIX',/,1X,T4,'SYMBOL',T17,'PHASE',
     &T28,'(G-MOLES)',T40,'(KCAL/G-MOLE)',T55,13(A2,4X),/,'+',
     &12('_'),T15,9('_'),T25,14('_'),T40,13('_'),T55,78('_'))
      DO 440 I=1,VSC
      WRITE(IWRT,430) (SPECIE(I,K),K=1,3),(PHASE(I,K),K=1,3),N(I),
     &            STDCP(I)
       IF(I.EQ.V) WRITE(IWRT,430) (INERT(K),K=1,3),(PHASE(I,K),K=1,3),
     &                    ZV,STDCPZ
  430 FORMAT(1X,3A4,T15,3A3,T25,E14.7,T42,F9.3)
  440 CONTINUE
      IF(ISS.GT.0) WRITE(IWRT,445) XIII
  445 FORMAT(4X,'X=',F6.4)
      WRITE(IWRT,450)
  450 FORMAT('0',/,'0',T44,'TOTAL GRAM-MOLES OF EACH ELEMENT FROM IN',
     &     'PUT DATA',/,1X,T40,'AND AS CALCULATED FROM THE INITIAL',
     &     ' COMPOSITION ESTIMATES',/,'0',4(4X,'INPUT DATA',3X,
     &     'CALCULATED',5X))
      NPRT=E/4
      NCHK=NPRT*4
      IF(NCHK.NE.E) NPRT=NPRT+1
      ISTRT=1
      DO 470 K=1,NPRT
      NEND=ISTRT+3
```

```
   IF(NEND.GT.E) NEND=E
   WRITE(IWRT,460) (ELMNT(J),B(J),BCALC(J),J=ISTRT,NEND)
 460 FORMAT(1X,4(A2,1X,E12.5,1X,E12.5,4X))
   ISTRT=NEND+1
 470 CONTINUE
 472 CONTINUE
   IPAGE=IPAGE+1
   WRITE(IWRT,400) (TITLE(K),K=1,20),IPAGE
   WRITE(IWRT,410) T,P
   WRITE(IWRT,475)
 475 FORMAT('0',T58,'EXECUTION DIAGNOSTICS',/,'+',T58,9('_'),1X,
  &       11('_'),/,'0')
 476 CONTINUE
C
C  DIVIDE THE STANDARD STATE CHEMICAL POTENTIALS BY RT
C
   RT=0.0019872*T
   DO 480 I=1,VSC
   STDCP(I)=STDCP(I)/RT
 480 CONTINUE
   STDCPZ=STDCPZ/RT
C
C  CALCULATE THE TOTAL SILICON AND THE III/V RATIO IN THE VAPOR PHASE
C  AND WRITE-OUT THE INITIAL RESULTS TO THE WRAPUP FILE
C
   IF(ITP.GT.1.OR.IWRAP.EQ.0) GO TO 485
   CALL TOTSI(A,ELMNT,FRAC,N,SITOT,SIMF,ACTSIS,T,P,IDIM1,IDIM2,V,E)
   CALL RATIO(A,ELMNT,FRAC,N,STDCP,ACTGAS,ACTINS,ACTASS,ACTPS,
  &          RIIIV,RGAAS,RINP,T,P,T0,P0,IDIM1,IDIM2,V,E)
   ITBST=1
   BSTCVG=0
   CALL WRAPUP(TITLE,SPECIE,INERT,N,FRAC,QUES,ZV,FRACZ,SITOT,SIMF,
  &        ACTSIS,ACTGAS,ACTINS,ACTPS,ACTASS,RIIIV,RGAAS,RINP,
  &   BSTCVG,ITBST,CNVG,CNVG,ISS,XIII,T,P,IDATA,IDIM1,IFILE,V,VSC,
  &   IOPT,ITP,NTP,ITAB,ICMP,IWRAP,GFE,STDCP,RT)
 485 CONTINUE
C
C  ITERATIVE SOLUTION FOR THE EQUILIBRIUM COMPOSITIONS
C
   RELMAX=1.0E10
   IACFF=0
   DO 600 ITER=1,MAXIT
C
C  DETERMINE THE OPTIMUM SET OF BASIS SPECIES
C
   CALL OPTBAS(N,BESTN,A,D,DPRME,STDCP,SPECIE,PHASE,A0,A1,A2,A3,A4,
  &BQUES,DH0,DS0,ICP,IDXBAS,ITER,IDIM1,IDIM2,V,S,C,E,ISTOP,ICHNG,
  &IWRT,FRAC)
   IF(ISTOP.EQ.1) GO TO 604
   IF(ITER.GT.1.AND.ICHNG.EQ.0) GO TO 500
   IF(IDEBUG.LT.2) GO TO 490
```

```
      CALL IPVEC(IDXBAS,IDIM2,E,6HIDXBAS,IWRT)
      CALL PMAT(A,IDIM1,IDIM2,VSC,E,6HA     ,IWRT)
      CALL PMAT(D,IDIM2,IDIM2,E,E,6HD     ,IWRT)
      CALL DPMAT(DPRME,IDIM2,IDIM2,E,E,6HDPRME ,IWRT)
  490 CONTINUE
C
C CALCULATE THE STOICIOMETRIC COEFFICIENTS AND THE EQUILIBRIUM
CONSTANTS
C
      CALL EQCON(A,D,DD,DINV,DG,GNU,STDCP,KEQ,IDXBAS,WKA,
     &           IDIM1,IDIM2,V,S,C,E,ISTOP)
      IF(ISTOP.EQ.1) GO TO 604
      IF(IDEBUG.LT.2) GO TO 500
      CALL DPMAT(DINV,IDIM2,IDIM2,E,E,6HDINV  ,IWRT)
      CALL PMAT(GNU,IDIM1,IDIM2,VSC,E,6HGNU   ,IWRT)
      CALL PVEC(keq,IDIM1,VSC,6HKEQ   ,IWRT)
  500 CONTINUE
C
C  CALCULATE THE ACTIVITY COEFFICIENTS
C
      CALL ACTCOF(FRAC,ACOEF,ISPCE,SPECIE,INDEX,IDIM1,RELMAX,IXSCOR,
     &            AXS,BXS,T,IACFF,V,S,C,IWRT)
C
C  CALCULATE THE EQUILIBRIUM CONSTANTS FROM THE CURRENT
COMPOSITIONS
C
      CALL CALCQ(GNU,N,ACOEF,FRAC,PHASE,VAPOR,SOLN,IDXBAS,Q,
     &           ZV,FRACZ,P,P0,V,S,C,E,IDIM1,IDIM2)
C
C  CALCULATE THE ERROR BETWEEN THE EQUILIBRIUM CONSTANTS
C  CALCULATED BY THE COMPOSITIONS AND THE EQUILIBRIUM CONSTANTS
C  CALCULATED FROM THE GIBBS FREE ENERGY CHANGE
C
      RELMAX=0.
      DO 590 I=1,VSC
      QUES(I)=BLNKS
      DO 570 J=1,E
      IF(I.EQ.IDXBAS(J)) GO TO 590
  570 CONTINUE
      relerr=(-1.0)*rt*dg(i)+rt*dlog(q(i))
C
C  ASSIGN "?" TO QUES(I) IF THE CONVERGENCE CRITERION IS NOT MET
C  AND "??" TO QUES(I) IF THERE IS LESS THAN ONE SIGNIFICANT FIGURE
C
      IF(ABS(RELERR).GT.CNVG) QUES(I)=QUEST1
      IF(ABS(RELERR).GT.0.001) QUES(I)=QUEST2
      IF(ABS(RELERR).GT.RELMAX.AND.N(I).GT.1.0D-75)
     &               RELMAX=ABS(RELERR)
  590 CONTINUE
C
C  KEEP THE BEST ESTIMATE TO THE EQUILIBRIUM SOLUTION
```

```
C  IN CASE THE NUMERICAL PROCEDURE DIVERGES
C
      IF(ITER.GT.1.AND.RELMAX.GT.BSTCVG) GO TO 594
      BSTCVG=RELMAX
      ITBST=ITER
      DO 593 IBEST=1,VSC
      BQUES(IBEST)=QUES(IBEST)
      BESTN(IBEST)=N(IBEST)
  593 CONTINUE
  594 CONTINUE
      IF(RELMAX.LE.CNVG) GO TO 610
      IF(IDEBUG.EQ.2) CALL PVEC(frac,IDIM1,VSC,6HFRAC  ,IWRT)
      IF(IDEBUG.GE.1) CALL PVEC(q,IDIM1,VSC,6HQ     ,IWRT)
      IF(ITER.EQ.MAXIT) GO TO 595
C
C  MAKE ADJUSTMENTS TO THE EXTENTS OF REACTION
C
      CALL ADJEXT(N,Q,GNU,DZETA,IDXBAS,COND,PHASE,IDIM1,IDIM2,
     &           V,S,C,E,dg)
      CALL CNVFRC(N,NTEMP,STDCP,ACOEF,DZETA,GNU,IDXBAS,VAPOR,
     &SOLN,PHASE,ZV,RT,P,P0,RLXMIN,LAMBDA,IDIM1,IDIM2,V,S,C,E)
      CALL CORMOL(N,DZETA,GNU,IDXBAS,IDIM1,IDIM2,LAMBDA,VSC,E)
  595 IF(ITER.LT.MAXIT) GO TO 597
C
C  IF THE SOLUTION DID NOT CONVERGE TRANSFER THE BEST ESTIMATE
C  TO THE EQUILIBRIUM SOLUTION FROM VECTOR BESTN INTO N.
C
      DO 596 IBEST=1,VSC
      QUES(IBEST)=BQUES(IBEST)
      N(IBEST)=BESTN(IBEST)
  596 CONTINUE
  597 CONTINUE
      CALL CALCQ(GNU,N,ACOEF,FRAC,PHASE,VAPOR,SOLN,IDXBAS,Q,
     &          ZV,FRACZ,P,P0,V,S,C,E,IDIM1,IDIM2)
      IF(IDEBUG.EQ.0) GO TO 600
      CALL GIBBS(N,STDCP,STDCPZ,ACOEF,FRAC,ZV,FRACZ,COND,SOLN,PHASE,
     &          RT,P,P0,IDIM1,V,S,C,GFE)
c
c ********************************************************************
c
      if(iter.eq.1) igfe=100
      if(iter.eq.igfe.or.iter.eq.maxit) then
      write(IGIB,540) iter,gfe
  540 format(1x,'iter=',3x,i5,5x,'totgibbs=',3x,e12.5)
      igfe=igfe+100
      else
      go to 541
      endif
  541 continue
c
c*********************************************************************
```

```
c
      CALL DEBUG(N,DZETA,VSC,IDIM1,ITER,LAMBDA,GFE,RELMAX,IWRT)
  600 CONTINUE
  604 CONTINUE
      IF(IWRAP.LT.3) WRITE(IWRT,605)MAXIT,RELMAX,BSTCVG,ITBST
  605 FORMAT('0','***** ITERATION FOR EQUILIBRIUM COMPOSITION ',
     &      'DID NOT CONVERGE *****',
     &'     (AFTER ',I4,' ITERATIONS RELMAX =',E12.5,' )',
     &/,'0',' BEST CONVERGENCE=',E12.5,' AT ITERATION ',I4)
  610 CONTINUE
c
c ***********************************************************************
c
      DO 572 J=1,E
      K=IDXBAS(J)
      DO 573 L=1,3
      BASIS(J,L)=SPECIE(K,L)
 573  CONTINUE
 572  CONTINUE
C-------------------------------------------------------
      DO 574 I=1,VSC
      DO 575 J=1,E
      IF(I.EQ.IDXBAS(J)) GO TO 574
  575 CONTINUE
      WRITE(IGIB,576) (GNU(I,J),(BASIS(J,K),K=1,3),J=1,E)
  576 FORMAT(4(F5.2,3A4,1x))
      F1=(-1.0)*rt*dg(i)
      F2=rt*dlog(q(i))
      FREE=(-1.0)*rt*dg(i)+rt*dlog(q(i))
      WRITE(IGIB,577) (SPECIE(I,L),L=1,3),F1,F2,FREE
  577 FORMAT(1X,3A4,3(3X,E12.5))
      WRITE(IGIB,*) ' '
  574 CONTINUE
      write(igib,*) ' '
      write(igib,701)
  701 format(5x,'final elemental abundances and difference (b-b*)')
      DO 702 J=1,E
      BCALC(J)=0.
      DO 703 I=1,VSC
      BCALC(J)=A(I,J)*N(I)+BCALC(J)
  703 continue
      b(j)=b(j)-bcalc(j)
      write(igib,704) elmnt(j),bcalc(j),b(j)
  704 format(3x,a2,2(2x,e12.5))
  702 CONTINUE
      WRITE(IGIB,*) ' '
      WRITE(IGIB,*) ' '
c
c ***********************************************************************
c
      CALL GIBBS(N,STDCP,STDCPZ,ACOEF,FRAC,ZV,FRACZ,COND,SOLN,PHASE,
     &          RT,P,P0,IDIM1,V,S,C,GFE)
c
c ******************************************************
c
      write(IGIB,540) iter,gfe
      write(igib,*)
      write(igib,*)
      write(igib,569) t,iter-1
 569  format(2x,'temp=',2x,f8.2,5x,'# iter=',3x,i5)
c
c *****************************************************
C
C  CALCULATE THE GRAM-MOLES OF EACH ELEMENT AFTER THE ITERATIONS
C
      DO 700 J=1,E
      BCALC(J)=0.0
      DO 700 I=1,VSC
      BCALC(J)=BCALC(J)+A(I,J)*N(I)
  700 CONTINUE
C
C  CALCULATE THE CHEMICAL POTENTIAL OF EACH SPECIE
C
      write(igib,*) '  species         st. st. chem. pot. (KJ/mol)    ch
     &em. pot. (KJ/mol)'
      write(igib,*) ' '
      DO 800 I=1,vsc+ix
      PP0=1.0
      IF(PHASE(I,1).EQ.VAPOR(1)) PP0=P/P0
      ARG=FRAC(I)*ACOEF(I)*PP0
      if(i.gt.vsc) arg=1.0
      CHMPT(I)=RT*(STDCP(I)+dlog(arg))
      if(i.gt.vsc) chmpt(I)=STDCP(I)
      stp=4.184*rt*stdcp(I)
      chm=4.184*chmpt(I)
      write(igib,801) (specie(i,j),j=1,3),stp,chm
  801 format(2x,3a4,12x,f12.5,15x,f12.5)
  800 CONTINUE
      write(igib,*) ' '
      write(igib,*) '------------------------------------------------ '
      write(igib,*) ' '
      write(igib,*) ' '
      ARG=1.0
      IF(FRACZ.GT.0.0) ARG=FRACZ*P/P0
      CHMPTZ=RT*(STDCPZ+ALOG(ARG))
      DO 810 I=1,VSC
      DO 810 K=1,3
      BSPCE(I,K)=SPECIE(I,K)
  810 CONTINUE
C
C  PUT THE MATRICIES AND VECTORS INTO THE ORIGINAL PROBLEM STATEMENT
ORDER
```

```
C
      CALL ORDER(ISPCE,SPECIE,PHASE,N,A,STDCP,A0,A1,A2,A3,A4,DH0,DS0,
     &DZETA,CHMPT,ACOEF,FRAC,QUES,DG,Q,KEQ,ICP,IDIM1,IDIM2,E,VSC)
C
C  CALCULATE THE TOTAL SILICON AND THE III/V RATIO IN THE VAPOR PHASE
C
      CALL TOTSI(A,ELMNT,FRAC,N,SITOT,SIMF,ACTSIS,T,P,IDIM1,IDIM2,V,E)
      CALL RATIO(A,ELMNT,FRAC,N,STDCP,ACTGAS,ACTINS,ACTASS,ACTPS,
     &          RIIIV,RGAAS,RINP,T,P,T0,P0,IDIM1,IDIM2,V,E)
      IF(IWRAP.GT.1) GO TO 971
C
C  WRITE-OUT THE RESULTS
C
       IPAGE=IPAGE+1
      WRITE(IWRT,400) (TITLE(K),K=1,20),IPAGE
      WRITE(IWRT,410) T,P
      WRITE(IWRT,900) ITBST,GFE,BSTCVG,CNVG,LAMBDA
  900 FORMAT('0',/,1X,T45,'EQUILIBRIUM COMPOSITIONS AFTER ',I5,
     &' ITERATIONS',/,'0',T42,'SYSTEM GIBBS FREE ENERGY = ',E14.7,
     &' (KCAL)',
     & /,'0','RELATIVE ERROR = ',E12.5,5X,'CONVERGENCE CRITERION = ',
     & E12.5,5X,'RELAXATION PARAMETER AT LAST ITERATION = ',E12.5,
     & /,'0',T57,'ESTIMATED',/,1X,T25,'EQUILIBRIUM',T39,'EQUILIBRIUM',
     & T56,'COMPOSITION',T92,'CHEMICAL',
     & /,1X,T4,'SPECIE',T29,'MOLE',T39,'COMPOSITION',T56,
     & 'UNCERTAINTY',T91,'POTENTIAL',T109,'ACTIVITY',
     & /,1X,T4,'SYMBOL',T17,'PHASE',T27,'FRACTION',T40,'(G-MOLES)',
     & T57,'(G-MOLES)',T90,'(KCAL/G-MOLE)',T107,'COEFFICIENT',
     & /,'+',12('_'),T15,9('_'),T25,12('_'),T37,14('_'),T54,
     & 14('_'),T89,14('_'),T106,12('_'))
      ZZETA=0.0
      ZACT=1.0
      DO 920 I=1,VSC
      WRITE(IWRT,910) (SPECIE(I,K),K=1,3),(PHASE(I,K),K=1,3),FRAC(I),
     &               N(I),DZETA(I),CHMPT(I),ACOEF(I)
      IF(I.EQ.V) WRITE(IWRT,910) (INERT(K),K=1,3),(PHASE(I,K),K=1,3),
     &                         FRACZ,ZV,ZZETA,CHMPTZ,ZACT
  910 FORMAT(1X,3A4,T15,3A3,T24,E12.5,T37,E14.7,T54,E14.7,T92,F9.3,
     &T106,E12.5)
  920 CONTINUE
      IF(ISS.GT.0) WRITE(IWRT,445) XIII
      WRITE(IWRT,930) SIMF
  930 FORMAT('0',T35,'MOLE FRACTION OF SILICON SPECIES IN ',
     &      'VAPOR PHASE = ',E12.5)
      WRITE(IWRT,940) RIIIV
  940 FORMAT('0',T50,'III/V RATIO IN THE VAPOR PHASE = ',E9.4)
      WRITE(IWRT,950)
  950 FORMAT('0',/,'0',T44,'TOTAL GRAM-MOLES OF EACH ELEMENT FROM IN',
     &'PUT DATA',/,1X,T42,'AND AS CALCULATED FROM THE EQUILIBRIUM',
     &      ' COMPOSITIONS',/,'0',4(4X,'INPUT DATA',3X,
     &      'CALCULATED',5X))
```

```
      NPRT=E/4
      NCHK=NPRT*4
      IF(NCHK.NE.E) NPRT=NPRT+1
      ISTRT=1
      DO 970 K=1,NPRT
      NEND=ISTRT+3
      IF(NEND.GT.E) NEND=E
      WRITE(IWRT,960) (ELMNT(J),B(J),BCALC(J),J=ISTRT,NEND)
  960 FORMAT(1X,4(A2,1X,E12.5,1X,E12.5,4X))
      ISTRT=NEND+1
  970 CONTINUE
  971 CONTINUE
      IF(IWRAP.GT.0)CALL WRAPUP(TITLE,SPECIE,INERT,N,FRAC,QUES,ZV,FRACZ,
     &SITOT,SIMF,ACTSIS,ACTGAS,ACTINS,ACTPS,ACTASS,RIIIV,RGAAS,RINP,
     &BSTCVG,ITBST,RELMAX,CNVG,ISS,XIII,T,P,IDATA,IDIM1,IFILE,V,VSC,
     &IOPT,ITP,NTP,ITAB,ICMP,IWRAP,GFE,STDCP,RT)
      IF(ITP.GT.1.OR.ICMP.GT.1.OR.IWRAP.GT.1) GO TO 1900
C
C  WRITE-OUT THE INDEPENDENT REACTION EQUATIONS
C
      IPAGE=IPAGE+1
      WRITE(IWRT,400) (TITLE(K),K=1,20), IPAGE
      WRITE(IWRT,410) T,P
      WRITE(IWRT.980)
  980 FORMAT('0',T34,'A SET OF INDEPENDENT REACTION EQUATIONS FOR ',
     &      'THIS SYSTEM IS AS FOLLOWS:',/,'0')
      DO 1100 I=1,VSC
C
C  DETERMINE THE NUMBER OF BASIS SPECIES IN EACH FORMATION REACTION
C
      NSPEC=0
      DO 990 K=1,E
      IF(I.EQ.IDXBAS(K)) GO TO 1100
      IF(ABS(GNU(I,K)).LT.1.0E-6) GO TO 990
      NSPEC=NSPEC+1
  990 CONTINUE
C
C  FILL THE CHARACTER ARRAY "STRING" WITH THE FORMATION REACTION
SPECIES
C
      NLOOP=1
      IF(NSPEC.GT.4) NLOOP=FLOAT(NSPEC)/4.0+0.9
      DO 1000 K=1,3
      STRING(1,K)=BSPCE(I,K)
 1000 CONTINUE
      STRING(1,4)=RPAS
      COEFF(1)=1.0
      IST=1
      ICNT=0
      DO 1060 ILOOP=1,NLOOP
      NCNT=NSPEC-ICNT+1
      IF(NCNT.GT.5) NCNT=5
      DO 1020 IDX=2,NCNT
      ICNT=ICNT+1
      DO 1015 IBASE=IST,E
      IF(ABS(GNU(I,IBASE)).LT.1.0E-6) GO TO 1015
      IDXB=IDXBAS(IBASE)
      DO 1010 K=1,3
      STRING(IDX,K)=BSPCE(IDXB,K)
 1010 CONTINUE
      COEFF(IDX)=GNU(I,IBASE)
      STRING(IDX,4)=RPSPS
      GO TO 1018
 1015 CONTINUE
 1018 IST=IBASE+1
 1020 CONTINUE
      STRING(NCNT,4)=RPBL
      IF(ILOOP.EQ.1) WRITE(IWRT,1040)(LP,COEFF(IJK),
     &                       (STRING(IJK,K),K=1,4),IJK=1,NCNT)
 1040 FORMAT('0',A1,F5.2,4A4,4(A1,E10.3,4A4))
      IF(ILOOP.GT.1) WRITE(IWRT,1050) SSPS,(LP,COEFF(IJK),
     &                        (STRING(IJK,K),K=1,4),IJK=2,NCNT)
 1050 FORMAT(1X,T20,A4,4(A1,E10.3,4A4))
 1060 CONTINUE
 1100 CONTINUE
C
C  WRITE-OUT A COMPARISON BETWEEN THE EQUILIBRIUM CONSTANTS
C  AS CALCULATED BY THE GIBBS FREE ENERGY CHANGE AND BY COMPOSITION
C
      IPAGE=IPAGE+1
      WRITE(IWRT,400) (TITLE(K),K=1,20), IPAGE
      WRITE(IWRT,410) T,P
      WRITE(IWRT,1110)
 1110 FORMAT('0',/,1X,T40,'EQUILIBRIUM CONSTANTS FOR THE INDEPENDENT',
     &' REACTIONS',/,'0',T20,'GIBBS FREE ENERGY CHANGE',T47,
     &'EQUILIBRIUM CONSTANT',T73,'EQUILIBRIUM CONSTANT',/,1X,
     &'REACTION PRODUCT',T25,'(KCAL/G-MOLE)',T46,'FROM GIBBS FREE ',
     &'ENERGY',T70,'FROM PREDICTED COMPOSITION',/,'+',16('_'),T20,
     &24('_'),T46,22('_'),T70,26('_'))
      DO 1200 I=1,VSC
      IF(N(I).GT.1.00E-21) WRITE(IWRT,1120) (SPECIE(I,K),K=1,3),DG(I),
     &                                KEQ(I),Q(I)
      IF(N(I).LE.1.00E-21) WRITE(IWRT,1121) (SPECIE(I,K),K=1,3),DG(I),
     &                                KEQ(I),Q(I)
 1120 FORMAT(1X,3A4,T28,F8.3,T51,E12.5,T77,E12.5)
 1121 FORMAT(1X,3A4,T28,F8.3,T51,E12.5,T77,E12.5,2X,'(NOT BINDING)')
 1200 CONTINUE
      IF(ISS.GT.0) WRITE(IWRT,445) XIII
 1900 IF(ISTOP.EQ.1) GO TO 3000
 2000 CONTINUE
 3000 WRITE(IWRT,3001)
 3001 FORMAT('1',")
```

```
      CALL SPECIL(N,A,E,V,S,SPECIE,ELMNT,IFILE)
 4002 STOP
      END
      SUBROUTINE STSTCP(A0,A1,A2,A3,A4,A0Z,A1Z,A2Z,A3Z,A4Z,DH0,DS0,DH0Z,
     & DS0Z,STDCP,STDCPZ,ICP,ICPZ,T0,T,IDIM1,V,S,C,e,idim2,a,ireac,ix)
C
C  THIS SUBROUTINE CALCULATES THE STANDARD STATE CHEMICAL
POTENTIALS
C  REFERENCE STATE: PURE COMPONENT (APPROPRIATE PHASE)
C                AT TEMPERATURE T AND PRESSURE P0.
C
      DIMENSION A0(IDIM1),A1(IDIM1),A2(IDIM1),A3(IDIM1),A4(IDIM1),
     &          DH0(IDIM1),DS0(IDIM1),STDCP(IDIM1),ICP(IDIM1),
     &          ireac(idim2),a(idim1,idim2)
      INTEGER V,S,C,VSC,e
      VSC=V+S+C
      DT=T-T0
      DT2=T**2-T0**2
      DT3=T**3-T0**3
      DT4=T**4-T0**4
      DTM1=1.0/T-1.0/T0
      DTM2=1.0/T/T-1.0/T0/T0
      DLNT=ALOG(T)-ALOG(T0)
      DLNT2=ALOG(T)**2-ALOG(T0)**2
      DTLNT=T*ALOG(T)-T0*ALOG(T0)
      DHPT=T**0.5-T0**0.5
      DIHPT=(1.0/(T**0.5))-(1.0/(T0**0.5))
C
C CHEMICAL POTENTIALS FOR THE VAPOR, SOLUTION AND CONDENSED PHASES
C
      DO 100 I=1,VSC+ix
      DELH=A0(I)*DT+A1(I)*DT2/2.-A2(I)*DTM1+A3(I)*(DTLNT-DT)
      DELS=A0(I)*DLNT+A1(I)*DT-A2(I)*DTM2/2.+A3(I)*DLNT2/2.
      IF(ICP(I).EQ.1) DELH=A0(I)*DT+A1(I)*DT2/2.+A2(I)*DT3/3.
     &               +A3(I)*DT4/4.
      IF(ICP(I).EQ.1) DELS=A0(I)*DLNT+A1(I)*DT+A2(I)*DT2/2.
     &               +A3(I)*DT3/3.
      IF(ICP(I).EQ.2) DELH=A0(I)*DT+A1(I)*DT2/2.+A2(I)*DT3/3.
     &               -A3(I)*DTM1
      IF(ICP(I).EQ.2) DELS=A0(I)*DLNT+A1(I)*DT+A2(I)*DT2/2.
     &               -A3(I)*DTM2/2.
      IF(ICP(I).EQ.4) DELH=A0(I)*DT+A1(I)*DT2/2.-A2(I)*DTM1
     &               +A3(I)*DT3/3.+A4(I)*DHPT/0.5
      IF(ICP(I).EQ.4) DELS=A0(I)*DLNT+A1(I)*DT-A2(I)*DTM2/2.
     &               +A3(I)*DT2/2.-A4(I)*DIHPT/0.5
      IF(ICP(I).EQ.3) THEN
        IF(T.LE.317.3) THEN
           DELH=(15.49918*(T-298.15)+(0.027908/2.0)*(T**2-
     &       (298.15)**2))/4184.0
           DELS=(15.49918*(alog(T/298.15))+0.027908*(T-298.15))
     &        /4184.0
```

```
      ELSEIF(T.GT.317.3.and.T.LE.1180.0) Then
         DELH=((26.326*(T-317.3))+15.49918*(317.3-298.15)
     &        +(0.027908/2.0)*((317.3)**2-(298.15)**2)+657.5)
     &        /4184.0
         DELS=(26.326*ALOG(T/317.3)+15.49918*(alog(317.3/298.15))
     &        +0.027908*(317.3-298.15)+2.0728)/4184.0
      ELSE
         DELH=((26.326*(1180.0-317.3))+15.49918*(317.3-298.15)
     &        +(0.027908/2.0)*((317.3)**2-(298.15)**2)
     &        +18.6*(T-1180.0)+64390.0)/4184.0
         DELS=(26.326*ALOG(1180.0/317.3)+15.49918*
     &        (alog(317.3/298.15))+0.027908*(317.3-298.15)
     &        +18.6*alog(T/1180.0)+56.083)/4184.0
      ENDIF
     ELSEIF(ICP(I).EQ.5) THEN
      IF(T.LE.332.5) THEN
        DELH=(78.76570*(T-298.15)-(0.0104196/2.0)*((T**2)-
     &   ((298.15)**2)))/4184.0
        DELS=(78.76570*(alog(T/298.15))-0.0104196*(T-298.15))
     &    /4184.0
       ELSE
         DELH=(33.8979*(T-332.5)+(0.0106738/2)*((T**2)-
     &        (332.5)**2)-(0.0000113343/3)*((T**3)-((332.5)**3))+
     &        (0.00000000550009/4)*((T**4)-((332.5)**4))
     &        -(0.000000000000936565/5)*((T**5)-((332.5)**5))
     &        +78.76570*(332.5-298.15)-(0.0104196/2.0)*
     &        (((332.5)**2)-((298.15)**2))+29564.0)/4184.0
         DELS=(33.8979*ALOG(T/332.5)+0.0106738*(T-332.15)-
     &        (0.0000113343/2)*((T**2)-((332.5)**2))+
     &        (0.00000000550009/3)*((T**3)-((332.5)**3))-
     &        (0.000000000000936565/4)*((T**4)-((332.5)**4))+
     &        78.76570*(alog(332.5/298.15))-
     &        0.0104196*(332.5-298.15)+88.911)/4184.0
       ENDIF
C    H3B:NH3 - COMPLETED
     ELSEIF(ICP(I).EQ.10) THEN
      IF(T.LE.1000) THEN
       DELH=0.0019872*(1.9486989*(T-298.15)+(0.020093319/2)*((T**2)-
     &     (298.15)**2)-(0.0000050634675/3)*((T**3)-(298.15)**3)-
     &     (0.0000000033493641/4)*((T**4)-(298.15)**4)+
     &     (0.0000000000017462886/5)*((T**5)-(298.15)**5))
       DELS=0.0019872*(1.9486989*ALOG(T/298.15)+(0.020093319)*
     &     (T-298.15)-(0.0000050634675/2)*((T**2)-(298.15)**2)-
     &     (0.0000000033493641/3)*((T**3)-(298.15)**3)+
     &     (0.0000000000017462886/4)*((T**4)-(298.15)**4))
      ELSE
       DELH=0.0019872*(2.2071150*(T-298.15)+(0.021525925/2)*((T**2)-
     &     (298.15)**2)-(0.00010696339/3)*((T**3)-(298.15)**3)+
     &     (0.0000000025848974/4)*((T**4)-(298.15)**4)-
     &     (0.000000000000024612315/5)*((T**5)-(298.15)**5))
       DELS=0.0019872*(2.2071150*ALOG(T/298.15)+(0.021525925)*
  &        (T-298.15)-(0.000010696339/2)*((T**2)-(298.15)**2)+
  &        (0.0000000025848974/3)*((T**3)-(298.15)**3)-
  &        (0.00000000000024612315/4)*((T**4)-(298.15)**4))
      ENDIF
C   H2BNH2 - COMPLETED
    ELSEIF(ICP(I).EQ.11) THEN
     IF(T.LE.1000) THEN
      DELH=0.0019872*(0.4193633*(T-298.15)+(0.023120948/2)*((T**2)-
  &        (298.15)**2)-(0.000018491259/3)*((T**3)-(298.15)**3)+
  &        (0.0000000084716927/4)*((T**4)-(298.15)**4)-
  &        (0.0000000000016998117/5)*((T**5)-(298.15)**5))
      DELS=0.0019872*(0.4193633*ALOG(T/298.15)+(0.023120948)*
  &        (T-298.15)-(0.000018491259/2)*((T**2)-(298.15)**2)+
  &        (0.0000000084716927/3)*((T**3)-(298.15)**3)-
  &        (0.0000000000016998117/4)*((T**4)-(298.15)**4))
     ELSE
      DELH=0.0019872*(3.0438396*(T-298.15)+(0.014103071/2)*((T**2)-
  &        (298.15)**2)-(0.0000067818204/3)*((T**3)-(298.15)**3)+
  &        (0.0000000016085416/4)*((T**4)-(298.15)**4)-
  &        (0.00000000000015269824/5)*((T**5)-(298.15)**5))
      DELS=0.0019872*(3.0438396*ALOG(T/298.15)+(0.014103071)*
  &        (T-298.15)-(0.0000067818204/2)*((T**2)-(298.15)**2)+
  &        (0.0000000016085416/3)*((T**3)-(298.15)**3)-
  &        (0.00000000000015269824/4)*((T**4)-(298.15)**4))
      ENDIF
C   H2BNH - COMPLETED
    ELSEIF(ICP(I).EQ.12) THEN
     IF(T.LE.1000) THEN
      DELH=0.0019872*(2.4812213*(T-298.15)+(0.015474766/2)*((T**2)-
  &        (298.15)**2)-(0.000014128864/3)*((T**3)-(298.15)**3)+
  &        (0.0000000079911700/4)*((T**4)-(298.15)**4)-
  &        (0.0000000000020319425/5)*((T**5)-(298.15)**5))
      DELS=0.0019872*(2.4812213*ALOG(T/298.15)+(0.015474766)*
  &        (T-298.15)-(0.000014128864/2)*((T**2)-(298.15)**2)+
  &        (0.0000000079911700/3)*((T**3)-(298.15)**3)-
  &        (0.0000000000020319425/4)*((T**4)-(298.15)**4))
     ELSE
      DELH=0.0019872*(3.9564653*(T-298.15)+(0.009516611/2)*((T**2)-
  &        (298.15)**2)-(0.0000047139857/3)*((T**3)-(298.15)**3)+
  &        (0.0000000011349029/4)*((T**4)-(298.15)**4)-
  &        (0.00000000000010764237/5)*((T**5)-(298.15)**5))
      DELS=0.0019872*(3.9564653*ALOG(T/298.15)+(0.009516611)*
  &        (T-298.15)-(0.0000047139857/2)*((T**2)-(298.15)**2)+
  &        (0.0000000011349029/3)*((T**3)-(298.15)**3)-
  &        (0.00000000000010764237/4)*((T**4)-(298.15)**4))
      ENDIF
C   HBNH2 - COMPLETED
    ELSEIF(ICP(I).EQ.13) THEN
     IF(T.LE.1000) THEN
      DELH=0.0019872*(1.2969619*(T-298.15)+(0.018873270/2)*((T**2)-
  &        (298.15)**2)-(0.000018102730/3)*((T**3)-(298.15)**3)+
     &        (0.000000010181584/4)*((T**4)-(298.15)**4)-
     &        (0.0000000000024043388/5)*((T**5)-(298.15)**5))
         DELS=0.0019872*(1.2969619*ALOG(T/298.15)+(0.018873270)*
     &        (T-298.15)-(0.000018102730/2)*((T**2)-(298.15)**2)+
     &        (0.000000010181584/3)*((T**3)-(298.15)**3)-
     &        (0.0000000000024043388/4)*((T**4)-(298.15)**4))
        ELSE
         DELH=0.0019872*(3.4942392*(T-298.15)+(0.009863196/2)*((T**2)-
     &        (298.15)**2)-(0.0000043446503/3)*((T**3)-(298.15)**3)+
     &        (0.00000000090653661/4)*((T**4)-(298.15)**4)-
     &        (0.00000000000074574453/5)*((T**5)-(298.15)**5))
         DELS=0.0019872*(3.4942392*ALOG(T/298.15)+(0.009863196)*
     &        (T-298.15)-(0.0000043446503/2)*((T**2)-(298.15)**2)+
     &        (0.00000000090653661/3)*((T**3)-(298.15)**3)-
     &        (0.00000000000074574453/4)*((T**4)-(298.15)**4))
         ENDIF
C    B(NH2)2 - COMPLETED
      ELSEIF(ICP(I).EQ.14) THEN
        IF(T.LE.1000) THEN
         DELH=0.0019872*(2.3853503*(T-298.15)+(0.028621000/2)*((T**2)-
     &        (298.15)**2)-(0.000030284743/3)*((T**3)-(298.15)**3)+
     &        (0.000000018423211/4)*((T**4)-(298.15)**4)-
     &        (0.0000000000046834331/5)*((T**5)-(298.15)**5))
         DELS=0.0019872*(2.3853503*ALOG(T/298.15)+(0.028621000)*
     &        (T-298.15)-(0.000030284743/2)*((T**2)-(298.15)**2)+
     &        (0.000000018423211/3)*((T**3)-(298.15)**3)-
     &        (0.0000000000046834331/4)*((T**4)-(298.15)**4))
        ELSE
         DELH=0.0019872*(6.2477507*(T-298.15)+(0.012884149/2)*((T**2)-
     &        (298.15)**2)-(0.0000058229691/3)*((T**3)-(298.15)**3)+
     &        (0.0000000012606148/4)*((T**4)-(298.15)**4)-
     &        (0.00000000000010815990/5)*((T**5)-(298.15)**5))
         DELS=0.0019872*(6.2477507*ALOG(T/298.15)+(0.012884149)*
     &        (T-298.15)-(0.0000058229691/2)*((T**2)-(298.15)**2)+
     &        (0.0000000012606148/3)*((T**3)-(298.15)**3)-
     &        (0.00000000000010815990/4)*((T**4)-(298.15)**4))
         ENDIF
C    HBNH - COMPLETED
      ELSEIF(ICP(I).EQ.15) THEN
        IF(T.LE.1000) THEN
         DELH=0.0019872*(2.3193329*(T-298.15)+(0.015323100/2)*((T**2)-
     &        (298.15)**2)-(0.000021011123/3)*((T**3)-(298.15)**3)+
     &        (0.000000016044587/4)*((T**4)-(298.15)**4)-
     &        (0.0000000000048276744/5)*((T**5)-(298.15)**5))
         DELS=0.0019872*(2.3193329*ALOG(T/298.15)+(0.015323100)*
     &        (T-298.15)-(0.000021011123/2)*((T**2)-(298.15)**2)+
     &        (0.000000016044587/3)*((T**3)-(298.15)**3)-
     &        (0.0000000000048276744/4)*((T**4)-(298.15)**4))
        ELSE
         DELH=0.0019872*(4.2145555*(T-298.15)+(0.005561448/2)*((T**2)-
     &        (298.15)**2)-(0.0000023877281/3)*((T**3)-(298.15)**3)+
     &       (0.00000000050186293/4)*((T**4)-(298.15)**4)-
     &       (0.0000000000000041915774/5)*((T**5)-(298.15)**5))
         DELS=0.0019872*(4.2145555*ALOG(T/298.15)+(0.005561448)*
     &       (T-298.15)-(0.0000023877281/2)*((T**2)-(298.15)**2)+
     &       (0.00000000050186293/3)*((T**3)-(298.15)**3)-
     &       (0.0000000000000041915774/4)*((T**4)-(298.15)**4))
         ENDIF
C    BNH2 - COMPLETED
      ELSEIF(ICP(I).EQ.16) THEN
        IF(T.LE.1000) THEN
         DELH=0.0019872*(3.0264833*(T-298.15)+(0.010551614/2)*((T**2)-
     &       (298.15)**2)-(0.000010757413/3)*((T**3)-(298.15)**3)+
     &       (0.0000000065359666/4)*((T**4)-(298.15)**4)-
     &       (0.000000000000016255074/5)*((T**5)-(298.15)**5))
         DELS=0.0019872*(3.0264833*ALOG(T/298.15)+(0.010551614)*
     &       (T-298.15)-(0.000010757413/2)*((T**2)-(298.15)**2)+
     &       (0.0000000065359666/3)*((T**3)-(298.15)**3)-
     &       (0.000000000000016255074/4)*((T**4)-(298.15)**4))
        ELSE
         DELH=0.0019872*(4.1846862*(T-298.15)+(0.005313243/2)*((T**2)-
     &       (298.15)**2)-(0.0000021639674/3)*((T**3)-(298.15)**3)+
     &       (0.00000000043137685/4)*((T**4)-(298.15)**4)-
     &       (0.0000000000000034195004/5)*((T**5)-(298.15)**5))
         DELS=0.0019872*(4.1846862*ALOG(T/298.15)+(0.005313243)*
     &       (T-298.15)-(0.0000021639674/2)*((T**2)-(298.15)**2)+
     &       (0.00000000043137685/3)*((T**3)-(298.15)**3)-
     &       (0.0000000000000034195004/4)*((T**4)-(298.15)**4))
         ENDIF
C    H2BN - COMPLETED
      ELSEIF(ICP(I).EQ.17) THEN
        IF(T.LE.1000) THEN
         DELH=0.0019872*(1.6880774*(T-298.15)+(0.013942306/2)*((T**2)-
     &       (298.15)**2)-(0.000012349144/3)*((T**3)-(298.15)**3)+
     &       (0.0000000064602304/4)*((T**4)-(298.15)**4)-
     &       (0.000000000000015665199/5)*((T**5)-(298.15)**5))
         DELS=0.0019872*(1.6880774*ALOG(T/298.15)+(0.013942306)*
     &       (T-298.15)-(0.000012349144/2)*((T**2)-(298.15)**2)+
     &       (0.0000000064602304/3)*((T**3)-(298.15)**3)-
     &       (0.000000000000015665199/4)*((T**4)-(298.15)**4))
        ELSE
         DELH=0.0019872*(3.2827991*(T-298.15)+(0.008348944/2)*((T**2)-
     &       (298.15)**2)-(0.0000044948262/3)*((T**3)-(298.15)**3)+
     &       (0.0000000011527939/4)*((T**4)-(298.15)**4)-
     &       (0.00000000000011476111/5)*((T**5)-(298.15)**5))
         DELS=0.0019872*(3.2827991*ALOG(T/298.15)+(0.008348944)*
     &       (T-298.15)-(0.0000044948262/2)*((T**2)-(298.15)**2)+
     &       (0.0000000011527939/3)*((T**3)-(298.15)**3)-
     &       (0.00000000000011476111/4)*((T**4)-(298.15)**4))
         ENDIF
C    BNH - COMPLETED
      ELSEIF(ICP(I).EQ.18) THEN
```

```
          IF(T.LE.1000) THEN
            DELH=0.0019872*(2.9255150*(T-298.15)+(0.008966532/2)*((T**2)-
     &          (298.15)**2)-(0.000012284371/3)*((T**3)-(298.15)**3)+
     &          (0.0000000093288082/4)*((T**4)-(298.15)**4)-
     &          (0.0000000000027872964/5)*((T**5)-(298.15)**5))
            DELS=0.0019872*(2.9255150*ALOG(T/298.15)+(0.008966532)*
     &          (T-298.15)-(0.000012284371/2)*((T**2)-(298.15)**2)+
     &          (0.0000000093288082/3)*((T**3)-(298.15)**3)-
     &          (0.0000000000027872964/4)*((T**4)-(298.15)**4))
           ELSE
            DELH=0.0019872*(4.1529691*(T-298.15)+(0.002941866/2)*((T**2)-
     &          (298.15)**2)-(0.0000011461845/3)*((T**3)-(298.15)**3)+
     &          (0.00000000021661728/4)*((T**4)-(298.15)**4)-
     &          (0.000000000000016079884/5)*((T**5)-(298.15)**5))
            DELS=0.0019872*(4.1529691*ALOG(T/298.15)+(0.002941866)*
     &          (T-298.15)-(0.0000011461845/2)*((T**2)-(298.15)**2)+
     &          (0.00000000021661728/3)*((T**3)-(298.15)**3)-
     &          (0.000000000000016079884/4)*((T**4)-(298.15)**4))
            ENDIF
C     HBN - COMPLETED
        ELSEIF(ICP(I).EQ.19) THEN
          IF(T.LE.1000) THEN
            DELH=0.0019872*(2.1678647*(T-298.15)+(0.010299223/2)*((T**2)-
     &          (298.15)**2)-(0.000011718176/3)*((T**3)-(298.15)**3)+
     &          (0.0000000078508956/4)*((T**4)-(298.15)**4)-
     &          (0.0000000000022467092/5)*((T**5)-(298.15)**5))
            DELS=0.0019872*(2.1678647*ALOG(T/298.15)+(0.010299223)*
     &          (T-298.15)-(0.000011718176/2)*((T**2)-(298.15)**2)+
     &          (0.0000000078508956/3)*((T**3)-(298.15)**3)-
     &          (0.0000000000022467092/4)*((T**4)-(298.15)**4))
           ELSE
            DELH=0.0019872*(3.4676306*(T-298.15)+(0.004857775/2)*((T**2)-
     &          (298.15)**2)-(0.0000025506615/3)*((T**3)-(298.15)**3)+
     &          (0.00000000064115057/4)*((T**4)-(298.15)**4)-
     &          (0.000000000000062795245/5)*((T**5)-(298.15)**5))
            DELS=0.0019872*(3.4676306*ALOG(T/298.15)+(0.004857775)*
     &          (T-298.15)-(0.0000025506615/2)*((T**2)-(298.15)**2)+
     &          (0.00000000064115057/3)*((T**3)-(298.15)**3)-
     &          (0.000000000000062795245/4)*((T**4)-(298.15)**4))
            ENDIF
C     BN - COMPLETED
        ELSEIF(ICP(I).EQ.20) THEN
          IF(T.LE.1000) THEN
            DELH=0.0019872*(3.7776064*(T-298.15)-(0.002727947/2)*((T**2)-
     &          (298.15)**2)+(0.0000082596218/3)*((T**3)-(298.15)**3)-
     &          (0.0000000074915752/4)*((T**4)-(298.15)**4)+
     &          (0.0000000000023074239/5)*((T**5)-(298.15)**5))
            DELS=0.0019872*(3.7776064*ALOG(T/298.15)-(0.002727947)*
     &          (T-298.15)+(0.0000082596218/2)*((T**2)-(298.15)**2)-
     &          (0.0000000074915752/3)*((T**3)-(298.15)**3)+
     &          (0.0000000000023074239/4)*((T**4)-(298.15)**4))
```

```
        ELSE
         DELH=0.0019872*(2.9023763*(T-298.15)+(0.0021631386)*((T**2)-
     &        (298.15)**2)-(0.0000012385196/3)*((T**3)-(298.15)**3)+
     &        (0.00000000033237094/4)*((T**4)-(298.15)**4)-
     &        (0.0000000000000034236397/5)*((T**5)-(298.15)**5))
         DELS=0.0019872*(2.9023763*ALOG(T/298.15)+(0.0021631386)*
     &        (T-298.15)-(0.0000012385196/2)*((T**2)-(298.15)**2)+
     &        (0.00000000033237094/3)*((T**3)-(298.15)**3)-
     &        (0.0000000000000034236397/4)*((T**4)-(298.15)**4))
         ENDIF
C    B3N3H6 - COMPLETED
      ELSEIF(ICP(I).EQ.21) THEN
        IF(T.LE.1000) THEN
         DELH=0.0019872*(-5.994433*(T-298.15)+(0.082459624/2)*((T**2)-
     &        (298.15)**2)-(0.000088959868/3)*((T**3)-(298.15)**3)+
     &        (0.000000051292394/4)*((T**4)-(298.15)**4)-
     &        (0.000000000012333185/5)*((T**5)-(298.15)**5))
         DELS=0.0019872*(-5.994433*ALOG(T/298.15)+(0.082459624)*
     &        (T-298.15)-(0.000088959868/2)*((T**2)-(298.15)**2)+
     &        (0.000000051292394/3)*((T**3)-(298.15)**3)-
     &        (0.000000000012333185/4)*((T**4)-(298.15)**4))
        ELSE
         DELH=0.0019872*(8.1091459*(T-298.15)+(0.030955806)*((T**2)-
     &        (298.15)**2)-(0.000016341882/3)*((T**3)-(298.15)**3)+
     &        (0.0000000041535622/4)*((T**4)-(298.15)**4)-
     &        (0.00000000000041209942/5)*((T**5)-(298.15)**5))
         DELS=0.0019872*(8.1091459*ALOG(T/298.15)+(0.030955806)*
     &        (T-298.15)-(0.000016341882/2)*((T**2)-(298.15)**2)+
     &        (0.0000000041535622/3)*((T**3)-(298.15)**3)-
     &        (0.00000000000041209942/4)*((T**4)-(298.15)**4))
         ENDIF
C    CL3B:NH3 - COMPLETED
      ELSEIF(ICP(I).EQ.22) THEN
        IF(T.LE.1000) THEN
         DELH=0.0019872*(3.3004107*(T-298.15)+(0.043921800/2)*((T**2)-
     &        (298.15)**2)-(0.000061316269/3)*((T**3)-(298.15)**3)+
     &        (0.000000044561820/4)*((T**4)-(298.15)**4)-
     &        (0.000000000012760718/5)*((T**5)-(298.15)**5))
         DELS=0.0019872*(3.3004107*ALOG(T/298.15)+(0.043921800)*
     &        (T-298.15)-(0.000061316269/2)*((T**2)-(298.15)**2)+
     &        (0.000000044561820/3)*((T**3)-(298.15)**3)-
     &        (0.000000000012760718/4)*((T**4)-(298.15)**4))
        ELSE
         DELH=0.0019872*(10.672418*(T-298.15)+(0.011079021)*((T**2)-
     &        (298.15)**2)-(0.0000050888600/3)*((T**3)-(298.15)**3)+
     &        (0.0000000011473083/4)*((T**4)-(298.15)**4)-
     &        (0.00000000000010284438/5)*((T**5)-(298.15)**5))
         DELS=0.0019872*(10.672418*ALOG(T/298.15)+(0.011079021)*
     &        (T-298.15)-(0.0000050888600/2)*((T**2)-(298.15)**2)+
     &        (0.0000000011473083/3)*((T**3)-(298.15)**3)-
     &        (0.00000000000010284438/4)*((T**4)-(298.15)**4))
```

```
        ENDIF
C    H3N:BCL2NH2 - COMPLETED
      ELSEIF(ICP(I).EQ.23) THEN
        IF(T.LE.1000) THEN
          DELH=0.0019872*(4.3319819*(T-298.15)+(0.043504102/2)*((T**2)-
     &        (298.15)**2)-(0.000053588016/3)*((T**3)-(298.15)**3)+
     &        (0.000000036948205/4)*((T**4)-(298.15)**4)-
     &        (0.000000000010279360/5)*((T**5)-(298.15)**5))
          DELS=0.0019872*(4.3319819*ALOG(T/298.15)+(0.043504102)*
     &        (T-298.15)-(0.000053588016/2)*((T**2)-(298.15)**2)+
     &        (0.000000036948205/3)*((T**3)-(298.15)**3)-
     &        (0.000000000010279360/4)*((T**4)-(298.15)**4))
         ELSE
          DELH=0.0019872*(10.430558*(T-298.15)+(0.016185565)*((T**2)-
     &        (298.15)**2)-(0.0000070991712/3)*((T**3)-(298.15)**3)+
     &        (0.0000000015318220/4)*((T**4)-(298.15)**4)-
     &        (0.00000000000013186112/5)*((T**5)-(298.15)**5))
          DELS=0.0019872*(10.430558*ALOG(T/298.15)+(0.016185565)*
     &        (T-298.15)-(0.0000070991712/2)*((T**2)-(298.15)**2)+
     &        (0.0000000015318220/3)*((T**3)-(298.15)**3)-
     &        (0.00000000000013186112/4)*((T**4)-(298.15)**4))
          ENDIF
C    HCLBNH2 - COMPLETED
      ELSEIF(ICP(I).EQ.24) THEN
        IF(T.LE.1000) THEN
          DELH=0.0019872*(0.4418683*(T-298.15)+(0.032025491/2)*((T**2)-
     &        (298.15)**2)-(0.000038260171/3)*((T**3)-(298.15)**3)+
     &        (0.000000024991354/4)*((T**4)-(298.15)**4)-
     &        (0.0000000000066704942/5)*((T**5)-(298.15)**5))
          DELS=0.0019872*(0.4418683*ALOG(T/298.15)+(0.032025491)*
     &        (T-298.15)-(0.000038260171/2)*((T**2)-(298.15)**2)+
     &        (0.000000024991354/3)*((T**3)-(298.15)**3)-
     &        (0.0000000000066704942/4)*((T**4)-(298.15)**4))
         ELSE
          DELH=0.0019872*(5.4814084*(T-298.15)+(0.011357911)*((T**2)-
     &        (298.15)**2)-(0.0000054962072/3)*((T**3)-(298.15)**3)+
     &        (0.0000000013080063/4)*((T**4)-(298.15)**4)-
     &        (0.00000000000012307055/5)*((T**5)-(298.15)**5))
          DELS=0.0019872*(5.4814084*ALOG(T/298.15)+(0.011357911)*
     &        (T-298.15)-(0.0000054962072/2)*((T**2)-(298.15)**2)+
     &        (0.0000000013080063/3)*((T**3)-(298.15)**3)-
     &        (0.00000000000012307055/4)*((T**4)-(298.15)**4))
          ENDIF
C    CL2BNH2 - COMPLETED
      ELSEIF(ICP(I).EQ.25) THEN
        IF(T.LE.1000) THEN
          DELH=0.0019872*(1.6111386*(T-298.15)+(0.036173832/2)*((T**2)-
     &        (298.15)**2)-(0.000049919403/3)*((T**3)-(298.15)**3)+
     &        (0.000000035397672/4)*((T**4)-(298.15)**4)-
     &        (0.000000000098978999/5)*((T**5)-(298.15)**5))
          DELS=0.0019872*(1.6111386*ALOG(T/298.15)+(0.036173832)*
  &        (T-298.15)-(0.000049919403/2)*((T**2)-(298.15)**2)+
  &        (0.000000035397672/3)*((T**3)-(298.15)**3)-
  &        (0.0000000000098978999/4)*((T**4)-(298.15)**4))
      ELSE
       DELH=0.0019872*(8.3411997*(T-298.15)+(0.0076665966)*((T**2)-
  &        (298.15)**2)-(0.000032517436/3)*((T**3)-(298.15)**3)+
  &        (0.0000000066381355/4)*((T**4)-(298.15)**4)-
  &        (0.0000000000000054527459/5)*((T**5)-(298.15)**5))
       DELS=0.0019872*(8.3411997*ALOG(T/298.15)+(0.0076665966)*
  &        (T-298.15)-(0.000032517436/2)*((T**2)-(298.15)**2)+
  &        (0.0000000066381355/3)*((T**3)-(298.15)**3)-
  &        (0.0000000000000054527459/4)*((T**4)-(298.15)**4))
       ENDIF
C    CLB(NH2)2 - COMPLETED
   ELSEIF(ICP(I).EQ.26) THEN
     IF(T.LE.1000) THEN
       DELH=0.0019872*(1.9105125*(T-298.15)+(0.041847052/2)*((T**2)-
  &        (298.15)**2)-(0.000051964008/3)*((T**3)-(298.15)**3)+
  &        (0.000000035646261/4)*((T**4)-(298.15)**4)-
  &        (0.000000000010056248/5)*((T**5)-(298.15)**5))
       DELS=0.0019872*(1.9105125*ALOG(T/298.15)+(0.041847052)*
  &        (T-298.15)-(0.000051964008/2)*((T**2)-(298.15)**2)+
  &        (0.000000035646261/3)*((T**3)-(298.15)**3)-
  &        (0.000000000010056248/4)*((T**4)-(298.15)**4))
      ELSE
       DELH=0.0019872*(8.0587679*(T-298.15)+(0.015654719)*((T**2)-
  &        (298.15)**2)-(0.0000081648086/3)*((T**3)-(298.15)**3)+
  &        (0.0000000020318401/4)*((T**4)-(298.15)**4)-
  &        (0.00000000000019694852/5)*((T**5)-(298.15)**5))
       DELS=0.0019872*(8.0587679*ALOG(T/298.15)+(0.015654719)*
  &        (T-298.15)-(0.0000081648086/2)*((T**2)-(298.15)**2)+
  &        (0.0000000020318401/3)*((T**3)-(298.15)**3)-
  &        (0.00000000000019694852/4)*((T**4)-(298.15)**4))
       ENDIF
C    HB(NH2)2 - COMPLETED
   ELSEIF(ICP(I).EQ.27) THEN
     IF(T.LE.1000) THEN
       DELH=0.0019872*(0.7074587*(T-298.15)+(0.037546266/2)*((T**2)-
  &        (298.15)**2)-(0.000040400690/3)*((T**3)-(298.15)**3)+
  &        (0.000000025177066/4)*((T**4)-(298.15)**4)-
  &        (0.0000000000065373221/5)*((T**5)-(298.15)**5))
       DELS=0.0019872*(0.7074587*ALOG(T/298.15)+(0.037546266)*
  &        (T-298.15)-(0.000040400690/2)*((T**2)-(298.15)**2)+
  &        (0.000000025177066/3)*((T**3)-(298.15)**3)-
  &        (0.0000000000065373221/4)*((T**4)-(298.15)**4))
      ELSE
       DELH=0.0019872*(5.3313244*(T-298.15)+(0.017685809)*((T**2)-
  &        (298.15)**2)-(0.0000081717344/3)*((T**3)-(298.15)**3)+
  &        (0.0000000018050633/4)*((T**4)-(298.15)**4)-
  &        (0.00000000000015768405/5)*((T**5)-(298.15)**5))
       DELS=0.0019872*(5.3313244*ALOG(T/298.15)+(0.017685809)*
     &        (T-298.15)-(0.0000081717344/2)*((T**2)-(298.15)**2)+
     &        (0.0000000018050633/3)*((T**3)-(298.15)**3)-
     &        (0.000000000000015768405/4)*((T**4)-(298.15)**4))
         ENDIF
C     B(NH2)3 - COMPLETED
      ELSEIF(ICP(I).EQ.28) THEN
        IF(T.LE.1000) THEN
         DELH=0.0019872*(3.6530985*(T-298.15)+(0.041482257/2)*((T**2)-
     &        (298.15)**2)-(0.000046943381/3)*((T**3)-(298.15)**3)+
     &        (0.000000030913755/4)*((T**4)-(298.15)**4)-
     &        (0.0000000000083890618/5)*((T**5)-(298.15)**5))
         DELS=0.0019872*(3.6530985*ALOG(T/298.15)+(0.041482257)*
     &        (T-298.15)-(0.000046943381/2)*((T**2)-(298.15)**2)+
     &        (0.000000030913755/3)*((T**3)-(298.15)**3)-
     &        (0.0000000000083890618/4)*((T**4)-(298.15)**4))
        ELSE
         DELH=0.0019872*(8.4127036*(T-298.15)+(0.019469817)*((T**2)-
     &        (298.15)**2)-(0.0000089816447/3)*((T**3)-(298.15)**3)+
     &        (0.0000000019891808/4)*((T**4)-(298.15)**4)-
     &        (0.00000000000017338987/5)*((T**5)-(298.15)**5))
         DELS=0.0019872*(8.4127036*ALOG(T/298.15)+(0.019469817)*
     &        (T-298.15)-(0.0000089816447/2)*((T**2)-(298.15)**2)+
     &        (0.0000000019891808/3)*((T**3)-(298.15)**3)-
     &        (0.00000000000017338987/4)*((T**4)-(298.15)**4))
         ENDIF
C     CL2BNH - COMPLETED
      ELSEIF(ICP(I).EQ.29) THEN
        IF(T.LE.1000) THEN
         DELH=0.0019872*(3.1037539*(T-298.15)+(0.025930864/2)*((T**2)-
     &        (298.15)**2)-(0.000038729895/3)*((T**3)-(298.15)**3)+
     &        (0.000000028489750/4)*((T**4)-(298.15)**4)-
     &        (0.0000000000081415790/5)*((T**5)-(298.15)**5))
         DELS=0.0019872*(3.1037539*ALOG(T/298.15)+(0.025930864)*
     &        (T-298.15)-(0.000038729895/2)*((T**2)-(298.15)**2)+
     &        (0.000000028489750/3)*((T**3)-(298.15)**3)-
     &        (0.0000000000081415790/4)*((T**4)-(298.15)**4))
        ELSE
         DELH=0.0019872*(8.1855453*(T-298.15)+(0.003898850)*((T**2)-
     &        (298.15)**2)-(0.0000018073858/3)*((T**3)-(298.15)**3)+
     &        (0.00000000041360457/4)*((T**4)-(298.15)**4)-
     &        (0.000000000000037721658/5)*((T**5)-(298.15)**5))
         DELS=0.0019872*(8.1855453*ALOG(T/298.15)+(0.003898850)*
     &        (T-298.15)-(0.0000018073858/2)*((T**2)-(298.15)**2)+
     &        (0.00000000041360457/3)*((T**3)-(298.15)**3)-
     &        (0.000000000000037721658/4)*((T**4)-(298.15)**4))
         ENDIF
C     CLBNH2 - COMPLETED
      ELSEIF(ICP(I).EQ.30) THEN
        IF(T.LE.1000) THEN
         DELH=0.0019872*(1.8171184*(T-298.15)+(0.024164438/2)*((T**2)-
     &        (298.15)**2)-(0.000030408483/3)*((T**3)-(298.15)**3)+
     &      (0.000000020427987/4)*((T**4)-(298.15)**4)-
     &      (0.0000000000054712704/5)*((T**5)-(298.15)**5))
          DELS=0.0019872*(1.8171184*ALOG(T/298.15)+(0.024164438)*
     &      (T-298.15)-(0.000030408483/2)*((T**2)-(298.15)**2)+
     &      (0.000000020427987/3)*((T**3)-(298.15)**3)-
     &      (0.0000000000054712704/4)*((T**4)-(298.15)**4))
         ELSE
          DELH=0.0019872*(5.9002683*(T-298.15)+(0.006970581)*((T**2)-
     &      (298.15)**2)-(0.0000028384537/3)*((T**3)-(298.15)**3)+
     &      (0.00000000053689880/4)*((T**4)-(298.15)**4)-
     &      (0.000000000000039504979/5)*((T**5)-(298.15)**5))
          DELS=0.0019872*(5.9002683*ALOG(T/298.15)+(0.006970581)*
     &      (T-298.15)-(0.0000028384537/2)*((T**2)-(298.15)**2)+
     &      (0.00000000053689880/3)*((T**3)-(298.15)**3)-
     &      (0.000000000000039504979/4)*((T**4)-(298.15)**4))
          ENDIF
C    CLBNH - COMPLETED
      ELSEIF(ICP(I).EQ.31) THEN
         IF(T.LE.1000) THEN
          DELH=0.0019872*(2.5918568*(T-298.15)+(0.022736363/2)*((T**2)-
     &      (298.15)**2)-(0.000036393493/3)*((T**3)-(298.15)**3)+
     &      (0.000000028764736/4)*((T**4)-(298.15)**4)-
     &      (0.0000000000087021588/5)*((T**5)-(298.15)**5))
          DELS=0.0019872*(2.5918568*ALOG(T/298.15)+(0.022736363)*
     &      (T-298.15)-(0.000036393493/2)*((T**2)-(298.15)**2)+
     &      (0.000000028764736/3)*((T**3)-(298.15)**3)-
     &      (0.0000000000087021588/4)*((T**4)-(298.15)**4))
         ELSE
          DELH=0.0019872*(6.5995152*(T-298.15)+(0.003613156)*((T**2)-
     &      (298.15)**2)-(0.0000014917860/3)*((T**3)-(298.15)**3)+
     &      (0.00000000030031014/4)*((T**4)-(298.15)**4)-
     &      (0.000000000000023890943/5)*((T**5)-(298.15)**5))
          DELS=0.0019872*(6.5995152*ALOG(T/298.15)+(0.003613156)*
     &      (T-298.15)-(0.0000014917860/2)*((T**2)-(298.15)**2)+
     &      (0.00000000030031014/3)*((T**3)-(298.15)**3)-
     &      (0.000000000000023890943/4)*((T**4)-(298.15)**4))
          ENDIF
C    CL2BN - COMPLETED
      ELSEIF(ICP(I).EQ.32) THEN
         IF(T.LE.1000) THEN
          DELH=0.0019872*(2.9048020*(T-298.15)+(0.023454774/2)*((T**2)-
     &      (298.15)**2)-(0.000034454677/3)*((T**3)-(298.15)**3)+
     &      (0.000000024568659/4)*((T**4)-(298.15)**4)-
     &      (0.0000000000068890384/5)*((T**5)-(298.15)**5))
          DELS=0.0019872*(2.9048020*ALOG(T/298.15)+(0.023454774)*
     &      (T-298.15)-(0.000034454677/2)*((T**2)-(298.15)**2)+
     &      (0.000000024568659/3)*((T**3)-(298.15)**3)-
     &      (0.0000000000068890384/4)*((T**4)-(298.15)**4))
         ELSE
          DELH=0.0019872*(7.9110437*(T-298.15)+(0.003052099)*((T**2)-
     &      (298.15)**2)-(0.0000018323017/3)*((T**3)-(298.15)**3)+
     &        (0.0000000050696803/4)*((T**4)-(298.15)**4)-
     &        (0.00000000000053289094/5)*((T**5)-(298.15)**5))
          DELS=0.0019872*(7.9110437*ALOG(T/298.15)+(0.0030520990)*
     &        (T-298.15)-(0.0000018323017/2)*((T**2)-(298.15)**2)+
     &        (0.0000000050696803/3)*((T**3)-(298.15)**3)-
     &        (0.00000000000053289094/4)*((T**4)-(298.15)**4))
          ENDIF
C    BNCL2 - COMPLETED
      ELSEIF(ICP(I).EQ.33) THEN
        IF(T.LE.1000) THEN
          DELH=0.0019872*(4.0543637*(T-298.15)+(0.018339636/2)*((T**2)-
     &        (298.15)**2)-(0.000025543760/3)*((T**3)-(298.15)**3)+
     &        (0.000000017534109/4)*((T**4)-(298.15)**4)-
     &        (0.0000000000047936684/5)*((T**5)-(298.15)**5))
          DELS=0.0019872*(4.0543637*ALOG(T/298.15)+(0.018339636)*
     &        (T-298.15)-(0.000025543760/2)*((T**2)-(298.15)**2)+
     &        (0.000000017534109/3)*((T**3)-(298.15)**3)-
     &        (0.0000000000047936684/4)*((T**4)-(298.15)**4))
         ELSE
          DELH=0.0019872*(7.9558725*(T-298.15)+(0.0029812492)*((T**2)-
     &        (298.15)**2)-(0.0000017900249/3)*((T**3)-(298.15)**3)+
     &        (0.0000000049576603/4)*((T**4)-(298.15)**4)-
     &        (0.00000000000052181544/5)*((T**5)-(298.15)**5))
          DELS=0.0019872*(7.9558725*ALOG(T/298.15)+(0.0029812492)*
     &        (T-298.15)-(0.0000017900249/2)*((T**2)-(298.15)**2)+
     &        (0.0000000049576603/3)*((T**3)-(298.15)**3)-
     &        (0.00000000000052181544/4)*((T**4)-(298.15)**4))
          ENDIF
C    CLBN - COMPLETED
      ELSEIF(ICP(I).EQ.34) THEN
        IF(T.LE.1000) THEN
          DELH=0.0019872*(3.4053685*(T-298.15)+(0.010908439/2)*((T**2)-
     &        (298.15)**2)-(0.000014706586/3)*((T**3)-(298.15)**3)+
     &        (0.000000010453817/4)*((T**4)-(298.15)**4)-
     &        (0.0000000000030356048/5)*((T**5)-(298.15)**5))
          DELS=0.0019872*(3.4053685*ALOG(T/298.15)+(0.010908439)*
     &        (T-298.15)-(0.000014706586/2)*((T**2)-(298.15)**2)+
     &        (0.000000010453817/3)*((T**3)-(298.15)**3)-
     &        (0.0000000000030356048/4)*((T**4)-(298.15)**4))
         ELSE
          DELH=0.0019872*(5.4106426*(T-298.15)+(0.0028670155)*((T**2)-
     &        (298.15)**2)-(0.0000016494607/3)*((T**3)-(298.15)**3)+
     &        (0.0000000044274233/4)*((T**4)-(298.15)**4)-
     &        (0.00000000000045505023/5)*((T**5)-(298.15)**5))
          DELS=0.0019872*(5.4106426*ALOG(T/298.15)+(0.0028670155)*
     &        (T-298.15)-(0.0000016494607/2)*((T**2)-(298.15)**2)+
     &        (0.0000000044274233/3)*((T**3)-(298.15)**3)-
     &        (0.00000000000045505023/4)*((T**4)-(298.15)**4))
          ENDIF
      ELSE
         GO TO 150
      ENDIF
  150 STDCP(I)=DH0(I)+DELH-T*(DS0(I)+DELS)
  100 CONTINUE
c
c identify reference species
c
      do 200 i=1,e
      do 300 j=1,vsc+ix
      if(dh0(j).ne.0.0.or.a(j,i).eq.0.0) go to 300
      ireac(i)=j
      go to 200
  300 continue
  200 continue
c
c correct standard state chem. pot. for all non-reference species
c
      do 400 i=1,vsc+ix
      do 500 j=1,e
      k=ireac(j)
      if(k.eq.i) go to 400
      stdcp(i)=stdcp(i)-(a(i,j)/a(k,j))*stdcp(k)
  500 continue
  400 continue
c
c correct standard state chem. pot. For the reference species
c
      do 600 I=1,e
      k=ireac(I)
      stdcp(k)=0.0
  600 continue
C
C  INERT CHEMICAL POTENTIAL
C
      DELH=A0Z*DT+A1Z*DT2/2.-A2Z*DTM1+A3Z*(DTLNT-DT)
      DELS=A0Z*DLNT+A1Z*DT-A2Z*DTM2/2.+A3Z*DLNT2/2.
      IF(ICPZ.EQ.1) DELH=A0Z*DT+A1Z*DT2/2.+A2Z*DT3/3.
     &               +A3Z*DT4/4.
      IF(ICPZ.EQ.1) DELS=A0Z*DLNT+A1Z*DT+A2Z*DT2/2.
     &               +A3Z*DT3/3.
      IF(ICPZ.EQ.2) DELH=A0Z*DT+A1Z*DT2/2.+A2Z*DT3/3.
     &                -A3Z*DTM1
      IF(ICPZ.EQ.2) DELS=A0Z*DLNT+A1Z*DT+A2Z*DT2/2.
     &                -A3Z*DTM2/2.
      IF(ICPZ.EQ.4) DELH=A0Z*DT+A1Z*DT2/2.-A2Z*DTM1
     &                +A3Z*DT3/3.+A4Z*DHPT/0.5
      IF(ICPZ.EQ.4) DELS=A0Z*DLNT+A1Z*DT-A2Z*DTM2/2.
     &                +A3Z*DT2/2.-A4Z*DIHPT/0.5
      STDCPZ=DH0Z+DELH-T*(DS0Z+DELS)
      RETURN
      END
      SUBROUTINE ESTMTE(TOTMV,TOTMS,TOTMC,FRAC,N,FRACZ,ZV,IDIM1,
     &                V,S,C)
C
C  THIS SUBROUTINE CALCULATES AN INITIAL ESTIMATE
C  TO THE SYSTEM EQUILIBRIUM COMPOSITIONS
C
      DIMENSION TOTMC(IDIM1)
      INTEGER V,S,C,VS,VS1,VSC
      REAL*8 N(IDIM1),frac(idim1)
      VS=V+S
      VS1=VS+1
      VSC=V+S+C
      TOTMOL=TOTMV
      DO 50 I=1,VS
      IF(I.GT.V) TOTMOL=TOTMS
      N(I)=TOTMOL*FRAC(I)
   50 CONTINUE
      ZV=FRACZ*TOTMV
      IF(C.EQ.0) RETURN
      DO 60 I=VS1,VSC
      N(I)=TOTMC(I)
   60 CONTINUE
      RETURN
      END
      SUBROUTINE STEADY(SPECIE,A,STDCP,ELMNT,XIII,T,T0,V,S,C,IDIM1,
     &                IDIM2,ISS,IWRT)
C
C  SUBROUTINE TO CALCULATE THE SOLID-LIQUID EQUILIBRIUM COMPOSITIONS
C  FOR USE IN THE STEADY-STATE APPROXIMATION IN THE SOURCE ZONE
C
C   ISS    SYSTEM
C     1    GA(L)-AS(L)/GA-AS (S)
C     2    IN(L)-P(L)/IN-P (S)
C
      DIMENSION A(IDIM1,IDIM2),STDCP(IDIM1)
      INTEGER SPECIE(IDIM1,3),ELMNT(IDIM2),IIIEL(2),VEL(2),V,S,C,VSC,
     &      LAST/'1-X)'/,GA/'GA'/,AS/'AS'/,IN/'IN'/,P/' P'/
      DATA IIIEL(1)/' GAX'/,IIIEL(2)/' INX'/,
     &    VEL(1)/'-AS('/,VEL(2)/'- P('/
      THETA2(XV)=(TMIIIV*DSIIIV-AXS*(0.5-XV**2-(1.-XV)**2))/
     &      (DSIIIV-R*ALOG(4.*XV*(1.-XV))+BXS*(0.5-XV**2-(1.-XV)**2))
      VSC=V+S+C
      SPECIE(VSC,1)=IIIEL(ISS)
      SPECIE(VSC,2)=VEL(ISS)
      SPECIE(VSC,3)=LAST
      DT=T-T0
      DT2=T**2-T0**2
      DTM1=1.0/T-1.0/T0
      DTM2=1.0/T**2-1.0/T0**2
      DLNT=ALOG(T/T0)
      IF(ISS.EQ.2) GO TO 50
C
```

```
C  GA-AS SYSTEM
C
      TMIII=302.9
      TMV=1090.
      TMIIIV=1511.
      DSIII=0.004411
      DSV=0.0047
      DSIIIV=0.01664
      DCIII=-0.00005
      DCV=0.001
      AXS=4.666
      BXS=-0.008741
      GO TO 60
C
C  IN-P SYSTEM
C
   50 TMIII=429.8
      TMV=313.3
      TMIIIV=1332.2
      DSIII=0.001815
      DSV=0.0005011
      DSIIIV=0.01081
      DCIII=-0.0002
      DCV=0.000472
      AXS=32.75
      BXS=-0.02895
   60 CONTINUE
C
C  BINARY ROOT FINDING ROUTINE FOR THE GROUP III AND V COMPOSITIONS
C
      XV=0.5
      XMIN=0.0
      XMAX=1.0
      R=0.0019872
      THETA1=T
      XOLD=0.4
      THTOLD=THETA2(XOLD)
      DO 100 I=1,50
      THET2=THETA2(XV)
      ERR=(THET2-THETA1)/THETA1
      IF(ABS(ERR).LT.0.0001) GO TO 200
      SWTCH=(THET2-THTOLD)/(XV-XOLD)
      THTOLD=THET2
      XOLD=XV
      IF(SWTCH.GT.0.AND.THET2.LT.THETA1) GO TO 80
      IF(SWTCH.LT.0.AND.THET2.GT.THETA1) GO TO 80
      XMAX=XV
      XV=0.5*(XMIN+XV)
      GO TO 100
   80 XMIN=XV
      XV=0.5*(XMAX+XV)
```

```
  100 CONTINUE
      WRITE(IWRT,120)
  120 FORMAT('0','***** SUBROUTINE STEADY: ITERATION FOR SOURCE ',
     &       'COMPOSITION DID NOT CONVERGE')
  200 CONTINUE
C
C  CALCULATE THE STANDARD CHEMICAL POTENTIAL OF THE SOURCE
SOLUTION
C
      DGA=(1.0-XV)*(DSIII*(TMIII-T)+DCIII*(T-TMIII-T*ALOG(T/TMIII)))
      DGB=XV*(DSV*(TMV-T)+DCV*(T-TMV-T*ALOG(T/TMV)))
      DGC=(AXS+BXS*T)*XV*(1.-XV)+R*T*(XV*ALOG(XV)+(1.-XV)*ALOG(1.-XV))
      STDCP(VSC)=DGA+DGB+DGC
C
C  LOCATE THE GROUP III AND V ELEMENTS IN THE ELEMENTAL ABUNDANCE
ARRAY
C  AND INSERT THE CALCUALATED ABUNDANCES INTO THIS ARRAY
C
      IDX3=0
      IDX5=0
      DO 300 I=1,IDIM2
      IF(ISS.EQ.2) GO TO 250
      IF(ELMNT(I).EQ.GA) IDX3=I
      IF(ELMNT(I).EQ.AS) IDX5=I
      GO TO 300
  250 IF(ELMNT(I).EQ.IN) IDX3=I
      IF(ELMNT(I).EQ.P) IDX5=I
  300 CONTINUE
      A(VSC,IDX3)=1.0-XV
      A(VSC,IDX5)=XV
      XIII=1.0-XV
      RETURN
      END
      SUBROUTINE TOTSI(A,ELMNT,FRAC,N,SITOT,SIMF,ACTSIS,T,P,IDIM1,IDIM2,
     &              V,E)
C
C  SUBROUTINE TO CALCULATE THE TOTAL SI IN THE VAPOR PHASE
C  AND THE ACTIVITY OF SI IN A SOLID SOLUTION
C
      DIMENSION A(IDIM1,IDIM2)
      INTEGER ELMNT(IDIM2),V,E,SIVPR/'SI'/
      REAL*8 N(IDIM1),frac(idim1)
      T0=298.15
      P0=101325.0
      RT=0.0019872*T
C
C  DETERMINE THE TOTAL AMOUNT OF SILICON IN THE VAPOR
C
      SITOT=0.0
      SIMF=0.0
      ACTSIS=0.
      DO 100 J=1,E
      KSI=J
      IF(ELMNT(J).EQ.SIVPR) GO TO 130
  100 CONTINUE
      GO TO 300
  130 CONTINUE
      DO 140 I=1,V
      IF(A(I,KSI).LT.0.001) GO TO 140
      SITOT=SITOT+N(I)
      SIMF=SIMF+FRAC(I)
  140 CONTINUE
C
C  FIND SI(V) AND CALCULATE THE ACTIVITY OF SOLID SI IN SOLUTION
C
      DO 200 I=1,V
      ICNT=0
      IF(A(I,KSI).LT.0.001) GO TO 200
      DO 150 J=1,E
      IF(A(I,J).LT.0.001) GO TO 150
      ICNT=ICNT+1
  150 CONTINUE
      IF(ICNT.GT.1) GO TO 200
      DG=108.-0.00091*(T-T0)-5.011E-7/2.*(T**2-T0**2)-147.6*(1/T-1/T0)
     &  -T*(0.035637-0.00091*ALOG(T/T0)-5.011E-7*(T-T0)
     &      -147.6/2.*(1/T**2-1/T0**2))
      ACTSIS=FRAC(I)*P/P0*EXP(DG/RT)
      IF(N(I).LT.1.00E-38) ACTSIS=0.
      GO TO 300
  200 CONTINUE
  300 CONTINUE
      RETURN
      END
      SUBROUTINE RATIO(A,ELMNT,FRAC,N,STDCP,ACTGAS,ACTINS,ACTASS,
     &          ACTPS,RIIIV,RGAAS,RINP,T,P,T0,P0,IDIM1,IDIM2,V,E)
C
C  THIS SUBROUTINE CALCULATES THE VAPOR III/V RATIO,
C  THE GA, IN, AS AND P SOLID SOLUTION ACTIVITIES,
C  AND THE SATURATION RATIOS OF GA-AS AND IN-P.
C
      DIMENSION A(IDIM1,IDIM2),STDCP(IDIM1),KIII(5),KV(5)
      REAL*8 N(IDIM1),frac(idim1)
      INTEGER ELMNT(IDIM2),ELIII(5),ELV(5),V,E
      DATA ELIII(1)/' B'/,ELIII(2)/'AL'/,ELIII(3)/'GA'/,ELIII(4)/'IN'/,
     &   ELIII(5)/'TL'/,ELV(1)/' N'/,ELV(2)/' P'/,ELV(3)/'AS'/,
     &   ELV(4)/'SB'/,ELV(5)/'BI'/
      FNCDG(T)=DH+A1*(T-T0)+A2/2.*(T**2-T0**2)-A3*(1/T-1/T0)
     &  +A4*(T*ALOG(T)-T-T0*ALOG(T0)+T0)+A5/3.*(T**3-T0**3)
     &  -T*(DS+A1*ALOG(T/T0)+A2*(T-T0)-A3/2.*(1/T**2-1/T0**2)
     &     +A4/2.*(ALOG(T)**2-ALOG(T0)**2)+A5/2.*(T**2-T0**2))
      RT=0.0019872*T
C
```

```
C  DETERMINE WHICH INDECIES CORRESPOND TO COLUMN III AND V ELEMENTS
C
      DO 100 K=1,5
      KIII(K)=0
      KV(K)=0
      DO 100 J=1,E
      IF(ELMNT(J).EQ.ELIII(K)) KIII(K)=J
      IF(ELMNT(J).EQ.ELV(K)) KV(K)=J
  100 CONTINUE
C
C  SUM-UP THE GROUP III AND V SPECIES AND CALCULATE THE RATIO
C
      SUMIII=0.0
      SUMV=0.0
      DO 200 I=1,V
      DO 200 K=1,5
      IDXIII=KIII(K)
      IDXV=KV(K)
      IF(IDXIII.EQ.0) GO TO 120
      SUMIII=SUMIII+A(I,IDXIII)*FRAC(I)
  120 CONTINUE
      IF(IDXV.EQ.0) GO TO 200
      SUMV=SUMV+A(I,IDXV)*FRAC(I)
  200 CONTINUE
      RIIIV=1.0E10
      IF(SUMV.GT.0.0) RIIIV=SUMIII/SUMV
C
C  FIND THE SPECIES:  GA(V), IN(V), P(V) AND AS(V)
C  AND CALCULATE THE ACTIVITIES FOR GA, IN, AS AND P IN A SOLID SOLUTION
C
      ACTGAS=0.
      ACTINS=0.
      ACTASS=0.
      ACTPS=0.
      KGA=0
      KAS=0
      KIN=0
      KP=0
C
C  GA DATA
C
      KSPC=KIII(3)
      A1=0.023738
      A2=2.09E-6
      A3=-266.2
      A4=-0.003812
      A5=0.
      DH=65.0
      DS=0.030617
      DO 400 IJK=1,4
      GO TO(245,220,230,240),IJK
```

```
C
C  INDIUM DATA
C
 220 KSPC=KIII(4)
     A1=-0.001015
     A2=-1.614E-6
     A3=0.
     A4=0.
     A5=-1.689E-9
     DH=57.3
     DS=0.027687
     GO TO 245
C
C  PHOSPHOROUS (P) DATA
C
 230 KSPC=KV(2)
     A1=-0.000732
     A2=0.
     A3=0.
     A4=0.
     A5=0.
     DH=75.62
     DS=0.02916
     GO TO 245
C
C  ARSENIC (AS) DATA
C
 240 KSPC=KV(3)
     A1=-0.001768
     A2=-1.5E-6
     A3=15.04
     A4=0.0001967
     A5=0.
     DH=68.7
     DS=0.033081
 245 IF(KSPC.EQ.0) GO TO 400
     DO 300 I=1,V
     ICNT=0
     IF(A(I,KSPC).LT.0.001) GO TO 300
     DO 250 J=1,E
     IF(A(I,J).LT.0.001) GO TO 250
     ICNT=ICNT+1
 250 CONTINUE
     IF(ICNT.GT.1) GO TO 300
     IF(A(I,KSPC).GT.1.001) GO TO 300
     DG=FNCDG(T)
     ACTIV=FRAC(I)*P/P0*EXP(DG/RT)
     IF(IJK.EQ.1) ACTGAS=ACTIV
     IF(IJK.EQ.1) KGA=I
     IF(IJK.EQ.2) ACTINS=ACTIV
     IF(IJK.EQ.2) KIN=I
```

```
      IF(IJK.EQ.3) ACTPS=ACTIV
      IF(IJK.EQ.3) KP=I
      IF(IJK.EQ.4) ACTASS=ACTIV
      IF(IJK.EQ.4) KAS=I
      GO TO 400
  300 CONTINUE
  400 CONTINUE
C
C  CALCULATE THE SATURATION RATIOS FOR GA-AS AND IN-P.
C
      RGAAS=0.
      RINP=0.
C
C  GA-AS SYSTEM SATURATION RATIO
C
      A1=0.01046
      A2=2.8E-6
      A3=0.
      A4=0.
      A5=0.
      DH=-19.52
      DS=-0.002948
      K3=KGA
      K5=KAS
      DO 500 I=1,2
      IF(K3.EQ.0.OR.K5.EQ.0) GO TO 470
      IF(N(K3).LT.1.00E-38.OR.N(K5).LT.1.00E-38) GO TO 470
      DG=STDCP(K3)+STDCP(K5)-FNCDG(T)/RT
      RSAT=FRAC(K3)*FRAC(K5)*P**2*EXP(DG)/P0**2
      IF(I.EQ.1) RGAAS=RSAT
      IF(I.EQ.2) RINP=RSAT
C
C  IN-P SYSTEM SATURATION RATIO
C
  470 A1=0.01227
      A2=0.
      A3=-114.0
      DH=-14.0
      DS=-0.00936
      K3=KIN
      K5=KP
  500 CONTINUE
      RETURN
      END
      SUBROUTINE OPTBAS(N,BESTN,A,D,DPRME,STDCP,SPECIE,PHASE,A0,A1,A2,
     &A3,A4,BQUES,DH0,DS0,ICP,IDXBAS,ITER,IDIM1,IDIM2,V,S,C,E,ISTOP,
     &ICHNG,IWRT,FRAC)
C
C  THIS SUBROUTINE DETERMINES THE OPTIMUM SET OF BASIS SPECIES
C
      DIMENSION A(IDIM1,IDIM2),D(IDIM2,IDIM2),IDXBAS(IDIM2),
  &        STDCP(IDIM1),A0(IDIM1),A1(IDIM1),A2(IDIM1),A3(IDIM1),
  &        A4(IDIM1),DH0(IDIM1),DS0(IDIM1),ICP(IDIM1)
   REAL*8 N(IDIM1),BESTN(IDIM1),DPRME(IDIM2,IDIM2),TEMP,frac(idim1)
   INTEGER SPECIE(IDIM1,3),PHASE(IDIM1,3),BQUES(IDIM1),V,S,C,E,VSC,
  &       VSCM1
   ISTOP=0
   ICHNG=0
   VSC=V+S+C
   VSCM1=VSC-1
C
C  BUBBLE SORT THE N VECTOR INTO DESCENDING ORDER
C  AND ORDER STDCP, A, DH0, DS0, A0, A1, A2, A3, SPECIE, PHASE
C  AND ICP CORRESPONDINGLY
C
   DO 300 I=1,VSCM1
   IP1=I+1
   DO 200 II=IP1,VSC
   IF(N(II).LE.N(I)) GO TO 200
   ICHNG=1
   TEMP=N(I)
   N(I)=N(II)
   N(II)=TEMP
   TEMP=BESTN(I)
   BESTN(I)=BESTN(II)
   BESTN(II)=TEMP
   TEMP=FRAC(I)
   FRAC(I)=FRAC(II)
   FRAC(II)=TEMP
   TEMP=STDCP(I)
   STDCP(I)=STDCP(II)
   STDCP(II)=TEMP
   TEMP=A0(I)
   A0(I)=A0(II)
   A0(II)=TEMP
   TEMP=A1(I)
   A1(I)=A1(II)
   A1(II)=TEMP
   TEMP=A2(I)
   A2(I)=A2(II)
   A2(II)=TEMP
   TEMP=A3(I)
   A3(I)=A3(II)
   A3(II)=TEMP
   TEMP=A4(I)
   A4(I)=A4(II)
   A4(II)=TEMP
   TEMP=DH0(I)
   DH0(I)=DH0(II)
   DH0(II)=TEMP
   TEMP=DS0(I)
   DS0(I)=DS0(II)
```

```
      DS0(II)=TEMP
      ITEMP=BQUES(I)
      BQUES(I)=BQUES(II)
      BQUES(II)=ITEMP
      ITEMP=ICP(I)
      ICP(I)=ICP(II)
      ICP(II)=ITEMP
      DO 50 J=1,3
      ITEMP=SPECIE(I,J)
      SPECIE(I,J)=SPECIE(II,J)
      SPECIE(II,J)=ITEMP
      ITEMP=PHASE(I,J)
      PHASE(I,J)=PHASE(II,J)
      PHASE(II,J)=ITEMP
   50 CONTINUE
      DO 100 J=1,E
      TEMP=A(I,J)
      A(I,J)=A(II,J)
      A(II,J)=TEMP
  100 CONTINUE
  200 CONTINUE
  300 CONTINUE
C
C  IF THE PREVIOUSLY USED BASIS IS STILL THE OPTIMUM BASIS
C  SKIP THE REST OF THIS SUBROUTINE AND CONTINUE WITH THE
CALCULATIONS
C
      IF(ITER.GT.1.AND.ICHNG.EQ.0) GO TO 480
C
C  BUILD THE D MATRIX WHICH WILL CONTAIN THE OPTIMUM BASIS
C
      DO 320 J=1,E
      DPRME(1,J)=A(1,J)
  320 CONTINUE
      MA=0
      DO 400 MD=1,E
  340 MA=MA+1
      IF(MA.GT.VSC) GO TO 450
      DO 350 J=1,E
      D(MD,J)=A(MA,J)
  350 CONTINUE
      IDXBAS(MD)=MA
      IF(MD.EQ.1) GO TO 400
      CALL TESTD(D,DPRME,MD,E,IDIM2,ITST)
      IF(ITST.EQ.0) GO TO 340
  400 CONTINUE
      GO TO 480
  450 WRITE(IWRT,460) ITER
  460 FORMAT('0','***** ITERATION ',I5,' AN OPTIMUM SET OF BASIS ',
     &'SPECIES COULD NOT BE FOUND FOR THIS SYSTEM IN SUBROUTINE OPTBAS')
      ISTOP=1
  480 RETURN
      END
      SUBROUTINE TESTD(D,DPRME,MD,E,IDIM2,ITST)
C
C  THIS SUBROUTINE TESTS THE D MATRIX FOR LINEAR DEPENDENCE
C  USING A GRAM-SCHMIDT ORTHOGONALIZATION ALGORITHUM
C
      DIMENSION D(IDIM2,IDIM2)
      REAL*8 DPRME(IDIM2,IDIM2),ANUM,DENOM
      INTEGER E
      ITST=0
      DO 100 J=1,E
      DPRME(MD,J)=D(MD,J)
  100 CONTINUE
      MDM1=MD-1
      DO 400 L=1,MDM1
      ANUM=0.0
      DENOM=0.0
      DO 200 K=1,E
      ANUM=ANUM+D(MD,K)*DPRME(L,K)
      DENOM=DENOM+DPRME(L,K)**2
  200 CONTINUE
      DO 300 J=1,E
      DPRME(MD,J)=DPRME(MD,J)-DPRME(L,J)*ANUM/DENOM
  300 CONTINUE
  400 CONTINUE
C
C  TEST FOR "ZEROS" ON THE NEW ROW
C
      DO 500 J=1,E
      IF(DABS(DPRME(MD,J)).GT.1.0D-5) ITST=ITST+1
  500 CONTINUE
      RETURN
      END
      SUBROUTINE EQCON(A,D,DD,DINV,DG,GNU,STDCP,KEQ,IDXBAS,WKA,
     &            IDIM1,IDIM2,V,S,C,E,ISTOP)
C
C  THIS SUBROUTINE CALCULATES THE REACTION COEFFICIENT MATRIX
C  AND THE EQUILIBRIUM CONSTANTS FOR THE FORMATION REACTIONS
C
      DIMENSION A(IDIM1,IDIM2),D(IDIM2,IDIM2),DD(IDIM2,IDIM2),
     &      DINV(IDIM2,IDIM2),DG(IDIM1),GNU(IDIM1,IDIM2),
     &      IDXBAS(IDIM2),STDCP(IDIM1),WKA(IDIM2)
      DOUBLE PRECISION DD,DINV,WKA
      INTEGER V,S,C,E,VSC
      REAL*8 keq(idim1)
      VSC=V+S+C
      ISTOP=0
C
C  STORE ARRAY D IN ARRAY DD AND USE ARRAY DD IN THE CALL TO LINV1F
C
```

```
      DO 100 I=1,E
      DO 100 J=1,E
      DD(I,J)=D(I,J)
  100 CONTINUE
C
C  INVERT MATRIX DD USING IMSL SUBROUTINE LINV1F
C
      IDGT=4
      CALL LINV1F(DD,E,IDIM2,DINV,IDGT,WKA,IER)
      IF(IER.EQ.129) ISTOP=1
      IF(ISTOP.EQ.1) GO TO 600
C
C  CALCULATE THE REACTION COEFFICIENT MATRIX
C
      DO 300 I=1,VSC
      DO 300 J=1,E
      TEMP=0.0
      DO 200 JJ=1,E
      TEMP=TEMP+A(I,JJ)*DINV(JJ,J)
  200 CONTINUE
      GNU(I,J)=TEMP
  300 CONTINUE
C
C  CALCULATE THE EQUILIBRIUM CONSTANTS FOR THE FORMATION REACTIONS
C
      DO 500 I=1,VSC
      do 501 j=1,e
      if(I.eq.idxbas(j)) go to 500
  501 continue
      ARG=(-1.0)*STDCP(I)
      DO 400 K=1,E
      IDXB=IDXBAS(K)
      ARG=ARG+GNU(I,K)*STDCP(IDXB)
  400 CONTINUE
      DG(I)=ARG
      IF(arg.GT.500.0) arg=500.0
      KEQ(I)=DEXP(ARG)
  500 CONTINUE
  600 RETURN
      END
      SUBROUTINE ACTCOF(FRAC,ACOEF,ISPCE,SPECIE,INDEX,IDIM1,RELMAX,
     &                 IXSCOR,AXS,BXS,T,IACFF,V,S,C,IWRT)
C
C  SUBROUTINE TO CALCULATE ACTIVITY COEFFICIENTS FOR THE SOLUTION
PHASE
C
C  IXSCOR  ALGORITHUM
C      1  BINARY SIMPLE SOLUTION THEORY  GE=(AXS+BXS*T)*X1*X2
C      2  HENRY'S CONSTANT FOR THE FIRST SOLUTION SPECIE  H=AXS*EXP(BXS/T)
C      3  QUASI-CHEMICAL EQUILIBRIUM MODEL (STRINGFELLOW)
C      4  MODEL FOR LIQUID SOLUTION OF GA-IN
```

```
C      5  MODEL S.R.O.P. PLUS D.L.P.
C      6  TITANIUM CARBIDE MODEL
C
      DIMENSION ACOEF(IDIM1),INDEX(IDIM1)
      INTEGER ISPCE(IDIM1,3),SPECIE(IDIM1,3),V,S,C,VSC
      real*8 frac(idim1),x1,x2
      VSC=V+S+C
      DO 100 I=1,VSC
      ACOEF(I)=1.0
  100 CONTINUE
C   CHECK TO SEE IF WE NEED TO USE A SOLUTION MODEL YET
      IF(ABS(RELMAX).LT.0.1) IACFF=1
      IF(IXSCOR.EQ.2) IACFF=1
      IF(IXSCOR.EQ.3) IACFF=1
      IF(IXSCOR.EQ.4) IACFF=1
      IF(IXSCOR.EQ.5) IACFF=1
      IF(IXSCOR.EQ.6) IACFF=1
      IF(IXSCOR.LT.1.OR.IXSCOR.GT.6.OR.S.LE.1) IACFF=0
      IF(IACFF.EQ.0) GO TO 900
      RT=0.0019872*T
C
C  IDENTIFY THE SOLUTION SPECIES
C
      DO 150 J=1,S
      K=V+J
      DO 150 I=1,VSC
      IF(SPECIE(I,1).EQ.ISPCE(K,1).AND.
     &   SPECIE(I,2).EQ.ISPCE(K,2).AND.
     &   SPECIE(I,3).EQ.ISPCE(K,3)) INDEX(J)=I
  150 CONTINUE
      ITEST=1
      DO 155 J=1,S
      IF(INDEX(J).LT.1.OR.INDEX(J).GT.VSC) ITEST=0
  155 CONTINUE
      IF(ITEST.EQ.0) WRITE(IWRT,160)
  160 FORMAT('0','*****  THE SOLUTION SPECIES COULD NOT BE IDENTIFIED',
     &       ' IN SUBROUTINE ACTCOF')
      IF(IXSCOR.EQ.2) GO TO 200
      IF(IXSCOR.EQ.3) GO TO 300
      IF(IXSCOR.EQ.4) GO TO 400
      IF(IXSCOR.EQ.5) GO TO 500
      IF(IXSCOR.EQ.6) GO TO 600
C
C  BINARY SIMPLE SOLUTION THEORY
C
      IDX1=INDEX(1)
      IDX2=INDEX(2)
      X1=FRAC(IDX1)
      X2=1.0-X1
      ARG1=(AXS+BXS*T)*X2**2/RT
      ARG2=(AXS+BXS*T)*X1**2/RT
      ACOEF(IDX1)=EXP(ARG1)
      ACOEF(IDX2)=EXP(ARG2)
      GO TO 900
C
C  HENRY'S CONSTANT FOR THE FIRST SOLUTION SPECIE
C
 200 IDX1=INDEX(1)
      ACOEF(IDX1)=AXS*EXP(BXS/T)
      GO TO 900
C
C  STRINGFELLOW'S QUASI-CHEMICAL EQUILIBRIUM MODEL
C
 300  IDX1=INDEX(1)
      IDX2=INDEX(2)
C  OMEGA IS ONE OF HIS PARAMETERS, DEPENDS ON BINARY PAIR
      OMEGA=AXS
C  Z IS THE NUMBER OF NEAREST NEIGHBORS
      Z=BXS
      X1=FRAC(IDX1)
      X2=1.0-X1
      ETA=EXP(OMEGA/(Z*RT))
      BETA=(1.0+4.0*X1*X2*(ETA**2.0-1.0))**0.5
      ACOEF(IDX1)=((BETA-1.0+2.0*X1)/(X1*(BETA+1.0)))**(Z/2.0)
      ACOEF(IDX2)=((BETA+1.0-2.0*X1)/(X2*(BETA+1.0)))**(Z/2.0)
      GO TO 900
C
C  MODEL FOR LIQUID SOLUTION OF GA-IN
C
 400 IDX1=INDEX(1)
      IDX2=INDEX(2)
      X1=FRAC(IDX1)
      X2=1.0-X1
      AKOEF1=(X2**2./(RT*4.184E3))*(4450.+T*(1.19185+.25943*(3.-4.*X2)))
      AKOEF2=(X1**2./(RT*4.184E3))*(4450.+T*(1.19185+.25943*(3.-4.*X1)))
      ACOEF(IDX1)=EXP(AKOEF1)
      ACOEF(IDX2)=EXP(AKOEF2)
      GO TO 900
C
C  MODEL S.R.O.P. PLUS D.L.P.
C
 500 IDX1=INDEX(1)
      IDX2=INDEX(2)
C  AXS IS THE D.L.P. COEFF
C  Z IS THE NUMBER OF NEAREST NEIGHBORS
      Z=BXS
      X1=FRAC(IDX1)
      X2=1.0-X1
      AF1=(AXS*X2**2/RT)*(1.0+(2.*(2.*X1-1.)*ALOG(X2)-X1*4.*ALOG(X1))/Z)
      AF2=(AXS*X1**2/RT)*(1.0+(2.*(1.-2.*X1)*ALOG(X1)-X2*4.*ALOG(X2))/Z)
      ACOEF(IDX1)=EXP(AF1)
      ACOEF(IDX2)=EXP(AF2)
      GO TO 900
C
C TITANIUM CARBIDE MODEL
C
  600 IDX1=INDEX(1)
      IDX2=INDEX(2)
      X1=FRAC(IDX1)
      X2=1.0-X1
      IF(X1.LE.3.548387E-01)THEN
      IF(X1.NE.0.0)ACOEF(IDX1)=(3.032E-9)/X1
      IF(X1.EQ.0.0)ACOEF(IDX1)=0.0
      ACOEF(IDX2)=1.55187760
      ELSEIF(X1.GE.4.949495E-01)THEN
      ACOEF(IDX1)=2.02018569
      IF(X2.NE.0.0)ACOEF(IDX2)=(1.615E-7)/X2
      IF(X2.EQ.0.0)ACOEF(IDX2)=0.0
      ELSE
      ATRG1=73.648-168.785*X1-1812.998*X1**2+5585.855*X1**3-2556.939*X1
     &**4-2326.442*X1**5
      ATRG2=-239.332+5364.876*X2-24977.047*X2**2+27068.331*X2**3+
     &56130.868*X2**4-139229.645*X2**5+79647.620*X2**6
      ACOEF(IDX1)=EXP(ATRG1)
      ACOEF(IDX2)=EXP(ATRG2)
      ENDIF
  900 RETURN
      END
      SUBROUTINE CALCQ(GNU,N,ACOEF,FRAC,PHASE,VAPOR,SOLN,IDXBAS,Q,
     &              ZV,FRACZ,P,P0,V,S,C,E,IDIM1,IDIM2)
C
C  SUBROUTINE TO CALCULATE EQUILIBRIUM CONSTANTS FROM COMPOSITION
C
      DIMENSION GNU(IDIM1,IDIM2),ACOEF(IDIM1),IDXBAS(IDIM2)
      INTEGER V,S,C,E,VSC,PHASE(IDIM1,3),VAPOR(3),SOLN(3)
      REAL*8 N(IDIM1),NV,NS,q(idim1),frac(idim1)
      VSC=V+S+C
C
C  CALCULATE THE TOTAL NUMBER OF MOLES IN EACH PHASE
C
      NS=0.0
      NV=ZV
      DO 100 I=1,VSC
      IF(PHASE(I,1).EQ.VAPOR(1)) NV=NV+N(I)
      IF(PHASE(I,1).EQ.SOLN(1)) NS=NS+N(I)
  100 CONTINUE
C
C  CALCULATE THE MOLE FRACTIONS
C
      DO 200 I=1,VSC
      FRAC(I)=1.0
      IF(PHASE(I,1).EQ.VAPOR(1)) FRAC(I)=N(I)/NV
      IF(PHASE(I,1).EQ.SOLN(1)) FRAC(I)=N(I)/NS
```

```
 200 CONTINUE
     FRACZ=ZV/NV
C
C  CALCULATE THE EQUILIBRIUM CONSTANTS
C
     DO 400 I=1,VSC
     do 401 j=1,e
     if(I.eq.idxbas(j)) go to 400
 401 continue
     PP0=1.0
     IF(PHASE(I,1).EQ.VAPOR(1)) PP0=P/P0
     Q(I)=ACOEF(I)*FRAC(I)*PP0
     DO 300 J=1,E
     K=IDXBAS(J)
     PP0=1.0
     IF(PHASE(K,1).EQ.VAPOR(1)) PP0=P/P0
     Q(I)=Q(I)/(ACOEF(K)*FRAC(K)*PP0)**GNU(I,J)
 300 CONTINUE
 400 CONTINUE
     RETURN
     END
     SUBROUTINE ADJEXT(N,Q,GNU,DZETA,IDXBAS,COND,PHASE,IDIM1,IDIM2,
    &                 V,S,C,E,dg)
C
C  SUBROUTINE TO ADJUST THE EXTENTS OF REACTION
C
     DIMENSION IDXBAS(IDIM2),GNU(IDIM1,IDIM2),dg(idim1)
     INTEGER COND(3),PHASE(IDIM1,3),V,S,C,E,VSC
     REAL*8 N(IDIM1),dzeta(idim1),DENOM,TOTDN,q(idim1),test,akapa
     VSC=V+S+C
C
C  CALCULATE THE CHANGE IN REACTION EXTENT FOR EACH REACTION
C
     DO 200 I=1,VSC
     DELI=1.0
     IF(PHASE(I,1).EQ.COND(1)) DELI=0.0
     DENOM=DELI/N(I)
     DZETA(I)=0.0
     DO 100 J=1,E
     K=IDXBAS(J)
     IF(I.EQ.K) GO TO 200
     DELK=1.0
     IF(PHASE(K,1).EQ.COND(1)) DELK=0.0
     DENOM=DENOM+DELK*GNU(I,J)**2/N(K)
 100 CONTINUE
     IF(DENOM.EQ.0.0) DENOM=1.0
     DZETA(I)=(dg(I)-ALOG(Q(I)))/DABS(DENOM)
     IF(DZETA(I).LT.0.0.AND.DABS(DZETA(I)).GT.N(I))
    &                     DZETA(I)=(-1.0)*N(I)
     IF(N(I).LE.1.0D-75.and.dzeta(i).lt.0.0) DZETA(I)=0.0
 200 CONTINUE
```

```
C
C  LIMIT THE MAXIMUM ALLOWABLE DZETA VALUES
C  BASED ON NON-NEAGATIVITY OF THE BASIS SPECIES
C
     AKAPA=1.0
     DO 400 J=1,E
     K=IDXBAS(J)
     TOTDN=0.0
     DO 300 I=1,VSC
     TOTDN=TOTDN-GNU(I,J)*DZETA(I)
  300 CONTINUE
     TEST=N(K)+TOTDN*AKAPA
     IF(TEST.LT.0.0.AND.N(K).GT.1.0D-75) AKAPA=(-1.0)*N(K)/TOTDN
  400 CONTINUE
     DO 500 I=1,VSC
     DO 450 J=1,E
     IF(I.EQ.IDXBAS(J)) GO TO 500
  450 CONTINUE
     if(n(i).gt.1.0D-75) DZETA(I)=DZETA(I)*AKAPA
     if(n(i).le.1.0D-75.and.phase(i,1).ne.cond(1)) dzeta(i)=
    &                   n(i)*((exp(dg(i))/q(i))-1.0)
  500 CONTINUE
     RETURN
     END
     SUBROUTINE CNVFRC(N,NTEMP,STDCP,ACOEF,DZETA,GNU,IDXBAS,VAPOR,
    &            SOLN,PHASE,ZV,RT,P,P0,RLXMIN,LAMBDA,IDIM1,
    &            IDIM2,V,S,C,E)
C
C  SUBROUTINE TO CALCULATE THE CONVERGENCE FORCER LAMBDA
C
     DIMENSION IDXBAS(IDIM2),GNU(IDIM1,IDIM2),
    &        STDCP(IDIM1),ACOEF(IDIM1)
     INTEGER VAPOR(3),SOLN(3),PHASE(IDIM1,3),V,S,C,E,VSC
     REAL*8 N(IDIM1),NTEMP(IDIM1),dzeta(idim1),dgdl0,dgdl1,lambda,
    &     rlxmin,dgdlam
     VSC=V+S+C
C
C  CALCULATE DG/DLAMBDA AT LAMBDA=1.0
C
     LAMBDA=1.0
     DO 100 I=1,VSC
     NTEMP(I)=N(I)
  100 CONTINUE
     CALL CORMOL(NTEMP,DZETA,GNU,IDXBAS,IDIM1,IDIM2,LAMBDA,VSC,E)
     DGDL1=DGDLAM(N,NTEMP,STDCP,ACOEF,PHASE,VAPOR,SOLN,ZV,RT,P,P0,
    &          IDIM1,VSC)
      IF(DGDL1.LT.0.0) GO TO 500
C
C  CALCULATE DG/DLAMBDA AT LAMBDA=0.0
C
     DGDL0=(-1.0)*DGDLAM(NTEMP,N,STDCP,ACOEF,PHASE,VAPOR,SOLN,ZV,
     &                RT,P,P0,IDIM1,VSC)
      IF(DGDL0.EQ.DGDL1) DGDL1=-DGDL1
      LAMBDA=DGDL0/(DGDL0-DGDL1)
      IF(LAMBDA.LE.0.0.OR.LAMBDA.GE.1.0) LAMBDA=RLXMIN
  500 CONTINUE
      RETURN
      END
      FUNCTION DGDLAM(N1,N2,STDCP,ACOEF,PHASE,VAPOR,SOLN,ZV,RT,P,P0,
     &              IDIM1,VSC)
C
C  SUBPROGRAM TO CALCULATE DG/DLAMBDA
C
      DIMENSION ACOEF(IDIM1),STDCP(IDIM1)
      INTEGER PHASE(IDIM1,3),VAPOR(3),SOLN(3),VSC
      REAL*8 N1(IDIM1),N2(IDIM1),NV,NS,arg,dgdl,dgdlam
C
C  CALCULATE THE TOTAL NUMBER OF MOLES IN THE SOLUTION AND VAPOR
PHASES
C
      NS=0.0
      NV=ZV
      DO 100 I=1,VSC
      IF(PHASE(I,1).EQ.VAPOR(1)) NV=NV+N2(I)
      IF(PHASE(I,1).EQ.SOLN(1)) NS=NS+N2(I)
  100 CONTINUE
C
C  CALCULATE DG/DLAMBDA
C
      DGDL=0.0
      DO 200 I=1,VSC
      ARG=1.0
      IF(PHASE(I,1).EQ.VAPOR(1)) ARG=ACOEF(I)*N2(I)*P/P0/NV
      IF(PHASE(I,1).EQ.SOLN(1)) ARG=ACOEF(I)*N2(I)/NS
      DGDL=DGDL+(N2(I)-N1(I))*(STDCP(I)+dlog(arg))
  200 CONTINUE
      DGDLAM=DGDL*RT
      RETURN
      END
      SUBROUTINE CORMOL(N,DZETA,GNU,IDXBAS,IDIM1,IDIM2,LAMBDA,VSC,E)
C
C  SUBROUTINE TO CORRECT THE MOLAR AMOUNTS OF EACH SPECIE
C
      DIMENSION GNU(IDIM1,IDIM2),IDXBAS(IDIM2)
      REAL*8 N(IDIM1),dzeta(idim1),lambda
      INTEGER VSC,E
C
C  CORRECT EACH NONBASIS SPECIE
C
      DO 200 I=1,VSC
      DO 100 J=1,E
      IF(I.EQ.IDXBAS(J)) GO TO 200
```

```
 100 CONTINUE
     if(n(i).gt.1.0D-50) N(I)=N(I)+DZETA(I)*LAMBDA
     if(n(i).le.1.0D-50) n(i)=n(i)+dzeta(i)
     IF(N(I).LT.1.0D-75) N(I)=1.0D-75
 200 CONTINUE
C
C  CORRECT EACH BASIS SPECIE
C
     DO 400 J=1,E
     K=IDXBAS(J)
     DO 300 I=1,VSC
     N(K)=N(K)-GNU(I,J)*DZETA(I)*LAMBDA
 300 CONTINUE
     IF(N(K).LT.1.0D-75) N(K)=1.0D-75
 400 CONTINUE
     RETURN
     END
     SUBROUTINE ORDER(ISPCE,SPECIE,PHASE,N,A,STDCP,A0,A1,A2,A3,A4,DH0,
    &DS0,DZETA,CHMPT,ACOEF,FRAC,QUES,DG,Q,KEQ,ICP,IDIM1,IDIM2,E,VSC)
C
C  SUBROUTINE TO ORDER THE ARRAYS BACK TO THE ORIGINAL ORDER
C  OF THE PROBLEM STATEMENT
C
     DIMENSION A(IDIM1,IDIM2),STDCP(IDIM1),A0(IDIM1),A1(IDIM1),
    &A2(IDIM1),A3(IDIM1),A4(IDIM1),ACOEF(IDIM1),DH0(IDIM1),
    &DS0(IDIM1),DG(IDIM1),ICP(IDIM1)
     INTEGER QUES(IDIM1),ISPCE(IDIM1,3),SPECIE(IDIM1,3),
    &       PHASE(IDIM1,3),E,VSC,VSCM1
     REAL*8 N(IDIM1),dzeta(idim1),TEMP,q(idim1),keq(idim1),dtemp,
    &frac(idim1),chmpt(idim1)
     VSCM1=VSC-1
     DO 300 I=1,VSCM1
     IP1=I+1
     DO 200 II=IP1,VSC
     IF(ISPCE(I,1).EQ.SPECIE(II,1).AND.
    &   ISPCE(I,2).EQ.SPECIE(II,2).AND.
    &   ISPCE(I,3).EQ.SPECIE(II,3)) GO TO 50
     GO TO 200
  50 TEMP=N(I)
     N(I)=N(II)
     N(II)=TEMP
     TEMP=STDCP(I)
     STDCP(I)=STDCP(II)
     STDCP(II)=TEMP
     TEMP=A0(I)
     A0(I)=A0(II)
     A0(II)=TEMP
     TEMP=A1(I)
     A1(I)=A1(II)
     A1(II)=TEMP
     TEMP=A2(I)
  A2(I)=A2(II)
  A2(II)=TEMP
  TEMP=A3(I)
  A3(I)=A3(II)
  A3(II)=TEMP
  TEMP=A4(I)
  A4(I)=A4(II)
  A4(II)=TEMP
  TEMP=DH0(I)
  DH0(I)=DH0(II)
  DH0(II)=TEMP
  TEMP=DS0(I)
  DS0(I)=DS0(II)
  DS0(II)=TEMP
  ITEMP=ICP(I)
  ICP(I)=ICP(II)
  ICP(II)=ITEMP
  dtemp=DZETA(I)
  DZETA(I)=DZETA(II)
  DZETA(II)=dtemp
  TEMP=CHMPT(I)
  CHMPT(I)=CHMPT(II)
  CHMPT(II)=TEMP
  TEMP=ACOEF(I)
  ACOEF(I)=ACOEF(II)
  ACOEF(II)=TEMP
  dtemp=FRAC(I)
  FRAC(I)=FRAC(II)
  FRAC(II)=dtemp
  ITEMP=QUES(I)
  QUES(I)=QUES(II)
  QUES(II)=ITEMP
  TEMP=DG(I)
  DG(I)=DG(II)
  DG(II)=TEMP
  TEMP=Q(I)
  Q(I)=Q(II)
  Q(II)=TEMP
  dtemp=KEQ(I)
  KEQ(I)=KEQ(II)
  KEQ(II)=dtemp
  DO 60 J=1,3
  ITEMP=SPECIE(I,J)
  SPECIE(I,J)=SPECIE(II,J)
  SPECIE(II,J)=ITEMP
  ITEMP=PHASE(I,J)
  PHASE(I,J)=PHASE(II,J)
  PHASE(II,J)=ITEMP
60 CONTINUE
  DO 100 J=1,E
  TEMP=A(I,J)
```

```
    A(I,J)=A(II,J)
    A(II,J)=TEMP
100 CONTINUE
200 CONTINUE
300 CONTINUE
    RETURN
    END
    SUBROUTINE WRAPUP(TITLE,SPECIE,INERT,N,FRAC,QUES,ZV,FRACZ,SITOT,
   &  SIMF,ACTSIS,ACTGAS,ACTINS,ACTPS,ACTASS,RIIIV,RGAAS,RINP,
   & BSTCVG,ITBST,RELMAX,CNVG,ISS,XIII,T,P,IDATA,IDIM1,IFILE,V,VSC,
   & IOPT,ITP,NTP,ITAB,ICMP,IWRAP,GFE,STDCP,RT)
C
C SUBROUTINE TO WRITE-OUT A SUMMARY OF THE RESULTS TO A FILE
C
    DIMENSION INERT(3),TEMP(20),PRESS(20),
   &        IDCOMP(50,3),QUANT(50,20),CONV(50,20),STDCP(50)
    INTEGER TITLE(20),SPECIE(IDIM1,3),QUES(IDIM1),V,VSC,IQ(2),
   &      EL(5)/'SI','GA','IN',' P','AS'/
    REAL*8 N(IDIM1),frac(idim1),comp(50,20)
    IF(IDATA.EQ.0.AND.ICMP.EQ.1) WRITE(ITAB,50) (TITLE(K),K=1,20)
    IF(IDATA.EQ.0.AND.ICMP.EQ.1.AND.IWRAP.LT.7) WRITE(IFILE,50)
   &      (TITLE(K),K=1,20)
    IF(IDATA.EQ.0) WRITE(ITAB,51) ICMP
    IF(IDATA.EQ.0) WRITE(IFILE,51) ICMP
 50 FORMAT(/,1x,20A4)
 51 FORMAT(/,1X,'COMPOSITIONAL SET # ',I3)
    IF(IOPT.EQ.1.OR.IOPT.EQ.4)TEMP(ITP)=T
    IF(IOPT.EQ.2.OR.IOPT.EQ.5)PRESS(ITP)=P/1.01325E+05
    IF(IDATA.NE.0) WRITE(IFILE,55) T,P
 55 FORMAT(1x,'TEMPERATURE = ',F7.1,' K',/,' PRESSURE = ',E12.5,' PA')
    IF(ABS(RELMAX).GT.CNVG.AND.IDATA.NE.0.AND.IWRAP.LT.7)
   &     WRITE(IFILE,58) RELMAX,CNVG,BSTCVG,ITBST
 58 FORMAT(66('*'),/,'*',5X,'ITERATION FOR EQUILIBRIUM COMPOSITION ',
   &      'DID NOT CONVERGE',5X,'*',/,'*',1X,'MAXIMUM ERROR=',
   &      E12.5,2X,'CONVERGENCE CRITERION=',E12.5,1X,'*',
   &/,'*',9X,'BEST CONVERGENCE=',E12.5,' AT ITERATION ',I4,8X,'*',
   &/,'*',12X,'THE BEST OBTAINED RESULTS ARE SHOWN BELOW',11X,'*',
   &      /,66('*'))
    IF(IDATA.EQ.0) WRITE(ITAB,60)
    IF(IDATA.EQ.0.AND.IWRAP.LT.7) WRITE(IFILE,60)
 60 FORMAT(/,19X,'INITIAL COMPOSITIONS')
    IF(IWRAP.GE.7.AND.IDATA.NE.0) WRITE (IFILE,61)GFE
 61 FORMAT(/,5X,'TOTAL GIBBS = ',E12.5)
    IF(IWRAP.GE.7.AND.IDATA.NE.0) WRITE (IFILE,62)
 62 FORMAT(/,3X,'SPECIES',7X,'STD.ST.CHEM.POT.',5X,'CONVERGENCE')
    IF(IDATA.EQ.1.AND.IWRAP.LT.7) WRITE(IFILE,70)
 70 FORMAT(13X,'EQUILIBRIUM COMPOSITIONS')
    IF(IDATA.EQ.0.AND.IWRAP.LT.7) WRITE(IFILE,80)
    IF(IDATA.EQ.0) WRITE(ITAB,80)
 80 FORMAT(/,1X,'SPECIES',7X,'MOLE FRACTIONS',4X,'MOLE NUMBERS')
    M=0
```

```
      DO 200 I=1,VSC
       DO 201 L=1,3
       IDCOMP(I+M,L)=SPECIE(I,L)
201   CONTINUE
      COMP(I+M,ITP)=FRAC(I)
      QUANT(I+M,ITP)=N(I)
      IF(QUES(I).EQ.'??  ')THEN
      CONV(I+M,ITP)='*   '
      IA=1
      ELSE IF(QUES(I).EQ.'?   ')THEN
      CONV(I+M,ITP)='#   '
      IB=1
      ELSE
      CONV(I+M,ITP)='    '
      ENDIF
      IF(QUES(I).EQ.'    ') THEN
      IQ(1)='YES '
      ELSE
      IQ(1)='NO  '
      ENDIF
      STP=STDCP(I)*RT
      IF(IWRAP.LT.7) WRITE(IFILE,100) (SPECIE(I,K),K=1,3),FRAC(I),N(I),
     &     QUES(I)
      IF(IWRAP.GE.7.AND.IDATA.NE.0.and.I.gt.V) WRITE(IFILE,63)
     &     (SPECIE(I,K),K=1,3),STP,IQ(1)
 63 FORMAT(3A4,7X,F12.5,11X,A4)
      IF(I.NE.V) GO TO 200
       DO 202 J=1,3
       IDCOMP(V+1,J)=INERT(J)
202   CONTINUE
      COMP(V+1,ITP)=FRACZ
      QUANT(V+1,ITP)=ZV
      CONV(V+1,ITP)='  '
      M=1
      IF(IWRAP.LT.7) WRITE(IFILE,100) (INERT(K),K=1,3),FRACZ,ZV
100 FORMAT(3A4,2X,E12.5,2X,E12.5,1X,A4)
      IF(RIIIV.GT.0.AND.RIIIV.LT.1.0E6.AND.IWRAP.LT.7) WRITE(IFILE,105)
     &     RIIIV
105 FORMAT('VAPOR III/V ',10X,F9.4)
      IF(SITOT.GT.0.AND.IWRAP.LT.7) WRITE(IFILE,110) SIMF,SITOT
110 FORMAT('SI IN VAPOR ',2X,E12.5,2X,E12.5)
      IF(ACTSIS.GT.0.AND.IWRAP.LT.7) WRITE(IFILE,120) EL(1),ACTSIS
120 FORMAT(1A2,' ACTIVITY',13X,E12.5)
      IF(ACTGAS.GT.0.AND.IWRAP.LT.7) WRITE(IFILE,120) EL(2),ACTGAS
      IF(ACTINS.GT.0.AND.IWRAP.LT.7) WRITE(IFILE,120) EL(3),ACTINS
      IF(ACTPS.GT.0.AND.IWRAP.LT.7) WRITE(IFILE,120) EL(4),ACTPS
      IF(ACTASS.GT.0.AND.IWRAP.LT.7) WRITE(IFILE,120) EL(5),ACTASS
      IF(RGAAS.GT.0.AND.IWRAP.LT.7) WRITE(IFILE,130) RGAAS
130 FORMAT('GA-AS SATURATION RATIO  ',E12.5)
      IF(RINP.GT.0.AND.IWRAP.LT.7) WRITE(IFILE,135) RINP
135 FORMAT(' IN-P SATURATION RATIO  ',E12.5)
```

```
200 CONTINUE
  IF(IDATA.EQ.0) WRITE(ITAB,101) ((IDCOMP(J,K),K=1,3),COMP(J,1),
 &QUANT(J,1),J=1,VSC+1)
101 FORMAT(3A4,2X,E12.5,6X,E12.5)
  IF(ISS.GT.0.AND.IWRAP.LT.7) WRITE(IFILE,205) XIII
205 FORMAT(3X,'X=',F6.4)
  WRITE(IFILE,210)
210 FORMAT('     ')
  IDATA=1
  IF(ITP.EQ.NTP)THEN
  IF(IOPT.EQ.1.OR.IOPT.EQ.4)WRITE(ITAB,290) P/1.01325E+05
  IF(IOPT.EQ.2.OR.IOPT.EQ.5)WRITE(ITAB,295) T
290 FORMAT(/,/,/,' EQUILIBRIUM PRESSURE = ',F6.3,' ATM')
295 FORMAT(/,/,/,' EQUILIBRIUM TEMPERATURE = ',F7.1,' K')
  IF(IA.EQ.1.OR.IB.EQ.1)WRITE(ITAB,300)
300 FORMAT(/,72('$'),/,/,21X,'<<<< CONVERGENCE WARNING >>>>',/,/,
 &72('$'))
  IF(IB.EQ.1)WRITE(ITAB,301)
301 FORMAT(/,' -- EQUILIBRIUM COMPOSITIONS PRECEDED BY THE SYMBOL ',
 &'(#) DID NOT CONVERGE.',/,4X,'THE DISCREPANCY IS LESS THAN 10% ',
 &'OF DESIRED VALUE.',/,/,72('$'))
  IF(IA.EQ.1)WRITE(ITAB,302)
302 FORMAT(/,' -- EQUILIBRIUM COMPOSITIONS PRECEDED BY THE SYMBOL ',
 &'(*) DID NOT CONVERGE.',/,4X,'THE DISCREPANCY IS MORE THAN 10% ',
 &'OF DESIRED VALUE.',/,/,72('$'))
  DO 235 ILOOP=1,2
  IF(ILOOP.EQ.1)WRITE(ITAB,220)
  IF(ILOOP.EQ.2)WRITE(ITAB,225)
220 FORMAT(/,25X,'EQUILIBRIUM MOLE FRACTIONS')
225 FORMAT(/,/,/,26X,'EQUILIBRIUM MOLE NUMBERS')
  L=0
  M=0
270 L=M+1
  M=M+5
  IC=VSC+1-M
   IF(IC.GE.-4 .AND. IC.LE.0)THEN
   M=VSC+1
   GO TO 230
   ELSE IF(IC.GT.0)THEN
   GO TO 230
   ELSE
   GO TO 235
   END IF
230     IF(IOPT.EQ.1.OR.IOPT.EQ.4)THEN
    WRITE(ITAB,240) ((IDCOMP(I,J),J=1,3),I=L,M)
240     FORMAT(/,' TEMP(K)',1X,3(3A4,1X),2(3A4))
    DO 245 K=1,NTP
    IF(ILOOP.EQ.1)WRITE(ITAB,250) TEMP(K),(CONV(J,K),COMP(J,K),
 &   J=L,M)
    IF(ILOOP.EQ.2)WRITE(ITAB,250) TEMP(K),(CONV(J,K),QUANT(J,K),
 &   J=L,M)
 250    FORMAT(F7.1,5(1X,A1,E11.5))
 245    CONTINUE
      GO TO 270
      ELSE IF(IOPT.EQ.2.OR.IOPT.EQ.5)THEN
      WRITE(ITAB,255) ((IDCOMP(I,J),J=1,3),I=L,M)
 255    FORMAT(/,' PRESS(ATM)',1X,15A4)
      DO 260 K=1,NTP
      IF(ILOOP.EQ.1)WRITE(ITAB,265) PRESS(K),(COMP(J,K),CONV(J,K),
   &   J=L,M)
      IF(ILOOP.EQ.2)WRITE(ITAB,265) PRESS(K),(QUANT(J,K),CONV(J,K),
   &   J=L,M)
 265    FORMAT(F6.3,1X,5(1X,A1,E11.5))
 260    CONTINUE
      GO TO 270
      ELSE
      GO TO 235
      END IF
 235 CONTINUE
    ELSE
    GO TO 285
    END IF
 285 RETURN
    END
    SUBROUTINE GIBBS(N,STDCP,STDCPZ,ACOEF,FRAC,ZV,FRACZ,COND,SOLN,
   &              PHASE,RT,P,P0,IDIM1,V,S,C,GFE)
C
C  SUBROUTINE TO CALCULATE THE GIBBS FREE ENERGY OF THE SYSTEM
C
    DIMENSION STDCP(IDIM1),ACOEF(IDIM1)
    REAL*8 N(IDIM1),frac(idim1),arg
    INTEGER COND(3),SOLN(3),PHASE(IDIM1,3),V,S,C,VSC
    VSC=V+S+C
C
C  GAS CONSTANT IS IN UNITS OF: KCAL/G-MOLE-K
C
    ARG=1.0
    IF(FRACZ.GT.0.0) ARG=FRACZ*P/P0
    GSTAR=ZV*(STDCPZ+ALOG(ARG))
    DO 150 I=1,VSC
    ARG=ACOEF(I)*FRAC(I)*P/P0
    IF(PHASE(I,1).EQ.COND(1)) ARG=1
    IF(PHASE(I,1).EQ.SOLN(1)) ARG=ACOEF(I)*FRAC(I)
    GSTAR=GSTAR+N(I)*(STDCP(I)+dlog(arg))
 150 CONTINUE
    GFE=GSTAR*RT
    RETURN
    END
    SUBROUTINE DEBUG(N,DZETA,VSC,IDIM1,ITER,ALMBDA,GFE,
   &              RMX,IWRT)
C
C  ROUTINE TO WRITE-OUT N, DZETA, ALMBDA DURING THE ITERATON PROCESS
```

```
C
      REAL*8 N(IDIM1),dzeta(idim1),almbda
      INTEGER VSC
      WRITE(IWRT,10) ITER,ALMBDA,GFE,RMX
   10 FORMAT('0','ITERATION = ',I5,5X,'LAMBDA = ',E14.7,
     &      5X,'GIBBS FREE ENERGY = ',E14.7,' KCAL',
     &      5X,'RELATIVE ERROR = ',E12.5,/,1X,
     &      'N-VALUES',T20,'DELTA-ZETA VALUES')
      DO 50 I=1,VSC
      WRITE(IWRT,20) N(I),DZETA(I)
   20 FORMAT(1X,E14.7,T20,E14.7)
   50 CONTINUE
      RETURN
      END
      SUBROUTINE PMAT(MATRIX,NDIM1,NDIM2,L1,L2,NAME,IWRT)
C
C  SUBROUTINE TO WRITE-OUT REAL MATRICIES
C
      INTEGER*2 NAME(3)
      REAL MATRIX(NDIM1,NDIM2)
      WRITE(IWRT,10) (NAME(J),J=1,3)
   10 FORMAT('0','MATRIX ',3A2)
      DO 100 I=1,L1
      WRITE(IWRT,20) (MATRIX(I,J),J=1,L2)
   20 FORMAT(1X,10(E11.4,2X))
  100 CONTINUE
      RETURN
      END
      SUBROUTINE DPMAT(DMTRIX,NDIM1,NDIM2,L1,L2,NAME,IWRT)
C
C  SUBROUTINE TO WRITE-OUT DOUBLE PRECISION REAL MATRICIES
C
      DOUBLE PRECISION DMTRIX(NDIM1,NDIM2)
      INTEGER*2 NAME(3)
      WRITE(IWRT,10) (NAME(J),J=1,3)
   10 FORMAT('0','MATRIX ',3A2)
      DO 100 I=1,L1
      WRITE(IWRT,20) (DMTRIX(I,J),J=1,L2)
   20 FORMAT(1X,10(D11.4,2X))
  100 CONTINUE
      RETURN
      END
      SUBROUTINE PVEC(vector,NDIM,L,NAME,IWRT)
C
C  SUBROUTINE TO WRITE-OUT REAL VECTORS
C
      INTEGER*2 NAME(3)
      real*8 vector(NDIM)
      WRITE(IWRT,10) (NAME(J),J=1,3)
   10 FORMAT('0','THE TRANSPOSED ',3A2,' VECTOR IS:')
      WRITE(IWRT,20) (VECTOR(J),J=1,L)
  20 FORMAT(1X,10(E11.4,2X))
     RETURN
     END
     SUBROUTINE IPVEC(IVCTOR,NDIM,L,NAME,IWRT)
C
C  SUBROUTINE TO WRITE-OUT INTEGER VECTORS
C
     DIMENSION IVCTOR(NDIM)
     INTEGER*2 NAME(3)
     WRITE(IWRT,10) (NAME(J),J=1,3)
  10 FORMAT('0','THE TRANSPOSED ',3A2,' VECTOR IS:')
     WRITE(IWRT,20) (IVCTOR(J),J=1,L)
  20 FORMAT(1X,10(I11,2X))
     RETURN
     END
     SUBROUTINE LINV1F (A,N,IA,AINV,IDGT,WKAREA,IER)
C
C  IMSL SUBROUTINE FOR INVERTING REAL MATRICIES
C
     DOUBLE PRECISION A(IA,N),AINV(IA,N),WKAREA(1),ZERO,ONE
     DATA            ZERO/0.0D0/,ONE/1.0D0/
     IER=0
     DO 10 I=1,N
       DO 5 J=1,N
         AINV(I,J) = ZERO
   5   CONTINUE
       AINV(I,I) = ONE
  10 CONTINUE
     CALL LEQT1F (A,N,N,IA,AINV,IDGT,WKAREA,IER)
     IF (IER .EQ. 0) GO TO 9005
 9000 CONTINUE
 9005 RETURN
     END
     SUBROUTINE LEQT1F (A,M,N,IA,B,IDGT,WKAREA,IER)
C
C  IMSL SUBROUTINE LEQT1F FOR SOLVING THE MATRIX PROBLEM A*X=B
C
     DIMENSION         A(IA,1),B(IA,1),WKAREA(1)
     DOUBLE PRECISION   A,B,WKAREA,D1,D2,WA
C                          INITIALIZE IER
C                          FIRST EXECUTABLE STATEMENT
     IER=0
C                          DECOMPOSE A
     CALL LUDATF (A,A,N,IA,IDGT,D1,D2,WKAREA,WKAREA,WA,IER)
     IF (IER .GT. 128) GO TO 9005
C                          CALL ROUTINE LUELMF (FORWARD AND
C                          BACKWARD SUBSTITUTIONS)
     DO 10 J=1,M
       CALL LUELMF (A,B(1,J),WKAREA,N,IA,B(1,J))
  10 CONTINUE
 9005 RETURN
```

```
      END
      SUBROUTINE LUDATF (A,LU,N,IA,IDGT,D1,D2,IPVT,EQUIL,WA,IER)
C
C  THIS SUBROUTINE IS USED WITH SUBROUTINE LEQT1F
C
      DIMENSION          A(IA,1),LU(IA,1),IPVT(1),EQUIL(1)
      DOUBLE PRECISION   A,LU,D1,D2,EQUIL,WA,ZERO,ONE,FOUR,SIXTN,SIXTH,
     *                 RN,WREL,BIGA,BIG,P,SUM,AI,WI,T,TEST,Q,IPVT
      DATA               ZERO,ONE,FOUR,SIXTN,SIXTH/0.D0,1.D0,4.D0,
     *                 16.D0,.0625D0/
C                          FIRST EXECUTABLE STATEMENT
C                          INITIALIZATION
      IER = 0
      RN = N
      WREL = ZERO
      D1 = ONE
      D2 = ZERO
      BIGA = ZERO
      DO 10 I=1,N
        BIG = ZERO
        DO 5 J=1,N
          P = A(I,J)
          LU(I,J) = P
          P = DABS(P)
          IF (P .GT. BIG) BIG = P
    5   CONTINUE
        IF (BIG .GT. BIGA) BIGA = BIG
        IF (BIG .EQ. ZERO) GO TO 110
        EQUIL(I) = ONE/BIG
   10 CONTINUE
      DO 105 J=1,N
        JM1 = J-1
        IF (JM1 .LT. 1) GO TO 40
C                          COMPUTE U(I,J), I=1,...,J-1
        DO 35 I=1,JM1
          SUM = LU(I,J)
          IM1 = I-1
          IF (IDGT .EQ. 0) GO TO 25
C                          WITH ACCURACY TEST
          AI = DABS(SUM)
          WI = ZERO
          IF (IM1 .LT. 1) GO TO 20
          DO 15 K=1,IM1
            T = LU(I,K)*LU(K,J)
            SUM = SUM-T
            WI = WI+DABS(T)
   15     CONTINUE
          LU(I,J) = SUM
   20     WI = WI+DABS(SUM)
          IF (AI .EQ. ZERO) AI = BIGA
          TEST = WI/AI
        IF (TEST .GT. WREL) WREL = TEST
        GO TO 35
C                        WITHOUT ACCURACY
  25      IF (IM1 .LT. 1) GO TO 35
        DO 30 K=1,IM1
          SUM = SUM-LU(I,K)*LU(K,J)
  30      CONTINUE
        LU(I,J) = SUM
  35   CONTINUE
  40   P = ZERO
C                        COMPUTE U(J,J) AND L(I,J), I=J+1,...,
      DO 70 I=J,N
        SUM = LU(I,J)
        IF (IDGT .EQ. 0) GO TO 55
C                        WITH ACCURACY TEST
        AI = DABS(SUM)
        WI = ZERO
        IF (JM1 .LT. 1) GO TO 50
        DO 45 K=1,JM1
          T = LU(I,K)*LU(K,J)
          SUM = SUM-T
          WI = WI+DABS(T)
  45      CONTINUE
        LU(I,J) = SUM
  50      WI = WI+DABS(SUM)
        IF (AI .EQ. ZERO) AI = BIGA
        TEST = WI/AI
        IF (TEST .GT. WREL) WREL = TEST
        GO TO 65
C                        WITHOUT ACCURACY TEST
  55      IF (JM1 .LT. 1) GO TO 65
        DO 60 K=1,JM1
          SUM = SUM-LU(I,K)*LU(K,J)
  60      CONTINUE
        LU(I,J) = SUM
  65      Q = EQUIL(I)*DABS(SUM)
        IF (P .GE. Q) GO TO 70
        P = Q
        IMAX = I
  70   CONTINUE
C                        TEST FOR ALGORITHMIC SINGULARITY
      IF (RN+P .EQ. RN) GO TO 110
      IF (J .EQ. IMAX) GO TO 80
C                        INTERCHANGE ROWS J AND IMAX
      D1 = -D1
      DO 75 K=1,N
        P = LU(IMAX,K)
        LU(IMAX,K) = LU(J,K)
        LU(J,K) = P
  75   CONTINUE
      EQUIL(IMAX) = EQUIL(J)
```

```
   80   IPVT(J) = IMAX
        D1 = D1*LU(J,J)
   85   IF (DABS(D1) .LE. ONE) GO TO 90
        D1 = D1*SIXTH
        D2 = D2+FOUR
        GO TO 85
   90   IF (DABS(D1) .GE. SIXTH) GO TO 95
        D1 = D1*SIXTN
        D2 = D2-FOUR
        GO TO 90
   95   CONTINUE
        JP1 = J+1
        IF (JP1 .GT. N) GO TO 105
C                       DIVIDE BY PIVOT ELEMENT U(J,J)
        P = LU(J,J)
        DO 100 I=JP1,N
          LU(I,J) = LU(I,J)/P
  100     CONTINUE
  105 CONTINUE
C                       PERFORM ACCURACY TEST
      IF (IDGT .EQ. 0) GO TO 9005
      P = 3*N+3
      WA = P*WREL
      IF (WA+10.D0**(-IDGT) .NE. WA) GO TO 9005
      IER = 34
      GO TO 9005
C                       ALGORITHMIC SINGULARITY
  110 IER = 129
      D1 = ZERO
      D2 = ZERO
 9005 RETURN
      END
      SUBROUTINE LUELMF (A,B,IPVT,N,IA,X)
C
C  THIS SUBROUTINE IS USED WITH SUBROUTINE LEQT1F
C
      DIMENSION          A(IA,1),B(1),IPVT(1),X(1)
      DOUBLE PRECISION   A,B,X,SUM,IPVT
C                       FIRST EXECUTABLE STATEMENT
C                       SOLVE LY = B FOR Y
      DO 5 I=1,N
    5 X(I) = B(I)
      IW = 0
      DO 20 I=1,N
        IP = IPVT(I)
        SUM = X(IP)
        X(IP) = X(I)
        IF (IW .EQ. 0) GO TO 15
        IM1 = I-1
        DO 10 J=IW,IM1
          SUM = SUM-A(I,J)*X(J)
  10   CONTINUE
       GO TO 20
  15   IF (SUM .NE. 0.D0) IW = I
  20 X(I) = SUM
C                              SOLVE UX = Y FOR X
     DO 30 IB=1,N
       I = N+1-IB
       IP1 = I+1
       SUM = X(I)
       IF (IP1 .GT. N) GO TO 30
       DO 25 J=IP1,N
         SUM = SUM-A(I,J)*X(J)
  25   CONTINUE
  30 X(I) = SUM/A(I,I)
     RETURN
     END
     SUBROUTINE SPECIL(N,A,E,V,S,SPECIE,ELMNT,IFILE)
C
C SUBROUTINE TO CALCULATE SPECIAL RATIOS FOR SPECIFIC SPECIES
C AT EQUILIBRIUM
C
     REAL CLOUT, GAOUT, GEOUT, HOUT, INOUT, POUT, SIOUT,CLRAT,
    &MGAOUT,MINOUT
     REAL*8 N(50)
     DIMENSION A(50,13)
     INTEGER E,V,S,SPECIE(50,3),ELMNT(13),GA/'GA'/,GE/'GE'/,IN/'IN'/,
    &SA/'AS'/,SI/'SI'/,P/' P'/,MAS/'AS ('/,MGA/' GA-'/,MIN/' IN-'/,
    &CL/'CL'/, H/' H'/
     ASOUT=0.0
     CLOUT=0.0
     GAOUT=0.0
     GEOUT=0.0
     HOUT=0.0
     INOUT=0.0
     POUT=0.0
     SIOUT=0.0
     MGAOUT=0.0
     MINOUT=0.0
     KAS=0.0
     KCL=0.0
     KGA=0.0
     KGE=0.0
     KH=0.0
     KIN=0.0
     KP=0.0
     KSI=0.0
     KMGA=0.0
     KMIN=0.0
C
C CALCULATE THE TOTAL MOLES OF ELEMENTS IN THE VAPOR AT EQUILIBRIUM
C
```

```
      DO 10, J=1,E
      IF(ELMNT(J).EQ.SA) KAS=J
      IF(ELMNT(J).EQ.CL) KCL=J
      IF(ELMNT(J).EQ.GA) KGA=J
      IF(ELMNT(J).EQ.GE) KGE=J
      IF(ELMNT(J).EQ.H) KH=J
      IF(ELMNT(J).EQ.IN) KIN=J
      IF(ELMNT(J).EQ.P) KP=J
      IF(ELMNT(J).EQ.SI) KSI=J
 10   CONTINUE
C
C
      DO 20, I=1,V
      ASOUT=ASOUT+N(I)*A(I,KAS)
      CLOUT=CLOUT+N(I)*A(I,KCL)
      GAOUT=GAOUT+N(I)*A(I,KGA)
      GEOUT=GEOUT+N(I)*A(I,KGE)
      HOUT=HOUT+N(I)*A(I,KH)
      INOUT=INOUT+N(I)*A(I,KIN)
      POUT=POUT+N(I)*A(I,KP)
      SIOUT=SIOUT+N(I)*A(I,KSI)
 20   CONTINUE
C
C CALULATE CL/H RATIO IN THE VAPOR AT EQUILIBRIUM
C
      IF(CLOUT .EQ. 0 .OR. HOUT .EQ. 0) GO TO 30
      CLRAT=CLOUT/HOUT
      WRITE(IFILE,205) CLRAT
 205  FORMAT(1X,'CL/H =',E12.5)
      WRITE(IFILE,200)
 200  FORMAT(' ')
C
C CALCULATE GA/(GA+IN) RATIO IN THE VAPOR AT EQUILIBRIUM
C
 30   IF(GAOUT .EQ. 0 .OR. INOUT .EQ. 0) GO TO 40
      GARAT=GAOUT/(GAOUT+INOUT)
      WRITE(IFILE,210) GARAT
 210  FORMAT(1X,'GA/(GA+IN) (IN THE VAPOR) =',E12.5)
      WRITE(IFILE,200)
C
C CALCULATE METAL CHLORINE RATION AT EQUILIBRIUM IN THE VAPOR
C
40    IF(CLOUT .EQ. 0) GO TO 60
      IF(GEOUT .EQ. 0) GO TO 50
      GERAT=GEOUT/CLOUT
      WRITE(IFILE,220) GERAT
 220  FORMAT(1X,'GE/CL =',E12.5)
 50   IF(SIOUT .EQ. 0) GO TO 60
      SIRAT=SIOUT/CLOUT
      WRITE(IFILE,230) SIRAT
 230  FORMAT(1X,'SI/CL =',E12.5)
```

```
      IF(GEOUT .EQ. 0) GO TO 60
      GSRAT=GEOUT/(GEOUT+SIOUT)
      WRITE(IFILE,240)
 240  FORMAT(1X,'GE/(GE+SI) =',E12.5)
C
C CALCULATE GA/(GA+IN) IN SOLUTION IN THE SOLID PHASE AT EQUILIBRIUM
C
 60   IF(S .EQ. 0) GO TO 100
      DO 70, I=V+1,V+S
      IF(SPECIE(I,1).EQ.MGA.AND.SPECIE(I,2).EQ.MAS) KMGA=I
      IF(SPECIE(I,1).EQ.MIN.AND.SPECIE(I,2).EQ.MAS) KMIN=I
 70   CONTINUE
      IF(KMGA.EQ.0 .OR. KMIN.EQ.0) GO TO 100
      MGAOUT=N(KMGA)
      MINOUT=N(KMIN)
      X=MGAOUT/(MGAOUT+MINOUT)
      WRITE(IFILE,250) X
 250  FORMAT(1X,'X=GA-AS/(GA-AS+IN-AS) (IN SOLUTION) =',E12.5)
 100  WRITE(IFILE,200)
      RETURN
      END
```

APPENDIX B
USER GUIDE FOR THE FORTRAN SOURCE CODE OF APPENDIX A

This appendix is intended to function as a user manual for the FORTRAN source code supplied in Appendix A of this dissertation. First, an input file must be generated. This file will always be named chospec.dat. A general form for this file is shown in Figure B.1.

The chospec.dat file will always have the form shown in Figure B.1. Line (1) is an 80-character title line to remember what a particular chospec.dat file is for. It is up to the user to decide upon an adequate description for the file. Line (2) is an input line with nine entries, each separated by two or more spaces. These are: the number of different elements in the system, the number of vapor species, the number of solution species, the number of pure condensed (liquid or solid) species, the system's temperature (in K), the system's pressure (in Pa), the reference temperature (always 298.15 K), and the reference pressure (always 101325 Pa), and the number of reference species that are not considered as possible reactants/products in the equilibrium calculations. Therefore, in the case of Figure B.1, there are 4 elements, 30 vapor species, 0 solution species, and 1 pure condensed phase species. The system's temperature and pressure are 1000K and 101325 Pa, respectively. The reference temperature and pressure are as mentioned above. The final entry is to instruct the algorithm how many reference species located at the bottom of the species thermochemical data subblocks are not to be considered in the equilibrium calculations except to act as corrections for the various other species containing these reference species. In the case of Figure B.1 there are two of these species (B and P) whose thermochemical data is found in lines (97-102). The reference data for phosphorus was entered directly into the FORTRAN code and is identified as such by the last number '3' at the end of line (101). This number is unique for phosphorus and should not be used for any other element. A number '5' in this entry would identify the element as bromine. This too is written directly into the FORTRAN code to account for its change in reference state from liquid to gas over the typical temperature range of interest to persons modeling equilibrium processes. Similar to phosphorus, the number '5' should only be used to identify the element bromine.

Line (3) names the elements present in all the species (vapor, liquid, solid, and in solution) in the system. The number of elements must correspond to the first number in line (2).

The next lines are for entering the thermochemical data for each different species. The thermochemical data for the vapor species is entered first, followed by the solution species, and finally the pure condensed phase species. In this example, line (4) is the

Figure B.1 Example Chospec.dat input data file

```
(1)   BORON PHOSPHIDE SYSTEM
(2)      4   30     0    1   1000.00 101325.00    298.15 101325.00    2
(3)     H CL B P
(4)    H2     (V)  0.00        0.00
(5)    1.27061E-02 1.68758E-06-4.06750E+01-1.03000E-03 0.00000E+00 0
(6)   2.000 0.000 0.000 0.000
(7)    H-CL   (V) -2.20626E+01 2.36926E-03
(8)    7.23556E-03-1.74369E-06 3.08530E-09-1.01697E-12 0.00000E+00 1
(9)   1.000 1.000 0.000 0.000
(10)   B-H3   (V)  2.48900E+01-3.31967E-03
(11)   3.75562E-03 1.34189E-05-3.34771E-09 1.08523E+02 0.00000E+00 2
(12)  3.000 0.000 1.000 0.000
(13)   P-H3   (V)  1.29780E+00-6.42101E-03
(14)  -4.84111E-02-3.46993E-06 2.68585E+02 9.69254E-03 0.00000E+00 0
(15)  3.000 0.000 0.000 1.000
(16)   H      (V)  5.21028E+01 1.18013E-02
(16)   4.96797E-03 0.00000E+00 0.00000E+00 0.00000E+00 0.00000E+00 1
```

```
(17)   1.000 0.000 0.000 0.000
(18)    CL      (V)  2.89919E+01 1.27965E-02
(19)    6.02591E-03-8.90944E-07 2.26164E-10-5.03105E+01 0.00000E+00 2
(20)   0.000 1.000 0.000 0.000
(21)    CL2     (V)  0.00        0.00
(22)    8.66307E-03 4.57242E-07-1.10758E-10-6.03934E+01 0.00000E+00 2
(23)   0.000 2.000 0.000 0.000
(23)    B-CL    (V)  4.25200E+01 2.28813E-02
(24)    3.33090E-04-8.54180E-07-2.12120E+01 1.35505E-03 0.00000E+00 0
(25)   0.000 1.000 1.000 0.000
(26)    B-CL2   (V) -6.79000E+00 9.70270E-03
(27)    2.40318E-03-1.29203E-06-9.42679E+01 1.81742E-03 0.00000E+00 0
(28)   0.000 2.000 1.000 0.000
(29)    B-CL3   (V) -9.86300E+01-1.27159E-02
(30)   -6.01326E-03-2.67012E-06-1.16453E+02 4.03865E-03 0.00000E+00 0
(31)   0.000 3.000 1.000 0.000
(32)    B-H     (V)  1.05830E+02 2.40033E-02
(33)    5.64037E-03 2.89935E-06-6.71797E-10 4.81334E+01 0.00000E+00 2
(34)   1.000 0.000 1.000 0.000
(35)    B-H2    (V)  7.94300E+01 1.37468E-02
(36)    6.57204E-03 7.34826E-06-1.95425E-09-4.06785E+01 0.00000E+00 2
(37)   2.000 0.000 1.000 0.000
(38)    B-H-CL2(V) -6.06800E+01-6.55380E-03
(39)   -2.20923E-02-2.97364E-06-3.16838E+01 6.17562E-03 0.00000E+00 0
(40)   1.000 2.000 1.000 0.000
(41)    B-H2-CL(V) -1.89800E+01-3.40174E-03
(42)    4.90832E-03 1.86997E-05-9.92562E-09 2.03570E-12 0.00000E+00 1
(43)   2.000 1.000 1.000 0.000
(44)    B-H-CL (V)  3.45300E+01 1.35848E-02
(45)   -5.91154E-03-6.53786E-07-9.90270E+00 2.70359E-03 0.00000E+00 0
(46)   1.000 1.000 1.000 0.000
(47)    B2-CL4 (V) -1.16900E+02-2.36874E-02
(48)   -2.53415E-02-6.34570E-06-4.87600E+01 8.87746E-03 0.00000E+00 0
(49)   0.000 4.000 2.000 0.000
(50)    B2-H6   (V)  8.74761E+00-4.09787E-02
(51)   -1.20007E-01-7.63418E-06 3.83184E+02 2.31220E-02 0.00000E+00 0
(52)   6.000 0.000 2.000 0.000
(53)   B5-H9  (V)  1.75000E+01-8.17962E-02
(54)   -2.68602E-01-2.20755E-05 7.45679E+02 5.07514E-02 0.00000E+00 0
(55)   9.000 0.000 5.000 0.000
(56)    B       (V)  1.35038E+02 3.52357E-02
(57)    4.99907E-03-3.44357E-08 8.06867E-12-2.05847E+00 0.00000E+00 2
(58)   0.000 0.000 1.000 0.000
(59)    B2      (V)  1.99850E+02 4.54477E-02
(60)    6.18239E-03-4.23274E-08-1.63173E+02 5.52825E-04 0.00000E+00 0
(61)   0.000 0.000 2.000 0.000
(62)    P       (V)  7.56453E+01 2.91845E-02
(63)    4.95048E-03 9.51850E-08-1.39185E-10 5.92686E-14 0.00000E+00 1
(64)   0.000 0.000 0.000 1.000
(65)    P2      (V)  3.44168E+01 3.24931E-02
(66)    9.07471E-04-7.06630E-07-8.51824E+00 1.24740E-03 0.00000E+00 0
(67)   0.000 0.000 0.000 2.000
(68)    P3      (V)  5.01912E+01 3.35215E-02
(69)    3.19933E-03-1.14083E-06-6.81341E+01 1.82305E-03 0.00000E+00 0
(70)   0.000 0.000 0.000 3.000
(71)    P4      (V)  1.40774E+01 2.76092E-02
(72)    6.12806E-03-1.39655E-06-1.63210E+02 2.15589E-03 0.00000E+00 0
(73)   0.000 0.000 0.000 4.000
(74)    P-H     (V)  5.51511E+01 2.14984E-02
(75)    6.06489E-03 2.16326E-06-3.53638E-10 2.09641E+01 0.00000E+00 2
(76)   1.000 0.000 0.000 1.000
(77)    P-H2    (V)  2.85739E+01 9.76028E-03
(78)    6.04630E-03 6.80507E-06-1.68617E-09 2.61183E+01 0.00000E+00 2
```

```
(79)   2.000 0.000 0.000 1.000
(80)    P-CL   (V)  3.21759E+01 2.01364E-02
(81)    7.44766E-03 2.46764E-07-3.71181E+01 1.87886E-04 0.00000E+00 0
(82)   0.000 1.000 0.000 1.000
(83)    P-CL2  (V) -1.29761E+01 5.00789E-03
(84)    8.16544E-03-6.04316E-07-8.03903E+01 9.05729E-04 0.00000E+00 0
(85)   0.000 2.000 0.000 1.000
(86)    P-CL3  (V) -6.91922E+01-1.52979E-02
(86)    1.05141E-02-9.52029E-07-1.24263E+02 1.46819E-03 0.00000E+00 0
(87)   0.000 3.000 0.000 1.000
(88)    P-CL5  (V) -8.98662E+01-5.53503E-02
(89)    1.70049E-02-1.50168E-06-2.27131E+02 2.31970E-03 0.00000E+00 0
(90)   0.000 5.000 0.000 1.000
(91)    INERT  (V)  0.00        0.00
(92)    0.00        0.00        0.00        0.00        0.00        0
(93)   0.000 0.000 0.000 0.000
(94)    c-B-P(SOL) -2.75999E+01-4.82553E-03
(95)    5.25096E-03 6.69933E-06 0.00000E+00 0.00000E+00 0.00000E+00 0
(96)   0.000 0.000 1.000 1.000
(97)    B    (SOL)  0.00        0.00
(98)   -5.71212E-03-2.65664E-07-1.31516E+02 1.74736E-03 0.00000E+00 0
(99)   0.000 0.000 1.000 0.000
(100)   P    (SOL)  0.00        0.00
(101)   2.61138E-03 1.52649E-05-1.81035E-08 5.75251E-12 0.00000E+00 3
(102)  0.000 0.000 0.000 1.000
(103)      0    4    0    7 1000   10   1.0E-06   25.00    1  0.0  0.01
(104)   0  5  26 2   0  0  0  1  1  2  1.0e-01    1.0e-02     0.0    0.0
(105)  7.17997E+01
(106)  7.28454E-01 2.03959E-01 1.13311E-03 6.64534E-02 1.00000E-40 1.00000E-40
(107)  1.00000E-40 1.00000E-40 1.00000E-40 1.00000E-40 1.00000E-40 1.00000E-40
(108)  1.40000E-40 1.00000E-40 1.00000E-40 1.00000E-40 1.00000E-40 1.00000E-40
(109)  1.00000E-40 1.00000E-40 1.00000E-40 1.00000E-40 1.00000E-40 1.00000E-40
(110)  1.00000E-40 1.00000E-40 1.00000E-40 1.00000E-40 1.00000E-40 1.00000E-40
(111)  1.00000E-40
(112)  1.43600E-02
(113)  7.17997E+01
(114)  8.99087E-01 7.59848E-02 1.13311E-03 2.37952E-02 1.00000E-40 1.00000E-40
(115)  1.00000E-40 1.00000E-40 1.00000E-40 1.00000E-40 1.00000E-40 1.00000E-40
(116)  1.40000E-40 1.00000E-40 1.00000E-40 1.00000E-40 1.00000E-40 1.00000E-40
(117)  1.00000E-40 1.00000E-40 1.00000E-40 1.00000E-40 1.00000E-40 1.00000E-40
(118)  1.00000E-40 1.00000E-40 1.00000E-40 1.00000E-40 1.00000E-40 1.00000E-40
(119)  1.00000E-40
(120)  1.43600E-02
(121)  7.17997E+01
(122)  9.41745E-01 4.39912E-02 1.13311E-03 1.31307E-02 1.00000E-40 1.00000E-40
(123)  1.00000E-40 1.00000E-40 1.00000E-40 1.00000E-40 1.00000E-40 1.00000E-40
(124)  1.40000E-40 1.00000E-40 1.00000E-40 1.00000E-40 1.00000E-40 1.00000E-40
(125)  1.00000E-40 1.00000E-40 1.00000E-40 1.00000E-40 1.00000E-40 1.00000E-40
(126)  1.00000E-40 1.00000E-40 1.00000E-40 1.00000E-40 1.00000E-40 1.00000E-40
(127)  1.00000E-40
(128)  1.43600E-02
(129)  7.17997E+01
(130)  9.68406E-01 2.39952E-02 1.13311E-03 6.46538E-03 1.00000E-40 1.00000E-40
(131)  1.00000E-40 1.00000E-40 1.00000E-40 1.00000E-40 1.00000E-40 1.00000E-40
(132)  1.40000E-40 1.00000E-40 1.00000E-40 1.00000E-40 1.00000E-40 1.00000E-40
(133)  1.00000E-40 1.00000E-40 1.00000E-40 1.00000E-40 1.00000E-40 1.00000E-40
(134)  1.00000E-40 1.00000E-40 1.00000E-40 1.00000E-40 1.00000E-40 1.00000E-40
(135)  1.00000E-40
(136)  1.43600E-02
(137)  7.17997E+01
(138)  9.73739E-01 1.99960E-02 1.13311E-03 5.13231E-03 1.00000E-40 1.00000E-40
(139)  1.00000E-40 1.00000E-40 1.00000E-40 1.00000E-40 1.00000E-40 1.00000E-40
(140)  1.40000E-40 1.00000E-40 1.00000E-40 1.00000E-40 1.00000E-40 1.00000E-40
```

```
(141)  1.00000E-40 1.00000E-40 1.00000E-40 1.00000E-40 1.00000E-40 1.00000E-40
(142)  1.00000E-40 1.00000E-40 1.00000E-40 1.00000E-40 1.00000E-40 1.00000E-40
(143)  1.00000E-40
(144)  1.43600E-02
(145)  7.17997E+01
(146)  9.79071E-01 1.59968E-02 1.13311E-03 3.79924E-03 1.00000E-40 1.00000E-40
(147)  1.00000E-40 1.00000E-40 1.00000E-40 1.00000E-40 1.00000E-40 1.00000E-40
(148)  1.40000E-40 1.00000E-40 1.00000E-40 1.00000E-40 1.00000E-40 1.00000E-40
(149)  1.00000E-40 1.00000E-40 1.00000E-40 1.00000E-40 1.00000E-40 1.00000E-40
(150)  1.00000E-40 1.00000E-40 1.00000E-40 1.00000E-40 1.00000E-40 1.00000E-40
(151)  1.00000E-40
(152)  1.43600E-02
(153)  7.17997E+01
(154)  9.84403E-01 1.19976E-02 1.13311E-03 2.46618E-03 1.00000E-40 1.00000E-40
(155)  1.00000E-40 1.00000E-40 1.00000E-40 1.00000E-40 1.00000E-40 1.00000E-40
(156)  1.40000E-40 1.00000E-40 1.00000E-40 1.00000E-40 1.00000E-40 1.00000E-40
(157)  1.00000E-40 1.00000E-40 1.00000E-40 1.00000E-40 1.00000E-40 1.00000E-40
(158)  1.00000E-40 1.00000E-40 1.00000E-40 1.00000E-40 1.00000E-40 1.00000E-40
(159)  1.00000E-40
(160)  1.43600E-02
(161)  7.17997E+01
(162)  9.87602E-01 9.59808E-03 1.13311E-03 1.66634E-03 1.00000E-40 1.00000E-40
(163)  1.00000E-40 1.00000E-40 1.00000E-40 1.00000E-40 1.00000E-40 1.00000E-40
(164)  1.40000E-40 1.00000E-40 1.00000E-40 1.00000E-40 1.00000E-40 1.00000E-40
(165)  1.00000E-40 1.00000E-40 1.00000E-40 1.00000E-40 1.00000E-40 1.00000E-40
(166)  1.00000E-40 1.00000E-40 1.00000E-40 1.00000E-40 1.00000E-40 1.00000E-40
(167)  1.00000E-40
(168)  1.43600E-02
(169)  7.17997E+01
(170)  9.89735E-01 7.99840E-03 1.13311E-03 1.13311E-03 1.00000E-40 1.00000E-40
(171)  1.00000E-40 1.00000E-40 1.00000E-40 1.00000E-40 1.00000E-40 1.00000E-40
(172)  1.40000E-40 1.00000E-40 1.00000E-40 1.00000E-40 1.00000E-40 1.00000E-40
(173)  1.00000E-40 1.00000E-40 1.00000E-40 1.00000E-40 1.00000E-40 1.00000E-40
(174)  1.00000E-40 1.00000E-40 1.00000E-40 1.00000E-40 1.00000E-40 1.00000E-40
(175)  1.00000E-40
(176)  1.43600E-02
(177)  7.17997E+01
(178)  9.91068E-01 6.99860E-03 1.13311E-03 7.99842E-04 1.00000E-40 1.00000E-40
(179)  1.00000E-40 1.00000E-40 1.00000E-40 1.00000E-40 1.00000E-40 1.00000E-40
(180)  1.40000E-40 1.00000E-40 1.00000E-40 1.00000E-40 1.00000E-40 1.00000E-40
(181)  1.00000E-40 1.00000E-40 1.00000E-40 1.00000E-40 1.00000E-40 1.00000E-40
(182)  1.00000E-40 1.00000E-40 1.00000E-40 1.00000E-40 1.00000E-40 1.00000E-40
(183)  1.00000E-40
(183)  1.43600E-02
(184)  7.17997E+01
(185)  9.92402E-01 5.99880E-03 1.13311E-03 4.66576E-04 1.00000E-40 1.00000E-40
(186)  1.00000E-40 1.00000E-40 1.00000E-40 1.00000E-40 1.00000E-40 1.00000E-40
(187)  1.40000E-40 1.00000E-40 1.00000E-40 1.00000E-40 1.00000E-40 1.00000E-40
(188)  1.00000E-40 1.00000E-40 1.00000E-40 1.00000E-40 1.00000E-40 1.00000E-40
(189)  1.00000E-40 1.00000E-40 1.00000E-40 1.00000E-40 1.00000E-40 1.00000E-40
(190)  1.00000E-40
(191)  1.43600E-02
(192)  7.17997E+01
(193)  9.93468E-01 5.19896E-03 1.13311E-03 1.99962E-04 1.00000E-40 1.00000E-40
(194)  1.00000E-40 1.00000E-40 1.00000E-40 1.00000E-40 1.00000E-40 1.00000E-40
(195)  1.40000E-40 1.00000E-40 1.00000E-40 1.00000E-40 1.00000E-40 1.00000E-40
(196)  1.00000E-40 1.00000E-40 1.00000E-40 1.00000E-40 1.00000E-40 1.00000E-40
(197)  1.00000E-40 1.00000E-40 1.00000E-40 1.00000E-40 1.00000E-40 1.00000E-40
(198)  1.00000E-40
(199)  1.43600E-02
(200)  7.17997E+01
(201)  9.94001E-01 4.79904E-03 1.13311E-03 6.66556E-05 1.00000E-40 1.00000E-40
(202)  1.00000E-40 1.00000E-40 1.00000E-40 1.00000E-40 1.00000E-40 1.00000E-40
```

```
(203)  1.40000E-40 1.00000E-40 1.00000E-40 1.00000E-40 1.00000E-40 1.00000E-40
(204)  1.00000E-40 1.00000E-40 1.00000E-40 1.00000E-40 1.00000E-40 1.00000E-40
(205)  1.00000E-40 1.00000E-40 1.00000E-40 1.00000E-40 1.00000E-40 1.00000E-40
(206)  1.00000E-40
(207)  1.43600E-02
(208)  7.17997E+01
(209)  9.94267E-01 4.39971E-03 1.26658E-03 6.66648E-05 1.00000E-40 1.00000E-40
(210)  1.00000E-40 1.00000E-40 1.00000E-40 1.00000E-40 1.00000E-40 1.00000E-40
(211)  1.40000E-40 1.00000E-40 1.00000E-40 1.00000E-40 1.00000E-40 1.00000E-40
(212)  1.00000E-40 1.00000E-40 1.00000E-40 1.00000E-40 1.00000E-40 1.00000E-40
(213)  1.00000E-40 1.00000E-40 1.00000E-40 1.00000E-40 1.00000E-40 1.00000E-40
(214)  1.00000E-40
(215)  4.78666E-03
(216)  7.17997E+01
(217)  9.94520E-01 4.15986E-03 1.29996E-03 2.00019E-05 1.00000E-40 1.00000E-40
(218)  1.00000E-40 1.00000E-40 1.00000E-40 1.00000E-40 1.00000E-40 1.00000E-40
(219)  1.40000E-40 1.00000E-40 1.00000E-40 1.00000E-40 1.00000E-40 1.00000E-40
(220)  1.00000E-40 1.00000E-40 1.00000E-40 1.00000E-40 1.00000E-40 1.00000E-40
(221)  1.00000E-40 1.00000E-40 1.00000E-40 1.00000E-40 1.00000E-40 1.00000E-40
(222)  1.00000E-40
(223)  2.39333E-03
```

beginning of the vapor species subblock. The first entry is the species name (10 character maximum), the second entry is the species' enthalpy of formation, and the third entry is the species' entropy of formation. The entropy of formation must be calculated by the user since thermochemical databases such as the JANAF tables, Gurvich, and Barin and O'Knacke [454-456] report only entropy values instead of enthalpy of formation values. The units for all thermochemical data must be kcal/mol for enthalpy of formation values and kcal/mol-K for entropy of formation and heat capacity values.

Line (5) is for the heat capacity terms of the species of Line (4). These values are necessary to correct the enthalpy of formation and entropy at the given system's temperature. There are several equations a species' heat capacity can be fitted to. These are:

(0) $Cp = A_0 + A_1T + A_2/T + A_3\ln(T)$ Equation B.1

(1) $Cp = A_0 + A_1T + A_2T^2 + A_3T^3$ Equation B.2

(2) $Cp = A_0 + A_1T + A_2T^2 + A_3/T^2$ Equation B.3

(4) $Cp = A_0 + A_1T + A_2/T^2 + A_3T^2 + A_4/T^{1/2}$ Equation B.4

The number of the equation used (i.e. 0, 1, 2, or 4 to the left of the equations) is entered at the end of line (5) to identify to the program the heat capacity fitting equation. Equation (3) is not listed because it is written directly into the FORTRAN algorithm to account for the change in the reference state of phosphorus from solid to liquid to gas depending on the system's temperature.

Line (6) tells the program how many of each element are present in the particular species' whose thermochemical data is shown just above these numbers. There must be as many numbers as elements named in Line (3). Furthermore, the order in which the numbers in line (6) are entered must match exactly the order of the element names in line (3). For example, in the case of Figure B.1, the number of hydrogen atoms a given species contains is listed first, the number of chlorine atoms second, the number of boron atoms third, and the number of phosphorus atoms last. Lines (4), (5), and (6) compose a subblock that is unique to the first vapor phase species.

The remainder of lines (7) through (90) simply contain the thermochemical data for other vapor phase species to be included in the equilibrium calculations. Each subbblock has a structure identical to that of lines (4-6). The total number of vapor phase subblocks must match the number of vapor phase species entered in line (2).

An inert species is always listed in the chospec.dat file even if the number of moles of an inert gas is selected to equal zero. By definition, an inert gas changes the each vapor phase species' mole fraction by increasing the overall number of vapor moles in the system but does not participate physically in any reaction. Thus, the inert gas species could be argon or another inert or non-reacting gas. The inert gas is found in lines (91-93) of Figure B.1.

The next section contains the solution species thermochemical information. It is analogous to the vapor species and is broken into subblocks, one for each solution species in the system. If there are no solution species in the system, this subblock(s) will not be entered into the chospec.dat data file. Since there are no solution species in the example shown in Figure B.1 (see the third entry on line (2)) this subblock does not appear in the example chospec.dat data file.

The final subblock containing thermochemical information is for the pure condensed phase species. These can be either liquids or solids. The thermochemical data is entered in the same manner as that for vapor species. The only pure condensed phase in Figure B.1 is solid boron phosphide found in lines (94-96). Lines (97-102) contain thermochemical data for the reference species boron and phosphorus. It is necessary to include this data in the chospec.dat data file to calculate corrected standard state chemical potential of other species containing boron and/or phosphorus. Note that each reference species regardless of its location in the chospec.dat input file is identified by a zero value for its enthalpy and entropy of formation.

Following the thermochemical data for each species are two lines that tell the program what to do. The commands in line (103) are IDEBUG, IOPT, ISS, IWRAP, MAXIT, NMAX, CNVG, TINC, PINC, and RLXMIN. For simplicity these will be described as shown below:

IDEBUG – Debugging Option Parameter

0	Warning messages are printed when problems are encountered in the IMSL subroutines.

1	Prints IDEBUG=0 option plus composition changes and the Gibbs energy for each iteration.
2	Prints IDEBUG=1 option plus matrices and vectors D, DPRME, KEQ, and Q for each iteration.

IOPT – Looping Option Parameter

0	One Pass through routine
1	Temperature loop
2	Pressure loop
3	Composition loop
4	Temperature and composition loops
5	Pressure and composition loops

ISS – Source Zone Steady State Option Parameter

0	Steady state option is inactive
1	Ga/As liquid composition is at steady state with GaAs solid
2	In/P liquid composition is at steady state with InP solid

IWRAP – Data Output Option Parameter

0	Write-out input data, execution diagnostics, and results to a printer
1	IWRAP=0 function plus writes-out a concise wrap-up file
2	No printer output, just a wrap-up file
3	Write a wrap-up file to the printer
7	Create a minimum wrap-up file (to be used with the temperature and composition loop (i.e. ISS=4)).

MAXIT

Maximum number of iterations allowed for the equilibrium program to converge

NMAX

Maximum number of loops allowed for the IOPT parameter

CNVG

Convergence criterion

TINC

Temperature increment for each loop if IOPT = 1

NCL

Number of composition loops

PINC

Pressure increment for each loop if IOPT = 2

Line (104) contains code added to the algorithm by Roger Aparicio to facilitate the calculation of composition loops in a three initial species system (e.g., BCl_3-PCl_3-H_2 or $TiCl_4$-CH_4-H_2). It's parameters are ICOMI, ISP1, ISP2, ISP3, ISLV, ISLVI1, ISLVI2, ISPL1, ISPL2, IFCOMP, CLOOP1, CLOPP2, SLVF1, and SLVF2. These parameters are detailed below:

ISCOMI

0 The composition loop is turned off.

1 The composition loop is turned on.

ISP1

This is the number ID of the first species whose composition is to be varied. The number must correspond with its order in the chospec.dat file. For example, if the user wishes to vary the input BCl_3 partial pressure then this entry should be '29' corresponding to line (29) in Figure B.1.

ISP2

This is the number ID of the second species whose composition is to be varied. Its value should be entered following the same rules as ISP1.

ISP3

In a 3 component system this is the number ID of the reactive gas (e.g., H_2). In the case of the BCl_3-PCl_3-H_2 system, as the mole fraction of BCl_3 and PCl_3 are varied with each loop, the mole fraction of H_2 must be adjusted accordingly to ensure all initial mole fractions sum to unity.

ISLV

This is a switch to turn on/off the computation of the initial mole fraction of a species also identified by ISLV. This mole fraction will be calculated using isvi1, islv2, slvf1, and slvf2. A 0 value is off while any integer greater than zero is on. Typically this function is turned off. Occasionally, to enable the program to converge another species other than the primary reactant species (i.e. BCl_3 or PCl_3 in the BCl_3-PCl_3-H_2 system) must be used in the initial mole fractions. In other words, the equilibrium mole fraction of PCl_3 is too low for it to be used as a component species so its P and Cl atoms must be redistributed to other species. These other species then become the input reactant for the species using this internal computation. The initial mole fraction of the ISLV species is given by the linear combination of the mole fractions of species identified by ISLVI1 and ISLVI2 in conjunction with SLVF1 and SLVF2. The equation equating these species is:

frac(ISLV) = SLVF1*frac(ISLVI1) + SLVF2*frac(ISLVI2). Equation B.5

ISLVI1

Identifies a species whose mole fraction will be used in conjunction with ISLVI2, SLVF1, and SLVF2 to calculate an initial mole fraction for the species identified by the ISLV parameter.

ISLVI2

Similar function as ISLVI1.

ISPL1

This entry instructs the algorithm how many iterations of the loop to make for the first species. For example, to vary the species' mole fraction from 0.01 to 0.1 by 0.01 steps, ISPl1 must equal 10.

ISPL2

This is the same as ISPl1 but for the second species to be varied.

IFCOMP

This is a switch that allows the changes to the two species mole fractions identified by ISP1 and ISP2 to be either linear (e.g., 0.01, 0.02, 0.03, …) or logarithmic (0.1, 0.01, 0.001, …). A '1' value is linear and a '2' value is logarithmic.

CLOOP1

This parameter refers to the factor by which the mole fraction of the first species should be varied. For instance, in the linear example above CLOOP1=0.01 and in the logarithmic case CLOOP1=0.1. CLOOP1 is applied in an additive and multiplicative fashion for the linear and logarithmic cases, respectively. Therefore, if the user wants to change the mole fraction in an ascending manner, he/she must use positive values of CLOOP1 in the linear case and power of ten greater than zero (i.e. 10^1, 10^2, …) for the logarithmic case. If a descending effect is desired, then negative values must be used or powers of ten less than zero (i.e. 10^{-1}, 10^{-2}, ...) for the respective cases.

CLOOP2

This is the same as CLOOP1 but for the second species to be varied.

SLVF1

This is the multiplication factor for the species identified by ISLVI1. These are used in the calculation of the initial mole fraction of the species identified by ISLV.

SLVF2

Similar to SLVF1 except for the species identified by ISLVI2.

The remaining subblocks contain the total number of moles in the vapor phase, the initial mole fraction of each species, the total number of moles in the solution phase, the solution species mole fractions, instructions to the algorithm which activity coefficient solution model to use and that particular model's coefficients, and the number of moles of each pure condensed phase species. The total number of moles in the vapor phase is entered first as shown in line (105). Lines (106-110) instruct the algorithm how the amount of each vapor species present in this total number of moles (i.e. each species' mole fraction). The first entry in line (106) corresponds to the first vapor phase species entered in the chospec.dat file (line 4), the second entry in line (106) corresponds to the second species entered (line 7), etc.. For instance, in Figure B.1 diatomic hydrogen (H_2) has a mole fraction of 7.28454E-01 or 52.3028 moles. Hydrogen chloride gas (HCl) has a mole fraction of 2.03959E-01 or 14.6442 moles. The same procedure is repeated for all other vapor phase species. Since an absolute zero value would cause the algorithm convergence problems (division by zero), species that are not initially present at equilibrium are assigned a value of 1.00000E-40. This is much less the inverse of Avagadro's number (1.66E-24) and therefore, while mathematically not absolute zero, is absolute zero in terms of a species' chemical makeup. Note that the total number of mole fractions entered in lines (106-110) must match exactly the stated number of vapor species in line (2) plus the inert mole fraction.

Since there is no solid solution species in Figure B.1, there are no values given for the total number of moles of the solid solution, each species mole fraction, or the choice of the activity coefficient model to use. The final entry is for the initial total number of moles of the single pure condensed phase (c-B-P). Its value in the example is 1.43600E-02 moles.

The format of the entire chospec.dat data file (i.e. the spacing between numbers, the number of decimal places, the power of 10 notation, the number of entries in each line, etc.) is crucial. If this required format is violated the program will not run correctly. Also, the output files (mcmout.dat, table.dat, wrapup.dat and gibb.dat) must be renamed or deleted after the completion of each program run.

Equilibrium data will be recorded in a file entitled table.dat. This file will consist of the initial conditions of the system and 5 columns containing the equilibrium mole fractions of 5 different species. These columns are repeated for the next 5 species, again for the next 5 species, and so on. These equilibrium mole fractions are listed as a function of the variable changed during the calculation (typically the system temperature). The table.dat file can be imported into a spreadsheet program and manipulated to easily produce graphical representations of the system's equilibrium.

The gibb.dat file can be used to determine several thermodynamic/reaction properties of the system and aid in troubleshooting if convergence is difficult. An example gibb.dat file is shown in Figure B.2 for the homogeneous B-P-H-Cl system.

Figure B.2 Example Gibb.dat output file.

```
initial elemental abundances

 H   .13778E+03
CL   .45051E+01
 B   .93856E-01
 P   .14078E+01



iter=   100   totgibbs=   -.18337E+03
iter=   200   totgibbs=   -.18340E+03
 iter=   265   totgibbs=   -.18340E+03



 temp=  1700.00    # iter=    264
-1.00 H2    (V)  1.00 H-CL   (V)   .00 P2    (V)  1.00 B-H-CL2(V)
 B-CL3  (V)    -.48471E+01    .48471E+01    .14457E-06

 1.00 H2    (V) -1.00 H-CL   (V)   .00 P2    (V)  1.00 B-H-CL2(V)
 B-H2-CL(V)     .13674E+02   -.13674E+02   -.95242E-07

 .50 H2    (V)   .00 H-CL   (V)   .00 P2    (V)   .00 B-H-CL2(V)
 H      (V)     .29800E+02   -.29800E+02    .11063E-09

 1.00 H2    (V)   .00 H-CL   (V)   .50 P2    (V)   .00 B-H-CL2(V)
 P-H2   (V)     .24883E+02   -.24883E+02    .22179E-09

 1.50 H2    (V)   .00 H-CL   (V)   .50 P2    (V)   .00 B-H-CL2(V)
 P-H3   (V)     .26799E+02   -.26799E+02    .33332E-09

 .50 H2    (V)   .00 H-CL   (V)   .50 P2    (V)   .00 B-H-CL2(V)
 P-H    (V)     .29571E+02   -.29571E+02    .10866E-09

 .00 H2    (V)   .00 H-CL   (V)  2.00 P2    (V)   .00 B-H-CL2(V)
 P4     (V)     .63537E+01   -.63537E+01   -.10085E-10

 2.00 H2    (V) -2.00 H-CL   (V)   .00 P2    (V)  1.00 B-H-CL2(V)
 B-H3   (V)     .33848E+02   -.33848E+02    .52732E-07

 -.50 H2    (V)  1.00 H-CL   (V)   .00 P2    (V)   .00 B-H-CL2(V)
 CL     (V)     .30660E+02   -.30660E+02   -.35658E-08

 .00 H2    (V) -1.00 H-CL   (V)   .00 P2    (V)  1.00 B-H-CL2(V)
 B-CL   (V)     .26496E+02   -.26496E+02    .49363E-07

 .00 H2    (V)   .00 H-CL   (V)   .50 P2    (V)   .00 B-H-CL2(V)
 P      (V)     .35204E+02   -.35204E+02   -.32817E-11

 .00 H2    (V)   .00 H-CL   (V)  1.50 P2    (V)   .00 B-H-CL2(V)
 P3     (V)     .22489E+02   -.22489E+02   -.75890E-11
```

```
(50)
(51)      -.50 H2    (V)   .00 H-CL  (V)   .00 P2    (V)  1.00 B-H-CL2(V)
(52)      B-CL2  (V)     .24472E+02   -.24472E+02    .46798E-07
(53)
(54)      -.50 H2    (V)  1.00 H-CL  (V)   .50 P2    (V)   .00 B-H-CL2(V)
(55)       P-CL   (V)     .33172E+02   -.33172E+02   -.35662E-08
(56)
(57)       .50 H2    (V) -1.00 H-CL  (V)   .00 P2    (V)  1.00 B-H-CL2(V)
(58)       B-H-CL (V)     .35923E+02   -.35923E+02    .50547E-07
(59)
(60)      1.50 H2    (V) -2.00 H-CL  (V)   .00 P2    (V)  1.00 B-H-CL2(V)
(61)       B-H2   (V)     .55378E+02   -.55378E+02    .54288E-07
(62)
(63)     -1.00 H2    (V)   .00 H-CL  (V)   .00 P2    (V)  2.00 B-H-CL2(V)
(64)       B2-CL4 (V)     .16763E+02   -.16763E+02    .93877E-07
(65)
(66)     -1.00 H2    (V)  2.00 H-CL  (V)   .50 P2    (V)   .00 B-H-CL2(V)
(67)       P-CL2  (V)     .38412E+02   -.38412E+02   -.71286E-08
(68)
(69)      1.00 H2    (V) -2.00 H-CL  (V)   .00 P2    (V)  1.00 B-H-CL2(V)
(70)       B-H    (V)     .63126E+02   -.63126E+02    .54179E-07
(71)
(72)     -1.00 H2    (V)  2.00 H-CL  (V)   .00 P2    (V)   .00 B-H-CL2(V)
(73)       CL2    (V)     .50084E+02   -.50084E+02   -.71265E-08
(74)
(75)     -1.50 H2    (V)  3.00 H-CL  (V)   .50 P2    (V)   .00 B-H-CL2(V)
(76)       P-CL3  (V)     .39896E+02   -.39896E+02   -.10691E-07
(77)
(78)       .50 H2    (V) -2.00 H-CL  (V)   .00 P2    (V)  1.00 B-H-CL2(V)
(79)       B      (V)     .71438E+02   -.71438E+02    .54068E-07
(80)
(81)      4.00 H2    (V) -4.00 H-CL  (V)   .00 P2    (V)  2.00 B-H-CL2(V)
(82)       B2-H6  (V)     .82676E+02   -.82676E+02    .10851E-06
(82)
(83)      1.00 H2    (V) -4.00 H-CL  (V)   .00 P2    (V)  2.00 B-H-CL2(V)
(84)       B2     (V)     .11668E+03   -.11668E+03    .10814E-06
(85)
(86)      7.00 H2    (V) ***** H-CL  (V)   .00 P2    (V)  5.00 B-H-CL2(V)
(87)       B5-H9  (V)     .15940E+03   -.15940E+03    .27135E-06
(88)
(89)     -2.50 H2    (V)  5.00 H-CL  (V)   .50 P2    (V)   .00 B-H-CL2(V)
(90)       P-CL5  (V)     .13354E+03   -.13354E+03   -.17817E-07
(91)
(92)
(93)         final elemental abundances and difference (b-b*)
(94)        H    .13778E+03   -.25580E-12
(95)       CL    .45051E+01   -.88818E-15
(96)        B    .93856E-01   -.20817E-15
(97)        P    .14078E+01   -.59952E-14
```

Lines (1-6) contain the initial elemental abundances of each element specified in line (3) of the chospec.dat file. Lines (9-11) inform the user of the progression towards an equilibrium value at iteration intervals of 100. For this particular example convergence occurred at iteration number 265. Line (14) informs the reader the equilibrium temperature (if a temperature loop is selected) and, again, the iteration where convergence occurred.

Lines (15-16) are representative of the body of the gibb.dat file. Shown in these lines are formation reactions of one of the non-component species. In the case of lines (15-16) this non-component species is $BCl_3(v)$. As described in section 1.3.2 of this dissertation, the species in the system are divided into components, equal in number to the elements present (in this case 4), and non-components, the rest. There will be as many formation reactions as non-component species. In each formation reaction one mole of the non-component species (i.e. species in lines (16, 19, 22, ...)) is produced from linear combinations of the same four component species (species in line (15) which are the same for lines (18, 21, 24, ...)). At equilibrium, the Gibbs free energies for each of these reactions must be, in principle, zero. Practically this is not computationally possible, so a convergence criterion is selected. The user in line (103) of the chospec.dat file specifies this criterion. In Figure B.1 its value is 1.0E-06.

The Gibbs free energy of reaction is the sum of two components:

$$\Delta G_{rxn} = \Delta G^{o}_{rxn} + RT\ln(K_{rxn}) \qquad \text{Equation B.6}$$

At equilibrium this equation is:

$$\Delta G^{o}_{rxn} + RT\ln(K_{rxn}) \leq 1.0\text{E-06} \qquad \text{Equation B.7}$$

where:

$\Delta G^o_{rxn} = \Sigma(\nu_i \mu^o_i)$, where ν_i is the stoichiometric coefficient and μ^o_i is the standard state chemical potential which is calculated by the program from the $\Delta H^o_{i,\ 298K}$, $\Delta S^o_{i,\ 298K}$, and Cp^o_i values that are input into the chospec.dat file.

and

$RT\ln(K_{rxn}) = \Pi(X_i^{\nu i})$, where ν_i is as before and X_i is the species mole fraction.

The gibb.dat file can be used to obtain both the ΔG^o_{rxn} and $RT\ln(K_{rxn})$ values for each species at each equilibrium condition. ΔG^o_{rxn} is the first number of line (16). It represents the thermodynamic data that was entered into the chospec.dat data file. It is constant for a given set of species. $RT\ln(K_{rxn})$ is the second number of line (16). It represents the program's calculation of the equilibrium state (i.e. all the species mole fractions). This is what the program varies to find the equilibrium state. The third and final number of line (16) is the sum of the ΔG^o_{rxn} and $RT\ln(K_{rxn})$ terms. It gives verification that the criterion for equilibrium has been satisfied or, in the case of non-convergence, which formation reaction, and thus which non-component species, is causing non-convergence.

Similar information is given for each of the remaining non-component species of lines (18-90). Lines (93-97) contain the final elemental abundances calculated by the program and the difference between the initial and final values for each element.

The mcmout.dat and wrapup.dat files, though generated with each program run, are rarely used due to the limited information each contains.

APPENDIX C
FORTRAN SOURCE CODE FOR ENSURING ACCURATE THERMOCHEMICAL DATA TRANSFER TO CHOSPEC.DAT INPUT FILE

```
C  MCMPEC.STOIC .... MULTICOMPONENT MULTIPHASE EQUILIBRIUM CODE
C               STOICIOMETRIC FORMULATION
C
C
      DIMENSION A(50,13),A0(50),A1(50),A2(50),A3(50),A4(50),DH(50),
     &         DH0(50),DS0(50),FRAC(50),FRACIN(50),
     &         ICP(50),INERT(3),STDCP(50),TOTMC(50),ireac(13)
      INTEGER PHASE(50,3),SPECIE(50,3),TITLE(20),V,S,C,E,VP1,VPS,
     &       VPSP1,VSC,VSCE,
     &       ELMNT(13)/13*' '/,VAPOR(3)/'  V','APO','R  '/,
     &       SOLN(3)/'SOL','UTI','ON '/,COND(3)/'CON','DEN','SED'/
C
C  A(I,J)   : ELEMENTAL ABUNDANCE MATRIX
C  B(J)     : TOTAL NUMBER OF GRAM-MOLES OF ELEMENT J
C  DH0(I)   : ENTHALPY OF FORMATION OF SPECIES I
C  DS0(I)   : ENTROPY OF FORMATION OF SPECIES I
C  STDCP(I) : STANDARD CHEMICAL POTENTIAL OF SPECIES I
C
C  **********  HEAT CAPACITY CORRELATIONS  **********
C  ICP(I)=0 : CP(I) = A0(I) + A1(I)*T + A2(I)/T**2 + A3(I)*ALOG(T)
C  ICP(I)=1 : CP(I) = A0(I) + A1(I)*T + A2(I)*T**2 + A3(I)*T**3
C  ICP(I)=2 : CP(I) = A0(I) + A1(I)*T + A2(I)*T**2 + A3(I)/T**2
C
      OPEN(UNIT=5,FILE='CHOSPEC.DAT',STATUS='OLD')
      open(unit=9,file='Jan.dat',status='new')
      igib=9
      IRD=5
      IDIM1=50
      IDIM2=13
      FRCZIN=0.0
      DH0Z=0.0
      DS0Z=0.0
      A0Z=0.0
      A1Z=0.0
      A2Z=0.0
      A3Z=0.0
      TOTMV=0.0
C
C  READ TITLE
C
```

```
      READ(IRD,5) (TITLE(K),K=1,20)
    5 FORMAT(20A4)
C
C  NUMBER OF ELEMENTS, VAPOR SPECIES, SOLUTION SPECIES,
C  CONDENSED PURE PHASES, SYSTEM TEMPERATURE (K) AND PRESSURE (PA)
C
      READ(IRD,10) E,V,S,C,T,P,T0,P0,IX
   10 FORMAT(4I5,4F10.0,I5)
      VP1=V+1
      VPS=V+S
      VPSP1=V+S+1
      VSC=V+S+C
      VSCE=V+S+C+E
C
C  READ ELEMENTS
C
      READ(IRD,15) (ELMNT(J),J=1,E)
   15 FORMAT(13(1X,A2))
C
C  VAPOR SPECIES INFORMATION
C
      IF(V.EQ.0) GO TO 118
      DO 110 I=1,V
      READ(IRD,20) (SPECIE(I,K),K=1,3),DH0(I),DS0(I)
      READ(IRD,21) A0(I),A1(I),A2(I),A3(I),A4(I),ICP(I)
      READ(IRD,22) (A(I,J),J=1,13)
   20 FORMAT(3A4,2E12.5)
   21 FORMAT(5E12.5,I2)
   22 FORMAT(13(F5.0,1X))
      DO 110 J=1,3
      PHASE(I,J)=VAPOR(J)
  110 CONTINUE
C
C  INERT SPECIE
C
      READ(IRD,20) (INERT(K),K=1,3),DH0Z,DS0Z
      READ(IRD,21) A0Z,A1Z,A2Z,A3Z,A4Z,ICPZ
      READ(IRD,22) DUMMY
  118 CONTINUE
C
C  SOLUTION SPECIES INFORMATION
C
      IF(S.EQ.0) GO TO 125
      DO 120 I=VP1,VPS
      READ(IRD,20) (SPECIE(I,K),K=1,3),DH0(I),DS0(I)
      READ(IRD,21) A0(I),A1(I),A2(I),A3(I),A4(I),ICP(I)
      READ(IRD,22) (A(I,J),J=1,13)
      DO 120 J=1,3
      PHASE(I,J)=SOLN(J)
  120 CONTINUE
  125 CONTINUE
```

```
C
C  CONDENSED PHASE DATA
C
      IF(C.EQ.0) GO TO 135
      DO 130 I=VPSP1,VSC
      READ(IRD,20) (SPECIE(I,K),K=1,3),DH0(I),DS0(I)
      READ(IRD,21) A0(I),A1(I),A2(I),A3(I),A4(I),ICP(I)
      READ(IRD,22) (A(I,J),J=1,13)
      FRAC(I)=1.0
      FRACIN(I)=1.0
      DO 130 J=1,3
      PHASE(I,J)=COND(J)
  130 CONTINUE
  135 CONTINUE
c
c  read additional reference species to compute st. st. chem. pot.
c
      IF(ix.EQ.0) GO TO 131
      DO 132 I=vsc+1,vsc+ix
      READ(IRD,20) (SPECIE(I,K),K=1,3),DH0(I),DS0(I)
      READ(IRD,21) A0(I),A1(I),A2(I),A3(I),A4(I),ICP(I)
      READ(IRD,22) (A(I,J),J=1,13)
  132 CONTINUE
  131 CONTINUE
C
C  MAXIMUM NUMBER OF ITERATIONS, CONVERGENCE CRITERION AND OPTIONS
C
      READ(IRD,136) IDEBUG,IOPT,ISS,IWRAP,MAXIT,NMAX,CNVG,TINC,PINC,
     &              RLXMIN
  136 FORMAT(6I5,E10.1,3F10.1)
C
C  SET THE LOOP LIMITS FOR THE TEMPERATURE, PRESSURE AND COMPOSITION
C  LOOPS.  THE COMPOSITION LOOP STARTS HERE
C
      NTP=1
      IF(IOPT.EQ.1.OR.IOPT.EQ.2) NTP=NMAX
C
C  TOTAL NUMBER OF MOLES OF VAPOR AND MOLE FRACTIONS
C
      IF(V.EQ.0) GO TO 138
      READ(IRD,137) TOTMV
      READ(IRD,137) (FRACIN(I),I=1,V),FRCZIN
  137 FORMAT(6E12.5)
C
C  TOTAL NUMBER OF MOLES OF SOLUTION SPECIES, MOLE FRACTIONS
C  AND EXCESS FREE ENERGY CORRELATION PARAMETERS
C
  138 CONTINUE
      IF(S.EQ.0) GO TO 140
      READ(IRD,137) TOTMS
      READ(IRD,137) (FRACIN(I),I=VP1,VPS)
      READ(IRD,139) IXSCOR,AXS,BXS
  139 FORMAT(I5,2E12.5)
  140 CONTINUE
C
C  TOTAL NUMBER OF MOLES IN PURE CONDENSED PHASES
C
      IF(C.EQ.0) GO TO 142
      READ(IRD,137) (TOTMC(I),I=VPSP1,VSC)
  142 CONTINUE
C
C  THE TEMPERATURE AND PRESSURE LOOPS BEGIN HERE
C
      DO 2000 ITP=1,NTP
      IF(IOPT.EQ.1.AND.ITP.GT.1) T=T+TINC
C
C  CALCULATE THERMAL DATA
C
C+++++++++++++++++++++++++++++++++++++++++++++++++++++++++++++++++++++++
C
      DT=T-T0
      DT2=T**2-T0**2
      DT3=T**3-T0**3
      DT4=T**4-T0**4
      DTM1=1.0/T-1.0/T0
      DTM2=1.0/T/T-1.0/T0/T0
      DLNT=ALOG(T)-ALOG(T0)
      DLNT2=ALOG(T)**2-ALOG(T0)**2
      DTLNT=T*ALOG(T)-T0*ALOG(T0)
      DHPT=T**0.5-T0**0.5
      DIHPT=(1.0/(T**0.5))-(1.0/(T0**0.5))
C
C CHEMICAL POTENTIALS FOR THE VAPOR, SOLUTION AND CONDENSED PHASES
C
      WRITE(IGIB,*)'    '
      WRITE(IGIB,*)'    '
      write(igib,301) T
  301 format(2x,'Temperature (K) =',f9.2)
      WRITE(IGIB,*)'    '
      WRITE(IGIB,*)'   SPECIES             HC            DH
     &DS         ststchp'
      WRITE(IGIB,*)'    '
      DO 100 I=1,VSC+ix
      DELH=A0(I)*DT+A1(I)*DT2/2.-A2(I)*DTM1+A3(I)*(DTLNT-DT)
      DELS=A0(I)*DLNT+A1(I)*DT-A2(I)*DTM2/2.+A3(I)*DLNT2/2.
      IF(ICP(I).EQ.1) DELH=A0(I)*DT+A1(I)*DT2/2.+A2(I)*DT3/3.
     &                 +A3(I)*DT4/4.
      IF(ICP(I).EQ.1) DELS=A0(I)*DLNT+A1(I)*DT+A2(I)*DT2/2.
     &                 +A3(I)*DT3/3.
      IF(ICP(I).EQ.2) DELH=A0(I)*DT+A1(I)*DT2/2.+A2(I)*DT3/3.
     &                 -A3(I)*DTM1
      IF(ICP(I).EQ.2) DELS=A0(I)*DLNT+A1(I)*DT+A2(I)*DT2/2.
     &                -A3(I)*DTM2/2.
      IF(ICP(I).EQ.4) DELH=A0(I)*DT+A1(I)*DT2/2.-A2(I)*DTM1
     &                +A3(I)*DT3/3.+A4(I)*DHPT/0.5
      IF(ICP(I).EQ.4) DELS=A0(I)*DLNT+A1(I)*DT-A2(I)*DTM2/2.
     &                +A3(I)*DT2/2.-A4(I)*D1HPT/0.5
      delhj=delh*4.184
      delsj=dels*4.184
c      if(i.eq.13)write(*,*)T,delhj,delsj
      IF(ICP(I).EQ.3) THEN
        IF(T.LE.317.3) THEN
           DELH=(15.49918*(T-298.15)+(0.027908/2.0)*(T**2-
     &      (298.15)**2))/4184.0
           DELS=(15.49918*(alog(T/298.15))+0.027908*(T-298.15))
     &       /4184.0
            delhj=delh*4.184
            delsj=dels*4.184
C            write(*,*) delhj,delsj
         ELSEIF(T.GT.317.3.and.T.LE.1180.0) Then
            DELH=((26.326*(T-317.3))+15.49918*(317.3-298.15)
     &           +(0.027908/2.0)*((317.3)**2-(298.15)**2)+657.5)
     &           /4184.0
            DELS=(26.326*ALOG(T/317.3)+15.49918*(alog(317.3/298.15))
     &           +0.027908*(317.3-298.15)+2.0728)/4184.0
            delhj=delh*4.184
            delsj=dels*4.184
c            write(*,*) delhj,delsj
         ELSE
            DELH=((26.326*(1180.0-317.3))+15.49918*(317.3-298.15)
     &           +(0.027908/2.0)*((317.3)**2-(298.15)**2)
     &           +18.6*(T-1180.0)+64390.0)/4184.0
            DELS=(26.326*ALOG(1180.0/317.3)+15.49918*
     &           (alog(317.3/298.15))+0.027908*(317.3-298.15)
     &           +18.6*alog(T/1180.0)+56.083)/4184.0
            delhj=delh*4.184
            delsj=dels*4.184
c            write(*,*) delhj,delsj
        ENDIF
      ELSEIF(ICP(I).EQ.5) THEN
        IF(T.LE.332.5) THEN
           DELH=(78.76570*(T-298.15)-(0.0104196/2.0)*((T**2)-
     &      ((298.15)**2)))/4184.0
           DELS=(78.76570*(alog(T/298.15))-0.0104196*(T-298.15))
     &       /4184.0
            delhj=delh*4.184
            delsj=dels*4.184
            write(*,*) delhj,delsj
         ELSE
            DELH=(33.8979*(T-332.5)+(0.0106738/2)*((T**2)-
     &           (332.5)**2)-(0.0000113343/3)*((T**3)-((332.5)**3))+
     &           (0.00000000550009/4)*((T**4)-((332.5)**4))
     &           -(0.00000000000936565/5)*((T**5)-((332.5)**5))
     &         +78.76570*(332.5-298.15)-(0.0104196/2.0)*
     &         (((332.5)**2)-((298.15)**2))+29564.0)/4184.0
            DELS=(33.8979*ALOG(T/332.5)+0.0106738*(T-332.15)-
     &         (0.0000113343/2)*((T**2)-((332.5)**2))+
     &         (0.00000000550009/3)*((T**3)-((332.5)**3))-
     &         (0.00000000000936565/4)*((T**4)-((332.5)**4))+
     &         78.76570*(alog(332.5/298.15))-
     &         0.0104196*(332.5-298.15)+88.911)/4184.0
            delhj=delh*4.184
            delsj=dels*4.184
            write(*,*) T,delhj,delsj
         ENDIF
      ELSE
         GO TO 150
      ENDIF
  150 STDCP(I)=DH0(I)+DELH-T*(DS0(I)+DELS)
C
C++++++++++++++++++++++++++++++++++++++++++++++++++++++++++++++++++++++++++
C
      HC=A0(I)+A1(I)*T+A2(I)/T**2+A3(I)*LOG(T)
      IF(ICP(I).EQ.1) HC=A0(I)+A1(I)*T+A2(I)*T**2+A3(I)*T**3
      IF(ICP(I).EQ.2) HC=A0(I)+A1(I)*T+A2(I)*T**2+A3(I)/T**2
      IF(ICP(I).EQ.4) HC=A0(I)+A1(I)*T+A2(I)/T**2+A3(I)*T**2+
     &            A4(I)/T**0.5
      IF(ICP(I).EQ.3) THEN
         IF(T.LE.317.3) THEN
            HC=(15.49918+0.027908*T)/4184.0
         ELSEIF(T.GT.317.3.AND.T.LE.1180) THEN
            HC=26.326/4184.0
         ELSE
            HC=18.620/4184.0
         ENDIF
      ELSEIF(ICP(I).EQ.5) THEN
         IF(T.LE.332.5) THEN
            HC=(78.7657-0.0104196*T)/4184.0
         ELSE
            HC=(33.8979+0.0106738*T-0.0000113343*(T**2)+
     &        0.00000000550009*(T**3)-0.00000000000936565*(T**4))
     &        /4184.0
         ENDIF
      ELSE
         GO TO 250
      ENDIF
  250 CONTINUE
      DH(I)=DH0(I)+DELH
      DS=DS0(I)+DELS
      HC=4184*HC
      DH(I)=4.184*DH(I)
      DS=4184*DS
      stdcp(i)=4.184*stdcp(i)
      write(igib,801) (specie(i,j),j=1,3),HC,DH(I),DS,stdcp(i)
```

```
 801 format(2x,3a4,4(2x,f12.2))
C
C++++++++++++++++++++++++++++++++++++++++++++++++++++++++++++++++++++++
C
 100 CONTINUE
c
c identify reference species
c
      do 200 i=1,e
      do 300 j=1,vsc+ix
      if(dh0(j).ne.0.0.or.a(j,i).eq.0.0) go to 300
      ireac(i)=j
      go to 200
 300 continue
 200 continue
c
c correct standard state chem. pot. for all species
c
      WRITE(IGIB,*)'    '
      WRITE(IGIB,*)'   SPECIES          DHc        STSTCHPc'
      WRITE(IGIB,*)'  '
      do 400 i=1,vsc+ix
      do 500 j=1,e
      k=ireac(j)
      if(i.eq.k) go to 400
      stdcp(i)=stdcp(i)-(a(i,j)/a(k,j))*stdcp(k)
      dh(i)=dh(i)-(a(i,j)/a(k,j))*dh(k)
 500 continue
 400 continue
      do 600 i=1,e
      k=ireac(i)
      stdcp(k)=0.0
      dh(k)=0.0
 600 continue
      do 700 i=1,vsc+ix
      write(igib,802) (specie(i,j),j=1,3),dh(i),stdcp(i)
 802 format(2x,3a4,2(2x,f12.2))
 700 continue
C
C  INERT CHEMICAL POTENTIAL
C
      DELH=A0Z*DT+A1Z*DT2/2.-A2Z*DTM1+A3Z*(DTLNT-DT)
      DELS=A0Z*DLNT+A1Z*DT-A2Z*DTM2/2.+A3Z*DLNT2/2.
      IF(ICPZ.EQ.1) DELH=A0Z*DT+A1Z*DT2/2.+A2Z*DT3/3.
     &              +A3Z*DT4/4.
      IF(ICPZ.EQ.1) DELS=A0Z*DLNT+A1Z*DT+A2Z*DT2/2.
     &              +A3Z*DT3/3.
      STDCPZ=DH0Z+DELH-T*(DS0Z+DELS)
C
C++++++++++++++++++++++++++++++++++++++++++++++++++++++++++++++++++++++
C
```

```
2000 CONTINUE
     END
```

APPENDIX D
USER GUIDE FOR THE FORTRAN SOURCE CODE OF APPENDIX C

The FORTRAN source code shown in Appendix C is intended to facilitate accurate thermochemical data transfer from the various thermochemical databases employed (i.e. JANAF tables, Gurvich, etc.) to the chospec.dat datafile. The chospec.dat data file described in Appendix B must first be create. Upon execution of the algorithm given in Appendix C, a series of thermochemical values will be calculated for each species at the temperature and pressure specified in line (2) of the chospec.dat data file. This data will be each species' heat capacity (HC), enthalpy of formation (DH), entropy of formation (DS), standard state chemical potential (ststchp), corrected enthalpy of formation value (DHc), and a corrected standard state chemical potential (STSTCHPc). The corrected enthalpy of formation should correspond very closely to the enthalpy of formation given in the thermochemical database from which that species' thermochemical data was taken. The corrected standard state chemical potential should, likewise, correspond very closely to the Gibbs energy of formation value given in the same database. If one or both of these calculated values significantly differs from the thermochemical data of the database then the outlying species' thermochemical data in the chospec.dat data file should be checked. An example jan.dat output file is shown in Figure D.1

The FORTRAN code given in Appendix C was created to assist in troubleshooting errors in the entered thermochemical data. Since all data must be entered manually, the likelihood of transposing a single number, moving a decimal point a single unit left or right, etc. was high. This allows the user to quickly and conveniently assess his/her input thermochemical data for each species and have a high degree of confidence of its accuracy. However, it must be emphasized that this program can only be used a check to determine if the thermochemical data was input correctly. It can not be used to determine the accuracy of the species' data in the chosen database.

Figure D.1 Example jan.dat output file

```
Temperature (K) =  1000.00

 SPECIES          HC        DH        DS      ststchp

 H2     (V)      30.28     20.70     35.55    -14.84
 H-CL   (V)      31.63    -71.25     45.93   -117.18
 B-H3   (V)      58.31    137.27     40.48     96.79
 P-H3   (V)      64.19     42.08     32.90      9.19
 H      (V)      20.79    232.59     74.53    158.06
 CL     (V)      22.22    137.11     80.79     56.32
 CL2    (V)      37.44     25.57     43.70    -18.13
 B-CL   (V)      36.89    202.60    137.70     64.90
 B-CL2  (V)      56.78      9.53    104.95    -95.42
 B-CL3  (V)      79.91   -360.40     34.89   -395.30
 B-H    (V)      33.12    464.44    137.25    327.19
 B-H2   (V)      49.90    362.59    107.77    254.81
 B-H-CL2(V)      73.48   -208.28     48.39   -256.67
 B-H2-CL(V)      65.76    -40.72     49.38    -90.10
 B-H-CL (V)      50.63    176.75    111.05     65.70
 B2-CL4 (V)     123.79   -408.69     36.20   -444.89
 B2-H6  (V)     135.83    109.45    -55.41    164.86
 B5-H9  (V)     253.74    206.80   -131.49    338.29
 B      (V)      20.80    579.60    172.61    407.00
 B2     (V)      40.99    863.06    235.48    627.59
 P      (V)      20.78    331.09    147.27    183.82
 P2     (V)      36.86    168.76    178.10     -9.34
 P3     (V)      61.02    250.93    209.82     41.11
 P4     (V)      81.42    113.28    207.74    -94.46
 P-H    (V)      33.03    252.41    126.79    125.63
 P-H2   (V)      46.82    148.25     88.78     59.47
 P-CL   (V)      37.47    160.14    127.89     32.26
 P-CL2  (V)      57.48    -15.18     87.70   -102.88
 P-CL3  (V)      81.92   -233.98     30.62   -264.60
 P-CL5  (V)     130.96   -287.42    -80.74   -206.68
 c-B-P(SOL)      50.00    -87.29     26.07   -113.36
 B    (SOL)      24.94     14.38     23.24     -8.86
 P    (SOL)      26.33     19.09     33.79    -14.70
```

SPECIES	DHc	STSTCHPc
H2 (V)	.00	.00
H-CL (V)	-94.39	-100.69
B-H3 (V)	91.84	127.92
P-H3 (V)	-8.07	46.15
H (V)	222.23	165.48
CL (V)	124.33	65.39
CL2 (V)	.00	.00
B-CL (V)	175.44	82.83
B-CL2 (V)	-30.41	-68.42
B-CL3 (V)	-413.13	-359.23
B-H (V)	439.72	343.48
B-H2 (V)	327.51	278.52
B-H-CL2(V)	-258.57	-222.25
B-H2-CL(V)	-88.58	-57.32
B-H-CL (V)	139.24	91.06
B2-CL4 (V)	-488.57	-390.89
B2-H6 (V)	18.59	227.12
B5-H9 (V)	41.75	449.40
B (V)	565.23	415.86
B2 (V)	834.31	645.32
P (V)	312.00	198.52
P2 (V)	130.57	20.06
P3 (V)	193.65	85.21
P4 (V)	36.92	-35.66
P-H (V)	222.97	147.75
P-H2 (V)	108.45	89.01
P-CL (V)	128.27	56.02
P-CL2 (V)	-59.83	-70.05
P-CL3 (V)	-291.42	-222.70
P-CL5 (V)	-370.43	-146.64
c-B-P(SOL)	-120.76	-89.79
B (SOL)	.00	.00
P (SOL)	.00	.00

BIOGRAPHICAL SKETCH

Steven W. Johnston was born on December 8, 1972, in Indianapolis, Indiana. He is the son of Wayne and Kay Johnston and has an older sister Stephanie and younger sister Andrea. He later lived with his family in Omaha, Nebraska; Alexandria, Alabama; Nashville, Tennessee; and Orangeburg, South Carolina before finally settling down in Columbia, South Carolina. He graduated from Columbia's Irmo High School in 1991 with highest honors. Following this he attended the Georgia Institute of Technology from 1991 to 1993 and the University of South Carolina from 1993 to 1995. In May 1995 he graduated cum laude with a B.S. in chemical engineering. During the spring of 1995 he was selected to receive the Southeastern Regional Fellowship in Chemical Engineering for a total of five years. In August 1995 he started graduate school at the University of Florida to pursue his doctoral degree in chemical engineering. Upon graduation he will work as a senior process engineer at Intel Corporation in Santa Clara, California.

I certify that I have read this study and that in my opinion it conforms to acceptable standards of scholarly presentation and is fully adequate, in scope and quality, as a dissertation for the degree of Doctor of Philosophy.

Timothy J. Anderson, Chairman
Professor of Chemical Engineering

I certify that I have read this study and that in my opinion it conforms to acceptable standards of scholarly presentation and is fully adequate, in scope and quality, as a dissertation for the degree of Doctor of Philosophy.

Lisa McElwee-White
Professor of Chemistry

I certify that I have read this study and that in my opinion it conforms to acceptable standards of scholarly presentation and is fully adequate, in scope and quality, as a dissertation for the degree of Doctor of Philosophy.

Fan Ren
Professor of Chemical Engineering

I certify that I have read this study and that in my opinion it conforms to acceptable standards of scholarly presentation and is fully adequate, in scope and quality, as a dissertation for the degree of Doctor of Philosophy.

Spyros Svoronos
Professor of Chemical Engineering

I certify that I have read this study and that in my opinion it conforms to acceptable standards of scholarly presentation and is fully adequate, in scope and quality, as a dissertation for the degree of Doctor of Philosophy.

Paul H Holloway

Paul H. Holloway
Professor of Materials Science and
Engineering

This dissertation was submitted to the Graduate Faculty of the College of Engineering and to the Graduate School and was accepted as partial fulfillment of the requirements for the degree of Doctor of Philosophy.

August 2000

M. J. Ohanian
Interim Dean, College of Engineering

Winfred M. Phillips
Dean, Graduate School

937 F8 566
10/16/00 34760